UNIVERSIDAD COMPLUTENSE DE MADRID

FACULTAD DE CIENCIAS FÍSICAS

Departamento de Física de la Tierra, Astronomía y Astrofísica I,

TESIS DOCTORAL

Interdecadal changes in ocean teleconnections with Sahel: Implications in rainfall predictability

Cambios interdecadales en las teleconexiones de los océanos con el Sahel: implicaciones en la predictibililidad de la lluvia

MEMORIA PARA OPTAR AL GRADO DE DOCTOR

PRESENTADA POR

Roberto Suárez Moreno

Directora

Belén Rodríguez de Fonseca

Madrid, 2018

UNIVERSIDAD COMPLUTENSE DE MADRID

FACULTAD DE CIENCIAS FÍSICAS

DEPARTAMENTO DE FÍSICA DE LA TIERRA, ASTRONOMÍA Y ASTROFÍSICA I

INTERDECADAL CHANGES IN OCEAN TELECONNECTIONS WITH THE SAHEL. IMPLICATIONS IN RAINFALL PREDICTABILITY

CAMBIOS INTERDECADALES EN LAS TELECONEXIONES DE LOS OCÉANOS CON EL SAHEL. IMPLICACIONES EN LA PREDICTIBILIDAD DE LA LLUVIA

Dirigida por:

Dra. Belén Rodríguez de Fonseca

Profesora titular UCM

Memoria presentada por:

Roberto Suárez Moreno

para optar al grado de Doctor en Física

Madrid, 2017

The research leading to this thesis was supported by the PREFACE-EU project (EU FP7/2007-2013) under grant agreement no. 603521, the Spanish national project MULCLIVAR (CGL2012-38923-C02-01), and the VR: 101/11 project from the VIII UCM Call for Cooperation and Development projects.

La investigación que ha dado lugar a esta tesis ha sido financiada por el proyecto europeo PREFACE-EU project (EU FP7/2007-2013) bajo el acuerdo de subvención no. 603521, el proyecto nacional español MULCLIVAR (CGL2012-38923-C02-01), y el proyecto de la VIII llamada de proyectos de cooperación y desarrollo UCM.

A David

Some people feel the rain. Others just get wet.

Algunas personas sienten la lluvia. Otros sólo se mojan.

Bob Marley

Agradecimientos

Gracias al viento, a la Casita Azul, a la playa de Bolonia, a ese claro entre las nubes. Gracias también a la roca en todas sus variantes, a la piedra del camino, a cierto tipo de música electrónica, a toda la música clásica, al año 1973, al pueblo de Azañón y sus gentes, a la Gazelle, a la isla de Goree, a la Madre de Dragones, a Ragnar Lothbrok, a Walter White, a los detectives Martin Hart y Rustin Cohle, al traductor de Google y a un sinfín de pequeños detalles que convierten mi mundo en un lugar especial.

Gracias a todos aquellos que sabéis o intuís a qué me refiero en el párrafo anterior, porque ya formáis parte de ese mundo.

Gracias sin nombres ni apellidos a todos los miembros del honorable Departamento de Física de la Tierra, Astronomía y Astrofísica I, y también del II, porqué no.

Gracias a ese mundo, por dejarme decir que es mío, y a los universos paralelos.

Gracias a todos mis amigos del laboratorio LPAOSF de Dakar: Baye Cheickh, Malick Wade, Abdou Lahat, Marie Jane, Souleymane, Amadou. Un trocito de mí se ha quedado para siempre en Senegal, os lo regalo.

Gracias a dos sengaleses muy especiales: Coumba Niang e Ibrahima Diouf. No he tenido tiempo para pedir a alguien que me ayudara a escribir algo en Wolof, pero ya os traduciré que sois dos fuera de serie. Cada uno a vuestra manera, me habéis dejado absorber un poquito de vuestra esencia. Eternamente agradecido.

Y de entre los miembros de tan honorable Departamento, gracias con nombres a los integrantes de mi equipo. Gracias a Antonio, frente a frente en el laboratorio Elvira Zurita, una parte de esta tesis, concretamente la carátula del CD, es obra tuya. Gracias a Ade, aunque serán más gracias cuando te curres ese bizcocho prometido. Gracias a Iñigo, Jorge, Mariano y Cahlo, sois excepcionales, realmente TOP. A ti también Jon, gracias campeón.

Gracias por supuesto a Elsa y Teresa, hacéis que la maquinaria del barco funcione, así es imposible que nos vayamos a pique. Os admiro en lo personal y lo profesional.

Gracias a tres personas muy especiales. Jesús, mi compañero de al lado, un placer haber compartido contigo tantos y tan buenos momentos. Seguiremos en contacto, seguro. Te toca Marta. Darte las gracias se queda corto. Admiro tu tesón y tu constancia, y me siento afortunado por haberte conocido. Me has ayudado hasta el último momento, eres una fenómena. Y un fenómeno es Julián, desde aquellas prácticas en la carrera y durante todo el camino que hemos recorrido después. Me alegro de comenzar una nueva etapa teniéndote cerca, suerte la mía.

Y llega el momento de dar las gracias a la capitana del barco. Qué bien traído está lo del barco, ¿verdad?. Belén, me diste la oportunidad de unirme a TROPA, y si he llegado hasta aquí, ha sido en gran parte por tu apoyo y dirección. Como se suele decir, sin ti no hubiera sido posible. Gracias jefa, mil gracias amiga.

A mi familia. No tiene sentido dar las gracias a mis padres, José y María del Carmen, y a mi Hermana, Cristina. Soy quien soy por vosotros y con vosotros.

A mis abuelos gracias también. A los que están y a los que ya se fueron. Especialmente a mi abuelo Nicolás, el primer y único superhéroe que he conocido. Gracias dondequiera que estés.

Ángela, sin comentarios, eres sencillamente genial, mi regalo de todos los días. Con nadie mejor que contigo. Gracias por ser, y estar.

Y termino dando las gracias a Gala, Mara, Marusa, Río y Antoñito. Hermosas criaturas.

Me dejo a muchos, lo sé. Gracias a todos ellos y ellas.

Madrid, Abril de 2017

x

SUMMARY

The West African Sahel is the transition region between the wet equatorial zone and the dry Sahara desert. Year-to-year, the Sahel alternates an extremely dry season with a strong rainfall regime from July to September. The water resources available during the long dry season depend almost entirely on the intensity of rainfall during the rainy season, also known as the West African Monsoon (WAM).

The WAM presents a marked variability at interannual time scales (e.g., Sultan et al. 2003; Sultan and Janicot 2003), being a major topic of study. The severe drought experienced in the Sahel from the 1970s to the 1990s, and the apparent recovery trend in the recent period, also reveals the pronounced interdecadal variability of the WAM (Hulme et al. 2001; Nicholson 2005; Lebel and Ali 2009).

The WAM system is primarily determined by the northward shift of the Inter-Tropical convergence Zone (ITCZ) along with a thermal gradient between the Sahara desert to the north and the Guinean Gulf to the south (e.g., Sultan and Janicot 2000; Chiang et al. 2000, 2002; Kushnir et al. 2003; Nicholson 2009). Thus, although land surface processes and internal variability cannot be neglected, the oceanic forcing plays the leading role in the predictability of the WAM (e.g., Folland 1986; Palmer 1986; Fontaine et al. 1998; Skinner et al. 2012; Rodriguez-Fonseca et al. 2015). On the one hand it is presented as the main driver of the decadal variability (e.g., Janicot et al. 2001; Biasutti et al. 2008; Mohino et al. 2011a; Martin et al. 2013). On the other hand, several observational studies address the interannual oceanic teleconnections from the tropical Pacific (Janicot et al. 2001; Rowell 2001; Joly and Voldoire 2009), the tropical Atlantic (Giannini et al. 2003; Polo et al. 2008; Joly and Voldoire 2009; Nnamchi and Li 2011) and the Mediterranean (Rowell 2003; Gaetani et al. 2010; Fontaine et al. 2011a).

Moreover, recent observational studies put forward interdecadal changes in the interannual sea surface temperature (SST)-forced response of the WAM (Janicot et al. 1996; Fontaine et al. 1998; Mohino et al. 2011b; Rodriguez-Fonseca et al. 2011, 2015;

Losada et al. 2012). Nevertheless, the underlying causes to this unstable teleconnections and its consequent implications in Sahel rainfall predictability have not been addressed so far, this being the leading motivation of the present thesis.

Objectives

The objectives were stated as follows:

- Design and creation of a statistical tool based on the SST capability to impact on climate-related variables, analyzing the non-stationary behavior of the potential teleconnections.

- Application of the statistical tool to conduct an observational analysis of the non-stationary SST-Sahel interannual teleconnections. The leading SST impacts are considered (tropical Atlantic, tropical Pacific, Mediterranean) to characterize the underlying dynamics.

- Characterization and analysis of the role of multidecadal SST varibility in driving the non-stationarity of interannual teleconnections, with especial emphasis on those teleconnections that may be dominating Sahel rainfall variability in the recent period.

Data and methodology

Different observational datasets have been used in order to avoid data-related uncertainties. Regarding SST, the Extended Reconstructed Sea Surface Temperature (ERSST; e.g., Smith and Reynolds 2004) and the Hadley Center Sea Ice and Sea Surface Temperature (HadISST; e.g., Rayner et al. 2003) databases have been used. For rainfall, a novel dataset of rain-gauge rainfall records across West Africa (Sanogo et al. 2015) has been used for the first time to assess the non-stationary SST-forced response of rainfall in the Sahel. In addition, data from the Climate Research Unit (CRU; e.g., Harris et al. 2014) and reanalysis from the Global Precipitation Climatology Centre (GPCC; e.g., Schneider et al. 2014) have been used. Moreover, the ERA-20C reanalysis from the European Centre for Medium-Range Weather Forecasts (ECMWF) has been used to

explore the atmospheric dynamical processes (Poli et al. 2016).

The statistical methodology used in this thesis mainly corresponds to the maximum covariance analysis (MCA). This technique is widely applied in climate variability to isolate co-variability coupled patterns between two fields (e.g., Bretherton et al. 1992). Based on the ability of the SST as predictor field, the MCA has been applied to analyze the predictability of Sahel rainfall. Both parametric (t-test) and non-parametric (Monte Carlo) methods have been used to assess the statistical significance.

A series of numerical experiments were conducted by using the Laboratoire de Meteorologie Dynamique Zoom (LMDZ, version 5A) atmospheric general circulation model (AGCM) (Hourdin et al. 2006), coupled with the land surface model Organizing Carbon and Hydrology in Dynamic Ecosystems (ORCHIDEE) (Krinner et al. 2005). LMDZ and ORCHIDEE are, respectively, the atmospheric and land components of the Institute Pierre Simon Laplace Earth system model (IPSL-CM5A) (Dufresne et al. 2013).

Results

The results obtained in this thesis can be expressed in three main blocks:

- ✓ The Sea Surface-based Statistical Seasonal foreCAST model **(S^{4}CAST, Suárez-Moreno and Rodríguez-Fonseca 2015)** has been designed and programmed on the basis of the SST capability to predict phenomena such as the WAM. The S^{4}CAST has been subjected to benchmarking. As a result, the tropical Atlantic (e.g., Polo et al. 2008; Rodríguez-Fonseca et al. 2011) and tropical Pacific (e.g., Rowell 2001; Joly and Voldoire 2009) teleconnections with the Sahel, the El Niño-Southern Oscillation (ENSO) teleconnection with the Euro-Mediterranean sector (López-Parages and Rodríguez-Fonseca 2012; López-Parages et al. 2015) and the tropical interbasin Atlantic-Pacific teleconnection (Martín-Rey et al. 2012, 2014) have been satisfactorily reproduced.

- ✓ The S^{4}CAST model has been used to explore the leading interannual SST teleconnections (tropical Atlantic, tropical Pacific, Mediterranean) with the Sahel. Robust non-stationary links have been found, consequently analyzing the

underlying dynamical mechanisms. The multidecadal SST background has been found to exert an influence in modulating interannual teleconnections, with the Atlantic Multidecadal Variability (AMV) and global warming (GW) playing an outstanding role (**Suárez-Moreno et al. 2017a, submitted**).

- ✓ The Mediterranean influence in the Sahel is found to be non-stationary, increasing its impact during recent decades (**Suárez-Moreno et al. 2017b, submitted**). A set of sensitivity experiments is conducted to show how a multidecadal SST warming in the North Atlantic promotes the impact on the Sahel associated with a warm Mediterranean event, resulting in a rainfall increase. Thus, the Mediterranean and North Atlantic become key factors for the improvement of Sahelian rainfall predictability.

RESUMEN (Spanish)

Dentro de África Occidental, el Sahel es la región de transición entre la zona húmeda ecuatorial y el desierto del Sahara. Año a año, el Sahel alterna una estación extremadamente seca con un fuerte régimen de lluvias desde Julio a Septiembre. Los recursos hídricos disponibles durante la larga estación seca dependen en su práctica totalidad de la intensidad de las lluvias durante la estación de lluvias, también conocida como el Monzón de África Occidental (WAM).

El WAM presenta una marcada variabilidad interannual (p.ej., Sultan et al. 2003; Sultan and Janicot 2003) que constituye el tema principal de esta tesis. La severa sequía experimentada en el Sahel entre las décadas de 1970 y 1990, y la aparente recuperación en el período reciente, también ponen de manifiesto la pronunciada variabilidad interdecadal del WAM (Hulme et al. 2001; Nicholson 2005; Lebel and Ali 2009).

El desarrollo del WAM está determinado por el desplazamiento hacia el norte de la Zona de Convergencia Intertropical (ITCZ[1]) junto con un gradiente térmico entre el desierto del Sáhara al norte y la región del Golfo de Guinea al sur (p.ej., Sultan and Janicot 2000; Chiang et al. 2000, 2002; Kushnir et al. 2003; Nicholson 2009). Así pues, aunque no se pueden descuidar los procesos de superficie y la variabilidad interna, el forzamiento oceánico juega el papel principal en la predictibilidad del WAM (p.ej., Folland 1986; Palmer 1986; Fontaine et al. 1998; Skinner et al. 2012; Rodríguez-Fonseca et al. 2015). Por un lado se presenta como el mayor conductor de la variabilidad decadal (p.ej., Janicot et al. 2001; Biasutti et al. 2008; Mohino et al 2011a; Martin et al. 2013). Por otra parte, varios estudios observacionales abordan las teleconexiones interannuales oceánicas desde el Pacífico tropical (Janicot et al. 2001; Rowell 2001; Joly and Voldoire 2009), el Atlántico tropical (Giannini et al. 2003; Polo et al. 2008; Joly and Voldoire 2009; Nnamchi and Li 2011) y el Mediterráneo (Rowell 2003; Gaetani et al. 2010; Fontaine et al. 2011a).

[1] Acrónimo del inglés Inter-tropical Convergence Zone

Por otra parte, recientes trabajos observacionales ponen de manifiesto cambios interdecadales en la respuesta interannual del WAM forzada por la temperatura de la superficie del mar (SST[2]) (Janicot et al. 1996; Fontaine et al. 1998; Mohino et al. 2011b; Rodríguez-Fonseca et al. 2011, 2015; Losada et al. 2012). Sin embargo, las causas subyacentes a la inestabilidad de estas teleconexiones y sus consecuentes implicaciones en la predictibilidad de las lluvias del Sahel no han sido abordadas hasta ahora, siendo esta la principal motivación de la presente tesis.

Objetivos

Los siguientes objetivos fueron planteados

- Diseño y creación de una herramienta estadística basada en la capacidad de la SST para impactar sobre variables relacionadas con el clima, analizando el comportamiento no estacionario de las potenciales teleconexiones.

- Aplicación de la herramienta estadística para llevar a cabo un estudio observacional de las teleconexiones interannuales no estacionarias de la SST con el Sahel. Los impactos principales de la SST (Atlántico tropical, Pacífico tropical, Mediterráneo) son considerados para caracterizar la dinámica subyacente.

- Caracterización y análisis del papel de la variabilidad multidecadal de SST en la conducción de la no estacionariedad de las teleconexiones interannuales, con especial énfasis en aquellas teleconexiones que pudieran estar dominando la variabilidad de la lluvia en el Sahel en el período reciente.

Datos y metodología

Se han utilizado diferentes bases de datos observacionales con el objetivo de evitar incertidumbres relacionadas con el uso de datos. Respecto a SST, se han utilizado las bases de datos del Extended Reconstructed Sea Surface Temperature (ERSST; p.ej., Smith and Reynolds 2004) y del Hadley Center Sea Ice and Sea Surface Temperature (HadISST; p.ej., Rayner et al. 2003). Para la lluvia, un conjunto de datos novedosos a

[2] Acrónimo del inglés Sea Surface Temperature

partir de registros pluviométricos a lo largo de África Occidental se ha utilizado por primera vez para evaluar teleconexiones no estacionarias forzadas por SST (Sanogo et al. 2015). Además, se han utilizado datos del Climate Research Unit (CRU; p.ej., Harris et al. 2014) y reanálisis del Global Precipitation Climatology Centre (GPCC; p.ej., Schneider et al. 2014). Por otra parte, se ha utilizado el reanálisis ERA-20C del European Centre for Medium-Range Weather Forecasts (ECMWF) para explorar los procesos dinámicos atmosféricos (Poli et al. 2016).

La metodología estadística utilizada en esta tesis corresponde principalmente al análisis de covarianza máxima (MCA[3]). Esta técnica es ampliamente aplicada en variabilidad climática para aislar patrones de co-variabilidad acoplados entre dos campos (p.ej., Bretherton et al. 1992). Basado en la habilidad de la SST como predictor, el MCA ha sido aplicado para analizar la predictibilidad de la lluvia en el Sahel. Se han utilizado tanto métodos paramétricos (t-test) como no paramétricos (Monte Carlo) para evaluar la significación estadística.

Se realizó una serie de experimentos numéricos mediante el uso del modelo atmosférico de circulación general (AGCM[4]) del Laboratoire de Meteorologie Dynamique Zoom (LMDZ, versión 5A) (Hourdin et al. 2006), acoplado con el modelo de superficie Organizing Carbon and Hydrology in Dynamic Ecosystems (ORCHIDEE) (Krinner et al. 2005). LMDZ5 y ORCHIDEE son, respectivamete, las componentes atmosférica y terrestre del Instituo Pierre Simon Laplace Earth system model (IPSL-CM5A) (Dufresne et al. 2013).

Resultados

Los resultados obtenidos en esta tesis se pueden expresar en tres bloques principales:

- ✓ El modelo estadístico de predicción basado en la temperatura de la superficie del mar **(S[4]CAST[5], Suárez-Moreno and Rodríguez-Fonseca 2015)** ha sido diseñado y programado basado en la capacidad de la SST para predecir fenómenos como el WAM. El S[4]CAST ha sido sometido a evaluación

[3] Acrónimo del inglés Maximum Covariance Analysis
[4] Acrónimo del inglés Atmospheric General Circulation Model
[5] Acrónimo del inglés Sea Surface-based Statistical Seasonal foreCAST model

comparativa. Como resultado las teleconexiones del Atlántico (p.ej., Polo et al. 2008; Rodríguez-Fonseca et al. 2011) y Pacífico tropicales (Rowell 2001; Joly and Voldoire 2009), la teleconexión del ENSO[6] con el sector Euro-Mediterráneo (López-Parages and Rodríguez-Fonseca 2012; López-Parages et al. 2015) y la teleconexión tropical entre Atlántico y Pacífico (Martín-Rey et al. 2012, 2014) han sido reproducidas satisfactoriamente.

- ✓ El modelo S^{4}CAST se ha utilizado para explorar las teleconexiones interannuales dominantes de la SST con el Sahel (Atlántico tropical, Pacífico tropical, Mediterráneo). Se han encontrado enlaces no estacionarios robustos, analizando en consecuencia los mecanismos dinámicos subyacentes. Se ha encontrado que el estado base multidecadal de SST ejerce una influencia en la modulación de las teleconexiones interannuales, con el papel sobresaliente de la variabilidad multidecadal del Atlántico (AMV[7]) y el calentamiento global (GW[8]) (**Suárez-Moreno et al. 2017a, enviado**).

- ✓ Se encuentra que la influencia del Mediterráneo en el Sahel no es estacionaria, aumentando su impacto durante décadas recientes (**Suárez-Moreno et al. 2017b, enviado**). Se realiza un conjunto de experimentos de sensibilidad para mostrar cómo un calentamiento multidecadal del Atlántico Norte estimula el impacto en el Sahel asociado a un evento cálido en el Mediterráneo, resultando en un aumento de la lluvia. Así pues, el Mediterráneo y el Atlántico Norte se convierten en factores clave para la mejora de la predictibilidad de las lluvias en el Sahel.

[6] Acrónimo del ingles El Niño-Southern Oscillation
[7] Acrónimo del inglés Atlantic Multidecadal Variability
[8] Acrónimo del inglés global warming

CHAPTER I

1 Motivation

The oceans have the capacity to accumulate heat in the surface layer. This energy is transferred to the atmosphere leading to changes in atmospheric circulation and consequent impacts in remote and nearby locations. Thus, the SST becomes a key variable to detect ocean sources of seasonal predictability from interannual to multidecadal time scales (e.g., Mohino et al 2011a; Skinner et a. 2012; Rodríguez-Fonseca et al. 2015). Global spatial patterns of SST anomalies (SSTA) are organized in the so-called modes of variability, which are particular of each ocean basin and determine the principal directions in which the variability takes place. In this framework, the anomalous monsoonal rainfall is strongly linked to SST variability. Regarding the WAM, leading patterns of SSTA play a key role when tackling rainfall variability (Folland et al. 1986; Palmer 1986; Xue and Shukla 1997; Fontaine et al. 1998; Rodríguez-Fonseca et al. 2011; 2015; Losada et al. 2010a; 2010b; Rowell 2013; Vera et al. 2013), becoming a key factor in the severe drought experienced in the Sahel from the early 1970s (Lu and Delworth 2005; Mohino et al. 2011a; Rodríguez-Fonseca et al. 2015). The West African Sahel is a narrow belt located around 15ºN between the Sahara desert to the north and the woody Sudanese savanna to the south, crossing Africa from the Atlantic Ocean to the Red Sea. Every year, the Sahel alternates a dry season, with total absence of precipitation, and a very wet season coinciding with the boreal summer months. Thus, the water resources available during the long dry season depend almost entirely on the intensity of precipitation during the rainy season.

In a general context, monsoonal rainfall takes place in tropical latitudes, determining the strongly seasonal rainfall regime in many regions within the tropical band. In particular, the vulnerability of West African societies to climate variability is expected to increase over the next decades as demand for resources increases under a rapidly growing population. Thus, the considerable fall in precipitation during the monsoon season

throughout the last decades of the 20th (Hulme et al. 2001; Dai et al. 2004; Held et al. 2005; Greene et al. 2009) century is causing a real human drama in a region whose economy and subsistence is determined by agriculture (Mortimore and Adams 2001; Batterbury and Warren 2001), in turn presenting an extreme dependence on the precipitation regime. Nonetheless, despite some uncertainties, rainfall in the Sahel seems to be undergoing a recovery trend (Nicholson 2005; Lebel and Ali 2009), although the humanitarian drama still continues.

In this framework, being able to determine the underlying causes of WAM variability, as well as to identify associated external forcing, would help to improve the predictability of the Sahel rainfall regime, allowing anticipation in situations of flood or drought events and reducing the drastic impact of these episodes on the population.

In the last decades, the WAM has become an important topic of study, mainly because of its interannual and intraseasonal variability (e.g., Janowiak 1988; Nicholson and Palao 1993; Sultan and Janicot 2000, 2003; Le Barbè et al. 2002; Lebel et al. 2003; Sultan et al. 2003; Moron et al. 2006; Nicholson 2013). This phenomenon takes place from July to September related to the semi-annual shift of the ITCZ along with a contrast or thermal gradient between the Sahara and the Gulf of Guinea (Sultan and Janicot 2000; Grist and Nicholson 2001; Kushnir 2003; Nicholson and Webster 2007). The ITCZ can be understood as a zonal belt of low pressure in tropical latitudes, being strongly influenced by SSTA, which becomes a powerful source of WAM predictability (e.g., Folland 1986; Palmer 1986; Fontaine et al. 1998).

The SSTA affects WAM variability from interannual to multidecadal time scales. On the one hand, several observational studies have addressed the influence of global SST on year-to-year variability of WAM, pointing to interactions with the ENSO (Janicot et al. 2001; Rowell 2001; Giannini 2005; Joly and Voldoire 2009; Mohino et al. 2011c), the tropical Atlantic (Janicot et al. 1998; Giannini et al. 2003; Polo et al. 2008; Joly and Voldoire 2010; Losada et al. 2010a; Nnamchi and Li 2011) and the Mediterranean (Rowell 2003; Jung et al. 2006; Fontaine et al. 2010, 2011a; Gaetani et al. 2010) all identified by their impact on the monsoon system and its predictability. On the other hand, SST variability at decadal-multidecadal time scales has been linked to persistently wet and dry periods in the Sahel throughout the 20th century (Folland 1986; Palmer

1986; Janicot et al. 2001; Lu and Delworth 2005; Parker et al. 2007; Biasutti et al. 2008; Findell and Delworth 2010; Mohino et al. 2011a; Li et al. 2012; Wang et al. 2013; García-García and Ummenhofer 2015). The most prominent patterns of multidecadal SST variability inducing rainfall anomalies in the Sahel are: the Atlantic Multidecadal Variability (AMV), the interdecadal Pacific oscillation (IPO), and the global warming (GW) trend (Fig. 1.1).

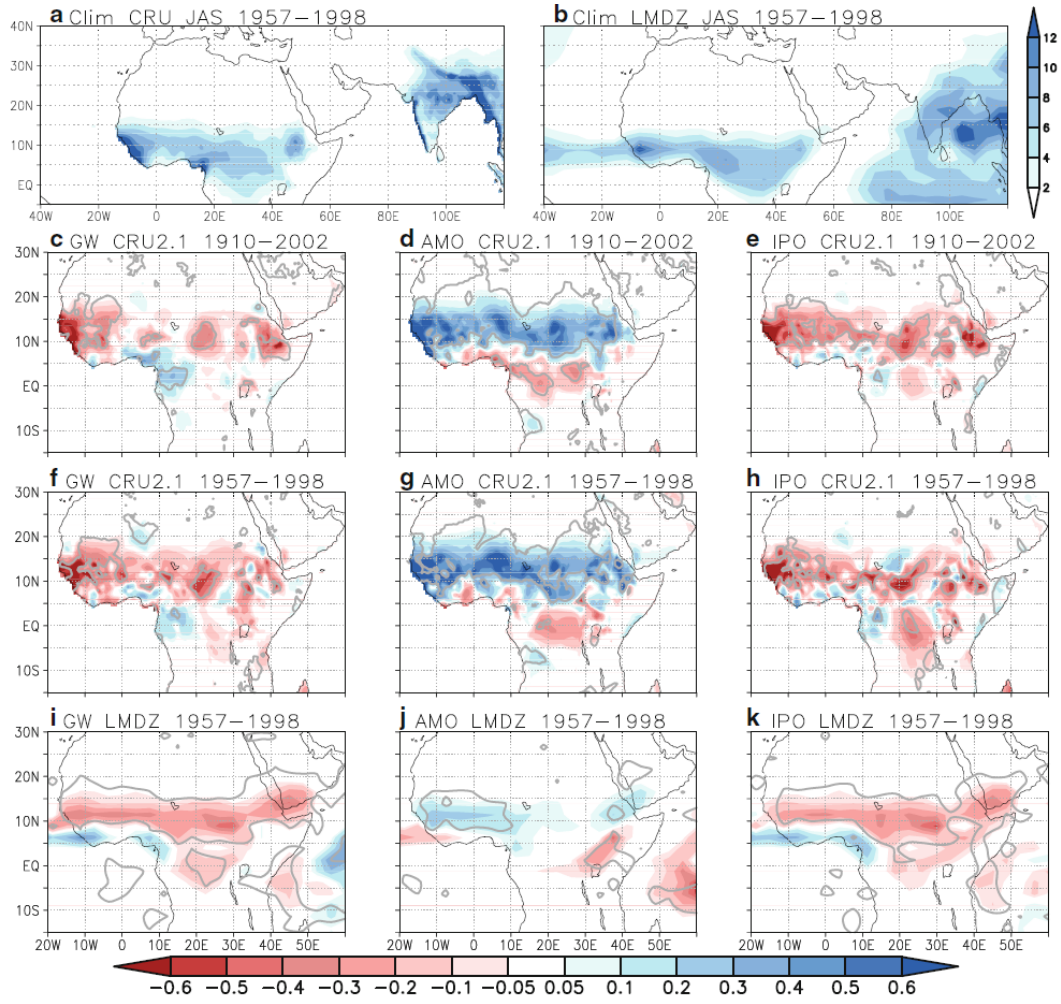

Fig. 1.1. Climatology of summer (July–September) rainfall (in mm/day) for CRU data (a) and LMDZ model (b) between 1957 and 1998. Regression of CRU summer precipitation onto the 1910-2002 GW (c), AMO (d) and IPO (e) indices derived from ERSST data set. Regression of CRU summer precipitation onto the 1957-1998 indices (f–h). Regression of LMDZ summer precipitation onto the 1957-1998 indices (i–k). Each index was standardized for each period. Grey contour marks 95% significant regions (according to a t-test). Units for the regressions are mm day^{-1} per standard deviation of the associated indices (from Mohino et al. 2011a).

The work performed along this thesis has aimed to give a step forward in the improvement of seasonal forecast of rainfall in the Sahel. The information comes from SSTA in nearby regions such as the tropical Atlantic, but also remote regions such as the

tropical Pacific, and the Mediterranean Sea. The physical mechanisms driving the different SST-Sahel links are the so-called atmospheric teleconnections. However, the impacts of these oceanic regions on WAM have been shown to be unstable throughout the 20th century (Fig. 1.2). Several authors have addressed this feature in terms of non-stationary teleconnections and associated impacts on the WAM depending on the considered sequence of decades (Janicot et al. 1996; Fontaine et al. 1998; Mohino et al. 2011b; Rodriguez-Fonseca et al. 2011, 2016; Losada et al. 2012). In this context, Rodríguez-Fonseca et al. (2011) put forward how, at interannual time scales, the leading modes of co-variability between SSTA in different ocean regions and Sahel rainfall change depending on the period under study. In particular, the periods 1957-1978 and 1979-1998 exhibits different impacts of the teleconnections with the Atlantic, Pacific and Mediterranean (Fig. 1.2). Nevertheless, the causes for this non-stationary teleconnections and its implication on Sahel rainfall predictability have not been addressed so far, this being the main motivation for the present thesis.

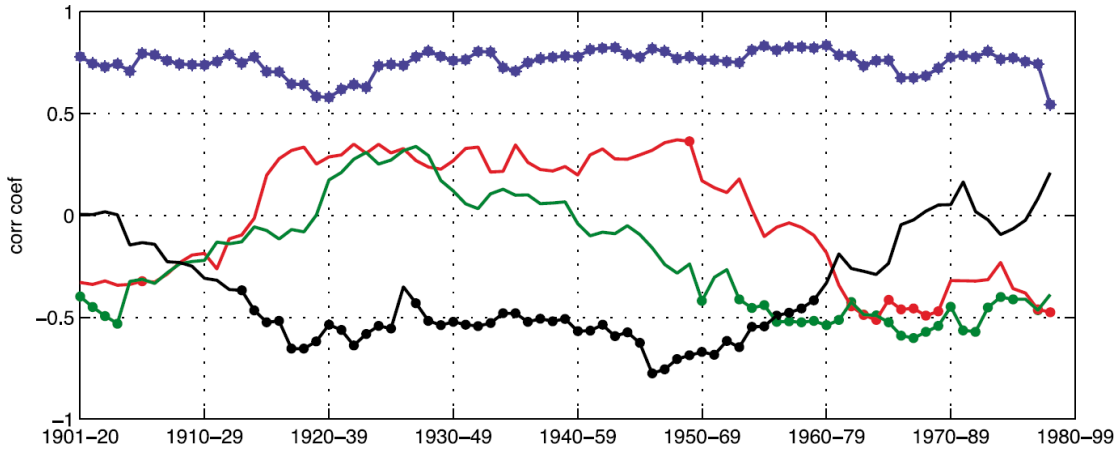

Fig. 1.2. Interdecadal changes in the SST-rainfall teleconnections pointed by twenty-year running correlation from 1901-1920 to 1980-1999, between observed June-to-September (JJAS) Atlantic 3 (ATL3) index and JJAS Guinean Gulf (GG) index (blue line); JJAS ATL3 index and Sahel JJAS rainfall index (black line), JJAS Niño 3 index and JJAS GG rainfall index (red line) and JJAS Niño 3 index and Sahel rainfall index (green line). Dots denote 90% significance correlations under a Monte Carlo test with 500 permutations (from Losada et al. 2012).

Moreover, robust non-stationary SST-teleconenctions have been recently found. This is the case of the ENSO teleconnection with the Euro-Mediterranean rainfall (López-Parages and Rodríguez-Fonseca 2012; López-Parages et al. 2015), showing strong impacts during the decades in which the ENSO also seems to improve its impact on the Sahel (Rodríguez-Fonseca et al. 2016). In addition, the tropical interbasin Atlantic-Pacific teleconnection has been shown to be non-stationary (Martín-Rey et al. 2012, 2014, 2015).

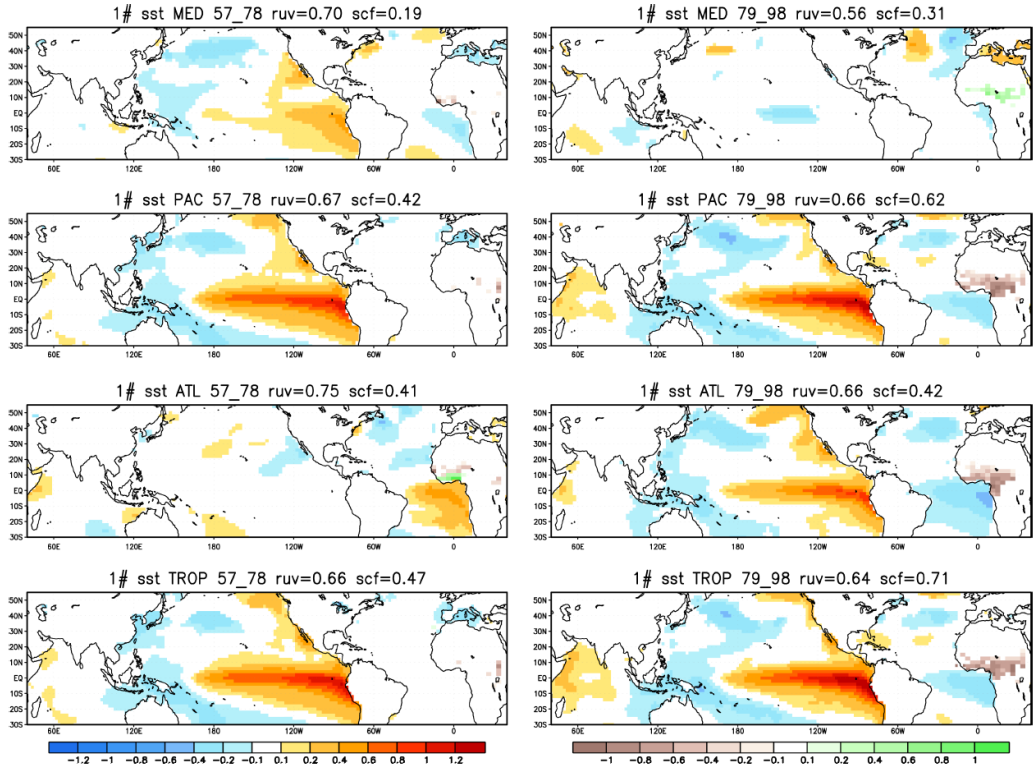

Fig. 1.3. June to September (JJAS) SST and rainfall regression patterns associated with the leading extended maximum covariance analysis (EMCA) mode obtained between (a) and (b) the Mediterranean, (c) and (d) Pacific, (e) and (f) Atlantic, and (g) and (h) global Tropics and the West African rainfall for the period before and after the 1970s. The squared covariance fraction and SST rainfall correlation score is indicated at the top of each map. Only regions 95% statistically significant under a t-test are gridded. Right and left color bars correspond to the rainfall and SST, respectively (from Rodríguez-Fonseca et al. 2011).

Otherwise, it has been recently proposed how the Northern-hemispheric differential warming could be inducing a significant increase in Sahel rainfall, in a way that this extratropical warming could be predominating over the drying effect of tropical SST warming (Park et al. 2015). Moreover, the warming component of the Mediterranean basin has been addressed by playing an outstanding role in the recent recovery trend of rainfall in the Sahel (Park et al. 2016).

As stated, the role of SSTA in driving interannual-to-multidecadal Sahel rainfall variability is undeniable. However, what has not been addressed so far is how the multidecadal SST background, noticeably the inter-hemispheric SST gradients, could be modulating the year-to-year SST impacts on the Sahel. Thus, multidecadal SST variability is studied in this thesis for its role in the non-stationarity of interannual SST teleconnections with the Sahel, which is potentially causing the dominance of some oceanic predictors over others in the last decades.

CHAPTER II

2 State-of-the-art

2.1 Introduction to the general circulation of the atmosphere and oceans

General circulation refers to the global motion of the atmosphere. This atmospheric motion is driven by the uneven surface distribution of net solar incoming radiation, with a surplus in the tropics and a deficit in the polar regions which is translated into larger outgoing long-wave radiation (OLR) than the one that is absorbed (Fig. 2.1). To compensate this imbalance, atmospheric and oceanic transport processes distribute the energy around the globe. Atmospheric winds and ocean currents accomplish this transport. From a dynamical point of view, the oceans and the atmosphere must be considered together as components of the climate system

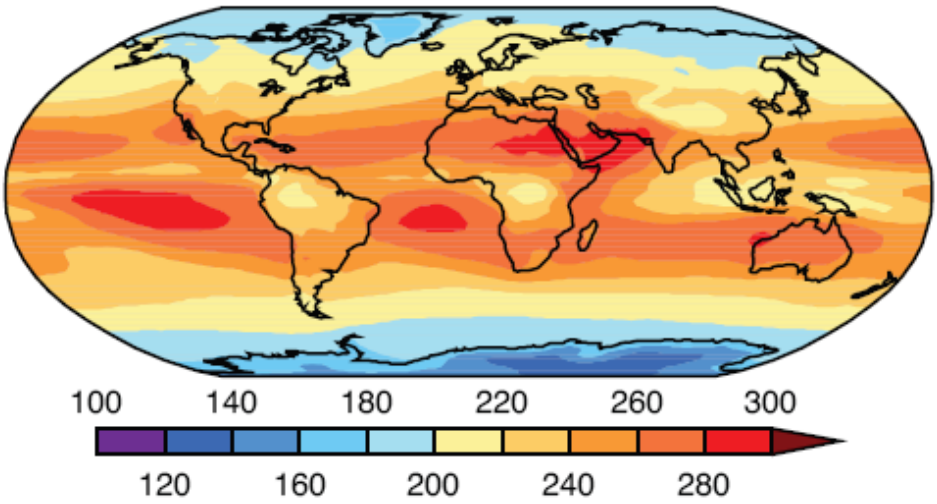

Fig. 2.1. Outgoing Long-wave Radiation (OLR, Wm^{-2}). Satellite measurement within the Earth Radiation Satellite Experiment (ERBE, 1985-1989). The amount of terrestrial radiation that is released into space and, by extension, the amount of cloud cover and water vapor that intercepts that radiation in the atmosphere defines OLR. (Source: *https://scienceofdoom.files.wordpress.com/2010/03/actual-average-olr.png*).

The climate system is defined by five subsystems: the atmosphere, the hydrosphere, the cryosphere, the lithosphere and the biosphere. The understanding of the interactions among the different components may improve the ability to forecast how one component or a combination of them may change in response to an external forcing (e.g., Turner et al. 2009).

The atmosphere and the oceans are the most important components coupled at interannual to decadal timescales. In the next section, these components are further described.

2.1.1 The Atmosphere

General circulation of the atmosphere can be understood as a global system of winds, transporting heat from the tropics, where solar heating is greater. This heat is directed towards polar latitudes, resulting in an energy balance and giving rise to the climate zones of the Earth. George Hadley proposed a single cell in each hemisphere that would transport heat from the tropics to the poles (Hadley 1735). Nevertheless, the impact of rotation and the role of angular momentum conservation were not considered in this early theory. In the 1850s, William Ferrell proposed that mid-latitude circulation cells with westerly winds were caused by air deflected by the Coriolis force (Ferrell 1856). Later, Wilhelm Bjerknes identified the polar easterlies and proposed that they resulted from a thermally indirect cell, the Ferrell cell, where balance was maintained by the mid-latitude cyclones (Bjerknes 1921).

Despite some seasonal variations, the atmospheric circulation is currently defined by mean zonal surface winds, with a well-defined three-cell structure. The Hadley subtropical cell is a broad belt of easterly winds located roughly between latitudes 30ºN and 30ºS, the flow being weaker near the boundaries and near the equator. The Ferrell mid-latitude cell consists of a wide belt of generally westerly winds locating between 30ºN and 60ºN and a corresponding belt between 30ºS and 60ºS. In high latitudes, north of 60ºN and south of 60ºS, zonal surface winds are easterly or nearly vanishing, defining the Polar cell. In this context, a picture of the general circulation emerges for an aqua planet, with tropical easterly surface winds, mid-latitude westerlies and polar easterlies

(Fig. 2.2a). When the impact of continents is added, more complex surface patterns develop (Fig. 2.2b). Instead of bands of low and high pressure, areas of high and low pressure form in different regions. Under this scenario, the high-pressure acting at Earth surface is balanced by low-pressure systems elsewhere.

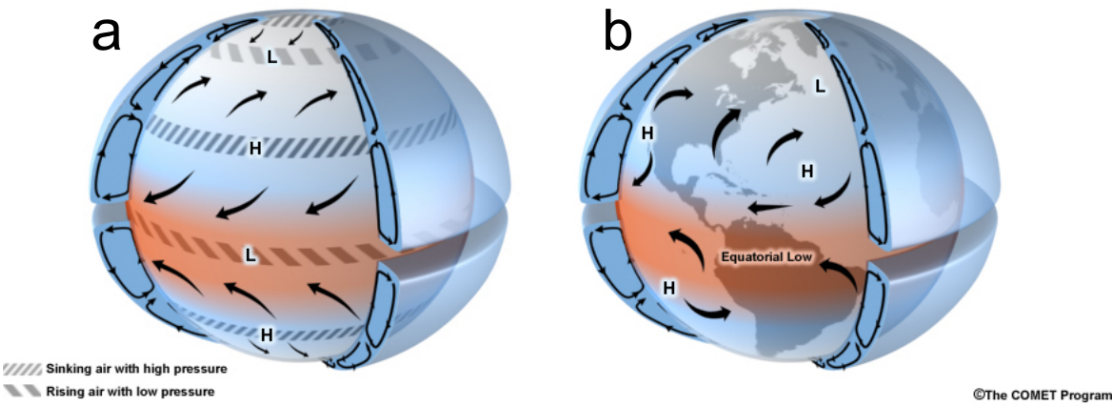

Fig. 2.2. The three-cell circulation model for (a) aqua planet and (b) with continents (Source: The COMET program; *http://www.comet.ucar.edu/*).

The two Hadley cells driven by the upward motions at the Equator, close with a downward branch at latitude of about 30º (Fig. 2.3). The northern boundary of these cells is marked by strong westerly winds in the upper troposphere called the tropospheric jets. At the surface, the rotation of the Earth is responsible for a deflection toward the right in the northern hemisphere and toward the left in the southern hemisphere (due to the Coriolis force) of the flow coming from the mid-latitudes to the Equator. This gives rise to the easterly trade winds characteristics of the tropical regions (Fig. 2.4).

The extratropical surface circulation is dominated by westerly winds which zonal symmetry is perturbed by large wave-like patterns and the continuous succession of disturbances that governs the day-to-day variations in the weather in these regions. The dominant feature of the meridional circulation at those latitudes is the Ferrell cell (Fig. 2.3), which is weaker than the Hadley cell. As it is characterized by rising motion in its poleward branch and downward motion at mid-latitudes, it is termed an indirect cell by contrast with the direct Hadley cell.

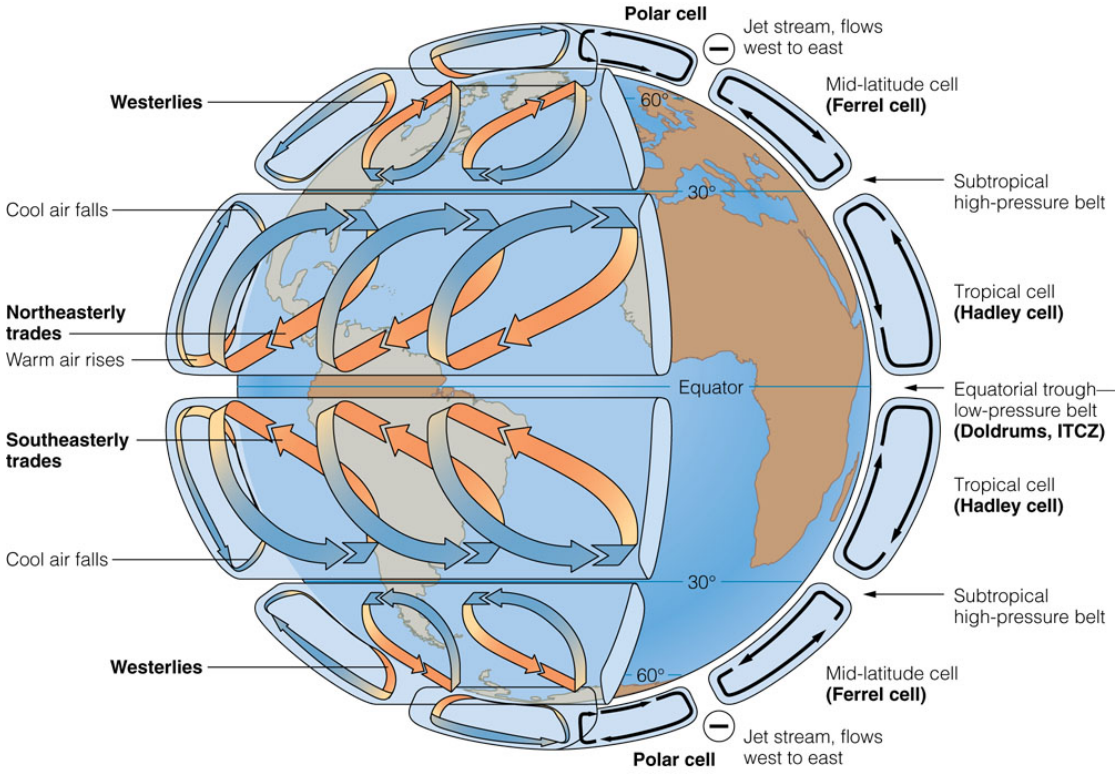

Fig. 2.3. Schematic representation of the annual mean general atmospheric circulation. (Source: *http://ksuweb.kennesaw.edu/~jdirnber/oceanography/LecturesOceanogr/LecCurrents/LecCurrents.html*).

Out from the narrow equatorial band, and above the surface boundary layer, the large-scale atmospheric circulation is close to geostrophic equilibrium. The surface pressure and winds are thus closely related. In the Northern Hemisphere, the winds rotate clockwise around high-pressure systems and counterclockwise around low pressure, while the opposite takes place in the Southern Hemisphere. Consequently, the mid-latitude westerlies are associated with high pressure in the subtropics and low pressure at around 50º-60º. Rather than a continuous structure, this subtropical high-pressure belt is characterized by distinct high-pressure centers, often referred to as the name of a region close to their maximum (e.g., Azores high, St Helena high). In the Northern Hemisphere, the low-pressure systems at around 50-60ºN are typically observed on climatological maps as cyclonic lobes called the Icelandic low and the Aleutian low. In the Southern Ocean, due to the absence of large landmasses, pressure is more zonally distributed, with a minimum in surface pressure around 60ºS.

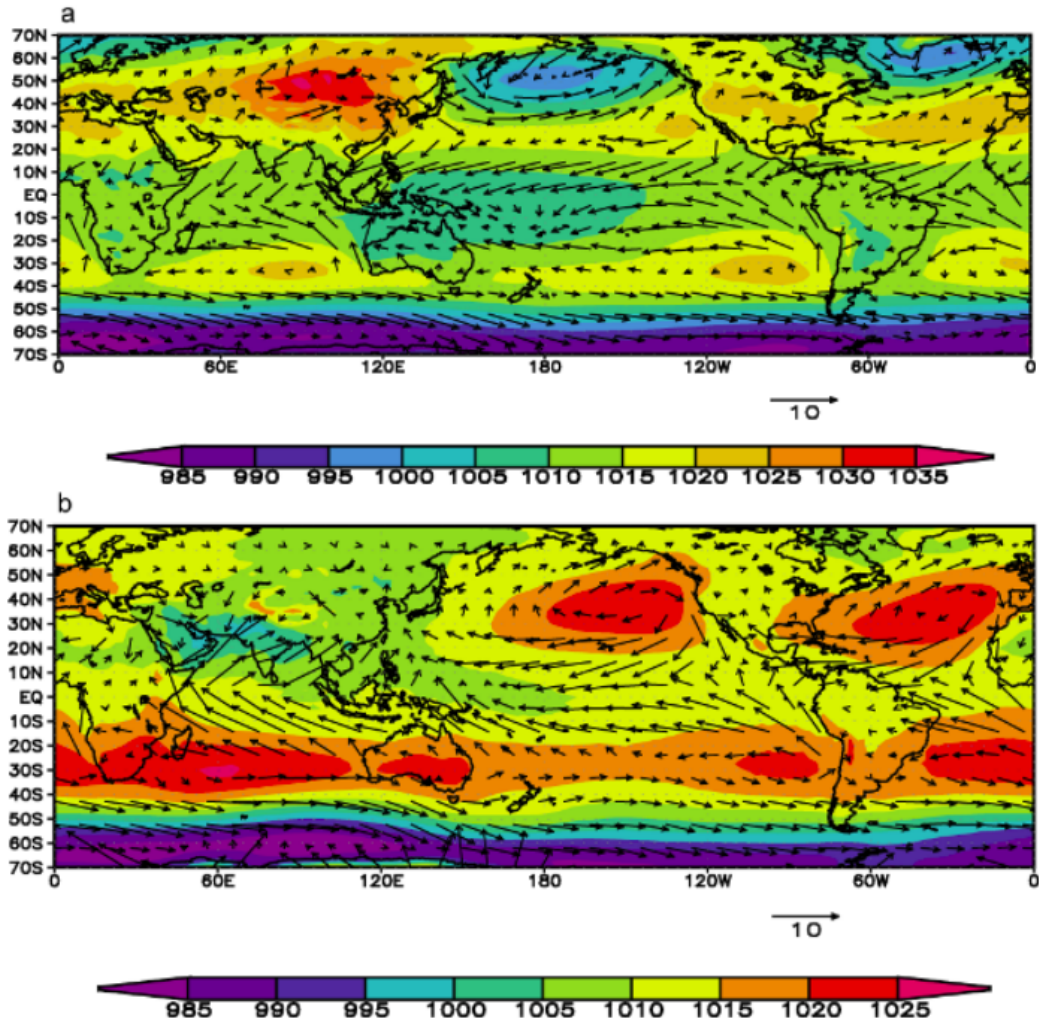

Fig. 2.4. Seasonal averages of 10m winds (arrows, in ms^{-1}) and sea level pressure (colours, in hPa) for (a) December-January-February and (b) June-July-August. Data source: NCEP/NCAR reanalyses (Data source: NCEP/NCAR reanalysis (Kalnay et al. 1996)).

In the real atmosphere, the convergence of surface winds associated with the Hadley circulation and the resulting ascendant motions does not occur exactly at the equator but in a band called the Inter-Tropical Convergence Zone (ITCZ). The ITCZ is characterized by a zonal diabatic heating (e.g., Ling and Zhang 2013) and associated formation of deep convective clouds. Because of the geometry introduced by the presence of continents, the ITCZ is located around 5°N, with some seasonal shifts. The presence of land surfaces also has a critical role in monsoon circulation. In summer, the continents warm faster than the oceans because of their lower thermal inertia, which induces a warming of the air close to the surface and a decrease in surface pressure. This pressure difference between land and sea induces moist transport from the sea to the land. In winter, the situation is opposite, with high-pressure over the cold continent and

a flow generally from land to sea. Such a monsoonal circulation, with seasonal inversions of the wind direction, is present in many tropical areas of Asia, Australia and Africa.

While the Hadley, Ferrell and Polar cells are the major components of global heat transport; east-west temperature differences also drive a longitudinally oriented circulation, referred to as the Walker cell (e.g., Walker 1925). The Walker circulation owns its name to Sir Gilbert Walker, who recognized its existence from observations of pressure oscillations between Darwin, in Australia, and Tahiti, in the Pacific. The Walker circulation was defined as an east-west circulation, characterized by rising motion associated with the surplus heating over the warm western Pacific (Fig. 2.5). The Walker Circulation now refers to the global mean east-west circulation, which consists of large regions of rising motion over the Maritime Continent, tropical South America, and tropical Africa with subsidence in between.

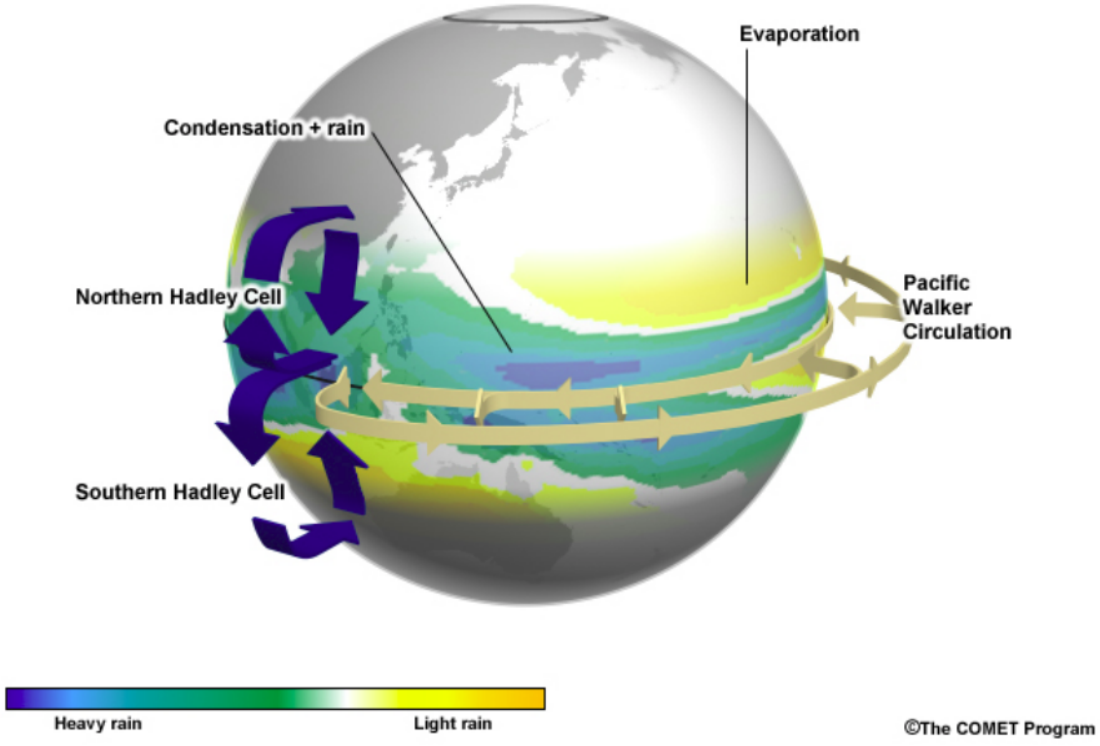

Fig. 2.5. Schematic of tropical circulations that result from anti-symmetric and symmetric components of diabatic heating about the equator, the Hadley and Walker circulation cells respectively. The background is mean precipitation from the Global Precipitation Climatology Project for 1979-2008. (Source: The COMET program; *http://www.comet.ucar.edu/*).

The Walker circulation is the atmospheric response to the pressure gradient force that results from a high-pressure system over the eastern Pacific Ocean, and a low-pressure

system over Indonesia. Particularly, the oscillation of pressure between Darwin and Tahiti has been denoted as the Southern Oscillation (SO). Cold upwelling in the east and warm SST in the west accompany the normal Walker circulation. During an El Niño event, the east and central Pacific become anomalously warm and the west anomalously cold. The atmospheric circulation shifts in response to the surface warming, producing a positive phase of the SO. The perturbation of the Walker circulation causes major shifts in atmospheric circulations, rainfall patterns, and seasonal climate across the globe.

2.1.2 The Oceans

The oceans are a determinant energy source for the general circulation of the atmosphere. The understanding of its general circulation and interactions with the rest of components of the climate system is crucial for the determination of the heat distribution and the description of the general movements taking place in the climate system.

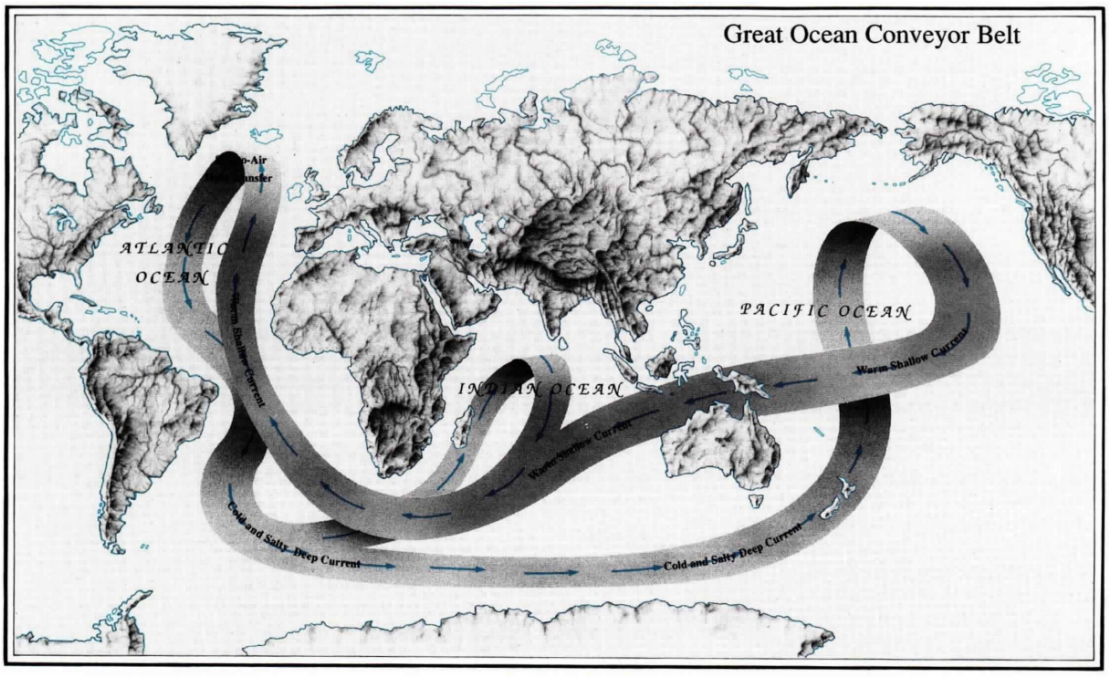

Fig. 2.6. The great ocean conveyor logo. (Illustration by Joe Le Monnier, Natural History Magazine). (from Broecker 1987).

From a global scale point of view, there is a large-scale ocean circulation pattern in which seawater moves around the world ocean. This pattern is driven by changes in water temperature and salinity that change the density of water. It is known as the Great Ocean

Conveyor or thermohaline circulation (Broecker 1992; Delworth and Greatbatch 2000) (Fig. 2.6). It affects water at the ocean surface and all the way to the deep ocean. The Great Ocean Conveyor slowly moves a great amount of water (~ 10 cm s^{-1}). The water moves mainly because of differences in relatively density. In the Atlantic, the circulation of seawater is driven mainly by temperature differences. Water heated near the equator travels at the surface of the ocean north into high latitudes where it loses some heat to the atmosphere (keeping temperatures in Northern Europe and North America relatively mild). The cooled water sinks to the deep ocean and travels the world ocean, possibly not surfacing for hundreds or even as much as a thousand years.

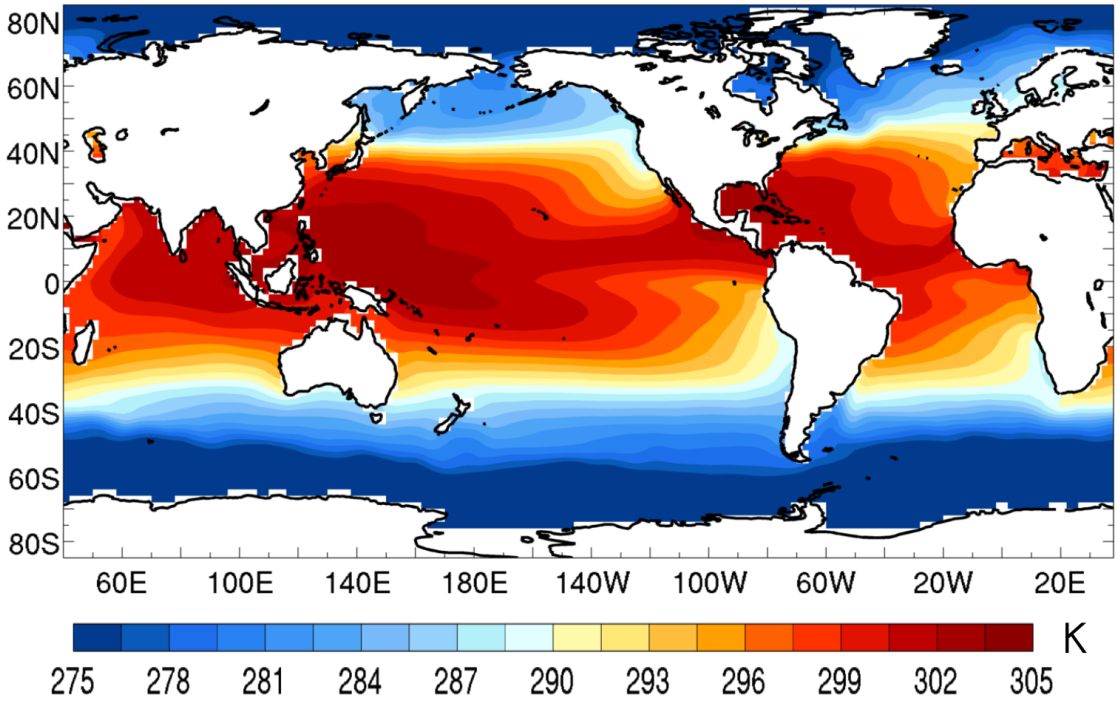

Fig. 2.7. Sea surface temperature (SST) climatology for the period 1942-2010. Computed from NOAA Extended Reconstructed SST (ERSST; see section 5.1.2).

At the surface, the ocean circulation is mainly driven by winds (e.g., Stommel 1948). The atmosphere transfers momentum (through wind stress) and heat fluxes (through radiative, latent and sensible heat). As stated, the global system of winds balances the uneven distribution of solar radiation (see section 2.1.1), which in turn has a direct effect on the pattern of ocean surface temperatures (Fig. 2.7).

At mid-latitudes, the atmospheric westerlies induce eastward currents in the ocean while the trade winds are responsible for westward currents in the tropics (Fig. 2.8). Because of the presence of continental barriers and Coriolis effect, those currents form loops called

the subtropical gyres. The surface currents in those gyres are intensified along the western boundaries of the oceans (the east coasts of continents) inducing well-known strong currents such as the Gulf Stream off the east coast of the USA and the Kuroshio off Japan. At higher latitudes in the Northern Hemisphere, the easterlies allow the formation of weaker sub polar gyres. In the Southern Ocean, because of the absence of continental barriers, a current that connects all the ocean basins can be maintained: the Antarctic Circumpolar Current (ACC). All these currents run basically parallel to the surface winds. By contrast, the equatorial counter-currents run in the direction opposite to the trade winds.

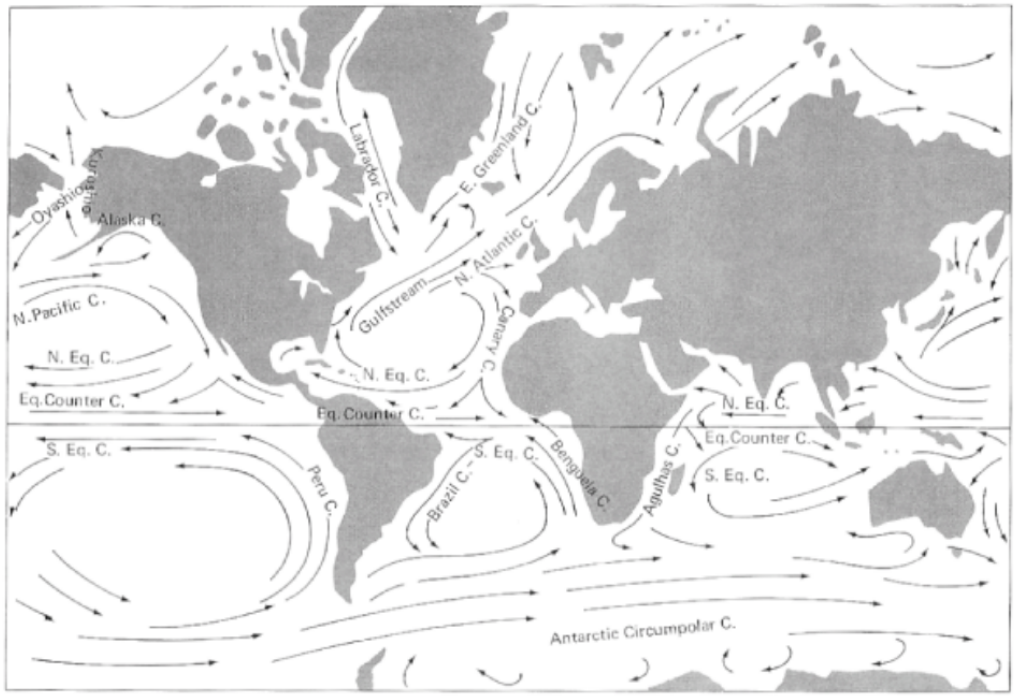

Fig. 2.8. Schematic representation of the major surface currents. Eq. is an abbreviation for equatorial, C. for current, N. for North, S. for South and E. East. Reprinted by permission of Waveland Press, Inc. (from Knauss 1997). (Long Grove, IL: Waveland Press, Inc, 1997 (reissued 2005)).

Because of the rotation of the Earth, the ocean transport induced by the wind is perpendicular to the wind stress (to the right in the Northern Hemisphere, to the left in the Southern Hemisphere). This transport, known as the Ekman transport (e.g., Price et al. 1987), plays a pivotal role in explaining the path of the wind-driven surface currents. In coastal upwelling, the wind stress has to be parallel to the coast, with the coast on the left when looking in the wind direction in the northern hemisphere (for instance, northerly winds along a coast oriented north-south). This causes an offshore transport and an upwelling of deep waters to compensate for this transport.

The path of the wind-driven surface currents aforementioned plays a key role in turbulent energy exchange at the surface, accompanying a radiative energy term. This energy is stored at the surface as heat. Approximately 3.5 m of water contains as much energy as an entire atmospheric column (e.g., Rimac et al. 2016). The heat content of the oceans directly affects the climate system.

The major role of the ocean in the climate system is partly due to the large heat-storage capacity aforementioned. The thermal inertia of the oceans is transferred to the atmosphere via turbulent and radiative energy exchange at the surface (e.g., Deser et al. 2003). These energy fluxes depend on a particular oceanic variable, the SST, as well as a series of atmospheric variables, namely, the wind speed, air temperature, humidity and cloudiness. Thus, the SST plays a crucial role in regulating climate and its variability, becoming a source of potential predictability for climate fluctuations on time scales of seasons and longer.

Acting as a coupled system, both atmospheric and oceanic processes control the SST and its variability. Regarding the former, wind speed, air temperature, humidity and cloudiness regulate the exchange of energy at the sea surface.

This exchange of energy is the base of the coupling between the atmosphere and the ocean. In its simplest representation, this energy exchange can be calculated from the so-called bulk formulas for the air-sea fluxes (e.g., Peixoto and Oort 1992; Hartmann 1994):

$$T = \rho_a C_D U_{10}^2 \tag{2.1}$$

$$Q_S = \rho_a C_p C_S U_{10} (t_s - t_a) \tag{2.2}$$

$$Q_L = \rho_a L_E C_L U_{10} (q_s - q_a) \tag{2.3}$$

The parameters involved in the bulk formulas (2.1)-(2.3) are described in Table 1.1:

On the oceanic side, the dominant factors influencing the SST are the heat transport by currents, vertical mixing and boundary layer depth. Ekman and geostrophic currents

contribute to the heat budget of the mixed layer through horizontal advection, whereas entrainment and Ekman pumping alter the SST through vertical advection. A complete discussion of the main contributors to the heat budget of the ocean may be found in standard oceanography texts such as Vallis (2006), and Stewart (2005). The net surface energy flux is decomposed into the sensible heat flux, the latent heat flux, the downward solar radiative flux minus that portion penetrating through the mixed layer, and the long-wave radiative flux. The turbulent energy flux is linearly proportional to the wind speed and the air-sea temperature or humidity difference. The radiative fluxes are functions of temperature, humidity and cloudiness.

Table 1.1 Notation describing fluxes in the bulk formulas (2.1)-(2.3)

Symbol	Variable	Value and Units
C_p	Specific heat capacity of air	1030 J Kg^{-1} K^{-1}
C_D	Drag coefficient	(0.50 + 0.071 U_{10}) x 10^{-3}
C_L	Latent heat transfer coefficient	1.2 x 10^{-3}
C_S	Sensible heat transfer coefficient	1.0 x 10^{-3}
L_E	Latent heat of evaporation	2.5 x 10^6 J Kg^{-1}
q_a	Specific humidity of air 10 m above the sea	Kg (water vapor) Kg^{-1} (air)
q_s	Specific humidity of air at the sea surface	Kg (water vapor) Kg^{-1} (air)
Q_S	Sensible heat flux	W m^{-2}
Q_L	Latent heat flux	W m^{-2}
T	Wind stress	Pascals
t_a	Temperature of the air 10m above the sea	K or ºC
t_s	Sea surface temperature	K or ºC
U_{10}	Wind speed at 10 m above the sea	m s^{-1}
ρ_a	Density of air	1.3 Kg m^{-3}

2.2 The West African Monsoon: a coupled ocean-atmosphere-land system

Monsoon systems develop over pairs of continents such as Asia and Australia, or continents lying on both sides of the Equator such as north-west and south-west Africa, and North and South America. These continental configurations define, respectively, the Asian–Australian monsoon, the West African monsoon, and the American monsoon systems. Each system is different in terms of intensity and atmospheric circulation features. For instance, the northern branch of the American monsoon is a relatively weak counterpart of the other major monsoon systems and there does not appear to be a perceptible cross-equatorial component during the summer. In this way, the North and South American monsoons may be considered as separate phenomena. Otherwise, precipitation that occurs over the continents spanning the Equator (e.g., equatorial Africa and South America, and Indonesia) is not strictly monsoonal rainfall, showing double rainfall maxima coinciding with the equinoxes. Meanwhile, purely Monsoon climates exhibit a single rainfall peak during the solstices, along which dry seasons occur for equatorial climates.

As it comes to the present thesis, the WAM is characterized by rainy periods in both the Northern and Southern Hemisphere across interior Africa. However, given the proximity to the strong monsoonal circulations of Asia and Australia/Maritime Continent, the monsoonal circulations of the WAM and their accompanying cross-equatorial flow present certain uncertainties, not being well defined. Precipitation is enhanced across interior Africa where warm, dry air from the Sahara intercepts relatively moist air from the south (i.e., South Atlantic Ocean). During boreal summer, this enhanced precipitation is located along the ITCZ, or near 10-15ºN, whereas during boreal winter, this enhanced precipitation is found across south-central Africa. Thus, to some extent, the WAM can be interpreted as an enhancement of the ITCZ across Africa during northern and southern hemisphere summer.

The West African region is characterized by a pronounced meridional gradient in land-surface conditions while such conditions are zonally uniform (Fig. 2.9). The south-north transition ranges from the Guinean Gulf waters to the extremely dry and dusty Sahara, through the equatorial rain forest and the woody Sahelian Savannah. The West African monsoon is characterized by a strongly seasonal rainfall regime over the continent during

boreal summer. The processes that couple the land, ocean and atmosphere involve multiple interacting space and time scales. As with all monsoon systems, the evolving ocean and land conditions determine the nature of the WAM and its variability.

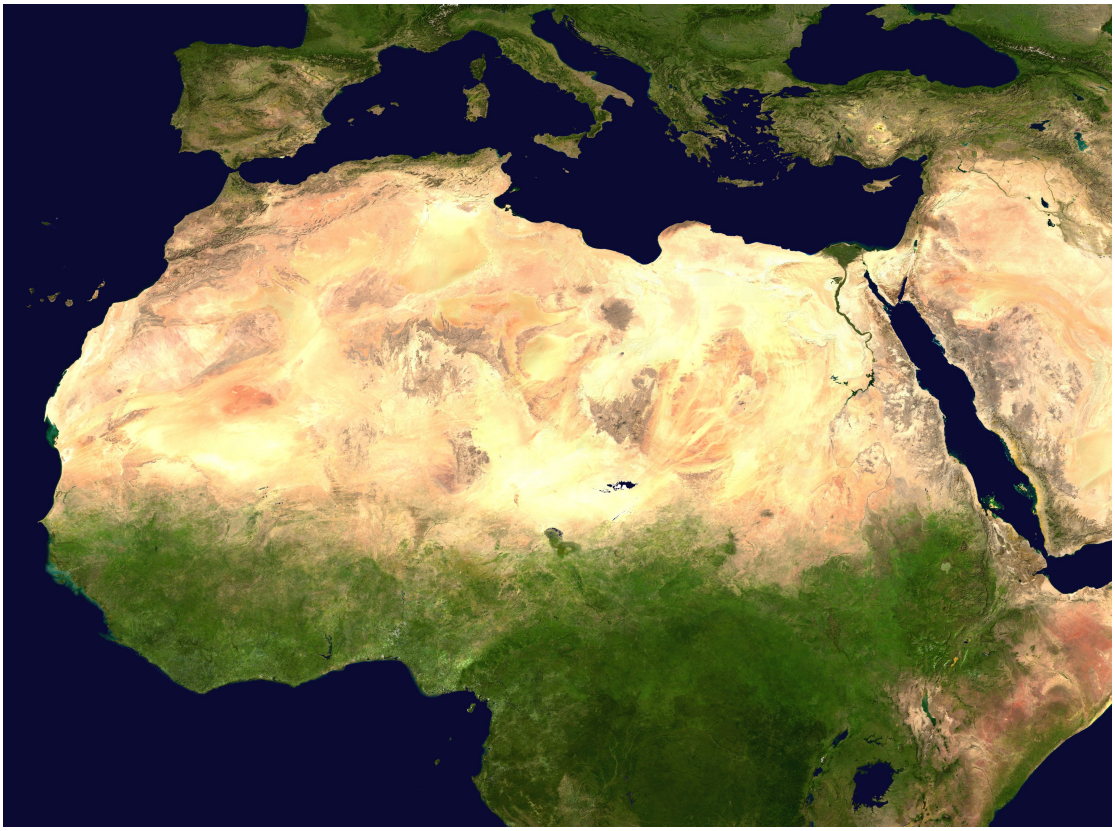

Fig. 2.9. Satellite image of the West African region. (Image by NASA World Wind: *https://worldwind.arc.nasa.gov/*).

The key features of the WAM are: the ITCZ, the Saharan heat low (SHL), the low-tropospheric African Westerly Jet (AWJ), the mid-tropospheric African Easterly Jet (AEJ) and the high-tropospheric Tropical Easterly Jet (TEJ). These features are partially illustrated in Figure 2.10.

The seasonal cycle of the WAM (Fig. 2.11) is defined by a south-north-south displacement of the ITCZ (e.g., Chiang et al. 2002; Kushnir et al. 2003) that in turn is strongly influenced by an inter-hemispheric SST contrast (e.g., Folland et al. 1986) and the accompanying surface pressure gradient (Nicholson 2009). This displacement of the ITCZ is characterized by an intermittent convective activity. First, rainy season takes place along the Guinea coast and comprises two active convection phases between early May and late June. Then, the ITCZ shifts northward, from 5ºN to 10ºN, corresponding

to a weakening of the convective activity (e.g., Sultan and Janicot 2000). This is named as "monsoon onset" and gives rise to the strongest convective phase accompanying the maximum rainfall over the Sahel (Le Barbè et al. 2002; Sultan and Janicot 2003; Gu and Adler 2004). Over the period 1968-2004, its average date is June 24th, with a standard deviation of 7 days. The WAM monsoon onset date has been linked to the amplification of the SHL (e.g., Lavaysse et al. 2009, 2010), perhaps through orographic interactions with the Atlas and Hoggar Mountains of northern Africa (Drobinski et al. 2005), or maybe it is the consequence of water vapor-forced greenhouse warming over the Sahara (Evan et al. 2015). Finally, the WAM begins its southern migration in late August and the coastal rainy season ends in early November.

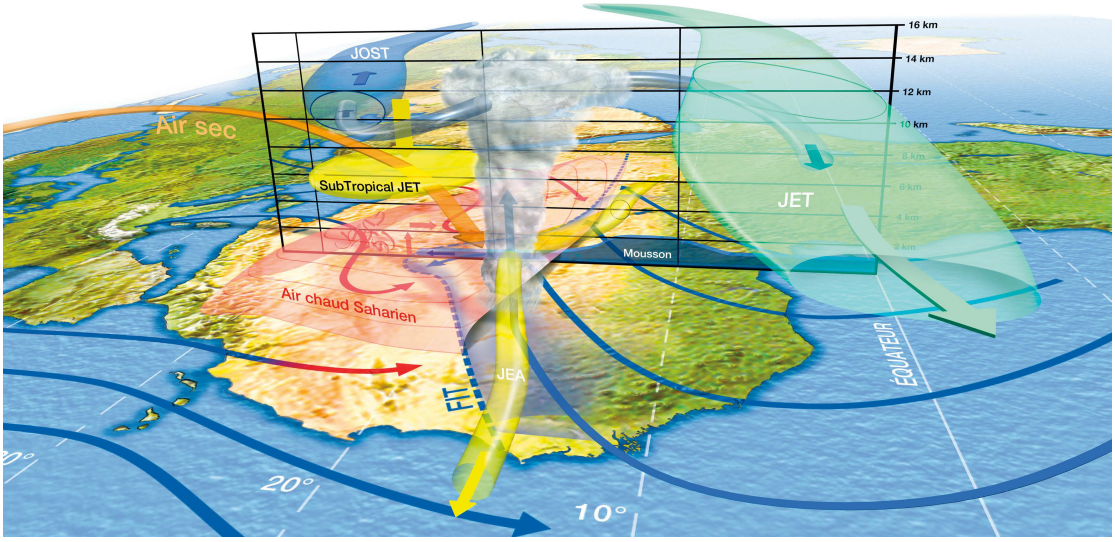

Fig. 2.10. Schematic view of the West African Monsoon System adopted from Lafore et al. (2010). FIT stands for ITD (InterTropical Discontinuity), "Air chaud Saharien" stands for 'Warm Saharian Air", JEA stands for AEJ (African Easterly Jet), JET stands for TEJ (Tropical Easterly Jet), "Air sec" stands for "Dry Air" (from Sylla et al. 2013).

The ITCZ annual cycle is potentially regulated by the coupled air-sea nature of the WAM. In the Gulf of Guinea, the annual cycle of the SST is identified by a transition from the highest values in April to the coldest SST in August and a subsequent warming up to the next April. There are several factors that determine this evolution: positive feedbacks between the enhancement of the monsoon winds above the Guinea Gulf and associated enhancement of convection in the ITCZ, the equatorial upwelling, the strengthening of the Santa Helena anticyclone associated with the cooling in the southern tropical Atlantic, the enhancement of the southern Hadley circulation, and the low-level

stratus clouds developing over these cold waters (e.g., Gu and Adler 2004; Okumura and Xie 2004).

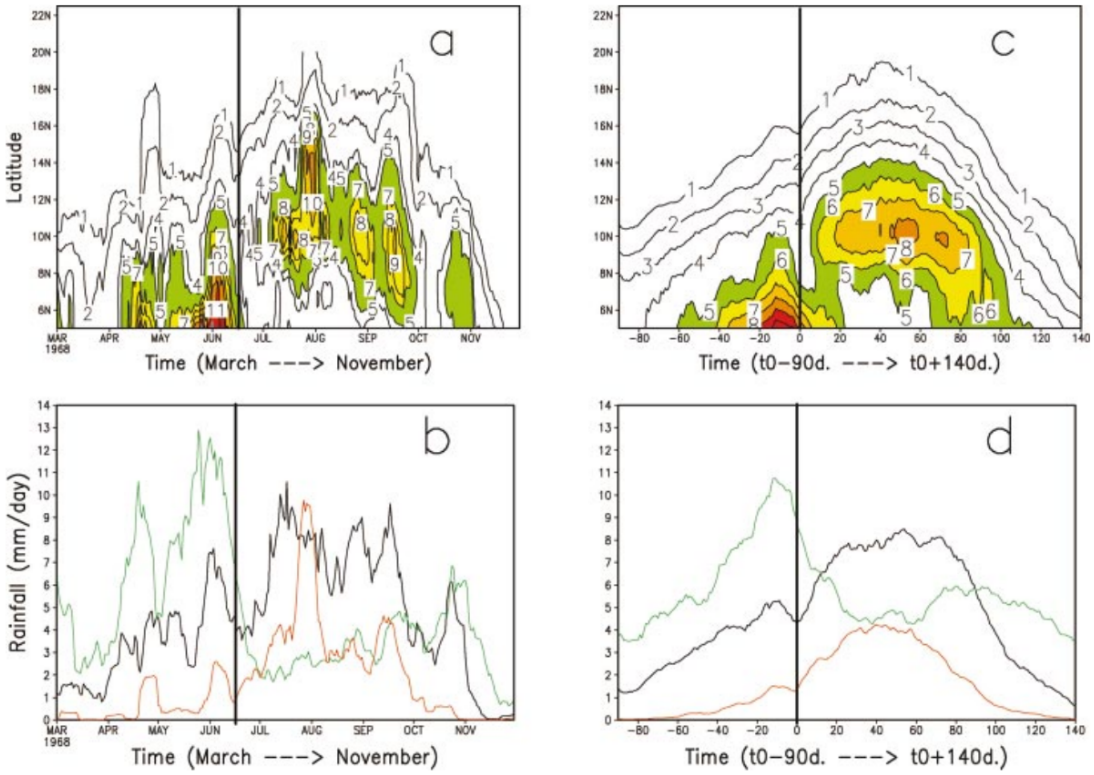

Fig. 2.11. (a) Time-latitude diagram from 1 Mar to 30 Nov 1978 of daily rainfall (mm day^{-1}), averaged over 10°W-10°E and filtered to remove variability lower than 10 days. Values greater than 5 mm day^{-1} are colored. (b) Time sections of diagram (a) at 5° (green curve), 10° (black curve), and 15°N (red curve). In (a) and (b), the vertical line localizes the date selected for the ITCZ shift (17 Jun). (c) Composite time–latitude diagram of daily rainfall (mm day^{-1}) averaged over 10°W-10°E, filtered to remove rainfall variability lower than 10 days, and averaged over the period 1968–90 by using as the reference date the shift date of the ITCZ for each year. Values are presented from t_0 (the shift date) -90 days to t_0 + 140 days. Values greater than 5 mm day^{-1} are colored. (d) Time sections of diagram (c) at 5° (green curve), 10° (black curve), and 15°N (red curve). In (c) and (d), the vertical line localizes the date of the ITCZ shift at t_0 (the mean date over the period 1968–90 is 24 Jun) (from Sultan and Janicot 2003).

By conducting a set of sensitivity experiments, Biasutti et al. (2003, 2004, 2005) concluded that the SST strongly influences the West African rainfall through the advection of marine boundary layer temperature anomalies over Africa, causing in turn anomalies in both sea level pressure and surface wind convergence. Additionally, they showed how seasonal changes in insolation are responsible for seasonal changes in the net budget of energy inlet in the atmospheric column, being balanced by horizontal energy output in the direct thermal circulation associated with convection in the ITCZ. As a result, this mechanism drives the moisture advection inland and the rainfall activity over West Africa.

The SHL, also termed the West African heat low (WAHL) is a region of high surface temperatures and low surface pressures. It is defined as a thermal depression generally below 700 hPa (e.g., Lavaysse et al. 2009, 2010), being stationary over the Sahara during the boreal summer season (Fig. 2.12). The SHL has been pointed out by playing a prominent role in the abrupt ITCZ shift into the Sahel. Thus, a hypothesis suggests the strengthening of the SHL at the time of the monsoon onset, enhancing the moisture advection from the ocean. This could be the result of interactions with the orography in North Africa (Dobrinski et al. 2005) combined with the spatial distribution of albedo and net shortwave radiative budget at the surface (Ramel et al. 2006). Lavaysse et al. (2010) establish a connection between strong (weak) convection activity and strong (weak) phases of the SHL. Moreover, Evan et al. (2015) put forward the role of the radiative flux associated with water vapor-forced greenhouse warming over the Sahara in the recent trend of increasing rainfall in the Sahel.

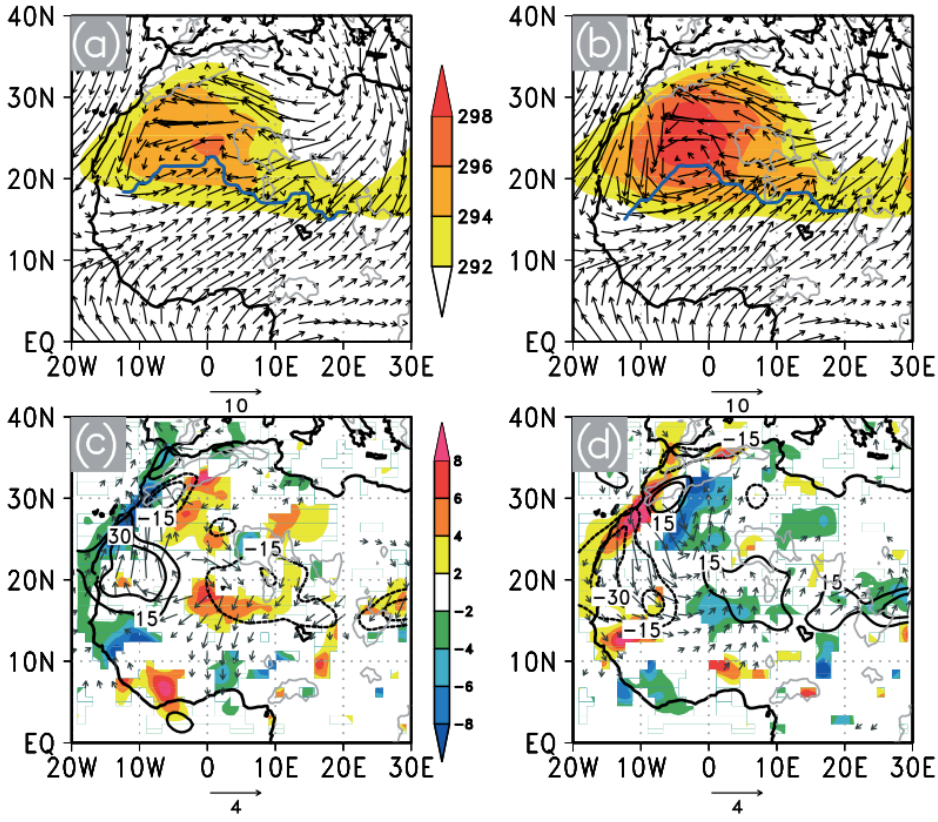

Fig. 2.12. Mean 925 hPa wind field (in m s^{-1}, vectors) and temperature averaged between 700 and 925 hPa (in K, colour) for the weak SHL composite (a) and the strong SHL composite (b). The position of the ITD is given by the blue line. Anomaly of the 925–850 hPa integrated water vapour flux divergence (in g kg^{-1} day^{-1}, colour shaded), of the 700–850 hPa integrated moisture advection (in g kg^{-1} day^{-1}, black contour) and anomaly of 925 hPa wind (vectors, with significant larger than 90% using Student's *t*-test) during weak

SHL (c) and strong SHL (d) phases with respect to the average of moisture advection and 925 hPa winds during the summer season (from Lavaysse et al. 2010).

The main tropical circulation features associated with the West African monsoon are the upper-level TEJ, the mid-level AEJ, and low-level equatorial westerlies associated with the southwest monsoon flow (Nicholson and Grist 2003), noticeably the AWJ. In wet years these westerlies become a reliable jet stream with a core near 850 hPa, being independent of the low-level monsoon flow (Grist and Nicholson 2001). In addition, the AEJ and monsoon westerlies become stronger over the western portion of the region, generating strong vertical shear, whereas the TEJ is more intense over the eastern part of the region. Multiscale interaction is characteristic of the WAM where mesoscale convective sytems (MCS), such as squall lines, move with and through synoptic-scale African Easterly Waves (AEW) (Riehl 1945; Reed et al. 1977). These waves are intrinsic phenomena to the WAM that occur every 3-5 days and have maximum amplitude at the level of the AEJ. Many Atlantic tropical cyclones form from easterly waves (Thorncroft and Hodges 2001) and its genesis is sometimes the results of easterly wave-MCS interactions (Berry and Thorncroft 2005; Lin et al. 2005).

Prospects for improving seasonal to interannual prediction of the WAM heavily rely on the potential predictability of surface conditions, the ability to observe key surface variables needed to initialize dynamical models, and the skill of these models to simulate subsequent evolution of the surface variables

An important remaining question is to what extent can we predict the variability of the WAM at interannual to decadal time scales and which are the associated surface conditions.

A key region in which the WAM acts is the Sahel, determining the hydrological cycle in this region, whose principal characteristics are described in the next sections.

2.2.1 The Sahel

The Sahel is a semi-arid transition region between the Sahara desert to the north and the humid savannahs to the south. It lies on western and north-central Africa, extending

from Senegal eastward to Sudan. The climate in the Sahel is similar to, but less extreme than, the climate of the Sahara desert, being sunny, dry, hot and somewhat windy all year long. An absolutely dry season prevails in the Sahel during most of the year, whereas a strongly seasonal rainfall regime brings the total amount of annual precipitation roughly coinciding with the summer months in the northern hemisphere (e.g., Ali and Lebel 2009; Lebel and Ali 2009; Nicholson et al. 2013). Considering the region as a whole, it receives between 100 mm and 600 mm of rainfall yearly. Indeed, based on the unequal distribution of annual rainfall, three types of climates are described in the region: the Saharan-Sahelian climate defined by mean annual precipitation ranging between 100 mm and 200 mm, the strict Sahelian climate, with values ranging between 200 mm and 600 mm, and the Sudanese-Sahelian climate, with mean annual precipitation between 200 mm and 400 mm. Furthermore, the low relative humidity in this steppe region ranges between 10% and 25% during the long dry season and between 25% and 75% during the rainy season. Temperatures show little variation in the Sahel throughout the year. Average high temperatures between 36ºC and 42ºC characterize the extremely dry and hot climate during the hottest period, whereas low temperatures are around 25ºC to 31ºC. During the period of lowest temperatures, coinciding with the rainy season, the highest average temperatures are between 27ºC and 33ºC, falling to minimum values between 15ºC and 21ºC and. Due to the tropical climate, the average temperature anywhere in the Sahel is above 18ºC.

Fig. 2.14. The road to Timbuktu, in Mali. Acacia trees in the Sahel sub-Saharan savannah eco-region. Author: Annabel Symington. (*Source: https://www.flickr.com/photos/belsymington/4102027841/*).

2.3 Sahel rainfall variability and predictability

During boreal summer, climate variability in the West African Sahel is dominated by the WAM, which brings a strong rainfall regime to the region from July to September (Nicholson 2013). The marked variability of this phenomenon makes the Sahel highly vulnerable to climate-related impacts (e.g., Sultan and Gaetani 2016). Indeed, the humanitarian consequences of desiccation during the 70s-90s have been dramatic (Mortimore and Adams 2001), leading to thorough research on both climate and socio-economic fields (Batterbury and Warren 2001; Hulme 2001; Held et al. 2005).

Being able to anticipate anomalously dry or wet episodes in the Sahel would imply a crucial advance for the inhabitants of this region. Nevertheless, a reliable seasonal forecast of Sahel rainfall has not been achieved so far.

In this section, a description of the state of the art regarding rainfall variability and predictability together with the remaining questions is stated.

2.3.1 Rainfall variability

Rainfall variability in the Sahel ranges from intraseasonal to multidecadal time scales. It is generally accepted that SST plays a major role in determining interannual-to-multidecadal variability of the West African monsoon (e.g., Ward 1998; Giannini et al. 2003; Hastenrath 2012). However, the influence of additional factors as internal variability and land surface processes cannot be neglected. An overview is presented in the following sections.

2.3.1.1 Interannual time scales

In the last decades, the WAM has become a major topic of study because of its interannual and intraseasonal variability (e.g., Janowiak 1988; Nicholson and Palao 1993;

Sultan and Janicot 2000; Le Barbè et al. 2002; Moron et al. 2006; Lebel et al. 2010). The interannual variability of Sahel rainfall is strongly linked to its seasonal cycle. This variability is closely related to changes in the zonal and meridional winds that are established in association with the meridional heating contrasts and associated thermally-direct circulations (Lebel et al. 2010). The mean monsoon-season winds are shown schematically in Figure 2.14. The African easterly jet is located in the region of strong low-level potential temperature (θ) gradients between the Sahara and the Guinea Coast, consistent with thermal wind balance, which reverses with height around the jet level (Cook 1999; Thorncroft and Blackburn 1999; Parker et al. 2005a). At low levels, southwesterlies from the Atlantic provide most of the moisture for the WAM, whilst northeasterlies advect relatively drier Saharan air into the rainy region. The low-level winds are part of a lower-tropospheric thermally direct meridional circulation (Thorncroft and Blackburn 1999; Trenberth and Caron 2000; Zhang and Delworth 2006) whose dry, southerly return-flow at around 600-700 hPa (Figure 2.14) is also related to the African easterly jet through the Coriolis acceleration.

The most prominent large-scale factor controlling the WAM is the Inter-Tropical Convergence Zone. In boreal winter the ITCZ locates around 5ºS over the tropical Atlantic, accompanying dry conditions over West Africa inland. During August, the ITCZ reaches its northernmost position, lying roughly between 10ºN and 12ºN. In September, the ITCZ retreats to the south. These excursions of the ITCZ are closely linked to interannual variability of SST in the tropical Atlantic (e.g., Fontaine and Janicot 1996; Chiang et al. 2002; Kushnir et al. 2003). Thus, during boreal spring (March-May), the Atlantic ITCZ shifts from its climatological position towards the anomalously warmer hemisphere. The associated SST pattern depicts an anomalous northward gradient in the tropical Atlantic region. Variability in the position of the ITZC has been atributed to changes in the north-south SST contrast, often referred to as the Atlantic Meridional Mode (AMM) of variability (e.g., Servain et al. 1999; Polo et al. 2008) (see section *2.4.1.2*). This SSTA pattern is associated with a northward cross equatorial surface wind anomaly, with weaker than normal trades in the tropical North Atlantic and stronger than normal trades in the tropical South Atlantic. This SST-wind pattern is associated with weaker than normal rainfall over the southern side of the climatological ITCZ position, being stronger than normal to the north, which implies a weakening in

the ITCZ strength along with a northward shift in its position towards the warmer hemisphere (Chiang et al. 2002).

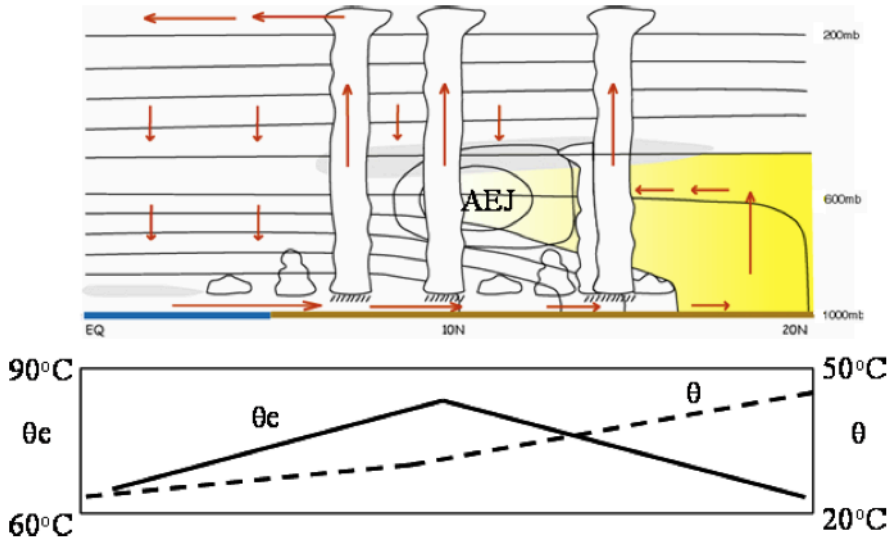

Fig. 2.14. Schematic of the atmospheric circulation in the West African monsoon system during the boreal summer. Closed solid lines represent the isotachs of the African Easterly Jet (AEJ), lying around 600 hPa. The red arrows show the thermally direct meridional monsoon circulation, and are typical of the time-mean winds in the peak monsoon season. This circulation will also be observed on many individual days, but there is strong variability over the diurnal cycle, and around mesoscale convective systems. The typical corresponding meridional variations in atmospheric boundary layer potential temperature (θ) and moist static energy equivalent potential temperature (θ_e) are given in the panel below. North of 10°N, θ_e starts to decrease while θ continues to increase, due to the drying of the boundary layer north of the core of the ITCZ. Grey stippled shading represents peak rainfall and yellow shading indicates the location of the Saharan Air Layer (SAL). North of the AEJ, convective systems are highly intermittent, commonly with an interval of several days between the occurrences of organized systems (from Lebel et al. 2010).

In the boreal summer (July-August), the ITCZ reaches its northernmost position over the tropical North Atlantic and West Africa, even reaching the Sahel. This coincides with the time when SST reaches its coldest annual climatology in the equatorial east Atlantic (e.g., Mitchell and Wallace 1992), the so-called Atlantic cold tongue region. Furthermore, regarding interannual variability this is the season of the years in which strong SST anomalies are prone to settle in this region, being similar to the Pacific El Niño (Zebiak 1993; Carton and Huang 1994) but no so persistent over time. This SSTA pattern is well documented as the Atlantic Niño or Atlantic equatorial mode (AEM) (e.g., Servain et al 1999; Polo et al. 2008). The AEM (see section *2.4.1.1*) accompanies a convergence of the surface winds towards the warmest region (Zebiak 1993). The effect on the ITCZ implies a southward shift and intensification in convection and rainfall (Carton and Huang 1994).

By contrast, under a negative phase of the AEM, cold SSTA consolidates the climatological background, keeping the ITCZ, and therefore rainfall, further north.

Regarding the AEJ, its variation is largely determined by the Saharan heat low (SHL, see section 2.2), which in turn presents significant fluctuations at various intraseasonal time-scales. Variability in the SHL seems to contribute to changes in the low-level monsoon moisture fluxes (Parker et al. 2005b). On the continental scale, the SHL drives a strong diurnal cycle in the monsoon circulation, which makes a significant contribution to the continental moisture transport (Lothon et al. 2008). Otherwise, smaller-scale structures also influences rainfall variability. First, the African easterly waves (AEW) developing in the African easterly jet (e.g. Hall et al. 2006; Kiladis et al. 2006) play an important role in triggering large, organized MCS, responsible for most of rainfall over the region. Secondly, the way in which these MCS interact with the surface and the large-scale environment, including the jets and monsoon-layer winds (e.g. Redelsperger et al. 2002), but also dusty harmattan winds, is a determining factor for the effective production of rainfall.

Changes in the interannual and decadal Sahel rainfall variability in JAS are depicted in figure 2.15 An important feature is that the standard deviation changes along the period of study, with some decades in which the amplitude of the anomalies are low and some others in which the anomalies increase. A general trend through an increase in the variability is observed. This suggests that the influence of Global Warming (GW) cannot be neglected but also other oscillation that seem to modulate the changes in the anomalies.

A remaining question to address in this thesis is the characterization of the main oceanic forcings that could explain this change in the amplitude of the anomalies.

2.3.1.2 Multidecadal time scales

The clear example of WAM multidecadal variability is the 20-year wet period, roughly between 1950 and 1969, followed by the Sahel big drought of the 1970s and 1980s (Lebel and Ali 2009) and the apparent trend to rainfall recovery during the recent decades

(Nicholson 2005; Hagos and Cook 2008) (Fig. 2.15). Thus, no shortage of work is aimed to disentangle both drought and recovery background conditions, which are mainly attributed to anthropogenic and natural causes (e.g., Giannini et al. 2008; Greene et al. 2009; Ting et al. 2009).

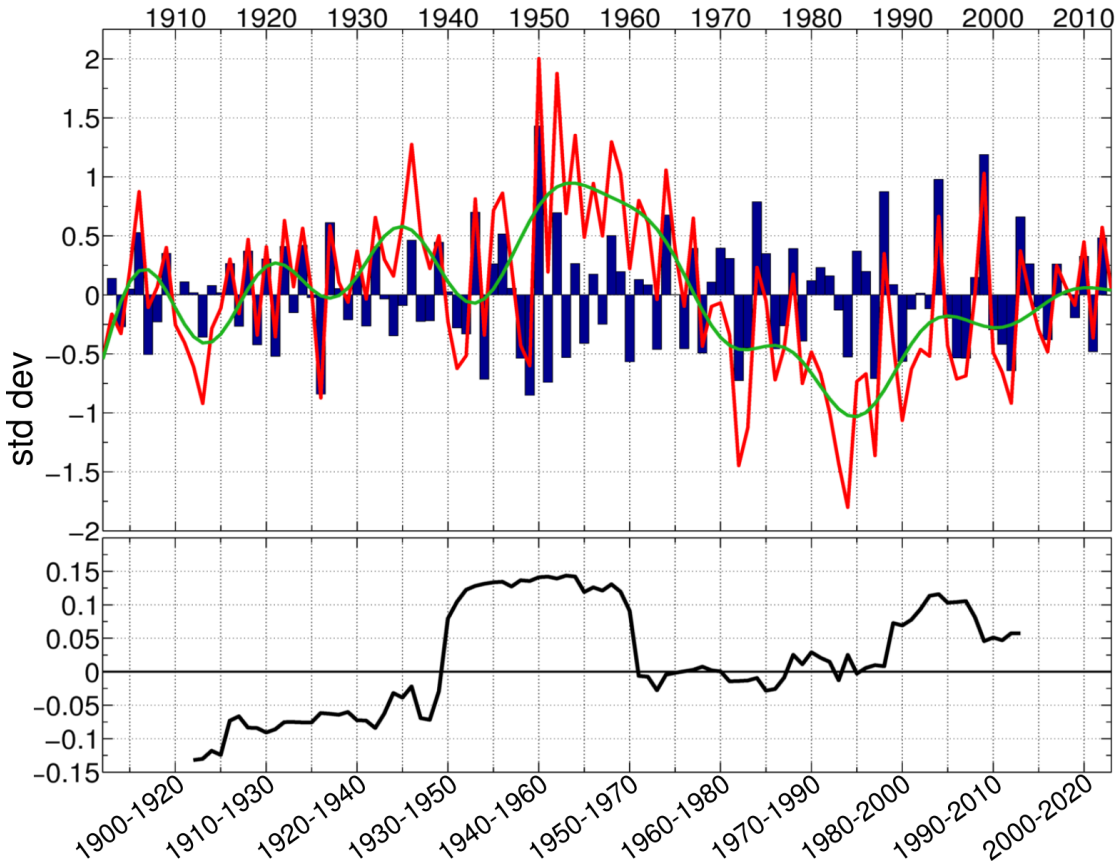

Fig. 2.15. (Top panel) Standardized index of anomalous rainfall (mm day^{-1}) in the Sahel (red line), together with its low frequency (green line) and high frequency (blue bars) components obtained by applying a Butterworth low pass (cutoff frequency of 2/13 years^{-1}) and high pass (cutoff frequency of 2/7 years^{-1}) filter respectively. The seasonal anomalies are calculated for the Sahel spatial domain (15ºW-15ºE, 10ºN-18ºN) during July-to-Sepetember (JAS) with respect to the 1902-2013 climatology using the CRU database (see section 2*a*). (Bottom panel) Variability of standard deviation calculated for the high frequency component of standardized rainfall (mm day^{-1}) index. The anomalous standard deviation (black line) is calculated as 21-years running means of the high frequency index (blue bars) minus the averaged standard deviation for the whole time series of the same index (from Suárez-Moreno et al. 2017a).

On the side of natural forcings, the SST variability has been identified as the leading factor underlying the observed interdecadal changes in the Sahel rainfall regime (e.g., Bader and Latif 2003; Giannini et al 2003; Lu and Delworth 2005; Lu 2009; Mohino et al. 2011a; Rodríguez-Fonseca et al. 2015). Moreover, the SST becomes a critical factor in the severe drought experienced in the Sahel from the 1970s to 1980s (Hulme et al. 2001;

Dai et al. 2004; Held et al. 2005; Greene et al. 2009), triggering a dramatic situation for the subsistence of the inhabitants of this region. In this context, seasonal rainfall regime is closely linked to survival of the growing population in the Sahel and Sudan regions, with an economy fully dependent on agriculture and, therefore, rainfall (Mortimore and Adams 2001; Batterbury and Warren 2001). In this context, the Atlantic Multidecadal Variability (AMV) is particularly relevant, with its negative phase underlying the Sahel big drought, whilst the positive phase before and after that period is related to wet years (e.g., Shanahan et al. 2009; Martin et al. 2013; Martin and Thorncroft 2014). This is directly related to the SSTA inter-hemispheric gradients, driving a northward (southward) shift of the ITCZ when the gradient being positive (negative) to the north (e.g., Chiang and Kushnir 2000). In this context, the northern-hemispheric differential warming has been pointed out by inducing a significant increase in Sahel rainfall (Park et al. 2015). Concerning the IPO, its positive phase produces subsidence over West Africa as a result of an anomalous Walker-type circulation leading to decreased rainfall. Conversely, a positive impact on Sahel rainfall is linked to the negative IPO phase (Villamayor et al. 2015). Moreover, the pronounced warming in the Indian Ocean SST during the second half of the 20th century is linked to drought spells in the Sahel. In particular, the westward propagating equatorial Rossby waves induce stabilization that acts to suppress the convection (Giannini et al. 2008; Lu 2009).

Regarding anthropogenic forcing, greenhouse gases (GHGs) have been addressed for influencing surface temperature and energy fluxes over West Africa (Biasutti 2013). Under increased atmospheric GHGs concentrations, climate models uniformly respond, wetting the Sahel (Biasutti 2013). Nevertheless, despite this uniformity, the paths of influence are different depending on the model being used (Held et al. 2005), resulting in a marked non-linearity (Biasutti et al. 2013; Rodríguez-Fonseca et al. 2015). Dry conditions in the Sahel have been also attributed to the global warming in a way that the GW-induced stabilization of the tropical troposphere weakens the monsoon circulation (Gaetani et al. 2016). The anthropogenic-warming component of the Mediterranean SST appears to positively impact on Sahel rainfall in the recent period. More controversial is a recent study that attributes the entire increase of Sahel rainfall in the last decades to GHGs, obviating the role of SST (Dong and Sutton 2015). Anyway, whether due to natural or anthropogenic causes, no cross-model consensus is observed when comparing

20th simulations and 21st projections of rainfall in the Sahel (Cook and Vizy 2012; Vizy and Cook 2013).

The role of land-surface processes is more difficult to quantify. Charney (1977) pointed out that vegetation degradation over the Sahel might induce a long-term inhibiting feedback on rainfall. This degradation mostly refers to deforestation and/or desertification. In this way, changes in the vegetation over the continent lead to a progressive shift in the meridional gradients of static energy, thus impacting on the signature of the oceans in terms of modifications in the global atmospheric circulation, induced by changes in the global SST field or in the atmosphere itself (Xue and Shukla 1993; Semazzi and Sun 1997; Zheng and Eltahir 1998; Nicholson 2000; Wang and Eltahir 2000). Most of these studies suggested that the positive feedback triggered by a change in land cover is a significant mechanism for drought persistence. The climate change due to a vegetation perturbation might be sufficient to prevent the vegetation from growing back, thus making the drought self-perpetuating.

An important remaining question is to determine the role of GHGs on the different regions of the world impacting the Sahel (including oceans) and the balance of forces acting in response to global warming.

An additional external forcing refers to the role of Saharan dust. In this way, Wang et al. (2012) suggest that surface processes over Africa may be more important than changes in the low-level winds over the tropical North Atlantic for dust cover in the Atlantic. That is, the dust changes in the tropical North Atlantic could be more due to increased dust production in the Sahel and Saharan regions and subsequent westward transport by the mean winds. This results in a feedback process between the AMV and dust in the tropical North Atlantic that may operate through Sahel rainfall variability. An initially warm North Atlantic Ocean is associated with a northward shift of the Atlantic ITCZ and southwesterly surface wind anomalies, resulting in an increase of rainfall in the Sahel. The increased rainfall leads to a decrease in source regions for mineral aerosols (Mahowald 2007). Associated with the decrease of aerosols in the semiarid regions of Africa is a decrease of atmospheric wind-blown dust over the tropical North Atlantic. This, in turn, is a positive feedback onto tropical North Atlantic SST via the aerosol direct effect by changing the amount of solar radiation reaching the surface of the ocean.

2.3.2 Rainfall predictability

Dynamical models of general circulation (GCMs) make use of the physics of the oceans, atmosphere, land and ice and the multiple complex interactions between them to estimate the most likely average climate state for several months ahead. These models are used for diverse purposes, from the study of the atmospheric dynamics of the observed climate system to projections of future climate evolution.

There are different types of GCMs that are focused on different components of the climate system. In this context, there are models focused on the simulation of ocean dynamics from information on heat budgets and momentum fluxes, while others simulate the dynamics of the atmosphere under a prescribed oceanic forcing. These models are the so-called oceanic general circulation models (OGGMs) and atmospheric general circulation models (AGCMs) respectively. Moreover, from these models, coupled models can be created, the so-called coupled atmosphere-ocean general circulation models (AOGCMs).

The study of the impacts of tropical climate variability has become increasingly important during the last decades, either at regional or global scale. In this way, along with dynamical models, there are statistical methodologies that attempt to define and predict the weather from intra-seasonal to multidecadal time scales. However, the study of climate variability is complex and recent and, despite the great progress made by the scientific community, it is still very difficult to make an accurate forecast of tropical climate variability in general, and of the WAM in particular. This difficulty is a direct consequence of the complex combination of processes controlling the WAM dynamics from interannual to multidecadal time scales (see section 2.2).

2.3.2.1 Biases in numerical models

Numerical models exhibit a series of systematic biases in forecasting climate variability

mainly in tropical regions where the ENSO in the Pacific, and the tropical Atlantic modes control most of the global climate variability. Accordingly, many studies have focused on the analysis and improvement of these models. Nevertheless, the difficulty of numerical models to reproduce much of the tropical climate variability remains a real problem. In this context, the ITZC dynamics is not properly reproduced in most GCMs, resulting in deflections of maximum rainfall over tropical Atlantic, even though these models accurately simulate the pattern of convergence in surface winds from SST maximum (Biasutti et al. 2006; Richter and Xie 2008).

In recent years the number of studies focusing on specific aspects of the biases from GCMs has increased exponentially, covering topics such as the warm bias in the tropical Atlantic SST temperature (Wahl et al. 2011), the biases in seasonal-interannual variations of the ITCZ in the Atlantic (Doi et al. 2012), the biases related to the surface wind stress and its relationship with the SST (Richter et al. 2012), the biases in the equatorial cold tongue and its relationship with ENSO (Vanniere et al. 2013), the reproduction of a double ITCZ (Li and Xie 2013), the southeast tropical Atlantic biases (Xue et al. 2013) and several studies analyzing collected biases in simulations of the Coupled Model Intercomparison Project Phase 3 and Phase 5 (CMIP3 and CMIP5 respectively) (Bellenguer et al. 2013; Brown 2013; Toniazzo and Woolnough 2014) among others. As a result of these biases in reproducing tropical Atlantic SST variability, and more concretely the ITCZ dynamics, GCMs are unable to properly simulate rainfall variability over West Africa.

Partly due to these biases, statistical modeling has evolved linked to numerical models, either as an alternative or within them as a hybrid model. Statistical models, despite a much lower computational cost, do not reproduce the non-linear behavior of the ocean-atmosphere interactions, leading to constant research in numerical modeling, capable of reproducing better and better these interactions (e.g., Peng et al. 2000).

Attempts to implement new statistical models constitute a fundamental contribution aimed to enhance and complement dynamical models.

2.3.2.2 Statistical modeling

There are several techniques used in the development of statistical models. Linear Inverse Modeling was firstly described by Penland and Sardeshmukh (1995) and has been used, for instance, to predict tropical Atlantic SST (Penland and Matrosova 1998) or more recently to analyze the predictability and variability of the Atlantic meridional mode (Vimont 2012). The Model Output Statistics (MOS) method goes further back in time, typically use to determine a statistical relationship between a given predictand field and a series of variables obtained from numerical models (Glahn and Lowry 1972; Klein and Glahn 1974; Vislocky and Fritsch 1995). Strictly, MOS is not a predictive method, but an analysis technique. Another type of statistical methods corresponds to stochastic climate models, defined in the 1970s to be primarily applied in predicting SST anomalies and thermocline variability (Hasselmann 1976; Frankignoul and Hasselmann 1977) and later addressing non-linearity problems (Majda 1999). More recently, statistical modeling with neural networks has emerged to be increasingly applied in climate forecasting (e.g., Gardner and Dorling 1998; Hsieh and Tang 1998; Knutti et al 2003) with the potential to be a non-linear method capable of addressing those problems in atmospheric processes that are overlooked in other statistical methods (Tang et al. 2000; Hsieh 2001).

Special mention deserves two linear statistical methods: The maximum covariance analysis (MCA) and canonical correlation analysis (CCA) (e.g., Newman and Sardeshmukh 1995; Cherry 1996, 1997; Widmann 2005). These methods have been widely used in seasonal climate forecasting, either to complement numerical models or to be applied independently. In essence, these techniques serve to isolate co-variability-coupled patterns between the time-series of two given variables (Bretherton et al. 1992). Based on the ability of the SST as predictor field, these methods were originally applied to analyze the predictability of variables associated with ENSO (Barnston and Ropelewski 1992), as 500 hPa geopotential height anomalies over the North Pacific (Wallace et al. 1992) or global surface temperature and rainfall (Barnston and Smith 1996). CCA has been applied to the African continent as a whole for specification and prediction of seasonal temperature and precipitation (Barnston and Smith 1996). This is a good approach despite the presence of several disparate climate regions, because aspects of the climate of the different regions could be addressed by using as many CCA modes as desired. Another approach is that of Barnston et al. (1996), conducting separate

analyses for each region thought to have a distinct large-scale climate. This might allow the CCA modes to account for the major predictor-predictand relationship of each region in greater detail.

When conducting a pooling about the performance of models, the conclusion reached is that, on the one hand, dynamical models produce an underestimation in the seasonal prediction of the evolution of the atmosphere, partly because the difficulty to reproduce the influence of SST on atmospheric dynamics, and, on the other hand, the chaotic behavior of the atmosphere is markedly exaggerated in these models. In contrast, statistical models, despite being a useful and effective supplement, they are unable to reproduce the non-linearity of the ocean-atmosphere interacting system.

Thus, it is important to use both, statistical techniques and dynamical models to determine the main observational relationships and to contrast the hypothesis statistically inferred from a more dynamical point of view.

2.4 SST-driven Sahel rainfall variability

Due to its thermal inertia, the SST becomes a key variable in predicting rainfall variability in the Sahel. Anomalous SST plays a major role in determining interannual-to-multidecadal variability of rainfall in the region (see section 2.3.1). For this reason, both statistical and dynamical models often use the SST as a key variable to perform estimates of seasonal rainfall in West Africa (see section 2.3.2). Therefore, the SST may be considered as a reliable source of predictability due to its direct influence on the atmosphere and, thus, in several climatic variables.

2.4.1 Patterns of SST variability

Patterns of SST variability on interannual and longer timescales are the result of a combination of atmospheric and oceanic processes. Accordingly, these patterns may be due to intrinsic modes of atmospheric circulation variability that imprint themselves

upon the SST field mainly via surface energy fluxes. This would be the case of the Interdecadal Pacific Oscillation. They may also result from coupled ocean-atmosphere interactions, such as the ENSO in the tropical Indo-Pacific, the Atlantic equatorial mode and the cross-equatorial meridional mode in the tropical Atlantic. Patterns of SST variability may also arise from intrinsic oceanic modes, noticeably the Atlantic Multidecadal Variability. In addition, the SST presents a marked long-term global warming trend that is the fingerprint of the GW, being defined as the GW SST pattern (e.g., Mohino et al. 2011a). There are other SST patterns following the classification aforementioned. However, as mentioned in previous sections, these are the most prominent SST patterns driving rainfall variability in the Sahel from interannual to multidecadal time scales.

As stated, much of the large-scale organization of SSTA results from the large-scale organization of atmospheric circulation anomalies and attendant changes in the turbulent and radiative energy fluxes at the air-sea interface and the local wind-driven Ekman currents (Cayan 1992; Alexander and Scott 1997; Deser and Timlin 1997; Marshall et al. 2001; Alexander et al. 2002; Visbeck et al. 2003) (see section *2.1.2.1*). Patterns of SST variability are organized in the so-called "modes of variability" which are particular of each ocean basin and determine the principal directions in which the variability takes place. In this way, tropical oceans are the most important source of predictability for the WAM. The large-scale patterns of atmospheric circulation variability in the tropics result primarily from interaction with the ocean. In other words, they would not exist in the absence of SST variability.

2.4.1.1 Identification of SST variability patterns

To determine the co-variability of SST anomalies at different locations, one commonly used methodology is empirical orthogonal function (EOF) analysis. This method calculates a spatio-temporal pattern of variability accounting for the maximum covariance between the SSTA time series at all pairs of grid points comprising the data set (von Storch & Zwiers 1999). Next, the remaining co-variability is subject to the same decomposition considering the constraint that the successive spatio-temporal EOF patterns are orthogonal (e.g., uncorrelated) to each other in both time and space

domains. In essence, only the first *n* leading modes (e.g., *n*~5) are robust as a result of the constraint aforementioned. Each EOF pattern is associated with a principal component (PC) time series, describing the temporal evolution of the EOF pattern. The PC time series may be obtained by regressing the EOF pattern onto the original SSTA field at each time step. Thus, the PC provides the amplitude and sign of the associated spatial pattern for a given time step. Note that, for this reason, the sign of the EOF is arbitrary, even though the product of the EOF and the PC time series for a selected time step retrieves the correct sign of the spatial mode for such time. The EOF analysis has its limitations, being subject to orthogonality, with the possibility of having different modes accounting for similar percentage of explained variance (e.g., North et al. 1982).

2.4.1.2 Modes of interannual SST variability

At interannual time scales, ENSO in the Pacific and the AEM and AMM in the tropical Atlantic are the main drivers of ocean variability and Sahel rainfall anomalies can be explained based on these drivers (e.g., Polo et al. 2008; Losada et al. 2010a, 2010b; Rowell 2001, 2013; Mohino et al. 2011b, 2011c; Rodríguez-Fonseca et al. 2011, 2015; Nicholson 2013).

The ENSO is considered as the leading mode of interannual SST variability, influencing global atmospheric circulation in general and the monsoon systems in particular (Stockdale et al. 2010; Clarke 2014). It is calculated as the leading EOF of monthly SST anomalies over the globe (Fig. 2.16). As its acronynm states, ENSO comprises two phenomena: El Niño and the Southern Oscillation (e.g., Clarke 2014; Wang et al. 2017). On the one hand, El Niño is a large-scale SST warming in the tropical Pacific that develops roughly every four to seven years. On the other hand, an interannual seesaw in the sea level pressure (SLP) between tropical western and tropical eastern Pacific characterizes the SO. A weakening and strengthening of the easterly trade winds over the tropical Pacific accompany this surface temperature seesaw. Bjerknes (1969) was the first to suggest that these two phenomena were strongly connected, identifying a positive ocean atmosphere feedback associated to the Walker circulation (see section 2.1.1) as the cause of the ENSO. Initially, positive SSTA in the eastern equatorial Pacific reduces the east-west SST gradient, weakening the Walker circulation (Gill 1980; Lindzen and Nigam

1987) and therefore the trade winds around the equator. Thus, the weaker trade winds induce alterations in the ocean circulation that in turn strengthen the SSTA. This warm state is termed as the positive phase of the ENSO (El Niño). The cold phase of the ENSO, termed as La Niña, was addressed later (e.g., Philander 1990).

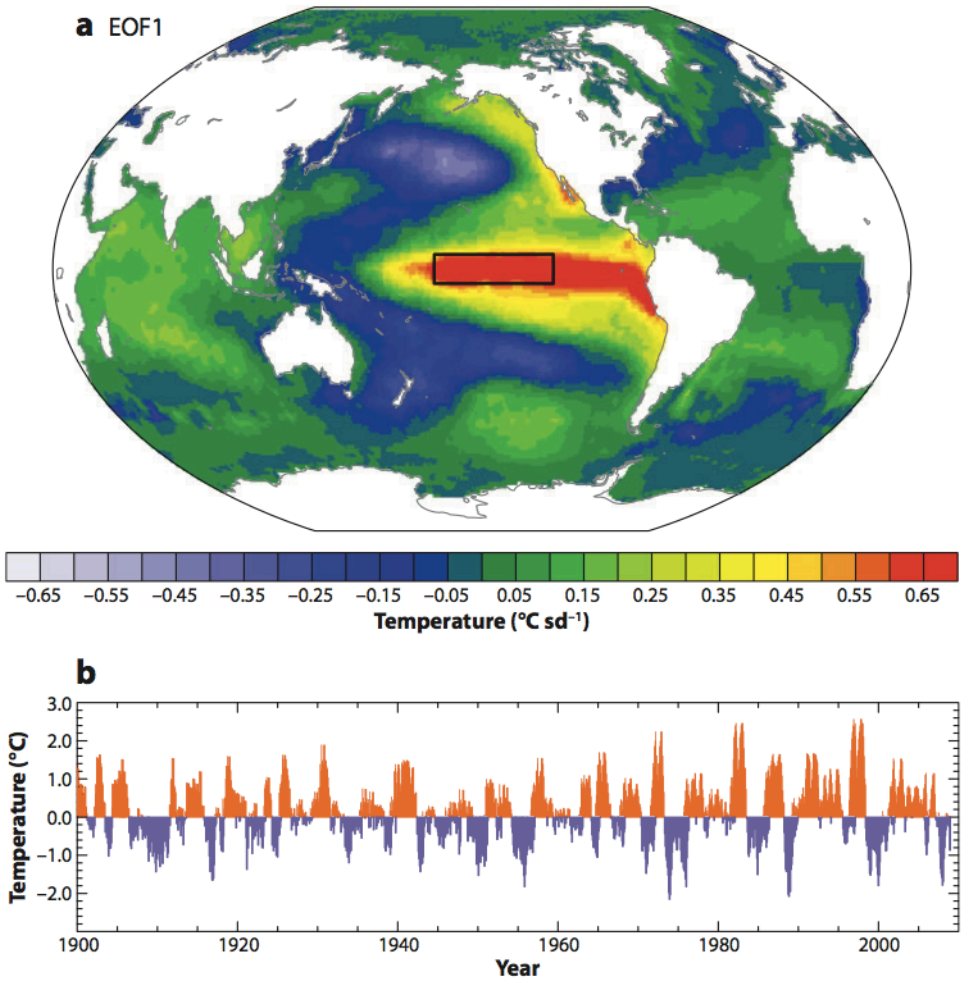

Fig. 2.16. (a) Leading empirical orthogonal function (EOF) of detrended monthly sea surface temperature (SST) anomalies over the global oceans based on the HadISST data set during 1900–2008. This mode, which accounts for 19% of the variance, depicts the El Niño-Southern Oscillation (ENSO) phenomenon. (b) Monthly SST anomaly time series in the Niño-3.4 region (5°N-5°S, 170°W-120°W; outlined by the rectangle on the EOF pattern) (from Deser et al. 2010).

The ENSO cycle has weather and climate implications in the tropics and across the extratropics of both hemispheres. Climatologically, the warmest water in the equatorial Pacific occurs in the so-called western Pacific warm pool (see Fig. 2.7). Rising air and therefore heavy precipitation occur in this region while the eastern Pacific is under the subsiding branch of the Walker circulation, so that it is relatively dry. El Niño causes shifts in tropical circulation (Fig. 2.17, central panel), which generally create drier than

average conditions in the western Pacific including Indonesia, Australia, India or even West Africa and above average precipitation over parts of South America. El Niño also tend to cause warmer than average conditions over parts of the tropics and into the extratropics (e.g., Halpert and Ropelewski 1992). This warming can also be detected in the globally averaged temperature. By contrast, La Niña is associated with enhanced rainfall in western Pacific regions and decreased rainfall in the central and east Pacific (Fig. 4.7, bottom panel). Moreover, La Niña is generally associated with cold regional anomalies, which are less easily seen in the globally averaged temperature.

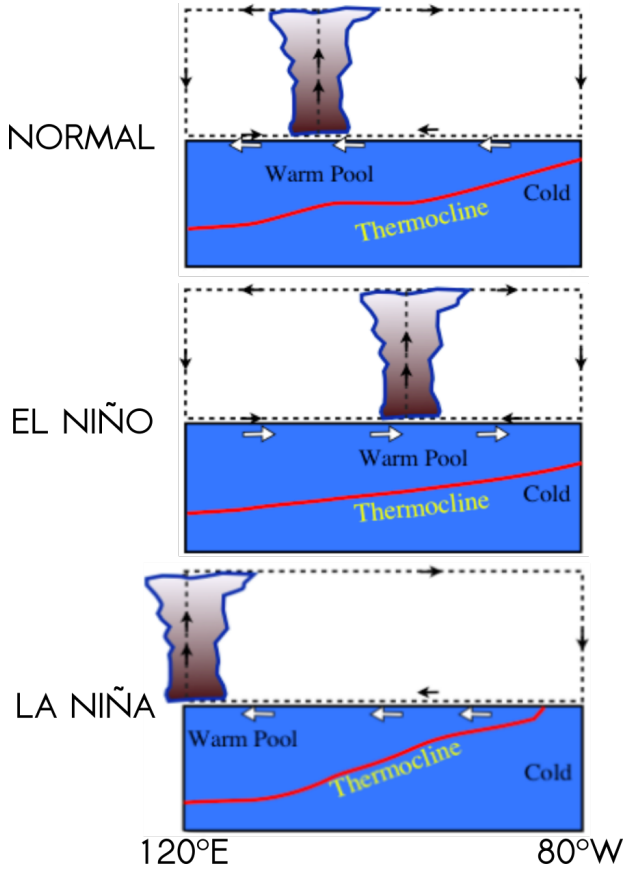

Fig. 2.17. Illustration of the oscillations in the Pacific Ocean during ENSO and non-ENSO years. The atmospheric circulation loops are shown in association with the location of deep convection. (Source: *http://nptel.ac.in/courses/119102007/12*).

Regarding the Atlantic basin, the leading EOF of monthly SSTA (June-August) is the Atlantic equatorial mode. The AEM peaks during boreal summer, when the anomalous conditions of the eastern equatorial upwelling can modify the zonal pressure gradient. Due to its similarity with the Pacific El Niño, the AEM is also known as the Atlantic Niño (e.g., Merle 1980; Zebiak 1993; Servain et al. 1999; Polo et al. 2008). This mode (Fig. 2.18a) is characterized by a relaxation in the equatorial trade winds, inducing SST

warming in the equatorial belt and a weakening in the equatorial thermocline slope. This results in an oscillatory ocean-atmosphere coupled mode (Zebiak 1993) affecting the heat content zonal gradient (Merle 1980; Servain et al. 1982; Carton and Huang 1994; Carton et al. 1996). During the warm phase of the AEM (Atlantic Niño), the zonal pressure gradient vanishes over the whole equatorial basin, triggering enhanced convective activity characterized by ascending motions of warm, moist air (Wang 2002). The oceanic component of the AEM seems to be mainly regulated through heat flux and momentum exchange between the ocean and the atmosphere in the South Atlantic (Sterl and Hazeleger 2003). While the heat flux generates SST anomalies in the mixed layer, the momentum exchange creates vertical turbulence and horizontal Ekman transport, in turn modifying the mean vertical and horizontal temperature gradient. Other features include transport by ocean geostrophic currents along the coast of Angola (Vauclair et al. 2004).

Regarding the AMM, it consists of a north-south dipolar SSTA pattern across the tropical Atlantic (Fig. 2.18b). This mode is the dominant pattern of tropical Atlantic SST variability during boreal spring (March-May) (Nobre and Shukla 1996; Seager et al. 2001; Kushnir et al. 2003). Notably, the centers of this mode coincide with the sub-tropical high-pressure systems and the eastern part of the subtropical gyres. In addition, the eastern upwelling systems are located over the northern and southern branches of the AMM. This intricate interaction is important in terms of air-sea interactions. Moreover, during the positive AMM phase a low-pressure system intensifies over the entire tropical basin, accompanying positive anomalies of rainfall over Northeast Brazil and the Gulf of Guinea, leading to enhanced Hadley circulation that affects the subtropical high-pressure systems, in turn influencing those centers of the AMM aforementioned. In another way, it has been suggested that an anomalous northward shift of the ITCZ would accompany a similar displacement of the northeastern trade winds and a strengthening of the southeastern trades winds along the equator (Servain et al. 1999). As a result, the thermocline slope would increase in the eastern equatorial Atlantic, generating cold SSTA in the subtropical south Atlantic due to enhanced evaporation and upwelling, thus giving rise to the negative phase of the AEM (La Niña) and positive SSTA north of the ITCZ by decreasing evaporation.

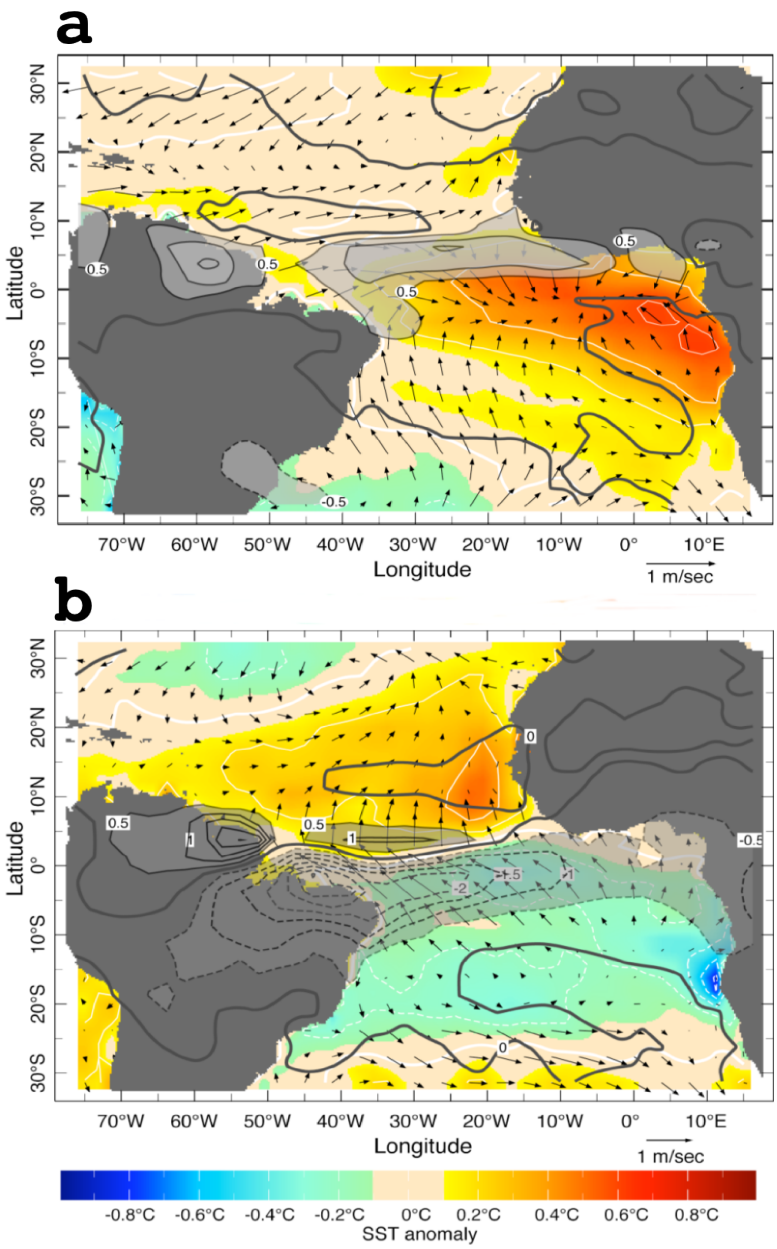

Fig. 2.18. (a) The dominant pattern of surface ocean-atmosphere variability in the tropical Atlantic region during boreal summer. The black contours depict the first EOF of the regional June-August rainfall anomaly (from GPCP data, 1979-2001) in units of mm day^{-1}. This EOF explains 23% of the seasonal variance. The colored field is the June-August SST anomaly regressed onto the principal component (PC) time series of the rainfall EOF (units are °C; white contours every 0.2° are added for further clarity). Arrows depict the seasonal surface wind vector anomaly in m s^{-1}, regressed on the same time series (see arrow scale below). (b) As in (a) but for the boreal spring season (March-April). The rainfall EOF of this season explains 33% of the variance (adapted from Kushnir et al. 2003).

2.4.1.3 Modes of decadal SST variability

The dominant patterns of multidecadal SST variability are the global warming, the Atlantic Multidecadal Variability and the Interdecadal Pacific Oscillation. Thus, decadal

variability over the Sahel can be explained on these principal directions of SST decadal variability. When used throughout this thesis, these patterns conform to the definition of Mohino et al. (2011a) (Fig. 2.19).

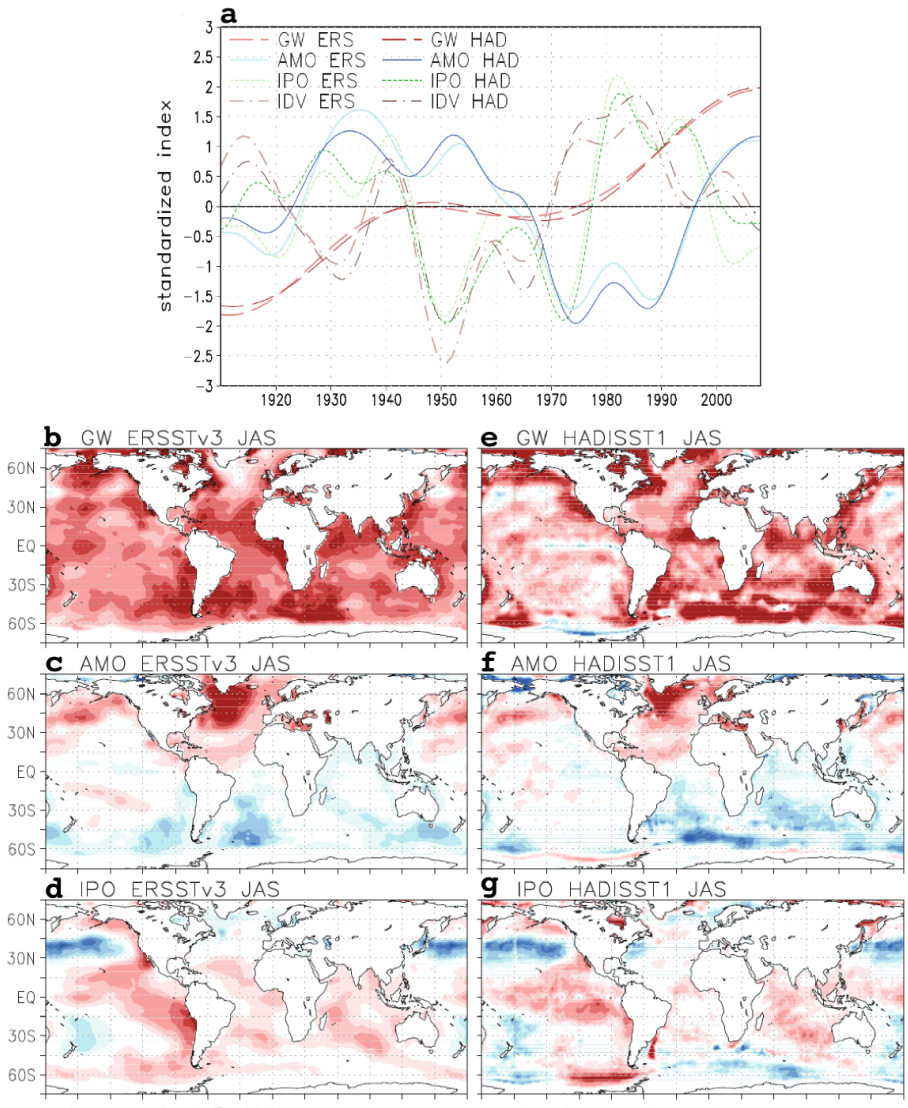

Fig. 2.19. (a) The 1910–2008 standardized GW, AMO and IPO indices obtained with ERSST (HadISST) data sets are shown in light (strong) red long dashed, light (strong) blue solid lines, light (strong) green short dashed and light (strong) brown dot dash lines, respectively. For the definition of each index see details in Mohino et al. 2011a. July to September average of the associated patterns calculated from ERSST data set for: (b) the GW, (c) the AMO, (d) and the IPO. Analogous patterns calculated from HadISST are shown in (e), (f), (g). The monthly GW, AMO and IPO associated SST patterns are defined as twice the regression of the observed monthly SST onto the 1910-2008 GW, AMO and IPO indices, respectively. Units are 0.5 K per standard deviation of the index (adapted from Mohino et al. 2011a).

There have been various attempts to remove the anthropogenic global warming signal from the time-evolving SST. These attempts include simple linear detrending, removal of the global mean temperature anomaly, and removal of model-based estimates of the

forced component of variability, the latter providing the best estimate (Ting et al. 2009). The GW index (Fig. 2.19a) shown here is based on yearly averaged global SST, being a good approach to that aforementioned.

The AMV, also termed Atlantic Multidecadal Oscillation (AMO) (Figs. 2.19c-2.19f) is considered as the low-frequency variability of SST in the Atlantic. The pattern is defined as the leading EOF of multidecadal SSTA variability in the Atlantic (45ºS-60ºN). Previous to the EOF analysis, the GW SST trend is calculated as explained above and removed from SSTA (e.g., Trenberth and Sea 2006). The warm phase of the AMV exhibits positive SSTA over the entire North Atlantic, with the largest magnitudes south of Greenland. This positive phase occurred in two distinct periods: from the late 1920s to the late 1960s and from the mid-1990s to the present. The opposite cold phases are observed between the 1900s and the 1920s, and from the early 1970s through the mid-1990s (Fig. 2.19a). The AMV is considered to be a natural mode of oscillation related to the Atlantic thermohaline circulation (Delworth and Mann 2000) (see section 2.1.2). Modeling studies indicate that this mode is intrinsic to the ocean and stochastically forced by atmospheric buoyancy fluxes (Delworth and Greatbatch 2000), even though the amplitude of the mode is increased due to coupled ocean-atmosphere interactions.

There is controversy about how anthropogenic forcing, particularly the GW associated to increasing GHGs affects natural variability modes and, in particular, the recent positive phase of AMV. It is for this reason that the GW trend should be removed as discussed above (Ting et al. 2009) to not confound the real state of the AMV. Moreover, the Atlantic thermohaline circulation may itself be altered under anthropogenic forcing as projected by some climate models (Dixon et al. 1999; Wood et al. 1999), but this is a different issue to that concerning the SST-based AMV index.

In addition to year-to-year variations associated with the ENSO phenomenon, SST in the tropical Pacific also fluctuate on timescales of decades and longer (e.g., Zhang et al. 1998; Power et al. 1999; Deser et al. 2004; Guan and Nigam 2008; Mohino et al. 2011a). This pattern of SST decadal variability is termed the Interdecadal Pacific Oscillation, being similar to, but not equal to the Pacific Decadal Oscillation (PDO) since the IPO refers to the Pacific basin-wide, whereas the PDO is mostly restricted to the tropical Pacific (Power et al. 1999). In the same way as explained above for the AMV, the leading EOF

is calculated in the Pacific to obtain the IPO SST pattern (Figs. 2.19d-2.19g) and associated index (Fig. 2.19a). This SSTA pattern is similar to that associated with the ENSO (see Fig 2.16). Nevertheless, the amplitude of the anomalies in the equatorial eastern Pacific is notably higher for the ENSO (e.g., Zhang et al. 1998; Deser et al. 2004). Different possibilities for the mechanism underlying the IPO have been proposed (Vimont 2005; Schneider and Cornuelle 2005; Qin et al. 2007; Newman 2007). Thus, these studies suggest that random and ENSO-induced variability in the Aleutian low play a major role via surface heat flux forcing, whereas the contribution from ocean currents is negligible. On decadal timescales, the contribution from the atmospheric tropical Indo-Pacific bridge changes in the North Pacific oceanic gyre circulation, and stochastic heat flux forcing is roughly equal. Moreover, winter excursions of the Kuroshio Current Extension over the western Pacific east of Japan are shown to be important (Nonaka et al. 2006; Taguchi et al. 2007). Taken these studies together, it can be concluded that the IPO is the sum of diverse phenomena.

2.4.1.4 The Mediterranean Sea

An additional basin closely linked to Sahel rainfall variability is the Mediterranean Sea. Unlike those SST variability patterns previously described, neither interannual nor multidecadal SST variability in the Mediterranean is typically defined by an EOF analysis. Contrary, ***there is still an open question about whether the Mediterranean SST variability is a fingerprint of large-scale forcing***. Indeed, when stating the AMV as the leading mode of SST variability in the Atlantic, by extension it comprises low-frequency variability in the Mediterranean (e.g., Mohino et al. 2011a). In this way, the Atlantic Multidecadal Oscillation seems to have a large influence on Mediterranean surface air temperatures and SST. Concretely, in an observational study (Mariotti and Del'Aquila 2012) the AMV is found to explain over 30% of regional decadal air temperature anomalies in summer (June-August), with decreasing influence in the transition seasons. Regarding the phases of the AMV, during July-to-August (JJA) the Mediterranean appears relatively cooler roughly during 1880–1920 and 1950–1990 and relatively warmer before 1880 and since 1990. Notably, the warming since the 1970s corresponds to a positive trend of the AMV index. Interestingly, Mediterranean SST shows multidecadal

AMV-like variability throughout the year, with over 30% of explained variance (Marullo et al. 2011).

2.4.2 SST-Sahel teleconnections

The term teleconnection is usually defined as a coherent atmospheric response to remote forcing such as particular SST or atmospheric pressure patterns. The term is usually applied to alterations in the atmospheric circulation, which are persistent and of large spatial scale. However, a more complete definition should refer to a teleconnection as any transmission of a coherent effect beyond the location at which a forcing occurred. Seasonal weather forecasters noticed certain persistent atmospheric circulation features and were using these teleconnection patterns for seasonal weather forecasts by the 1950s based on theoretical development by Bjerknes and Rossby in the previous decades (Namias 1953, 1959). As it concerns to the present thesis, SST-force teleconnetions with the Sahel rainfall are addressed.

The SST-precipitation links have been documented through works ranging from impacts on rainfall in North America (Shin and Sardeshmukh 2010), tropical America (Giannini et al. 2001), South America (Haylock et al 2006), Europe (Bulic and Kucharski 2012; López-Parages and Rodríguez-Fonseca 2012; López-Parages et al. 2015) and Australia (Drosdowsky and Chambers 2001) among others. In this framework, known to spare is the influence of the SST on the Indian monsoon (e.g., Rasmusson and Carpenter 1983; Ashok et al 2001; Chung and Ramathan 2006; Hoerling et al 2006; Kucharski et al 2008). Beyond these works, the focus of this thesis is on the WAM. In the last decades, this phenomenon has become an important topic of study owing to its marked variability from interannual to multidecadal time scales (see section 2.3.1). Thus, early studies establish the major role of SST variability as a root cause of Sahel rainfall fluctuations (e.g., Folland 1986; Palmer 1986; Fontaine et al. 1998; Ward 1998; Rodriguez-Fonseca et al. 2015).

On the one hand, the SST is presented as the main driver of decadal WAM variability, finding works dealing with the influence of the AMV (Knight et al. 2006; Shanahan et al 2009; Mohino et al. 2011a; Chiang et al. 2000; Martin et al. 2013; Martin and Thorncroft

2014), the GW (Biasutti et al. 2008; Mohino et al. 2011a; Munemoto and Tachinaba 2012; Park et al. 2015, 2016; Gaetani et al 2016), the IPO (Mohino et al. 2011a; Villamayor and Mohino 2015), and the warming trend of the Indian Ocean (Bader and Latif 2003; Chung and Ramathan 2006; Lu 2009). On the other hand, several works address the influence of global SST variability on the WAM at interannual time scales, finding robust changes associated with the ENSO (Janicot et al. 2001; Rowell 2001; Joly and Voldoire 2009; Rodríguez-Fonseca et al. 2011), the Atlantic Niño (Giannini et al. 2003; Kushnir et al. 2003; Polo et al. 2008; Joly and Voldoire 2009; Nnamchi and Li 2011; Rodríguez-Fonseca et al. 2011) and the Mediterranean Sea (Rowell 2003; Jung et al. 2006; Gaetani et al. 2010; Fontaine et al. 2011a; Rodríguez-Fonseca et al. 2011), all identified by their impact on the monsoon system and its predictability.

Moreover, several experiments based on GCMs were conducted within the international African Monsoon Multidisciplinary Analysis (AMMA) project. These experiments were planned in order to study the impacts of SST variability on the WAM system at different time scales (Fontaine et al. 2010; Losada et al. 2010a, 2010b; Rodríguez-Fonseca et al. 2011; Mohino et al. 2011b, 2011c). Together with previous studies, the results of the coupled models corresponding to the Fourth Assessment Report of the Intergovernmental Panel on Climate Change (IPCC-AR4) have been also analyzed (Joly et al. 2007; Joly and Voldoire 2009, 2010).

The ability to understand the underlying causes of WAM variability and associated external forcing and impacts would improve the predictability of monsoon rainfall in the Sahel, allowing anticipation of flood or drought events and thereby reducing dramatic socio-economic impacts.

To this aim, the teleconnections between the leading interannual SST variability patterns (see section *2.4.1.2*) and the Sahel rainfall are studied in the present thesis. In addition, the potential role of multidecadal SST variability patterns (see section *2.4.1.3*) in modulating the interannual SST-forced response of Sahel rainfall is investigated.

2.4.2.1 Mechanisms of SST-Sahel teleconnections

The mechanisms driving global SST-Sahel teleconnections are deeply described and analyzed throughout the present thesis, mainly to understand its possible changes allong the instrumental record.

The impacts associated with the AEM mainly affect the WAM. In this way, the monsoon onset, which is determined by the ITCZ, is in turn controlled by the land-ocean temperature and pressure contrast in the eastern equatorial Atlantic (Chiang et al. 2000; Kushnir et al. 2003; Okumura and Xie 2004; Nicholson 2009). Furthermore, a delay in the WAM onset with respect to its mean estimation could be partially explained by air-sea interactions in the Guinean Gulf region where the equatorial upwelling has shown a time lag with respect to the mean (Janicot et al. 2008). In this framework, the positive (negative) phase of the Atlantic Equatorial Mode (e.g., Polo et al. 2008; Losada et al. 2010a, 2010b) is related to decreased (increased) rainfall in the Sahel. Several studies have addressed the positive AEM as responsible for deep convection in the Gulf of Guinea, being concomitant with an equatorward position of the ITCZ and consequent decreased convergence over the Sahel, thus resulting in a rainfall dipole (Janowiak 1988; Fontaine and Janicot 1996; Janicot et al. 1998; Giannini et al. 2003; Joly and Voldoire 2010; Losada et al. 2010a) and decreased rainfall over the Sahel. On the contrary, the cold AEM accompanies a northward shift of the ITCZ, increasing rainfall in the Sahel and reversing the sign of the dipole.

Concerning the AMM, it mainly impacts rainfall in Northeast Brazil (Moura and Shukla 1981; Nobre and Shukla 1996). In this way, a northern-hemispheric SST gradient was found linked with a northward shift of the ITCZ and associated drought conditions in the region (Xie and Carton 2004). In the same context, this SST-induced migration of the ITCZ affects rainfall in the Guinean Gulf region through the anomalous cross-equatorial winds. The observed seasonality of this interaction is explained as the result of the spatially uniform warm climatological SST conditions in boreal spring, making the Atlantic ITCZ highly sensitive to small perturbations (Chiang et al. 2002).

Regarding the tropical Pacific, ENSO warm (cold) events are related to decreased (increased) rainfall in the Sahel. During El Niño events, the upper tropospheric heating

over the tropical Pacific triggers an atmospheric Kelvin wave that propagates eastward along the equatorial Atlantic sector causing anomalous subsidence over West Africa and associated decrease in rainfall. The opposite pattern is considered under La Niña events. This mechanism represents an anomalous Walker-type circulation for the ENSO-WAM teleconnection (Janicot et al. 2001; Rowell 2001; Giannini 2005; Joly and Voldoire 2009; Mohino et al. 2011c; Rodríguez-Fonseca et al. 2015).

The Mediterranean SST represents the leading forcing of WAM variability from the extratropics at interannual timescales. Anomalous warm events in the Mediterranean accompany positive anomalies of rainfall in the Sahel. Several authors have related this increase of rainfall to enhanced low-level moisture transport by the mean flow across the Sahara to the south, converging in the Sahel with the southwesterly monsoonal flow to increase precipitation (Rowell 2003; Jung et al. 2006; Fontaine et al. 2011a; Gaetani et al. 2010). This mechanism implies large-scale factors such as the Azores high, the Lybian high-pressure system or the Saharan heat low. On the contrary, a decrease in rainfall occurs when the Mediterranean is anomalously cold.

Although the mechanisms by which different ocean basins impact on the Sahel have been deeply studied, these mechanisms could be altered on time due to general circulation changes or non-linear interactions between the mean flow and the variability. Thus, observed changes in the rainfall anomalies amplitude in the Sahel could be due to changes in the oceanic forcing.

To what extent the changes in the amplitude of the SST anomalies associated with the leading modes of SST variability impacts on its dynamical response over the Sahel has not been studied so far.

As stated, rainfall variability in the Sahel keeps a robust link with global SSTA patterns at multidecadal time scales (e.g., Giannini et al. 2003; Mohino et al. 2011; Rodríguez-Fonseca et al. 2015). Regarding the AMV, under the warm phase (Figs. 2.18b-2.18e) tropical precipitation in the Atlantic sector shifts northward. Along with consistent changes in the trade winds, this fact implies northward displacement of the mean ITCZ. Northward movement of the summer (JAS) climatological ITCZ brings increased precipitation to the Sahel. This coincides with anomalous westerly winds carrying moist

Atlantic air into the region (Rowell et al. 1992). In the opposite AMV phase, the ITCZ is displaced southward, away from the Sahel, resulting in below average rainfall.

The GW trend has been addressed by inducing widespread drought conditions in West Africa (Sheffield and Wood 2008; Hagos and Cook 2008; Dai 2013). An explanation is based on the GW-induced stabilization of the tropical troposphere (Gaetani et al. 2016). In other way, the specific SST warming component in the subtropical North Atlantic has been associated with an increase in Sahel rainfall by providing sufficient moisture in the tropical monsoon flow to meet the threshold for convection (Giannini et al. 2008, 2013). Moreover, a teleconnection mechanism has been proposed on how extratropical North Atlantic cooling is related to decreased Sahel rainfall via a tropospheric cooling, so that a warming would have the opposite effect in terms of increasing rainfall (Liu et al. 2014). Additionally, the role of the northern-hemispheric differential warming has been recently suggested as the key factor in the projected increase of rainfall in the Sahel (Munemoto and Tachinaba 2012; Park et al. 2015). Moreover, a recent study propose the anthropogenic warming component in the Mediterranean Sea as a leading factor in the Sahel rainfall recovery, prevailing over the influence from tropical ocean basins (Park et al. 2016), which SST variability was historically the main driver of drought in the Sahel during the 20th century.

Up to now, few studies have addressed the potential impact of the IPO on Sahel rainfall (Mohino et al. 2011a; Villamayor and Mohino 2015), showing a negative correlation. In their work, Villamayor and Mohino (2015) put forward a robust IPO SST pattern associated with negative (positive) rainfall anomalies in the Sahel under its positive (negative) phase. This result agrees with observations, supporting the impact of the IPO on decadal variability of Sahel rainfall. The mechanism driving the teleconnection is explained in terms of an anomalous Walker-type circulation that produces subsidence over West Africa in the positive IPO phase. On the contrary, the negative phase favors the normal Walker circulation, promoting deep convection over West Africa.

2.4.3 Non-stationary SST teleconnections

Because of the persistence shown by SSTA, alterations that occur in the oceans are

slower than the changes occurring in the atmosphere. Thus, the energy stored for months in the ocean, inducing SSTA on its surface, can be released to the atmosphere when equilibrium is broken, inducing changes in atmospheric circulation during months before dissipating. As discussed in previous sections, these changes in turn have an influence on other atmospheric variables affecting rainfall.

An important question arises on how the oceanic forcing may not be associated with the same impact for a given period of study, thus being non-stationary on time. Conversely, a stationary behavior is considered when the co-variability pattern between two fields remains invariant for such a study period, as is the case of the nearby impacts of El Niño (always rain in Peru) or the Atlantic Equatorial Model on the Guinean Gulf region (always rain in the Gulf of Guinea under warmer conditions and the opposite for cooling).

Following this argument, the SSTA of a particular ocean basin could not contribute equally to the variability pattern of a given field in a particular place depending on the period under study.

In this context, the main task is to qualify and quantify such a non-stationary link, identifying potential underlying causes.

In this context, non-stationary SST impacts have been documented in different research topics. From health-related predictability studies, it has been shown that there is a strong concomitance between El Niño and the prevalence of cholera in Bangladesh during the last decades of the 20th century (1980-2001), while this relationship is weaker or even anti-correlated for the periods corresponding to the beginning of the 20th century (Rodó et al 2002). Related to vegetation, Rozas and García-González (2012) point a non-stationary and also non-linear relationship between ENSO dynamics and oak latewood growth in NW Iberian Peninsula, with significant correlations only during the period 1952-1980. Regarding the impact of SST itself, Rodríguez-Fonseca et al. (2009) suggest the changing connection between Pacific and Atlantic Niños during the 20th century, theory that has been further supported (Martín-Rey et al. 2012, 2014, 2015).

The impact of the ENSO on the Euro-Mediterranean rainfall during late winter-spring

(in the northern hemisphere) has also been shown to be non-stationary (Mariotti et al. 2002; Knippertz et al. 2003; Greatbatch et al. 2004). Nevertheless, a potential multidecadal modulation has been solely proposed by López-Parages and Rodríguez-Fonseca (2012). They put forward the fact that the correlation between the leading interannual rainfall mode and El Niño appears modulated in phase with multidecadal variability patterns, such as the AMV and IPO. Later, López-Parages et al. (2015) further explore this non-stationary link and associated modulation by using a GCM, confirming in this way that the natural variability has an effect in modulating the impacts of El Niño in the extratropical North Atlantic region.

As it concerns to this thesis, non-stationary links have been found between SST and the WAM. Thus, Janicot et al. (1996) suggested changes at high-frequency time scales in the association between eastern tropical Atlantic and Pacific basins and rainfall in West Africa after the 1970s. Later, Fontaine et al. (1998) pointed out the time-evolution in the anomalous SST-rainfall links due to the interactions between tropical ocean modes obtained from discriminant analysis techniques. At low-frequency time scales, these changes seem to affect co-variability patterns between Indian and equatorial Pacific SST and rainfall over West Africa from the 1970s. Afterwards, in one of the works carried out within the AMMA project, Rodríguez-Fonseca et al. (2011) put forward changes in the interannual teleconnection patterns between the whole tropical SSTA and precipitation in West Africa, showing changes for different periods. In the same context, Mohino el al. (2011b) denoted differences in the interannual SST-forced response of rainfall in the Sahel before and after the 1970s, suggesting that in turn, this could be the result of the non-stationary behavior in the teleconnection between Atlantic and Pacific SST co-variability modes (Rodríguez-Fonseca et al. 2009).

In fact, although the mechanisms leading the SSTA-driven teleconnections from the tropical Pacific, tropical Atlantic and Mediterranean with the WAM variability are widely described in the literature, there is the evidence of an unstable ocean impact on this phenomenon at interannual time scales.

This feature has been addressed in observational studies in terms of strengthened or weakened teleconnections and associated impacts depending on the considered sequence of decades (Janicot et al. 1996; Fontaine et al. 1998; Mohino et al. 2011b; Rodriguez-

Fonseca et al. 2011, 2015; Losada et al. 2012; Diatta and Fink 2014).

However, this evidence remains almost entirely observational, and dynamical mechanisms have been scarcely proposed so far.

In this thesis, the main motivation is to fully understand, including dynamics, the non-stationary SST-forced response of Sahel rainfall and its impact on predictability. The role of the underlying multidecadal SST variability is hypothesized and discussed as a potential cause of instability in the teleconnections.

CHAPTER III

3 Objectives

As stated, the non-stationary nature of the interannual SST-forced teleconnections with the Sahel rainfall have been merely found out in observational studies (e.g., Janicot et al. 1996; Fontaine et al. 1998; Mohino et al. 2011b; Rodriguez-Fonseca et al. 2011, 2015; Losada et al. 2012; Diatta and Fink 2014). In this way, the teleconnections are found to be strengthened or weakened depending on the sequence of decades under study. However, this evidence remains observational, and no physical explanation has been addressed so far, including the impact on predictability.

The main objective of this thesis is to determine the causes of a regime shift in the SST impact on Sahelian rainfall, clarifying the interdecadal changes in the SST-forced teleconnections to the Sahel, which in turn lead to improved predictability.

The specific objectives to achieve the main purpose stated above are:

- To create a statistical seasonal forecast model using the anomalous SST as predictor. The model will be able to consider different variables to predict, considering the non-stationary influence of the predictors. The time-windows in which predictability is enhanced or weakened must be included as output of the models. Also, the model will produce a cross-validated hindcast providing skill-scores for analyzing predictability. Finally, the model will be validated also for documented examples or non-stationary teleconnections, that will be used as bench mark

- To apply the model in order to explore the leading interannual SST teleconnections patterns with the Sahel rainfall. In particular, tropical Atlantic,

tropical Pacific and Mediterranean SST impacts on the anomalous Sahel rainfall will be studied along the observational record, analyzing the hypothetical instabilities of these links, its potential causes and the associated dynamics. A hypothesis from the observational analysis will be posed.

To determine the role of the different forcings, acting at different timescales, in the modulation of Sahel rainfall predictability. Reanalysis for the 20th century and observations from different SST and rainfall databases will be used to pose hypothesis on the mechanism involved in the teleconnection found. A series of sensitivity experiments with an AGCM will be conducted, prescribing different SSTA and climatologies with the aim of restating the working hypothesis to determine the optimum boundary conditions responsible for modifying the interannual teleconnection patterns.

CHAPTER IV

4 Physical background

4.1 General concepts on Monsoon dynamics

A monsoon is a circulation system with a set of well-defined features. During summer, winds in the low-level troposphere flow from the colder oceanic regions of the winter hemisphere toward heated continents. Conversely, winds flow from the summer to the winter hemisphere in the upper troposphere. Moreover, the so-called 'monsoon trough' determines the occurrence of rainfall during summer (e.g., Webster et al. 1998, 2002; Webster and Fasullo 2003). This trough of low pressure locates in the surroundings regions of the heated continents and the adjacent oceans and seas, on which precipitation mostly takes place. Most summer rainfall is associated with synoptic disturbances that propagate through the regions aforementioned. These disturbances are referred to as 'active monsoon periods', being grouped in periods of disturbed weather and heavy rainfall lasting from 10 to 30 days. The intervening periods of disruption in this strong convective activity are referred to as 'monsoon breaks'. The location of the monsoon trough and maximum monsoon precipitation is generally poleward of the position of the oceanic ITCZ, within which most of the tropical precipitation occurs. This location of maximum precipitation is the so-called 'tropical rain belt'. As stated in the introduction (see section 2.2), each system is different in terms of intensity and atmospheric circulation features. Purely Monsoon climates exhibit a single rainfall peak during the solstices, along which dry seasons occur for equatorial climates.

Monsoons arise from the development of cross-equatorial pressure gradients produced or modified by the following physical properties of, or processes associated with, the land–ocean–atmosphere system: differential heating of land and ocean produced by the different heat capacity of land and water; the different way in which heat is transferred

vertically and stored in the ocean and the land; modification of differential heating by moist processes; the generation of meridional pressure-gradient forces resulting from the differential heating; and the meridional transport of heat in the ocean by dynamical processes. Each of these processes and properties has to be considered relative to the rotation of the planet, and the influence of local effects such as the geography of the ocean and the landmasses, and regional topography.

Without distinguishing between the different monsoon systems, a characterization of the basic driving mechanisms of the monsoonal circulation is conducted in the next sections, providing an overview of the major physical processes that characterize the dynamics of monsoons.

4.1.1 Differential heating

There is a marked difference between the specific heat of water (~ 4218 J Kg^{-1} K^{-1}), dry soil (~ 1300 J Kg^{-1} K^{-1}) and wet soil (~ 1690 J Kg^{-1} K^{-1}). Given a net heating rate, the temperature increment of a mass of dry land will be roughly four times greater than that of a similar mass of water. Land-ocean heating gradients produced by its different heat capacity are the primary drivers of monsoon circulations. Sir Edmund Halley first formulated this theory in 1686 (Halley 1686), addressing the role of the annual cycle of solar heating in producing the strong seasonality of the monsoon and the reversal of the circulation during the winter. The theory was later used to explain aspects of the West African and South Asian surface monsoon winds that had been reported by explorers and traders.

On a physical basis starting from Halley's theory, if the heat flux into the surface layer is F (Wm^{-2}) and if there is no heat flux out of the bottom of the layer at a depth z (m), the heating rate of the layer will be determined by the flux divergence in the layer:

$$\frac{dT}{dt} = -\frac{1}{\rho C_p}\frac{dF}{dz} = -\frac{1}{\rho C_p}\frac{F_{z_0}}{\Delta z} \tag{4.1}$$

Where F_{z_0} is the net flux at the surface and Δz is the thickness of the layer.

Attending to (4.1), the heating rate of a parcel depends on the heat capacity of the layer, its thickness, and the net energy flux into or out of the layer at the surface. Meanwhile, the net heating at the surface determines the temperature of a static ocean parcel In the winter hemisphere, the ocean parcel would cool by a combination of evaporative cooling and negative net radiative heating. In the summer hemisphere, the ocean would heat if net radiational heating exceeds the evaporative cooling. During summer the land heats more rapidly than the adjacent ocean because of its smaller specific heat and shallow Δz. Overall, these factors are offset by the fact that dry land has a larger albedo (20-40%) than the ocean (10%). In the winter the land surface will cool much more quickly than the ocean simply because there is little available heat in the subsurface that can be made available to heat the surface on seasonal time scales because of the slowness of the diffusive processes. Given that the sensible heat exchange between the land surface and the atmosphere depends to a large degree on their temperature difference, the atmospheric column over the land will be warmer than over the ocean. Then, considering an idealized static ocean, an annual cycle of ocean-land temperature difference and meridional pressure-gradient force is attained.

When it comes to a naturally fluid ocean, wind forcing and gravitational instabilities formed by the cooling of the surface layer may induce turbulence and mixing of the surface and subsurface water. Wind stress also can move water mass horizontally, giving rise to ocean currents that can advect heat and mass from a given ocean basin to another. Stable layers near the surface can be generated by the freshening effect of precipitation. These layers may reduce the impact of wind stirring.

The impact of changes in heat storage on the ocean temperature is twofold. First, it moderates the SST, which in turn modulates the temperature and moisture content of the air adjacent to the ocean surface. Atmospheric turbulent mixing produced either mechanically by wind stress or by buoyancy effects extends the imprint of the SST into the troposphere. Second, the mixing processes in the ocean column produces the observed lags between the ocean temperature and the solar cycle. Land surface temperature tends to follow the solstices, although, because of moist processes, the maximum land temperature occurs before the onset of the summer rains.

4.1.2 Pressure gradient forces: thermal wind balance

As stated, monsoonal circulation is characterized by wind reversals. These wind reversals, interpreted as changes in wind magnitude with height, are driven by the horizontal pressure-gradient. Thus, the horizontal pressure-gradient force between both hemispheres (i.e., equatorial latitudes) may change with height or even reverse. From the hydrostatic equation and the equation of state, neglecting density, it follows that:

$$\frac{\partial p}{\partial z} = -\frac{g}{R}\frac{p}{\overline{T}} \tag{4.2}$$

Where p is the atmospheric pressure, z is the height, g is acceleration of gravity, $\overline{T}$ is the mean temperature of the atmospheric column and R is the gas constant. From (4.2) it is simply deduced that the variation of pressure with height is inversely proportional to the mean temperature of the column. Accordingly, over the colder region (i.e., cold ocean), the pressure increases with the height faster than over the warm region (i.e., warm continent). This is schematically illustrated in Figure 4.1. The different in pressure $\Delta \ln p(z)$ at the height $z = z_1$ between the warm and cold columns can be expressed as follows:

$$\Delta \ln p(z_1) = \frac{g}{R} z_1 \left(\frac{1}{\overline{T}_c} - \frac{1}{\overline{T}_w} \right) + \Delta \ln p(0) \tag{4.3}$$

Where $\overline{T}_c$ and $\overline{T}_w$ are the mean temperatures of the columns over the cold and the warm regions respectively, and the surface pressure difference between both columns is assumed to be zero $(\Delta \ln p(0) = 0)$. Then, assuming $\overline{T}_w > \overline{T}_c$, the air above the surface will be forced to flow from the colder (ocean) to the warmer (continent) regions. Due to mass continuity, the flow returns to the reverse in the lower troposphere.

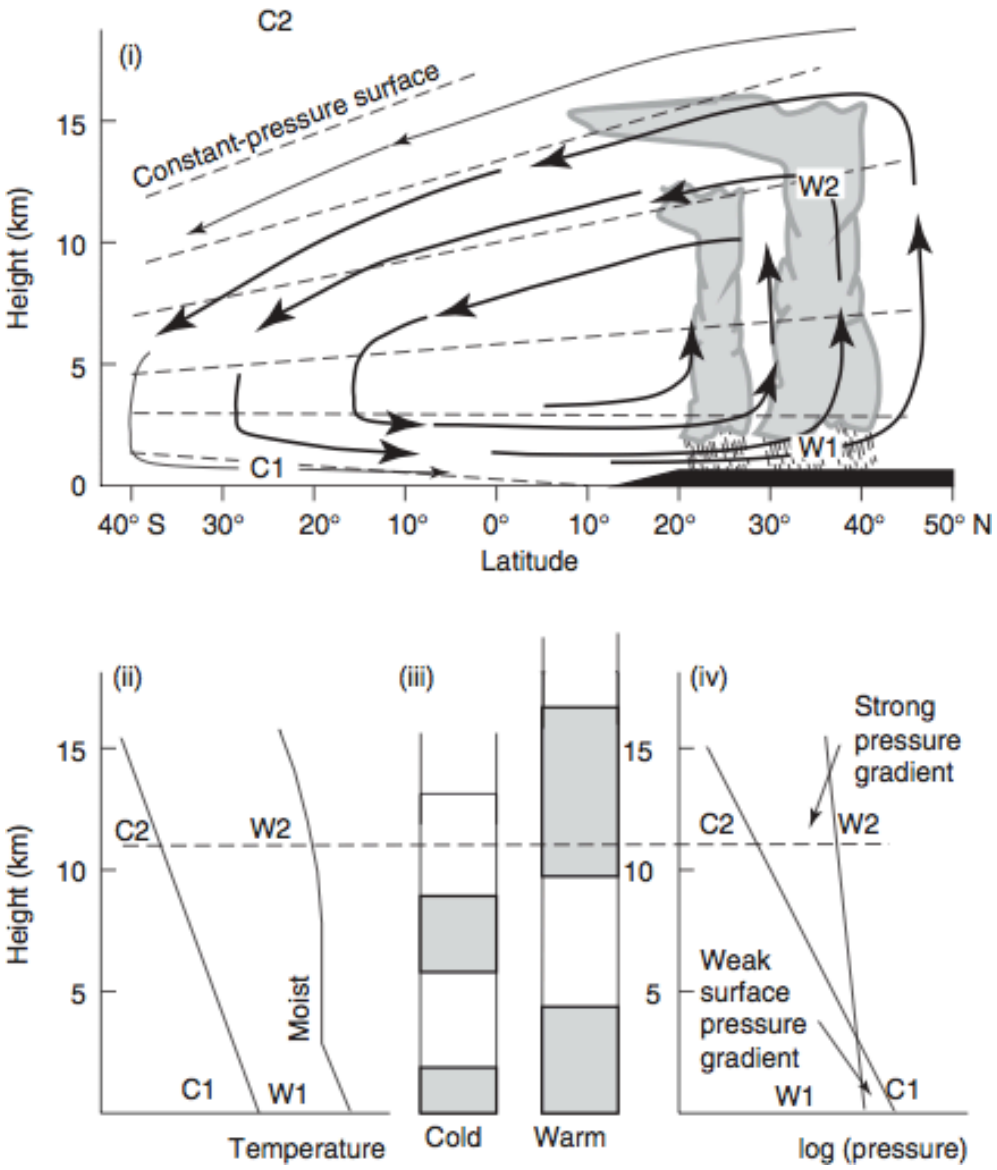

Fig. 4.1. A mechanistic view of the development of the meridional monsoon circulation when moist processes are taken in to account. The panels show (i) the resultant circulation, (ii) the temperature profiles, (iii) the distribution of mass in the vertical columns, and (iv) the change of pressure with height. Dashed lines in panel (i) show constant- pressure surfaces. Dashed lines in panels (ii)–(iv) denote a constant height. It is assumed that the difference in temperature of the warm and cold columns is sufficient to generate a reversing pressure gradient with height in the presence of the surface pressure gradient as described in eqn (4.4). (Adapted from Webster and Fasullo 2003).

In a better approach, as the solar heating increases over the continent, the surface pressure is higher over the colder ocean compared to the heated continent, so that $\Delta \ln p(0)$ becomes increasingly negative, and the assumption aforementioned $(\overline{T}_w > \overline{T}_c)$ does not guarantee a reversed upper tropospheric pressure gradient and the consequent return near the surface. Therefore, considering in (4.3) that $\Delta \ln p(z_1) > 0$ in the presence of a surface pressure gradient, it can be stated that there is a temperature threshold given by the expression:

$$\overline{T}_w > \frac{q z_1 \overline{T}_c}{g z_1 + R\Delta \ln p(0) \overline{T}_c} \tag{4.4}$$

If the condition in (4.4) is satisfied, a reverse pressure gradient in the upper troposphere is established in the presence of a surface pressure gradient. As a result, a direct thermal circulation is generated by pressure gradients throughout the troposphere, being in turn responsible for the onset of the monsoon seasons once the criterion in (4.4) is satisfied.

An additional factor involves the consideration of the Earth's rotation, that is, the Coriolis force. The effects of rotation are extremely important in the equatorial regions as the Coriolis force $(f = 2\Omega \sin\phi)$ changes sign and its gradient $(\beta = 2\Omega(\cos\phi)/a)$ is a maximum. As a consequence, the cross-equatorial monsoon circulation and associated pressure gradient is directly affected by the rotation effect. The 2-dimensional horizontal motion on a rotating surface is describes as follows:

$$\frac{dV}{dt} = -\frac{1}{\rho}\nabla p - f\ k \times V - \alpha V \tag{4.5}$$

Where $\alpha(s^{-1})$ is a dissipation coefficient, $\nabla p/\rho$ represents the pressure gradient force and $f\,K \times V$ is the Coriolis force. Then, considering the rotation of the Earth, steady flow comes about from a balance between the pressure gradient force and the Coriolis force, so that from (4.5) it follows that:

$$f\,K \times V + \alpha V = -\frac{1}{\rho}\frac{\partial p}{\partial y} \tag{4.6}$$

According to previous discussion, the flow in the upper troposphere is in the opposite meridional direction through the action of a reversed pressure gradient force that increases with height. Furthermore, compared to the surface boundary layer, the dissipation coefficient (α) is an order of magnitude smaller. Thus, the resulting flow is closer to geostrophic than the surface boundary layer flow but still cross-gradient as it spirals out of the upper anticyclone and moves westward. The trajectory that an upper-tropospheric air parcel takes is such that it will move a much greater distance in the

longitudinal direction (compared to the surface flow) before it crosses the Equator and eventually descends into the winter hemisphere. These strong upper tropospheric easterlies are at the origin of the TEJ that extends from South Asia across East and Central Africa, reaching speeds of approximately 40 ms^{-1}. Similarly, the mid tropospheric AEJ is generated over West Africa with maximum speeds of approximately 20 ms^{-1}. These easterly jets show the mean northern hemisphere 200 hPa and 650 hPa flow respectively (Fig. 4.2).

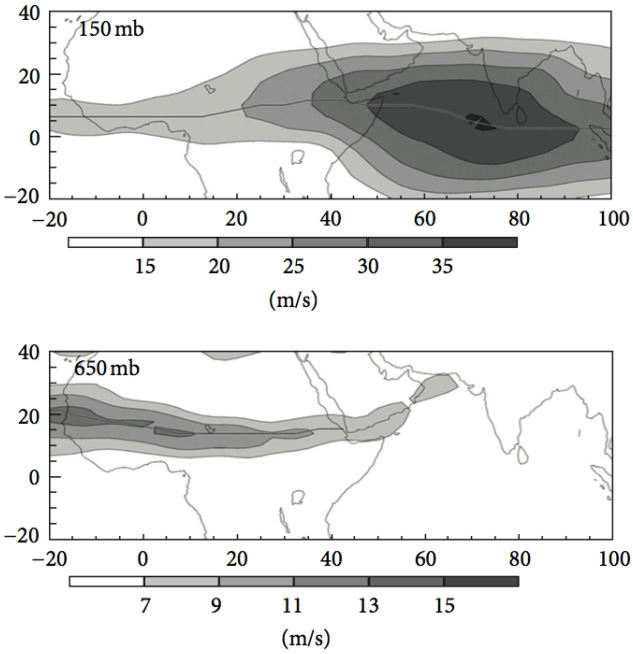

Fig. 4.2. Mean easterly wind speed (m s^{-1}) in August at 150 and 650 hPa, showing the Tropical Easterly Jet (TEJ, top panel) and the African Easterly Jet (AEJ, bottom panel), respectively (from Nicholson 2009).

The vertical variation of the geostrophic flow is given by the thermal wind equation, which can be obtained by differentiating (4.6) in the vertical, using the equation of state and neglecting frictional effects.

$$\frac{\partial V_g}{\partial z} = -\frac{g}{f\overline{T}} \nabla \overline{T} \times \tilde{k} \qquad (4.7)$$

Where $\overline{T}$ is the mean temperature of a layer. Accordingly, if $\overline{T}$ decreases towards the poles, the vertical shear will be positive (e.g., lower tropospheric easterlies and upper tropospheric westerlies) in either hemisphere. Nevertheless, in the monsoon regions, the shear is negative (low-level south westerlies and upper-level easterlies) so that the

temperature must increase towards the pole, as it is the case of the upper-troposphere of South Asia/Tibetan Plateau, with a mean temperature >5ºC than the Equator during the boreal summer. Thermal wind balance thus constrains the core of the TEJ at about 16 km altitude and 10ºN. A similar approach can be deducted for the AEJ. Roughly below 650 hPa the hot Sahara induces a temperature increase northwards, implying easterly vertical shear. Surface westerlies are thus overlain by easterlies. In the dry air over the Sahara there is a steep vertical temperature lapse rate, whereas further south the moister air cools more slowly with height, so that at about 650 hPa the meridional temperature gradient becomes positive, implying westerly shear with height (i.e., weakening easterlies). The AEJ thus develops at this transition point along with the monsoon flow in summer at about 15ºN. The location of both the AEJ and TEJ is illustrated in Figure 4.3 along with additional features of the WAM system.

4.2 ITCZ dynamics

It has been mentioned how the monsoon onset is related to a differential land-ocean temperature threshold that takes place during the boreal summer. Thus, the ITCZ can shift meridionally (Fig. 4.4) on seasonal and longer time scales depending on the underlying land-ocean background conditions. This section analyzes the ITCZ dynamics, showing the sensitivity of its position to cross-equatorial energy transport, which in turn depends on the net energy input to the equatorial atmosphere, that is, the net radiative energy input minus any energy uptake by the oceans (Bischoff and Schneider 2014).

Previous works have shown that the latitude of the ITCZ is negatively correlated with cross-equatorial atmospheric energy transport, showing how its seasonal migration tends to shift toward a differential warming hemisphere (e.g., Koutavas and Lynch-Stieglitz 2004; Chiang and Friedman 2012). The role of the cross-equatorial energy transport and the atmospheric energy budget in controlling the ITCZ location has been recently explored. In this way, the ITCZ shifts equatorward as the northward atmospheric energy transport across the Equator strengthens in response to a northern hemisphere cooling, to partially compensate this cooling (e.g., Kang et al. 2008, 2009; Frierson and Hwang 2012; Donohoe et al. 2013). In the same terms, recent studies focusing on the atmospheric energy transport are widely consistent with studies that highlight surface

temperature changes, including those in SST (e.g., Chiang et al. 2002, 2003; Chiang and Bitz 2005; Cvijanovic and Chiang 2013). Moreover, an additional factor involves the role of the ENSO, explained in terms of a southward shift of the ITCZ under El Niño events (e.g., Dai and Wigley 2000; Berry and Reeder 2014), not being easily related to cross-equatorial energy transport.

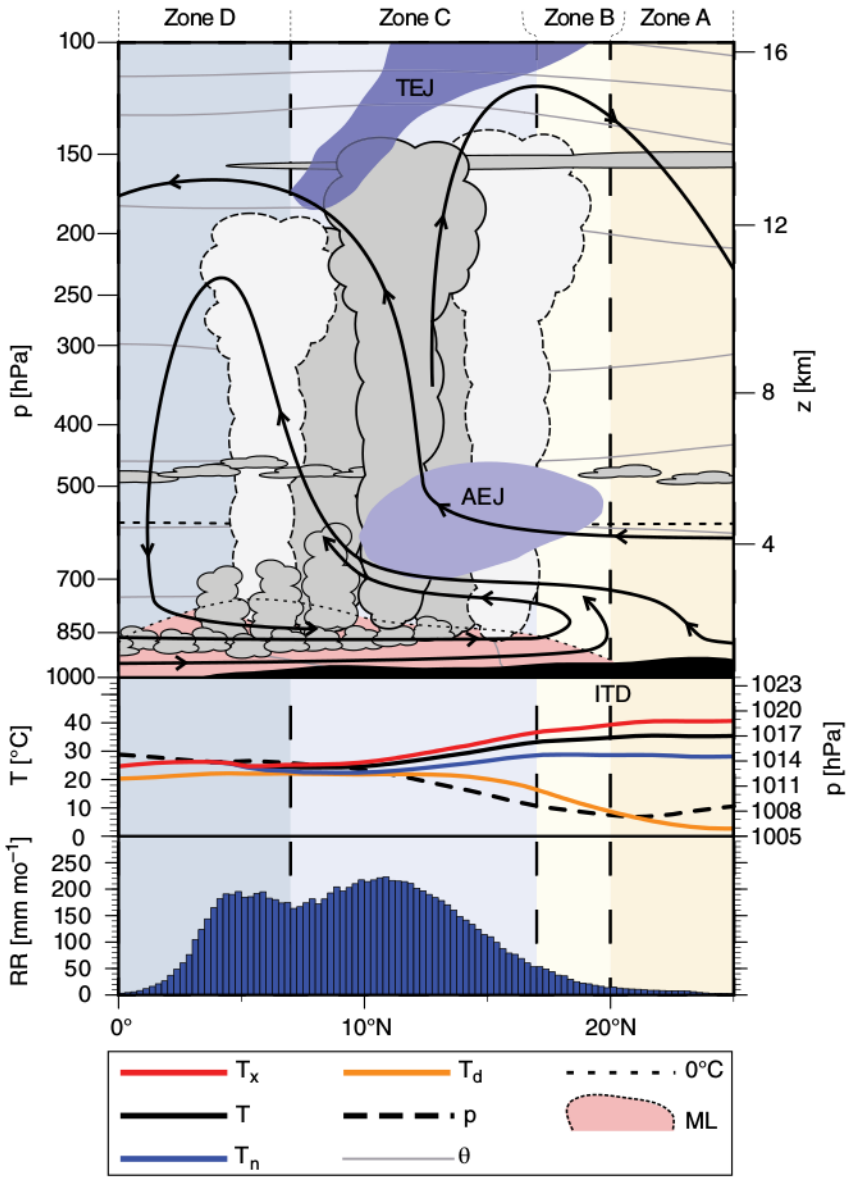

Fig. 4.3. Schematic cross-section of the atmosphere between 10°W and 10°E in July and illustration of the weather zones A–D of the West African monsoon. Shown are the positions of the ITD, upper-level jet streams (African easterly jet (AEJ), tropical easterly jet (TEJ)), the monsoon layer (ML) (as defined by westerly, i.e. positive, zonal winds), streamlines, clouds, the freezing level (0°C isotherm), isentropes (θ), minimum (T_n), maximum (T_x) and mean (T) and dew point temperatures (T_d), atmospheric pressures (p), and mean monthly rainfall totals (RR) (from Fink et al. 2017).

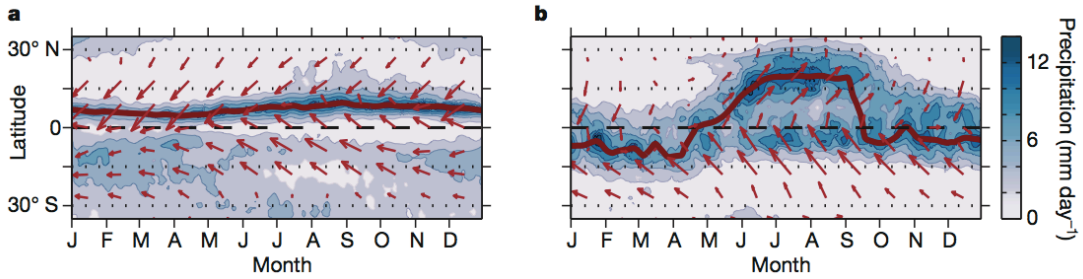

Fig. 4.4. Seasonal migration of the ITCZ over the Pacific and in the South Asian monsoon sector. Mean precipitation (color scale) and surface winds (vectors) as a function of time of year averaged zonally over the Pacific (160°E–100°W) (a) and the South Asian monsoon sector (65°E–95°E) (b). (The annual cycle over the Atlantic is similar to that over the Pacific shown here, with slightly farther-southward (down to 2°N) excursions of the ITCZ in boreal winter.) The ITCZ (precipitation maxima) is marked by red lines. The seasonal ITCZ migration is sinusoidal with moderate amplitude over the Pacific, away from continents; zonal winds remain easterly year-round (a). The seasonal ITCZ migration features abrupt and large shifts in the South Asian monsoon sector, marking the onset and retreat of the summer monsoon; zonal winds north of the Equator turn westerly at monsoon onset (b, see Box 1). The precipitation data are the daily TMPA data (Liu et al. 2012) averaged over 1998–2012. The data are smoothed temporally and meridionally by robust local linear regressions, spanning 11 days in time and 1° in latitude. The wind data are the 10-m winds from the ECMWF interim reanalysis (Dee et al. 2011) for the same years. The longest wind vector (in the South Asian monsoon sector at 18°S in September) corresponds to a wind speed of 9.1 m s^{-1}, and vector components to the left and right indicate westward and eastward wind components, respectively (from Schneider et al. 2014).

4.2.1 Moist static energy flux

Near the Equator, the energy relevant for transport consideration is the moist static energy (MSE), being generally greater than that of the air masses close to the surface (Neelin and Held 1987; Peixoto and Oort 1992). This is explained by the fact that the air masses diverging in the upper troposphere above the ITCZ are cooler and drier than those converging near the surface, so that their potential energy is greater. The vertically integrated MSE meridional flux over an atmospheric column is defined as follows:

$$F = \frac{1}{g}\int (c_p \overline{T} + g\,\overline{z} + L_v\,\overline{q})\,\overline{v}\,dp \qquad (4.8)$$

Where overbars denote zonal averages, c_p is the specific heat at constant pressure, T is the temperature, g is the gravity acceleration, z is the geopotential height, L_v is the vaporization latent heat, q is the specific humidity and v is the meridional velocity. The expression in (4.8) represents deep overturning circulations such as the meridional energy

transport by the Hadley circulation in the direction of their upper branches. Then, considering a wide enough longitudinal extent, the ITCZ is expected to lie near the energy flux equator (δ) (Broccoli et al. 2006; Kang et al. 2008), where the atmospheric MSE flux (F) changes its sign. Note that MSE neglects kinetic energy, which is rarely important for large-scale energy transport (Peixoto and Oort 1992; Trenberth and Stepaniak 2003; Marshall et al. 2014). The divergence of the MSE flux ($\partial F/\partial y$) is usually positive, indicating that energy is exported out of the tropics, so that F generally increases going northward in tropical regions. Thus, δ is expected to lie farther north (south) the stronger (weaker) southward is the cross-equatorial MSE flux (F_0) (Fig. 4.5). Furthermore, for a given fixed F_0, δ and therefore the ITCZ are expected to lie closer to the Equator for a more pronounced slope of F as a function of latitude (Bischoff and Schneider 2014; Schneider 2014) (see Fig. 4.5)

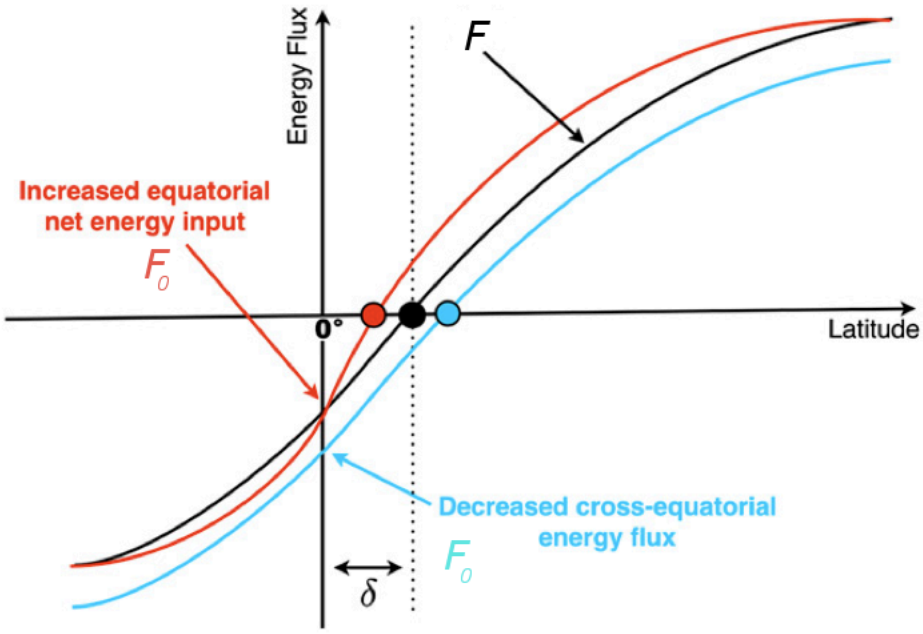

Fig. 4.5. Qualitatively behavior of the ITCZ position (large dots) as the northward cross-equatorial atmospheric energy flux (F_0) decreases (blue line) and as the net energy input to the equatorial atmosphere given in eqn (4.9) increases (red line). Decreased northward energy flux at the equator shifts the zero of the energy flux and hence the ITCZ poleward. Increased energy input increases the divergence (slope) of the energy flux and shifts its zero and hence the ITCZ equatorward (adapted from Bischoff and Schneider 2014).

Mathematically, δ is the zero of F. Given the equatorial values of the energy flux F_0 and of its slope with latitude ($\partial F_0/\partial y$), δ can be determined from $F_0 \approx -a\delta(\partial F_0/\partial y)$, where a is the radius of the Earth. As an example, if F_0 increases (decreases) as

indicated schematically by the red (blue) line in Fig. 4.5, δ moves southward (northward). Similarly, if $\partial F_0/\partial y$ increases (decreases), δ moves towards (away) the Equator.

More accurately, the energy balance integrated over atmospheric columns is (Neelin and Held 1987; Peixoto and Oort 1992):

$$S - L - O = \frac{\partial F}{\partial y} \tag{4.9}$$

Where $(S - L - O)$ represents the net energy input to the atmosphere, that is, the net incoming solar radiation (S) minus the outgoing long-wave radiation (L) and any net ocean energy uptake (O) by the oceans. Note that the relatively small kinetic energy of atmospheric motions and energy storage in the atmosphere and on land surfaces can be neglected in the tropics (Donohoe et al. 2013). Solving for δ and substituting in (4.9) for the atmospheric MSE flux divergence at the Equator, the ITCZ position can be defined as follows:

$$\delta = -\frac{1}{a}\frac{F_0}{S_0 - L_0 - O_0} \tag{4.10}$$

Thus, in a first-order approximation that assumes the linear variation of the energy flux with latitude, the expression in (4.10) provides a quantitative basis for explaining the anticorrelation between cross-equatorial energy transport and ITCZ position (e.g., Kang et al. 2008, 2009; Frierson and Hwang 2012; Donohoe et al. 2013). Moreover, it explains the ITCZ variability in response to equatorial changes that may not have a signature in cross-equatorial energy transport. This is the case, for instance, of the increased net energy input to the equatorial atmosphere during El Niño, implying an equatorward shift of the ITCZ (e.g., Dai and Wigley 2000; Berry and Reeder 2014). Additionally, changes in the net energy input to the equatorial atmosphere may also explain why the ITCZ shifts as tropical cloud parameterizations are varied in GCMs (Kang et al. 2008, 2009).

Thus, the annual-mean position of the ITCZ in the Northern Hemisphere is linked to the atmospheric energy transport, being directed from the warmer Northern Hemisphere

into the cooler Southern Hemisphere (Marshall et al. 2014; Frierson et al. 2013; Feulner et al. 2013). The Northern Hemisphere is warmer primarily due to the Atlantic thermohaline circulation, often referred to as the Atlantic Meridional Overturning Circulation (AMOC), which transports energy northward, increasing the mean temperature gradient. Thus, the AMOC dominates the cross-equatorial ocean energy transport, so that the resulting net northward transport across the Equator amounts to about 0.5 PW in the zonal mean (Fasullo and Trenberth 2008; Feulner et al. 2013; Marshall et al. 2014). Some of this ocean energy transport across the Equator is compensated by the southward atmospheric energy transport, mainly due to the Hadley cell with ascending branch and ITCZ north of the Equator. The AMOC energy transport displaces the ITCZ north of the Equator also in the Pacific (see Fig. 4.4a), because winds homogenize the effect of AMOC energy transport zonally in the extratropics. Thus, the partially compensating atmospheric energy transport is more zonally uniform and affects the ITCZ similarly over the Atlantic and Pacific (Kang et al. 2014). Moreover, local processes such as atmosphere-ocean interactions triggered by the shape of coastlines seem to be responsible for the annual-mean ITCZ position south of the Equator over the Indian Ocean. This southern ITCZ arises as a response to a secondary precipitation maximum that is maintained south of the Equator in the Indian Ocean even in boreal summer (Fig. 4.4b), probably due to the fact that northward monsoonal flow rises and generates precipitation south of the Equator (Pauluis 2004), before crossing the Equator in the free troposphere and continuing towards the primary convergence zone farther north.

4.3 SST-forced teleconnections

This section deals with the large-scale connectivity of the atmosphere-ocean coupled system, focusing on the leading SST-driven impacts on tropical and extratropical regions and associated mechanisms. Connections at a distance, or teleconnections, can occur by the direct transfer of mass due to changes in regular circulations or by propagating waves initiated by a variety of mechanisms (Chase et al. 2007).

4.3.1 Atmospheric response to tropical forcing

Rising motion due to convective storms in regions of high SST represent the starting point for the whole large-scale, tropical circulation, including the north-south Hadley cell and the east-west Walker cells (see section 2.1.1). Therefore, changes in the magnitude and spatial pattern of tropical convection alter the Walker circulation and affect the upper-level tropical outflow in the Hadley cell which feeds the higher latitude zonal jet (e.g., Krishnamurti 1961; Bjerknes 1969; Chen et al. 1988; Oort and Yienger 1996). The altered position of the Pacific Walker cell is such that large shifts in atmospheric mass occur with pressure drops in the eastern Pacific and increases to the west. This east-west change in pressure is the basis for the southern oscillation index (SOI), a measure of ENSO phase and strength.

The atmospheric response to a tropical SSTA (i.e., El Niño/La Niña) is associated with an upper-level anomalous circulation. Overall, atmospheric circulation in the tropics is simpler compared to extratropics due to the relatively weak eddy activity, especially in monthly time scales and longer. Thus, tropical climate phenomena, particularly tropical air-sea interactions associated with the ENSO, can be studied from a less complex model than that needed for extratropical circulation. The earlier Gill-Matsuno model (Matsuno 1966; Gill 1980) and later the Lindzen-Nigam model (Lindzen and Nigam 1987) have been broadly used for such purposes.

4.3.1.1 Gill-Matsuno and Lindzen-Nigam type responses

A major difference between the Lindzen-Nigam and Gill-Matsuno models is that the forcing component of the former belongs to the momentum equations, while the forcing component of the Gill model belongs to the thermodynamic equation. Local cumulus heating generates low-level flow in the Gill model, whereas the surface temperature gradient generates low-level flow in the Lindzen Nigam model (e.g., An 2011).

In the Gill model (Gill 1980; Philander et al. 1984), the latent heating of the atmosphere (i.e., cumulus heating of the middle and upper troposphere) drives low-level winds proportional to SST anomalies (Hirst 1986) or related to surface heat flux anomalies

(Zebiak 1982). The forcing of the Gill-type model, that is, cumulus heating (Zebiak 1984) is primarily proportional to the amount of surface evaporation, which depends on the surface temperature. Since the evaporation rate increases with temperature, an SST anomaly that occurs over a warm sea surface provides more cumulus heating compared to an equivalent anomaly that occurs over a relatively cool sea surface. Furthermore, some models have adopted the secondary feedback of the low-level moisture convergence (Zebiak 1986). The atmospheric response to an equatorial heating is well reproduced by baroclinic models (Davey and Gill 1987), being characterized by a pair of low (upper) level cyclones (anticyclones), which are located poleward and to the west of the heat source, whereas low pressure extends well to the east of the anomalous heating. To first order, this response to a heating anomaly is a classic Gill-Matsuno-type quadrupole (Matsuno 1966; Gill 1980). This atmospheric pattern is schematically illustrated in Figure 4.6.

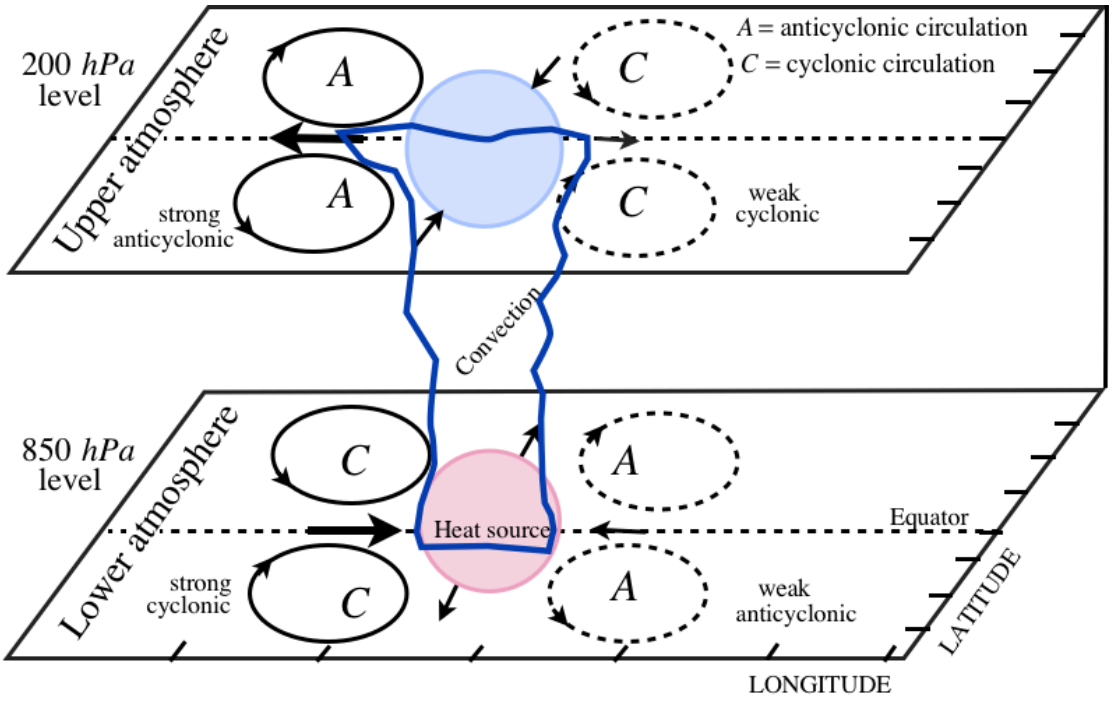

Fig. 4.6. Baroclinic response of the heat source placed on the Equator following the Gill's solution. (Source: *http://nptel.ac.in/courses/119102007/12*).

This equatorial signal is associated with a kelvin wave travelling to the east, while the off equatorial signature reflects the first center of action of a Rossby wave moving to the west (Fig. 4.7). This response has a baroclinic structure (see Fig. 4.6).

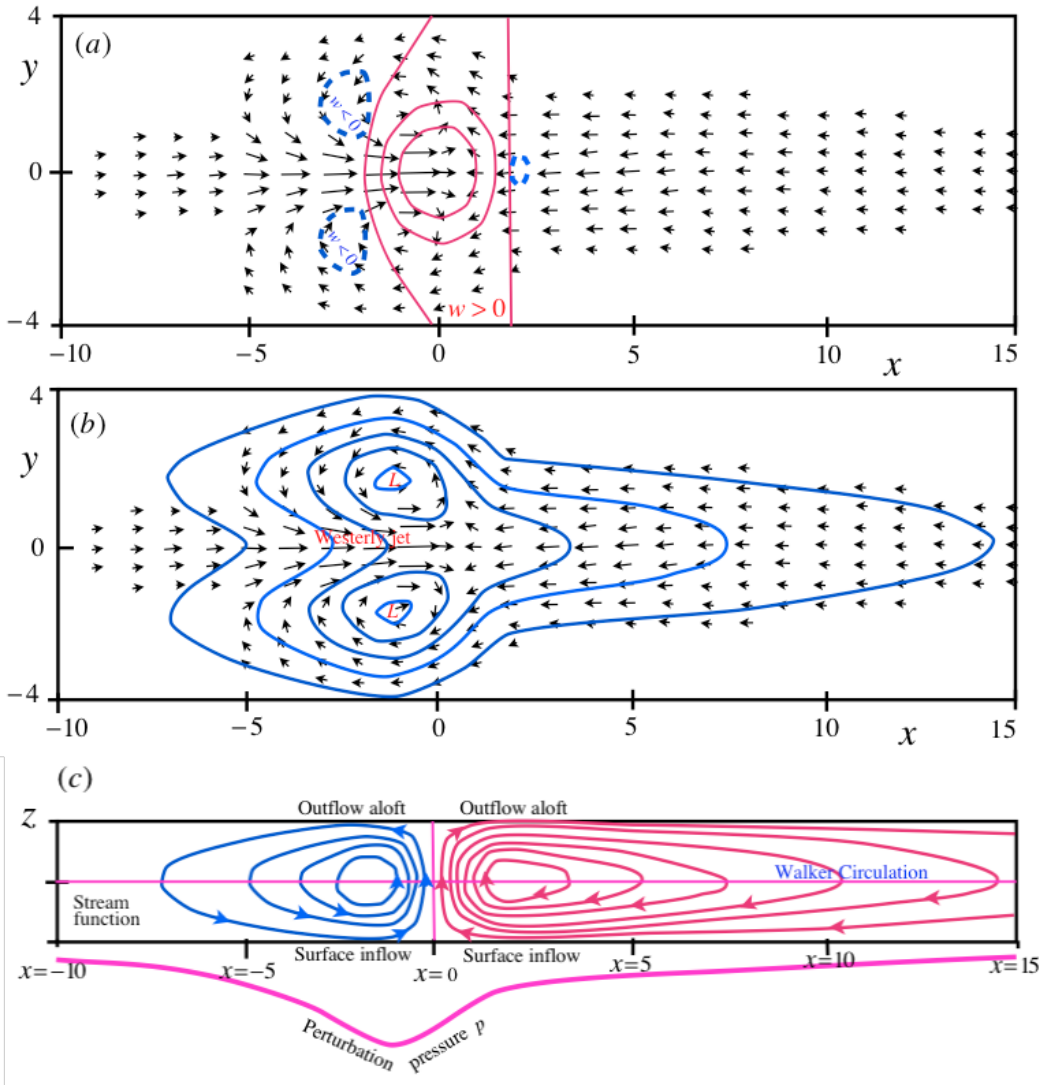

Fig. 4.7. Heat-induced tropical circulation with in the lower troposphere: (a) vertical velocity and wind field forced by heating located in the region |x| < 2; (b) the perturbation pressure with induced circulation showing strong inflow on the west and relatively weak inflow on east along with outflows in the meridional direction; (c) the meridionally integrated flow showing stream function with inflow at the surface and outflow aloft over the heating zone (adapted from Gill 1980).

The Lindzen-Nigam model (Lindzen and Nigam 1987) model calculates the boundary layer flow, which is directly forced by surface temperature based on the strong link between horizontal temperature gradients and horizontal pressure gradients. Thus atmospheric forcing in the Lindzen-Nigam forcing is expressed as a form of SST in the momentum equations of the model. The pressure gradient or the low-level wind in the Lindzen-Nigam model results from the SST distribution. In this model, the sea level pressure perturbation over a warmer surface is less sensitive to changes in SST due to the dependence of the density on the temperature. To some extent, the Lindzen-Nigam model can be transformed into the Gill model. This was shown by Neelin (1989) by neglecting the smaller terms, so that the atmospheric forcing, which is expressed as a

form of SST gradient in the momentum equations of the Lindzen-Nigam model, is moved into the thermodynamic equation as a form of the SST itself (Zebiak 1982). The latent heating in the Gill-type model is usually parameterized to be proportional to SST, which is based on the temperature dependency of the evaporation rate.

As stated, changes in upper level outflow from tropical convection affects the mean zonal and meridional flow in the tropics. Diabatic heating by organized tropical convection can excite atmospheric equatorial waves, namely, Rossby equatorial waves and Kelvin equatorial waves. These waves are trapped near the Equator (e.g., Pedlosky 1987), where the rotational flow can be neglected ($f \approx 0$). On the one hand, those waves propagating eastward are known as Kelvin waves. On the other hand, the so-called Rossby waves propagate westward. While Rossby waves have longer periods and a meridional component of velocity, Kelvin waves present a changing period, with a zonal-only velocity component, being non-dispersive waves (e.g., Holton 2004).

Following Matsuno (1966), the approximation to a negligible Coriolis force near the Equator is made by the equatorial β-plane, so that $f \approx \beta y$ where $\beta = \partial f / \partial y$ and y is the distance to the Equator. Assuming this approximation, linearized shallow water equations for perturbations on a motionless basic state of mean depth h_e are:

$$\frac{\partial u'}{\partial t} - \beta y v' = -\frac{\partial \Phi'}{\partial x} \tag{4.11}$$

$$\frac{\partial v'}{\partial t} + \beta y u' = -\frac{\partial \Phi'}{\partial y} \tag{4.12}$$

$$\frac{\partial \Phi'}{\partial t} + g h_e \left(\frac{\partial u'}{\partial x} + \frac{\partial v'}{\partial y} \right) = 0 \tag{4.13}$$

Where $\Phi' = g h'$ is the geopotential disturbance. The system of equations (4.11)-(4.13) has three different types of solutions: equatorial Rossby waves, Rossby-gravity waves and gravity waves, the former being those with a longer period and propagation velocity westward. Moreover, the β-plane constraint for equatorial latitudes forces the solutions

to be trapped in the Equator (Holton 2004). The wind and pressure structure of these waves is shown in Figure 4.8a.

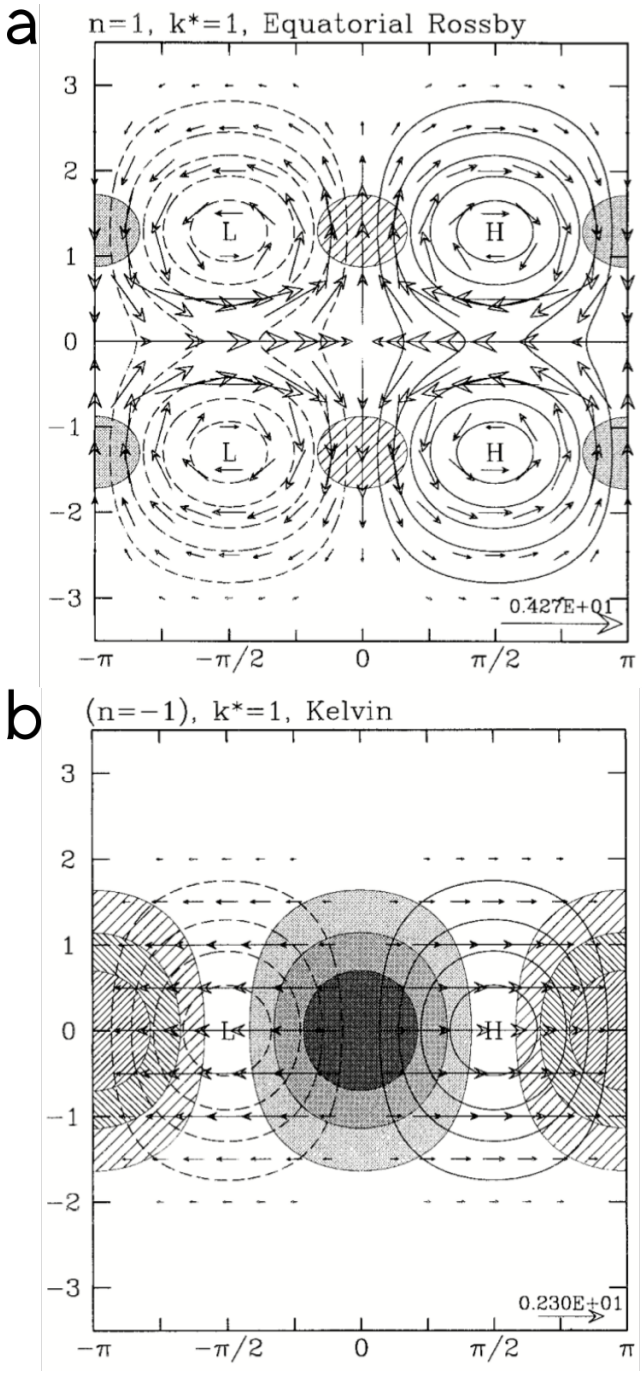

Fig. 4.8. (a) The theoretical equatorially trapped Rossby wave solution to the linear shallow water equations on an equatorial plane (Matsuno 1966) for a nondimensional zonal wavenumber 1. Hatching is for convergence and shading for divergence, with a 0.6 unit interval between successive levels of hatching or shading, and with the zero divergence contours omitted. Unshaded contours are for geopotential, with a contour interval of 0.5 units. Negative contours are dashed and the zero contours are omitted. The largest wind vector is 2.3 units, as marked. The dimensional scales are as in Matsuno (1966). (b) As in (a) except for the n = -1 Kelvin wave (adapted from Wheeler et al. 2000).

When it comes to Kelvin waves, assuming that the meridional component of the velocity is zero, the system of equations (4.11)-(4.13) is simpliefied:

$$\frac{\partial u'}{\partial t} = -\frac{\partial \Phi'}{\partial x} \tag{4.14}$$

$$\beta y u' = -\frac{\partial \Phi'}{\partial y} \tag{4.15}$$

$$\frac{\partial \Phi'}{\partial t} + g h_e \frac{\partial u'}{\partial x} = 0 \tag{4.16}$$

In this case, the solution of the equations (4.14)-(4.16) is a wave propagating eastward (i.e., Kelvin wave) with perturbations of the zonal velocity and geopotential constrained to the Equator (Holton 2004) (Fig. 4.8b). For the first baroclinic mode in the ocean, a typical phase speed would be about 2.8 ms^{-1}, triggering an equatorial Kelvin wave that roughly takes two months to cross the Pacific Ocean between New Guinea and South America. For higher ocean and atmospheric modes, the phase speeds are comparable to fluid flow speeds (Gill 1982).

CHAPTER V

5 Data

For an optimal interpretation of climate projections, a detailed examination of available data is essential. The knowledge of the main characteristics of the different types of data is important in order to correctly interpret the results obtained from them. The different studies conducted throughout this thesis have made use of different databases. These data can be classified into three fundamental groups:

1. Observed data, including gridded and station data.

2. Reanalysis data

3. Simulated data from sensitivity experiments with an atmospheric general circulation model (AGCM).

5.1 Observational data

For evaluation and assessment of the datasets it is important to understand their production method. Mostly non-homogenized observations are interpolated and homogenized with the use of different interpolation techniques and tests. Thus, observational products can be analyzed from in-situ observational emplacements or using interpolated gridded data, resulting in gridded values covering the entire globe.

In the present thesis, the SST impacts on Sahel rainfall are analyzed by using the available observations of two variables: sea surface temperature (SST) and rainfall. In this context, diverse databases have been used in order to avoid uncertainties. Thus, rainfall and SST

are based on gridded data from surface observations as well as reanalysis products. In addition, a novel dataset of in-situ measurements is used for rainfall.

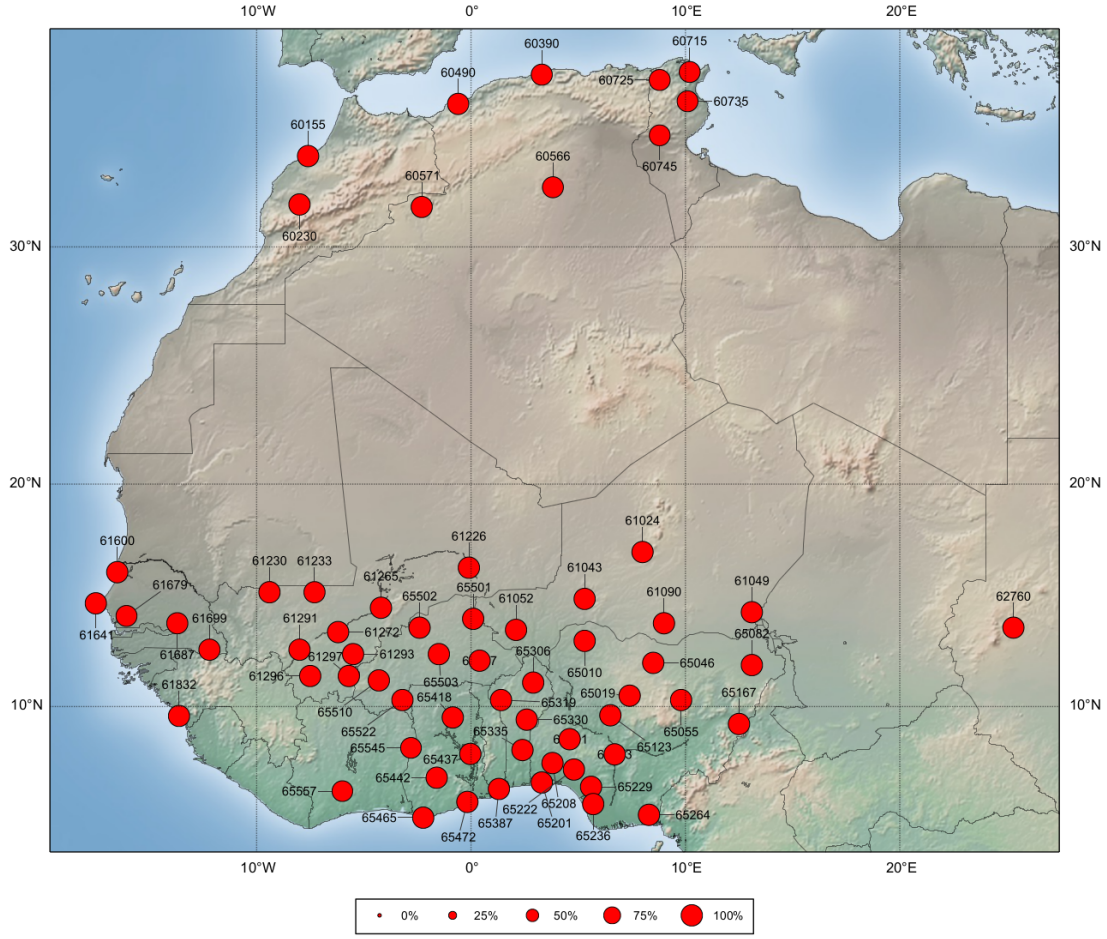

Fig. 5.1. Location of rain measuring stations with more than 80% data availability for the whole period 1921-2010 and more than 50% for each year. Number of stations: 60. (Source: *http://www.geomet.uni-koeln.de/en/the-institute/data/*).

5.1.1 Rainfall

Rainfall datasets used throughout the present thesis are listed below:

5.1.1.1 Rain-gauge station data

This database comprises a network of in-situ rain-gauge measurements, comprising 167 stations with daily data and 254 stations with monthly records (Fig. 5.1). Long-term

monthly rainfall time-series between 1921 and 2010 have been extracted from 67 stations with at least 90% data availability (Fig. 5.1). The observations were extracted from the database of the Institute of Geophysics and Meteorology of the University of Cologne (Germany). Monthly data can be downloaded from *http://www.geomet.uni-koeln.de/en/the-institute/data/*. Further description of the station data is provided in Sanogo et al. (2015). This dataset has been used in this thesis for the first time to assess the non-stationary character of SST-forced teleconnections with the Sahel (see section 8).

5.1.1.2 Gridded data

Two gridded rainfall datasets are used:

- The CRU TS (time-series) version 3.22 are month-by-month variations in climate over the period 1901-2013, on high resolution (0.5° x 0.5°) grids, produced by the Climatic Research Unit (CRU) at the University of East Anglia. CRU TS 3.22 variables are cloud cover, diurnal temperature range, frost day frequency, precipitation, daily mean temperature, monthly average daily maximum and minimum temperature, vapor pressure and wet day frequency for the period January 1901 – December 2013. Monthly gridded fields are based on monthly observational data, which are calculated from daily or sub-daily data by National Meteorological Services and other external agents. All CRU TS output files are actual values (not anomalies) and can be obtained in ASCII and netcdf formats. Further information is provided in Harris et al. (2014). CRU data can be downloaded from: *http://badc.nerc.ac.uk/data/cru/*.

- The Global Precipitation Climatology Centre (GPCC) Full Data Reanalysis version 6 is the centennial reanalysis of monthly global land-surface precipitation based on the 67200 stations world-wide that feature record durations of 10 years or longer. This product contains the monthly totals of rainfall on a regular grid with a spatial resolution of 0.5° x 0.5°, 1.0° x 1.0°, and 2.5° x 2.5° latitude by longitude (Schneider et al. 2011a, 2011b, 2011c). Precipitation anomalies at the stations are interpolated and then superimposed on the GPCC Climatology V2011 in the corresponding resolution. The temporal coverage of the dataset

ranges from January 1901 until December 2010. The GPCC Full Data Reanalysis is the most accurate in situ precipitation reanalysis data set of GPCC. Moreover it supports regional climate monitoring, model validation, analysis of climate variability and water resources assessment studies. Extended information is provided in Rudolf et al. (2011), Becker et al. (2013), and Schneider et al. (2014). Data can be downloaded from: *http://gpcc.dwd.de/*.

5.1.2 Sea surface temperature

Regarding SST, the databases used in this thesis are described as follows:

- The Extended Reconstructed Sea Surface Temperature (ERSST) dataset is a global monthly sea surface temperature analysis derived from the International Comprehensive Ocean-Atmosphere Dataset (ICOADS) with missing data filled in by statistical methods, with a resolution of 2.0º x 2.0º spanning the period from January 1854 to May 2015 (Smith and Reynolds 2003; 2004; Smith et al. 2008; Huang et al. 2015). This database includes anomalies computed with respect to a 1971-2000 monthly climatology. The newest version of ERSST, version 3b, is optimally tuned to exclude under-sampled regions for global averages. In contrast to previous versions, the version 3 (ERSSTv3b) does not include satellite data, which were found to cause cold bias significant enough to change the ranking of months. Generation of ERSST v3b uses in situ SST data and improved statistical methods that allow stable reconstruction using sparse data. ERSST is suitable for long-term global and basin-wide studies, and smoothed local and short-term variations are used in the dataset. ERSST data are available at: *http://www.ncdc.noaa.gov/oa/climate/research/sst/ersstv3.php*.

- Hadley Center Sea Ice and Sea Surface Temperature data set (HadISST) monthly means of SST with a resolution of 1.0º x 1.0º spanning the period Jan. 1870 - Sep. 2013. The SST data are taken from the Metoffice Marine Data Bank (MDB), which from 1982 onwards also includes data received through the Global Telecommunications System (GTS). In order to enhance data coverage, monthly median SST for 1871-1995 from the Comprehensive Ocean-Atmosphere Data

Set (COADS) (now ICOADS) was also used where there were no MDB data. The sea ice data are taken from a variety of sources including digitized sea ice charts and passive microwave retrievals. HadISST temperatures are reconstructed using a two-stage reduced-space optimal interpolation procedure, followed by superposition of quality improved gridded observations onto the reconstructions to restore local detail. The sea ice fields are made more homogeneous by compensating satellite microwave-based sea ice concentrations for the impacts of surface melt effects. A detailed description of the dataset and its production process is provided in Rayner et al. (2003). A link for downloading HadISST products can be found at *http://www.metoffice.gov.uk/hadobs/hadisst/*.

5.1.3 ERA-20C atmospheric reanalysis

A reanalysis is a fixed numerical weather prediction (NWP) system used in hindcast rather than forecast mode, ingesting the available historical observations presented to it. For climate monitoring and research applications, it has several distinct potential advantages over more traditional climate datasets in that it synthesizes all observations in a manner consistent with model (and therefore atmospheric) physics: it provides complete spatial and temporal coverage with physical rather than statistical interpolation into data void regions, and it provides information on unobservable parameters (e.g., potential vorticity). Reanalysis centers make these data available as gridded fields (e.g., temperatures at the surface and pressure levels, vorticity, precipitation, etc.) for bona fide research. They also save ancillary information, which has proven useful for some applications (e.g., Haimberger et al. 2008).

Climate reanalysis are intended as a systematic approach to produce datasets for climate monitoring and research (e.g., Bengtsson et al. 2007; Thorne and Vose 2010). Reanalysis datasets are based on, but are not limited to observations, including the information from radiosondes, satellites, buoys, aircrafts, ships and in-situ stations. Reanalysis are created from a data assimilation scheme and numerical climate models, which ingest all available observations every 6-12 hours, providing a dynamically consistent estimate of the climate state at each time step. Although reanalysis can be though as the best estimate on many atmospheric variables, such as wind and temperatures, its usage must be taken

with caution. Degradation of, replacement of, or changes to instruments such as satellites, and changes in methods of observation, may inject error (e.g., Trenberth et al. 2001). The largest difference between purely observational data and the re-analyses is that the latter is prepared by using not only observational data, but also short-term numerical forecasts. The result of this data-assimilation type production is that rather precise information at higher atmospheric levels and at data-poor regions is available.

In order to explore the dynamics involved in the SST-rainfall teleconnections, atmospheric variables are needed and, thus, the use of climate reanalysis is the most convenient alternative. Taking into account that, along this work, the problem of non-stationarities in rainfall-SST teleconnections along the instrumental record is tackled, long reanalysis products are needed. For this reason, atmospheric variables have been extracted from the atmospheric reanalysis of the 20th Century (ERA-20C) provided by the European Center for Medium-Range Weather Forecast (ECMWF). This database consists of a long gridded data set of climate variables at different pressure levels, spanning the period Jan. 1900 – Dec. 2010.

ERA-20C is ECMWF's first atmospheric reanalysis of the 20th century, from 1900-2010. It is an outcome of the ERA-CLIM project and was produced with the same surface and atmospheric forcing as the final version of the atmospheric model integration ERA-20CM. A coupled Atmosphere/Land-surface/Ocean-waves model is used to reanalyze the weather, by assimilating surface observations. The ERA-20C products describe the spatio-temporal evolution of the atmosphere (on 91 vertical levels, between the surface and 0.01 hPa), the land-surface (on 4 soil layers), and the ocean waves (on 25 frequencies and 12 directions). The horizontal resolution is approximately 125 km (spectral truncation T159). Note, atmospheric data are not only available on the native 91 model levels, but also on 37 pressure levels (as in ERA-Interim), 16 potential temperature levels, and the 2 PVU potential vorticity level. Monthly means, daily, and invariant data are available. The temporal resolution of the daily products is usually 3-hourly.

The assimilation methodology is 24-hour 4D-Var analyses, with variational bias correction of surface pressure observations. Analysis increments are at T95 horizontal resolution (aprox. 210 km). The analyses provide the initial conditions for subsequent forecasts that serve as backgrounds to the next analyses. A 10-member ensemble was

produced initially, to estimate the spatio-temporal evolution of the background errors. The observations assimilated in ERA-20C include surface pressures and mean sea level pressures from the International Surface Pressure Databank (ISPD) v3.2.6 observational datasets and the ICOADS v2.5.1, and surface marine winds from ICOADS v2.5.1. The observation feedback from ERA-20C is available. It includes the observations but also departures before and after assimilation and usage flags. Further information about ERA-20C reanalysis can be found in Poli et al. (2016). ERA-20C products can be downloaded from the ECMWF website: *http://www.ecmwf.int/en/research/climate-reanalysis/era-20c*.

Those variables from the ERA-20C reanalysis that have been specifically used in this thesis are listed in Table 5.1:

Table 5.1. Descriptive table on the variables from the ERA-20C reanalysis

Variable	Name	Application
u	Zonal wind component	Representation of the zonal jets (AEJ, TEJ, WAWJ) Calculation of velocity potential (χ) and stream function (ψ)
v	Meridional wind component	Calculation of moisture transport and convergence Calculation of moisture transport and convergence Calculation of mean meridional circulation (MMC)
w	Vertical wind component	Representation of upward (convection) and downward (subsidence) motions of air masses
z	Geopotential heigh	Study of the SHL
q	Specific humidity	Calculation of moisture transport and convergence
T	Temperature	Study of surface temperature gradients
slp	Sea level pressure	Study of pressure systems (cyclonic / anticyclonic activity)

The first column depicts the abbreviation of the variable typically used. The full name of the variables is shown in the second column. The third column shows the concrete application of the variable throughout the present thesis.

5.2 Simulated data

Specifically, an AGCM has been used in this thesis to conduct a series of sensitivity experiments. It corresponds to the Laboratoire de Meteorologie Dynamique Zoom (LMDZ). A description of this model is included below.

5.2.1 Sensitivity experiments with the LMDZ model

Numerical simulations with general circulation models are often used to unravel the physical mechanisms that control climate sensitivity, and to verify theoretical hypotheses or mechanisms while taking into account the complexity of the climate system. As discussed in section *2.3.2.1*, those numerical models however still provide only an approximate representation of the real climate system, which constitutes a major source of uncertainty for assessing future climate changes.

Within the framework of the preparation of CMIP5 (Taylor et al. 2012) at the Institut Pierre-Simon Laplace (IPSL), a systematic exploration of the impacts of changes in the atmospheric grid configuration of the LMDZ atmospheric general circulation model was conducted. The simulations were performed with the LMDZ4 version (Hourdin et al. 2006), the atmospheric component of the IPSL Coupled Model IPSL-CM4 (Braconnot et al. 2007; Marti et al. 2010) that took part in CMIP3 (Meehl et al. 2007). The results of this systematic exploration were used to choose the final configuration of the version 5A (LMDZ5A), the atmospheric component of the IPSL-CM5A model used for CMIP5.

A series of sensitivity experiments have been conducted within this thesis (section 9) by using the version 5A of the LMDZ AGCM (Hourdin et al. 2013). The dynamical part of the code is based on a finite-difference formulation of the primitive equations of meteorology on a staggered and stretchable longitude-latitude grid, with 39 vertical layers on a hybrid sigma-pressure coordinate. LMDZ is coupled with the land surface model Organizing Carbon and Hydrology in Dynamic Ecosystems (ORCHIDEE), which simulates the energy and water cycles of soil and vegetation, the terrestrial carbon cycle, and the vegetation composition and distribution (Krinner et al. 2005). The land surface in ORCHIDEE is described as a mosaic of twelve plant functional types (PFTs) and

bare soil, prescribing relevant biophysical and biogeochemical parameters for each PFT. When coupled, LMDZ and ORCHIDEE run at the same spatial resolution and time step. LMDZ and ORCHIDEE are, respectively, the atmospheric and land components of the Institute Pierre Simon Laplace Earth system model (Dufresne et al. 2013; Hourdin et al. 2013), which has been extensively used in the framework of the Coupled Model Intercomparison Project (CMIP), phases 3 and 5 (Meehl et al. 2007; Taylor et al. 2012).

CHAPTER VI

6 Methodology

The methodology applied along this thesis comes from a scientific method in which the available observational data are analyzed with the aim of posing preliminary working hypotheses to be tested with a dynamical model. This line of work starts with the pre-processing of data, a procedure that facilitates the subsequent application of the different methodologies.

6.1 Data pre-processing

Data pre-processing involves a series of mathematical calculations, which are detailed below.

6.1.1 Calculation of anomalies

Climate variability is mainly studied in terms of fluctuations of a specific variable (v) around its mean state or climatology. Thus, for a given time series, an anomaly in the time step (t), is defined as the deviation of the corresponding absolute value from the climatology:

$$v'(t) = v(t) - \bar{v} \tag{6.1}$$

Where overbar denotes average along time (mean) and prime denotes deviation or anomaly from the mean. This thesis is focused on the study of anomalous seasonal rainfall in the Sahel, being defined from the expression (6.1) for the boreal summer

period comprising July-August-September (JAS) during which the peak of rainfall takes place (see Fig. 2.11).

Accordingly, additional variables, noticeably the SST, are considered during this season. It is important to note that, when rainfall is studied over a large spatial domain, it does not meet a normal distribution due to substantial differences in mean and variance. Therefore, the use of standardized anomalies becomes a useful tool:

$$v'_{std} = \frac{v'}{std(v')} \tag{6.2}$$

6.1.2 Data time filtering

Data filtering is a widely used method to isolate either high or low frequency variability from the time series of a given climate field. Along this thesis, interannual and multidecadal variability are extracted by means of a Butterworth filter.

6.1.2.1 The Butterworth filter

The Butterworth filter was firstly described in 1930 by the British physicist Stepehen Butterworth (Butterworth 1930). It is a signal-processing filter designed to present as flat a frequency response as possible in the pass-band, thus providing a maximally flat response. This has the advantage that the calculations are somewhat simpler than those for other forms of filter. As the Butterworth filter is maximally flat, this means that it is designed so that, at zero frequency, the first 2n-1 derivatives for the power function with respect to frequency are zero. This filter can be designed as a high (low)-pass filter that passes signals with a frequency higher (lower) than a certain cutoff frequency and attenuates signals with frequencies lower (higher) than the cutoff frequency. In its more usual format, assuming the filter has no gain, the formula for the Butterworth filter frequency response in terms of the transfer function is:

$$|H(j\omega)| = \frac{1}{\sqrt{1+\left(1+\omega/\omega_c\right)^{2n}}} \tag{6.3}$$

Where $H(j\omega)$ is the transfer function at angular frequency ω, which in turn is equal to $2\pi f$ and ω_c is the cutoff frequency expressed as an angular value and it is equal to $2\pi f_c$. Particularly in this thesis, considering a particular period (T) above which we want to eliminate its information from the time series, and a sample interval (defined as the diference between 2 consecutive time steps), the cutoff frequency is defined as:

$$f_c = 2 \cdot dt/T \tag{6.4}$$

As an example, when working with seasonal anomalies, and considering one value per year ($dt = 1$) to remove frequencies above 7 years ($T = 7$), the Butterworth filter should be applied with a cutoff frequency $f_c = 2/7$, according to (6.4)

The Butterworth filter, either as high-pass or low-pass filter, is frequently used in climate-related studies (e.g., Roe and Steig 2004; Enfield and Cid-Serrano 2006; Mokhov and Smirnov 2006; Ault and George 2012; Schurer and Hegerl 2013).

6.2 Discriminant analysis methods

The complexity of the climate system and its variability make it difficult to focus on a particular climate process and its associated dynamical mechanism. The high number of degrees of freedom in which the relationships between different variables are organized, taking into account the spatial and temporal resolution and length of data, is difficult to tackle without reducing it. Discriminant analysis emerges to address this issue. It consists of a linear statistical method that simplifies the direction in which the variability takes place. When applied to the climate field, it provides the so-called modes of variability, determining the relationship between two or more anomalous climate fields in different

regions (Preissendorfer 1988). There are multiple discriminant analysis techniques but, in this thesis, the various analyzes carried out are based on the so-called maximum covariance analysis (MCA), which is performed between two different anomalous fields.

6.2.1 The maximum covariance analysis

The MCA is a broadly used statistical discriminant analysis methodology based on calculating principal directions of maximum covariance between two variables. This statistical analysis considers two fields, *Y* (predictor) and *Z* (predictand) for applying the Singular Value Decomposition (SVD) to the cross-covariance matrix (*C*), in order to maximize it (e.g., Bretherton et al. 1992; Cherry 1997; Widmann 2005). SVD is an algebraic technique that diagonalizes non-squared matrices, as it can be the case of two anomalous fields to be maximized (Fig. 6.1).

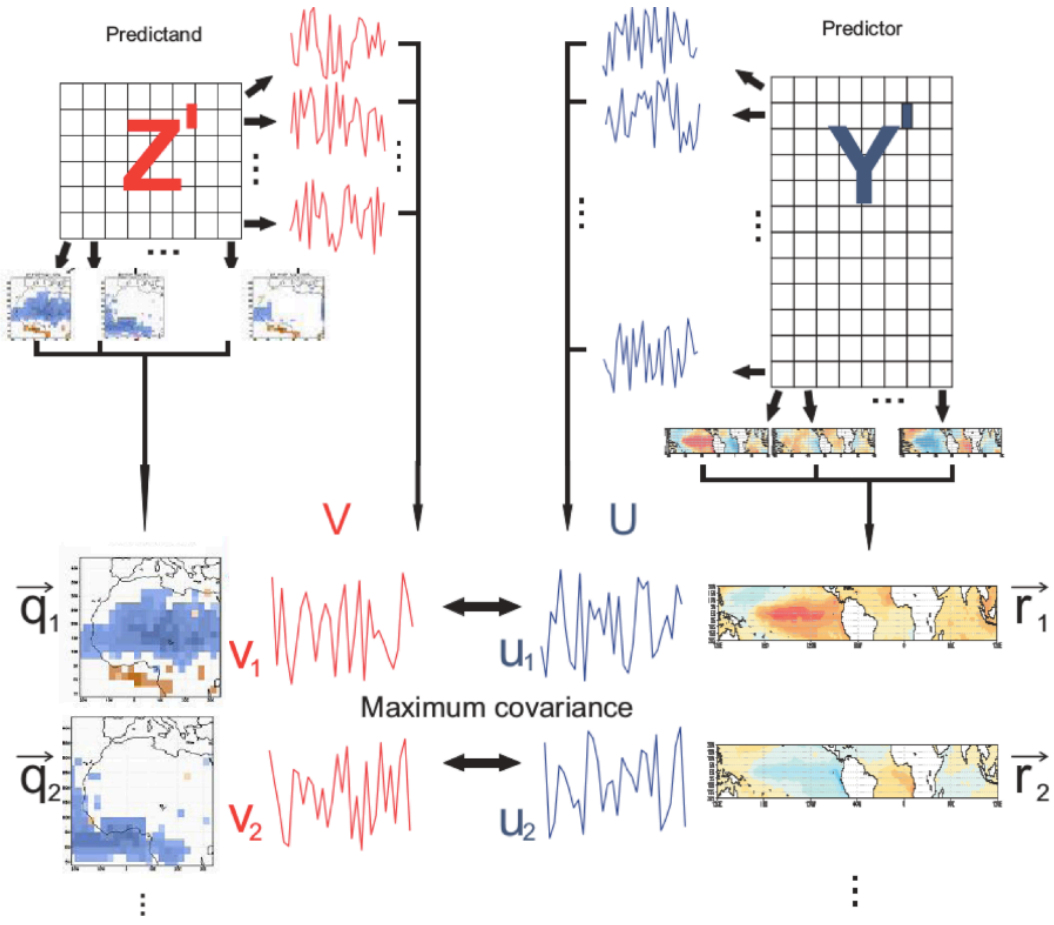

Fig. 6.1. Simplified sketch of the MCA analysis (adapted from Rodríguez-Fonseca 2001).

In the meteorological context, *C* is dimensioned in time (n_t) and space domains (n_Y and n_Z for *Y* and *Z* respectively), although the spatial domain can be more complex depending on the user requirements. MCA calculates linear combinations of the time series of *Y* and *Z,* named as expansion coefficients (hereinafter *U* and *V* for *Y* and *Z* respectively) which covariance among them is a maximum. The expansion coefficients are computed by diagonalization of *C*. As *C* is non-squared, diagonalization is first done to $A = CC^T$ and then to $B = C^TC$. The singular vectors *R* and *Q* are the resultant eigenvectors from each diagonalization, which are the spatial configurations of the co-variability modes. The associated loadings on time domain are the expansion coefficients *U* and *V*. The eigenvalues are a measure of the percentage of variance explained by each mode.

Mathematically, the time anomalies of both, *Z* and *Y* fields are calculated by removing the climatological seasonal cycle to the seasonal means.

$$Z' = Z - \bar{Z}, \tag{6.5}$$

$$Y' = Y - \bar{Y} \tag{6.6}$$

Then, the cross-covariance matrix is calculated as:

$$C_{YZ'} = \frac{Y'Z'^T}{(n_t - 1)} \tag{6.7}$$

MCA diagonalizes (6.7) by SVD methodology, obtaining the singular vectors *R* and *Q* from which the expansion coefficients are obtained according to the following expression:

$$U = R^TY, \tag{6.8}$$

$$V = Q^T Z \tag{6.9}$$

Using the eigenvectors, the percentage of explained covariance is calculated as:

$$scf_k = \frac{\lambda_k^2}{\sum_i^r \lambda_i^2}; \lambda_k = [\lambda_1, \lambda_2, ..., \lambda_n] \tag{6.10}$$

Where k is the eigenvalue for each k mode and r represents the number of modes taken into account for the analysis.

6.2.1.1 Application in forecasting

The expression from which an estimation of the predictand is obtained is a linear model as:

$$\hat{Z} = \Phi Y \tag{6.11}$$

Where Φ are the so-called regression coefficients and $\hat{Z}$ denotes an estimation (hindcast) of the data to be predicted. Taking into account that S is the regression map of the field Z onto the direction of U

$$S = UZ^T \tag{6.12}$$

And assuming good prediction $\hat{Z}$, it follows that

$$S = U\hat{Z}^T \tag{6.13}$$

Introducing the equality $\left(UU^T\right)\left(UU^T\right)^{-1} = I$ and multiplying in (6.13), the following expression is obtained:

$$\left(UU^T\right)\left(UU^T\right)^{-1} S = U\hat{Z}^T \tag{6.14}$$

Removing U from both terms

$$\hat{Z} = \left[U^T\left(UU^T\right)^{-1} S\right]^T \tag{6.15}$$

Considering now the expression $U = Y^T R$ it follows that

$$\hat{Z} = YR\left(UU^T\right)^{-1} S \tag{6.16}$$

Comparing this expression with (6.11) and introducing (6.12) it can be concluded that

$$\Phi = R\left(UU^T\right)^{-1} UZ^T \tag{6.17}$$

Where the regression coefficient (Φ) is calculated when defining the linear model from which the predictions and hindcasts are obtained.

6.2.1.2 Cross-validated skill-scores

Cross-validation is used in climate forecasting as part of statistical models when assessing forecast skill (e.g., Michaelsen 1987; Barnston and Van den Dool 1993; Elsner and Schmertmann 1994). This method is intended as a model validation technique, according to the following steps:

1. In a first step data for the predictor (*Y*) and the predictand (*Z*) for a given time step are removed.

2. Next, the MCA is applied with the remaining data to calculate the regression coefficients.

3. The regression coefficients and predictor data (that was also removed) are used to estimate the cross-validated hindcast ($\hat{Z}$).

This cross-validation technique is referred to as leave-one-out method (Dayan et al. 2014) and is the method applied throughout this thesis. Once the cross-validated hindcasts are obtained for the whole time series, the skill-score of the model is assessed by calculating the Pearson correlation coefficients (*r*) between Z and $\hat{Z}$:

$$r_{\hat{Z}Z} = \frac{\mathrm{cov}(\hat{Z}, Z)}{\sigma_{\hat{Z}}\sigma_{Z}} \tag{6.18}$$

6.3 Statistical field significance

In the climate framework, the limited number of samples makes necessary to estimate to what extent a result is significant, determining whether a given pattern is obtained by chance as a result of a mathematical artifact. Accordingly, statistical testing emerges as a procedure applied to climate data for weighting a hypothesis (von Storch and Zwiers 1999). This hypothesis testing takes into account an initial null hypothesis (H_0) to be accepted or rejected based on the statistical method applied for a given sample under

study. Then, an alternative hypothesis is considered (H_1), taken as true for a false H_0. If H_0 is not rejected, the evidence in the sample is not inconsistent with H_1.

There are different types of test. The use of a hypothesis test depends on the probability distribution of the sample under study and the null hypothesis. A test statistic, considered as a null distribution is computed together with the significance level $(1-\alpha)$ to determine the so-called non-rejection region of H_0. This region determines the rejection of the null hypothesis for the test statistic falling within it, whereas a test statistic outside the non-rejection region of H_0 indicates the acceptance of the alternative hypothesis under a significance level set to α (Fig. 6.2).

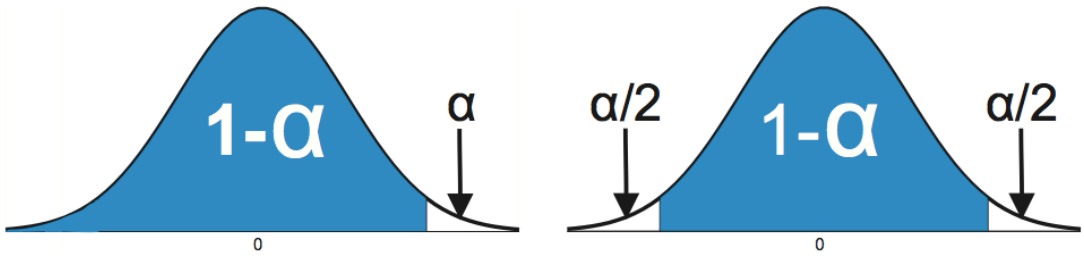

Fig. 6.2. Probability density function (PDF) of a statistic for a one-tailed (left) and two-tailed (right) test.

Two different types of hypothesis tests are commonly used. On the one hand, parametric tests are those following a theoretical distribution given by an appropriate representation of the data. On the other hand, non-parametric tests do not meet a specific probability distribution. A description of parametric and non-parametric tests used in this thesis is included below.

6.3.1 Parametric testing

The parametric test used herein is named as the t-Student or t-test. In statistics, this test meets a t-Student distribution if the null hypothesis is true. It applies when the population of the sample under study follows a normal distribution but the sample size is too small for the statistic on which the inference is based to be normally distributed. Then, an estimate of the standard deviation is used rather than the actual value. It is typically used in discriminant analysis.

6.3.1.1 T-test for equality of two means

This type of test consists of comparing the means of two different samples, determining whether the difference between means is equal to a hypothesized value. The test assumes the populations are normally distributed, with equal but unknown variances, to determine whether or not the two samples could have the same populations. Thus, given two random samples, which are extracted from populations with different and unknown means and sizes n_1 and n_2 respectively, if the mean values of both samples belong to the same population, anomalous values cannot be assumed and therefore the result is not significant.

Then, to compare the populations of two samples (s_1, s_2), the null and alternative hypothesis are considered as follows:

- H_0: Equal means between the populations of the two samples $(\tau_1 = \tau_2)$.
- H_1: Different means between the populations of the two samples $(\tau_1 \neq \tau_2)$.

To verify the null hypothesis the, z-statistic is calculated following the expression:

$$z = \frac{\overline{s}_1 - \overline{s}_2}{\left(\frac{\sigma_1^2}{n_1} + \frac{\sigma_2^2}{n_2}\right)^{1/2}} \tag{6.19}$$

Where σ_1, σ_2 and n_1, n_2 the standard deviations and sizes of the original samples (s_1, s_2) respectively and overbars denote means (von Storch and Zwiers 2001). The value of the z-statistic is compared with pre-tabulated values that, depending on the sample size, are allocated from a normal $(n_1 + n_2 > 30)$ or follow a t-Student distribution for small populations (Gorgas et al. 2009).

6.3.1.2 T-test for correlation

In this case, the parametric t-test estimates the statistical co-variability between two given samples (s_1, s_2), assessing the significance level of the Pearson correlation coefficients (see section *6.2.1.2*) between them:

$$r_{s_1 s_2} = \frac{\mathrm{cov}(s_1, s_2)}{\sigma_{s_1} \sigma_{s_2}} \tag{6.20}$$

Where $\mathrm{cov}(s_1, s_2)$ represents covariance between both samples and σ_1, σ_2 are the respective standard deviations. The correlation coefficient (r) ranges from 1 to -1 indicating maximum correlation or anti-correlation respectively. Conversely, $r = 0$ denotes that both samples are uncorrelated. Moreover, the percentage of explained variance by one of the samples as a linear representation of the remaining one is given by r^2 (von Storch and Zwiers 1999).

The correlation t-test determines whether the correlation is significant by a hypothesis test defined in this case as:

- H_0: The samples are independent ($r = 0$).
- H_1: The samples are linearly dependent ($r \neq 0$).

To determine if the null hypothesis is rejected, the z-statistic is calculated according to:

$$z = \frac{r(N-2)^{1/2}}{(1-r^2)^{1/2}} \tag{6.21}$$

Where z follows a t-Student distribution with N-2 degrees of freedom. Then, the null hypothesis is rejected under a given significance level α if $t > t_{\alpha/2}$.

In the present thesis, the parametric t-test in its forms previously explained, has been applied using the two-sample t-test libraries (*ttest2*) defined within the MATLAB®

statistics toolbox. This type of test has been used to assess the statistical significance of the results in sections 8 and 9.

6.3.2 The non-parametric Monte Carlo method

Monte Carlo method consists of computational algorithms based on repeated random sampling to obtain numerical results. This method is used when the distribution of a given sample (size = *n*) is unknown a priori, comparing the statistical parameters obtained under study (p_n) with those randomly created from the original sample. The method implies that the size of the sample (*n*) is large enough to be considered as a population.

The Monte Carlo method involves performing a large number ($N > 500$) of permutations from the original sample. Each permutation is then used to repeat the calculation and compare the obtained results with the real values. Once this is done, the values obtained with the *N* permutations are taken to create a random distribution to finally determine the position of the real value within the distribution, which will indicate the statistical significance of the obtained value. The method computes the numerical values of the test statistic z for each *n* dataset: $z_1, z_2, z_3 ... z_n$. Assuming *n* is large enough z_n is taken as a good approximation to the original sample. In this context, the real values can be considered as statistically significant, with a confidence level of $100(1-\alpha)$ if the absolute value of z is located before the $n(1-\alpha)-teeth$ position in the probability density function (PDF; see Fig. 6.2).

This method has been described and applied in various climate-related works (e.g., Livezey and Chen 1983; Barnett 1995; Maia et al. 2007; Rodríguez-Fonseca et al. 2011).

6.4 Streamfunction and velocity potential

Alterations in the large-scale zonal circulation can be explored in terms of the divergent and rotational circulations. Indeed, a wind field given over a limited domain can be partitioned into non-divergent and irrotational components in several ways. A particular solution, selected by requiring the velocity potential to vanish on the boundary, has minimum divergent kinetic energy and is numerically easy to obtain. Nevertheless, the reconstruction of the wind field from the vorticity and divergence together with the boundary velocity is more difficult, since the potential equations are coupled by the boundary conditions (e.g., Bijlsma et al. 1986).

The Helmholtz theorem allows partition of the horizontal wind field $\vec{V}(u,v)$ into nondivergent and irrotational components:

$$V = V_{\psi} + V_{\chi} = k \times \nabla\psi + \nabla\chi \qquad (6.22)$$

Where ψ is the streamfunction and χ is the velocity potential. The vorticity ζ is defined as the vertical component of the curl of velocity, and from (6.22) it follows that:

$$\nabla^2 \psi = \zeta \qquad (6.23)$$

Similarly, taking the divergence of (6.22):

$$\nabla^2 \chi = \delta \qquad (6.24)$$

Where δ is the velocity divergence.

The upper-level circulation related to the Walker cell is explored in this thesis by means of χ and ψ, which are calculated from the wind components (u,v) as solutions of two Poisson equations represented by expressions (6.23)-(6.24). In this context, the GrADS extensions (*gex*) with functions for computation of χ and ψ from wind components (*u, v*) at different pressure levels will be used to perform calculations using the classic *fishpak* Fortran library that can be obtained from: *http://opengrads.org/doc/udxt/fish/fish.html.*

6.5 Representation of the results

The results obtained from climate-related studies are often shown in terms of geographical maps representing a given variable in a given context. Concerning this thesis, these maps are almost entirely related to climatological anomalies representing climate variability relationships and associated impacts. Within the framework of variability modes obtained from the MCA analysis, different maps, described as follows, can be represented:

- **Regression Maps**. In this type of maps, a given field is depicted in a direction representing maximum variability. Such a direction comes from the time series of the field which variability and influence over the other field are being explored. In other words, a given variable ν defined in a period n_t is regressed into the time-series τ of the variable which variability is under study, thus defining a regression map:

$$R(n_s,1) = \nu(n_s,n_t)\cdot\tau(n_t,1) \tag{6.25}$$

Where n_s denotes the spatial dimension. Regression maps (R) can be either homogeneous or heterogeneous. The former option is considered when the variable is regressed into its own time series, whereas the latter refers to the regression into a different variable. By analogy with the MCA method:

$$R_Y(n_{SY},1) = Y(n_{SY},n_t)\cdot U(n_t.1)\,, \tag{6.26}$$

$$R_Z(n_{SZ},1) = Z(n_{SZ},n_t)\cdot U(n_t.1) \tag{6.27}$$

Where R_Y and R_Z are the homogeneous and heterogeneous regression maps for Y and Z respectively. In a forecasting context, the usual procedure is to represent the regression maps of the predictor variable and the heterogeneous maps of the variable to be predicted. However, not all the variability represented in these maps can be interpreted. Indeed, a test of statistical significance should be

applied to indicate the regions of robust variability. In this way, the significance level of regression maps throughout this thesis has been assessed by applying the Monte Carlo method (see section 6.3.2) to the expressions in (xxx) and (xxx), so that a large number of permutations ($p = 1000$) is performed on the time dimension (n_t), providing random samples to be compared with R_Y and R_Z .

- **Correlation maps.** The correlation maps are computed as the Pearson correlation coefficients (as in 6.18) between a particular time series (*T*) and each of the time series describing the evolution of a field (*F*) in each of the grid points (n_F) of a specific region (von Storch and Zwiers 1999). The time series can be standardized and are associated with the atmospheric or oceanic anomalies in a given region. Typically, these time series are the expansion coefficients obtained from the MCA analysis. A significance test (see section *6.3.1.2*) should be applied in order to assess the regions significantly influenced, which are those regions in which the evolution of a particular variable exhibits a significant relationship with the time series under study.

- **Composite maps**. Along with the regression maps, a remarkable part of the results obtained in this thesis correspond to composite maps. Seasonal or monthly composites are constructed from the averaged anomalies of a given variable with respect to, for instance, the mean state. Then, the mean state for those cases in which the value of the time series, namely the expansion coefficients, exceeds a previously established threshold, namely one standard deviation, is considered. Consequently, a t-test for equality of two means (see section *6.3.1.1*) is the most suitable option for assessing the statistical significance. Concerning the results in section 8, seasonal composites are performed for several atmospheric variables. These composites are defined as the subtraction of high (H) minus low (L) events, where H refers to those years in which the expansion coefficient time series (*U*) exceeds one standard deviation, whereas L corresponds to the years in which U is below one standard deviation.

- **Ensemble means and differences from sensitivity experiments.** The results related to simulated data (see section 5.2) are represented from the response of a given variable to a given forcing in, for example, a sensitivity experiment. Then,

the mean value of the variable in a control simulation is subtracted from the mean value of the same variable in the sensitivity experiment, thus representing the anomalous response to the forcing. A t-test for equality between means will indicate those values statistically significant, showing the anomalies that significantly deviate from the control simulation. The results in section 9 are depicted as has been posed herein.

CHAPTER VII

7 A Statistical Model based on Non-stationary Predictors

As stated, SST is the key variable when tackling seasonal to decadal climate forecast. Dynamical models are unable to properly reproduce tropical climate variability, introducing biases that prevent a skillful predictability. Statistical methodologies emerge as an alternative to improve the predictability and reduce these biases. As a starting point for this thesis, a statistical model was designed and created to improve the predictability and investigate potential non-stationary teleconnections. This model has been named as the Sea Surface Temperature based Statistical Seasonal foreCAST model (S^4CAST). The model is based on the MCA method, and introduces the novelty of considering the non-stationary links between the predictor and predictand fields. The results presented in this section are focused on the model development, integrating the methodologies described in section 6. The model has been published (**Suárez-Moreno and Rodríguez-Fonseca 2015**) and the code is freely available online (see section 7.6). The S^4CAST model has been created and used throughout this thesis to put forward a series of hypothesis. Most of the results collected in this section correspond to the publication aforementioned.

The S^4CAST model is conceived as a statistical tool to study the predictability and teleconnections of climate-related variables that strongly co-vary with SSTA in remote and nearby locations to a particular region of study. The code has been developed as a MATLAB® toolbox. The software requirements are variable and depend on user needs. The spatial resolution and size of data files used as inputs are directly proportional to computational memory requirements. The model software consists of three main modules (Fig. 7.1), each composed of a set of sub-modules which operation is described below.

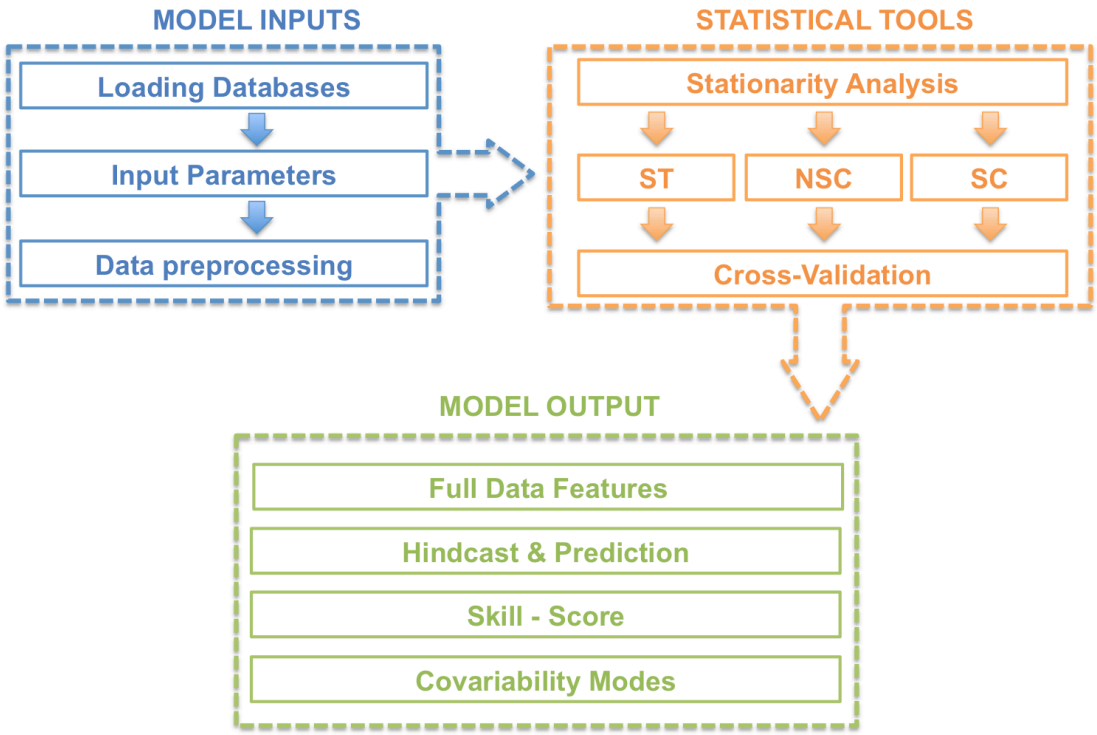

Fig. 7.1. Schematic diagram illustrating the structure of the model.

7.1 Model inputs

The S^{4}CAST present a direct execution mode. By simply typing *'S4cast'* in the command window, the user is prompted to enter a series of input parameters in a simple and intuitive way.

7.1.1 Loading databases

The model is ready to work with Network Common Data Form (NetCDF) data files. There are different conventions to set the attributes of the variables contained in NetCDF files. In this way, the data structure must conform as far as possible to the Cooperative Ocean/Atmosphere Research Service (COARDS) convention. Execution errors that may occur due to the selection of data files are easily corrected by minor

modifications of data assimilation scripts. Data files can be easily introduced at the request of the user. Once obtained, the user must insert the data files into a directory set by default (*S4CAST_v2.0/data_files)*.

7.1.2 Input parameters

In order to correctly introduce the input parameters, it is convenient to present some terms commonly used in seasonal forecasting. In this way, the forecast period corresponds to the n-month seasonal period concerning the predictand for which the forecast and hindcasts are performed. Moreover, the lead-time refers to time expressed in months between the last month comprising the predictor monthly period and the first month comprising the forecast period. Thus, medium-range forecast refers to a lead-time set to zero, while long-range forecast refers to a lead-time equal or larger than one month. Strictly, there is no lead-time when the predictor monthly period partially or totally overlaps the forecast period. In this case we refer to lag-time expressed in moths between the last month comprising the forecast period and the last month for predictor period. The relationship between lead-time and lag-time depends on the number of months comprising the forecast period. Finally, the forecast-time is commonly used to describe the time gap expressed in months between the predictor and predictand monthly periods, assuming the same concept represented by the lead-time.

In a first step, predictand and predictor data files are selected. In this way, the predictand field can be precipitation, SST, or any variable susceptible to be predicted from SSTA. The predictor is restricted to SST. Once the predictor and predictand fields are selected, the available common time period between them is analyzed and displayed so that the user is prompted to select the whole common period for analysis or other within it. The same temporal dimension in both fields is required in the statistical analysis to construct the cross-covariance matrix (see section 6.2.1).

In the next step, the n-month forecast period regarding the predictand is selected. The model allows a selection from one (n = 1) to four (n = 4) months. From the forecast

period, the user determines a specific lead-time, relative to the predictor, from which medium-range (lead-time 0) or long-range (lead-time > 0) forecast can be performed. In order to study and evaluate potential teleconnections, the temporal overlapping between the forecast period and the predictor is also available by defining the monthly lags between both fields: from monthly lag 0 (synchronous), referred to the case in which the predictor and the predictand fields are taken at the same n-month period, through partial overlapping to eliminate the overlapping (medium-range forecast). Note that synchronous and partially overlapping between predictor and predictand fields are not useful when referring to forecast, although this option is available in order to perform studies focused on teleconnections. Thus, the model is focused on the study of both the predictability and potential teleconnections between SST (predictor) and a predictand field.

Monthly lags indicating forecast times (lead-times) are user selectable. To illustrate the above, considering a hypothetical case in which the forecast period corresponds to the months from February to April (FMA), the synchronous option will consider the predictor in FMA, while partially overlapping occurs when the predictor is taken for January-to-March (JFM) and December-to-February (DJF). Avoiding overlapping, lead time 0 will be NDJ (November-to-January), lead time 1 will be OND (October-to-December), lead time 2 will be SON (September-to-November) and so on. Thus, the user can select any 3-month isolated period from FMA (synchronous) to MJJ (May-to-July).

Next, the spatial domains for both predictor and predictand fields are easily selected from its latitudinal and longitudinal values. Considering the above options, the user can select a sequence of successive monthly lags or only one, so that the predictor is taken for the total amount of selected information (e.g., NDJ+OND+SON).

Then, there is the possibility of applying a Butterworth filter to the time series of both predictor and predictand fields (see section 6.1.2). The current version uses a Butterworth filter, either as high-pass or low-pass filter, even though the selection of a low pass filter is not suitable for seasonal forecast and subsequently is not useful in the

current version. Anyway, the possibility of selecting a low pass filter is maintained in order to include decadal predictability in a future version of the model.

In case of multiple time selection for the predictor, statistical methodology is firstly applied for the largest lead-time and successively adding information for the remaining lead-times. Thus, continuing with the example above in which the forecast period corresponds to FMA, if selected lead-times from 0 to 3, the first predictor selection is made considering the 3-months lead-time period (SON). After, the 2-months lead-time period is added (ASO+SON). Next, up to the period 1-month delayed (ASO+SON+OND), and finally the case up to the period with a lead-time equal to zero (ASO+SON+OND+NDJ). This example is illustrated in Figure 7.2.

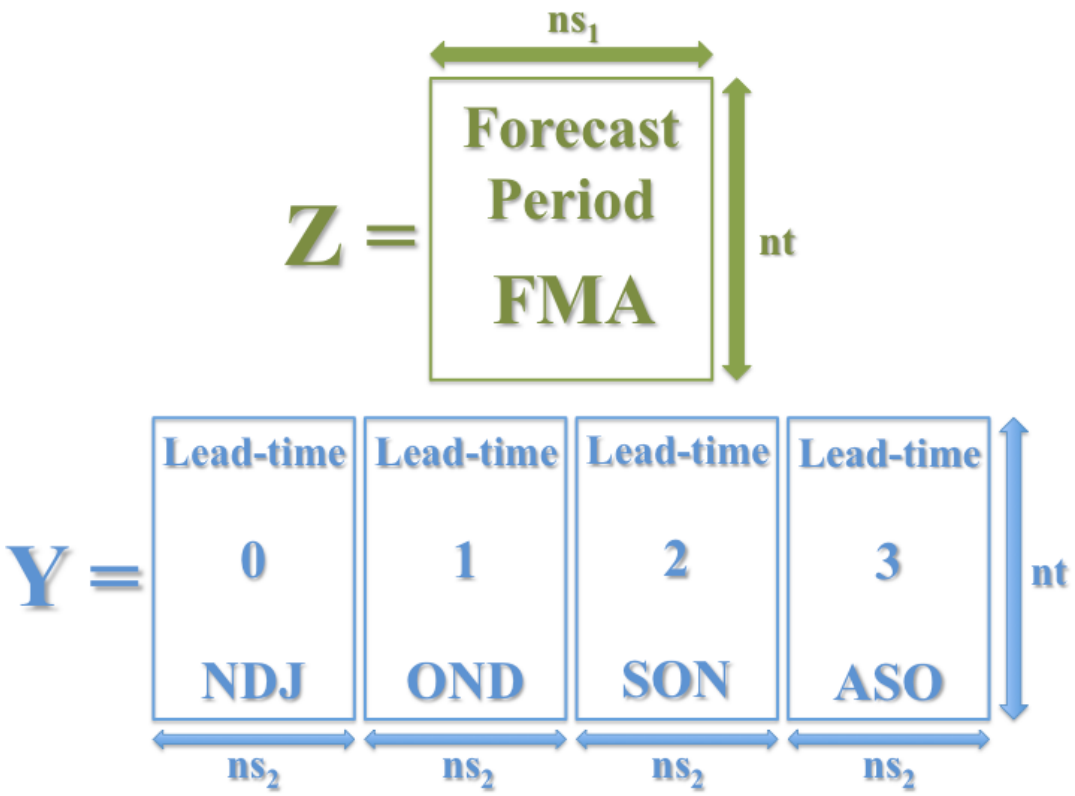

Fig. 7.2. Predictand (Z) and predictor (Y) fields represented by their corresponding data matrices. The illustration relates to an example in which the forecast period covers the months February-March-April (FMA) and the predictor is selected for four distinct seasons: August-September-October (ASO, lead-time=3); September-October-November (SON, lead-time=2); October-November-December (OND, lead-time=1); November-December-January (NDJ, lead-time=0). Each of these sub-matrices for the predictor has the same temporal dimension (nt) and spatial dimension (ns_2). The predictand may have a different spatial dimension (ns_1) but the same temporal dimension (nt) to enable matrix calculations required by MCA methodology.

Once the matrices are determined for each predictor time selection, the statistical methodology is applied. Up to now, the model applies the MCA method, although other statistical methodologies will be included in future releases, including CCA or non-linear methods as neural network and Bayesian methodologies. As indicated in the previous section, MCA determines a new vector base in which the relations between the variables are maximized. Thus, it is important to choose a number of modes (principal directions) to be considered in the computations, selecting either a single mode or a set of them, always consecutive. The analysis of stationarity is performed for a single mode selection. For multi-mode selection, the whole time series will be considered.

The level of statistical significance is set for the first time to assess an analysis of stationarity. Thus, the model runs for the entire period and for those periods for which the relationships are considered stationary within it. This is internally established by applying the method explained in section 7.2.1.

7.2 Analysis of stationarity. The COI index.

Stationarity refers to changes along time in the co-variability pattern between two variables. Thus, a stationary link refers to an invariant pattern invariant within a time period. By contrast, a link will be non-stationary when the pattern varies within a given period. The novelty of the S^{4}CAST is based on the evaluation of stationary periods, which is performed in terms of the correlation index (hereinafter COI) between the time series of the expansion coefficients of Y and Z (U and V respectively) obtained from the MCA (section *6.2.1.1*). The method is applied for the whole study record and the stationary periods correspond to those years in which the association between U and V remain invariant in terms of significant or non-significant correlation, which is calculated by applying 21-year sliding window correlation between U and V. This technique has been widely used to determine the stationarity of the relationships between the time series of climate indices (e.g., Camberlin et al. 2001; Rimbu et al. 2003; Van Oldenborgh and Burgers 2005). Next, the significance level of COI is calculated by applying a non-parametric Monte Carlo test (see section 6.2.1).

Three different types of 21-years moving correlation windows are user selectable: 'delayed' to correlate one year and the 20 previous years; 'centered' to correlate one year, the 10 previous years and the 10 next years; or 'advanced' to correlate one year and the 20 following years. In this way, COI can be defined as follows:

$$COI_{delayed} = corr(U(1,i-20:i),V(1,i-20:i)), \quad (7.1)$$

$$COI_{centered} = corr(U(1,i-10:i+10),V(1,i-10:i+10)), \quad (7.2)$$

$$COI_{advanced} = corr(U(1,i:i+20),V(1,i:i+20)) \quad (7.3)$$

Where i cover the temporal dimension (i = *1, 2, 3, ...* n_t). Note that delayed correlation coefficients are the most suitable option in a forecast context. Nevertheless, centered and advanced correlation coefficients are also available for application no matter the aim of the user.

By construction, *COI* evolves as a multidecadal index. A significance test is applied to determine two types of periods: the significant correlation period (hereinafter SC) in which the *COI* scores are statistically significant, and no-significant correlation period (hereinafter NSC). The model performs all calculations for each period separately and, from them, the hindcast ($\hat{Z}$) for each individual year is calculated by cross-validation (see section *6.2.1.2*).

7.3 Model outputs

Modes of co-variability are related to spatial patterns of different variables that co-vary over time, and thus, are linked to each other. In the case of MCA, the covariance matrix is computed and the SVD method is applied to provide a new basis of eigenvectors for the predictor and predictand fields which covariance is maximized. The obtained singular vectors describe spatial patterns of anomalies in each of the variables that tend to be related to each other. Regression and correlation maps and corresponding expansion coefficients determine each mode of co-variability for the predictor and predictand fields. The expansion coefficients indicate the weight of these patterns in each of the

time steps. Thus, regression and correlation co-variability maps can be represented. This is done with the original anomalous matrix, highlighting those grid points whose time series are highly correlated with the obtained expansion coefficients, showing large co-variability and determining the key regions of prediction. To represent it, regression and correlation maps are calculated to analyze the coupling between variables and to understand the physical mechanisms involved in the link.

Otherwise, the time series of the expansion coefficients determine the scores of the regression and correlation maps at each time along the study period. The model represent the expansion coefficients used to calculate the regression coefficients. Thus, those years in which the expansion coefficients for the predictor and the predictand are highly correlated will coincide with years in which we can expect a better estimation.

In the current version of the model, the root mean square error (*rmse*) and the Pearson correlation coefficients skill scores (see section *6.2.1.2*) have been included. These techniques are applied to compare the observed and simulated maps (hindcasts) of the predictand field, providing correlation and *rmse* maps and time series. On the one hand, maps are obtained calculating for each grid point the skill scores between the hindcast and the observed maps. On the other hand, time series are obtained for each time by applying correlation and *rmse* between the area average of the observed and estimated maps. Some comments on these techniques are addressed in Barnston (1992). The S^4CAST model generates the hindcast within the entire period (EP), SC and NSC periods separately from applying the one-leave-out method as explained in section *6.2.1.2*.

7.4 Application of the model: benchmark cases

Four different case studies have been conducted for benchmarking. Two of these cases are focused on the predictive ability of the tropical Atlantic SSTA whereas the remaining two consider the tropical Pacific SSTA as predictor field. In all four cases, the teleconnections under study have been shown to be non-stationary.

7.4.1 Case study I: Tropical Atlantic SST – Sahel rainfall

Firstly, the model has been applied to validate its use in the study of seasonal rainfall predictability in the Sahel from tropical Atlantic SSTA as predictor field. As a reminder, the interannual fluctuations in the Sahel rainfall regime are due to various causes, being the changes in global SST the main driver of WAM variability (Folland, 1986; Palmer 1986; Fontaine et al. 1998; Rodríguez-Fonseca et al. 2015). Particularly, several observational studies address the influence of tropical Atlantic SSTA on the WAM at interannual time scales (Giannini et al. 2003; Polo et al. 2008; Joly and Voldoire, 2009; Nnamchi and Li 2011).

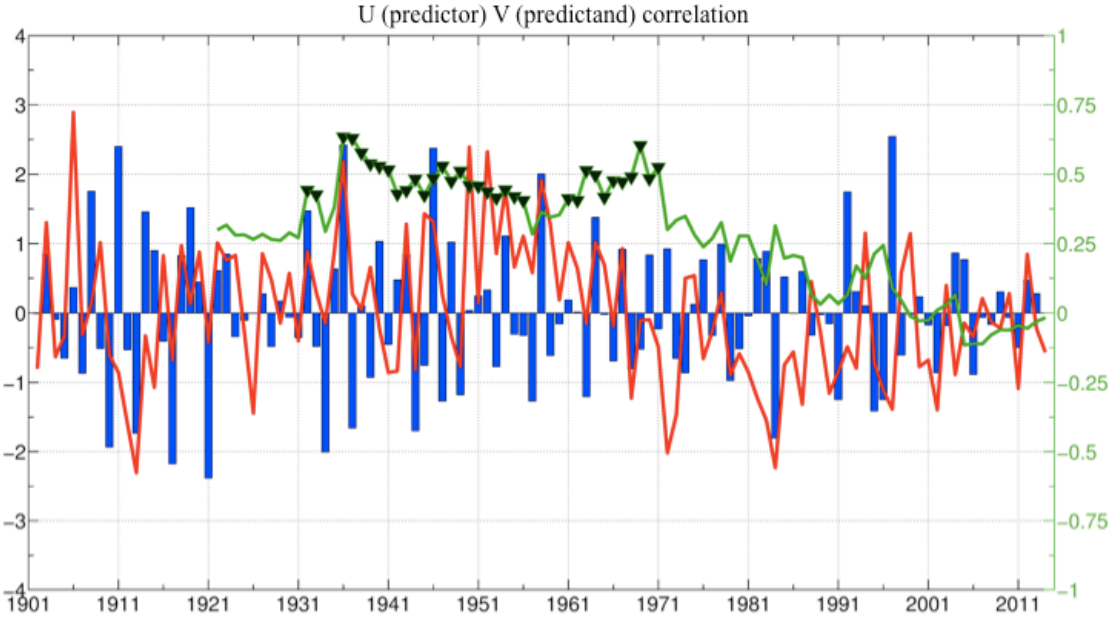

Fig. 7.3. 21 years moving correlation windows (green line) between the expansion coefficients U corresponding to tropical Atlantic SSTA (predictor, blue bars) and V corresponding to Sahelian anomalous rainfall (predictand, red line) obtained for the leading mode of co-variability from MCA analysis. Shaded triangles indicate significant correlation under a Montecarlo Test at 90%.

Regarding the input parameters, the predictand field corresponds to the GPCC rainfall dataset. The forecast period covers from July to September (JAS), computing seasonal anomalous rainfall in the Sahel spatial domain (18ºW-10ºE; 12ºN-18ºN). No frequency filter is applied for the predictand field. Regarding the predictor, the ERSST dataset has been selected. The spatial domain corresponds to the southern subtropical and equatorial Atlantic band (60ºW-20ºE; 20ºS-4ºN). A high pass Butterworth filter with cutoff frequency set to 7 years has been applied to the predictor time series in order to analyze

the influence of SSTA interannual variability (see section *6.1.2.1*). Medium-range forecast has been taken into account, setting the lead-time to zero (equivalent to monthly lag 3). In this way, April-to-June (AMJ) is the selected season for predictor. The leading MCA mode has been selected. The correlation curve (Fig 7.3) exhibits the stationary periods (SC and NSC) within EP period as stated in section 7.2. The SC period is almost restricted to years from 1932 to 1971 with some exceptions. The remaining years correspond to the NSC period.

Figure 7.4 depicts the regression maps for the leading MCA mode, where the squared covariance fractions (scf) for the SC, EP and NSC periods are 0.50 (50%), 0.32 (32%) and 0.41 (41%) respectively. For the SC period (Fig. 7.4, top panels), the co-variability pattern exhibits a quasi-isolated cooling in the tropical Atlantic associated with a rainfall dipole over West Africa with negative anomalies in the region of the Gulf of Guinea and opposite in the Sahel. The opposite co-variability pattern takes place under negative scores of the expansion coefficient. These results are in agreement with those found in the last decades of the 20th century by several authors who have discussed the role of the tropical Atlantic SST as a dominant factor in the WAM variability at interannual and seasonal time scales (Janowiak 1988; Janicot 1992; Fontaine and Janicot 1996). In particular, Losada et al. (2010b) describe the dipolar rainfall patterns in response to the equatorial Atlantic Niño, defined by negative anomalies of rainfall in the Sahel, being opposite in the Guinean Gulf (see Fig. 7.4). This is explained by changes in the sea-land pressure gradient between the Gulf of Guinea and the Sahel. Mohino et al. (2011b) and Rodríguez-Fonseca et al. (2011) have found in the observations how this dipolar behavior takes place for some particular decades coinciding with the SC periods, confirming in this way the correct determination of the leading co-variability mode by the model. When considering the EP period (Fig. 7.4, middle panels), a co-variability pattern similar to that observed for the SC period is observed. Regarding the predictand field, the anomalous rainfall signal is less intense when compared to SC. For the predictor, the cooling in the tropical Atlantic is accompanied by opposite weak anomalies in the north subtropical and tropical Pacific. Regarding the NSC period (Fig. 7.4, bottom panels), as for the previous periods (SC, EP) a cooling in the tropical Atlantic is observed concerning the predictor, being associated with negative rainfall anomalies in the Gulf of Guinea and a weak positive signal in the eastern Sahel, virtually disappearing the rainfall dipole. The global SSTA regression map shows a significant warming in the tropical

Pacific. The opposite pattern should be considered under negative scores of the expansion coefficient.

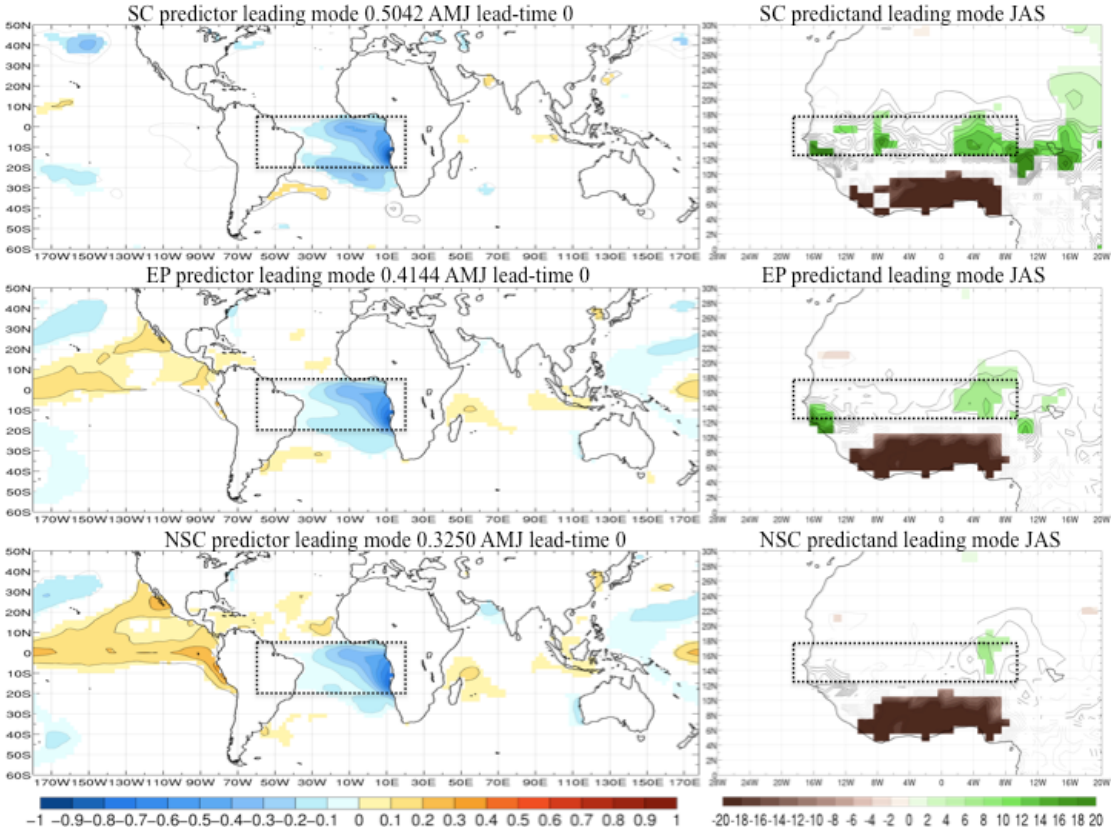

Fig. 7.4. Regression maps obtained for the leading mode by applying MCA between SSTA in the tropical Atlantic (predictor) and western Sahel rainfall (predictand). Left column represents the homogeneous regression map done by projecting the expansion coefficient U onto global SSTA (ºC). Right column represents the heterogeneous regression map done by projecting expansion coefficient U onto the anomalous Sahelian rainfall (mm/day). Period SC (top panels); EP (middle panels) and NSC (bottom panels). Rectangles show the selected regions for predictor and predictand fields considered in the MCA analysis. Values are plotted in regions where statistical significance under a Montecarlo test is higher than 90%.

The results presented above support the existence of a non-stationary behavior of the teleconnections between SSTA variability and rainfall associated with WAM. Several authors have addressed the dipolar anomalous rainfall pattern as a response of an isolated tropical Atlantic warming (cooling) (e.g., Rodríguez-Fonseca et al. 2011; Losada et al. 2010a; 2010b) restricted to the period 1957-78 in the observations. The uniform rainfall signal over the whole West Africa, with negative anomalies related to a cooling over tropical Atlantic and an opposite sign pattern over tropical Pacific is only observed for the period from 1979 in advance. These results agree with Losada et al. (2012), who focused on non-stationary influences of tropical global SST in WAM variability, explaining how the disappearance of the dipole was due to the counteracting effect of

the anomalous responses of the Pacific and Atlantic on the Sahel. Recently, Diatta and Fink (2014) have documented similar non-stationary relationships.

The associated skill of the model to reproduce the rainfall is shown in Figure 7.5 in terms of correlation maps and time series for SC and EP periods. A qualitative improvement is observed when considering the SC periods instead of the whole period (EP). This result points to a better spatial distribution of the significant values for particular decades in which the signal extends to a larger spatial domain. In order to analyze the performance of the simulation for each particular year, the correlation between observations and hindcasts at each time step is shown in Fig. 7.5 (right panles). Since it has only been considered the leading MCA mode, the time series of validation between observed and simulated rainfall should evolve following the absolute values of the expansion coefficients. Thus, when the expansion coefficient (*U*) of the predictor (SST) shows high scores in the leading mode, good hindcasts are generally obtained. Conversely, the skill gets significantly worse for the NSC period (Fig. 7.6).

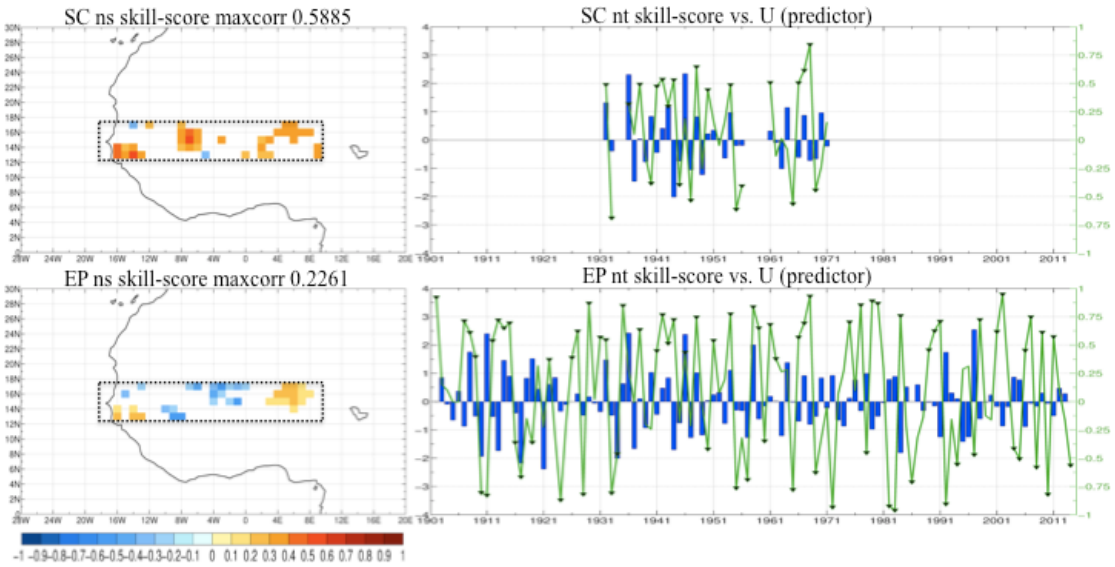

Fig. 7.5. Skill-score validation using Pearson correlation coefficients between observations and hindcasts. Left column corresponds to the spatial validation for each point in space. Right column corresponds to validation time series (green line) between hindcasts and observations considering only the regions indicated by positive significant spatial correlation. Period SC (top panels); EP (bottom panels). Significant correlation values for time series are indicated by shaded triangles. Blue bars correspond to the expansion coefficient (U) of the SSTA (predictor). Significant values are plotted from a 90% statistical significance under a Montecarlo test.

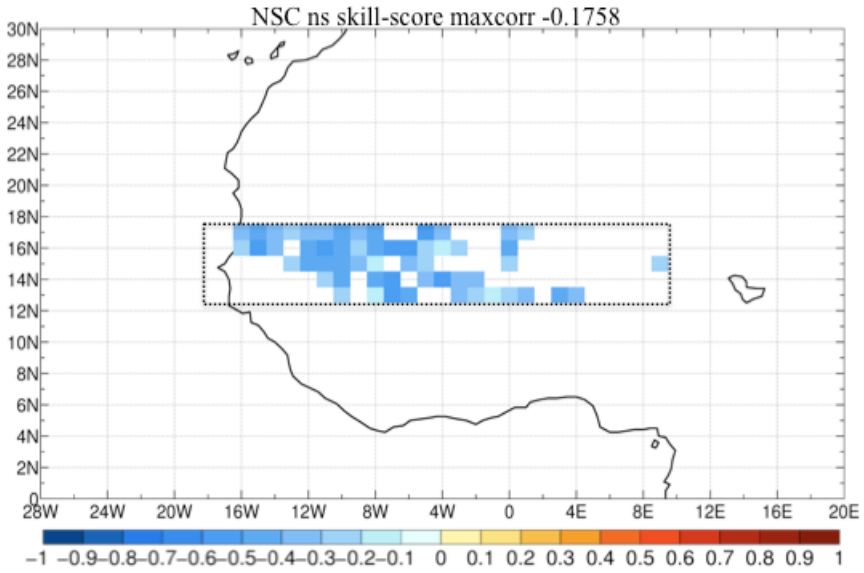

Fig. 7.6. Skill-score validation using Pearson correlation coefficients between observations and hindcasts for each point in space corresponding to NSC period. Significant values are plotted from a 90% statistical significance under a Montecarlo test.

7.4.2 Case study II: Tropical Atlantic SST – Tropical Pacific SST

A non-stationary behavior in the association between tropical Atlantic and tropical Pacific SSTA has been recently documented in some works suggesting that the tropical Atlantic SSTA during the boreal summer could be a potential predictor of winter tropical Pacific SSTA variability after the 1970s (Rodríguez-Fonseca et al. 2009; Ding et al. 2012). In this section, the S^{4}CAST model has been applied to corroborate the non-stationarity in the teleconnection between tropical Atlantic considered as predictor field and tropical Pacific, a feature that has been also demonstrated in Martín-Rey et al (2015).

Both predictor and predictand fields corresponds to the ERSST database, covering the period from January 1854 to May 2015. The forecast period consists of December-to-March (DJFM). The selected region for predictand corresponds to SSTA in the tropical Pacific domain (120ºE-60ºW; 30ºS-20ºN), while the predictor corresponds to tropical Atlantic SSTA (60ºW-20ºE; 20ºS-4ºN) and has been considered for the period July-to-October (JASO), which means long-range forecast, setting the lead-time to one month. A high pass filter with cutoff frequency set to 7 years has been applied to both predictor

and predictand time series in order to analyze the interannual predictability. As in the previous case, the leading MCA mode has been selected.

The correlation curve (Fig. 7.7) shows the SC period clearly divided into two intervals: from 1889 to 1939 and from 1985 up to the present (2015). Consequently, the NSC period corresponds to the remaining years within the study period (1854-2015).

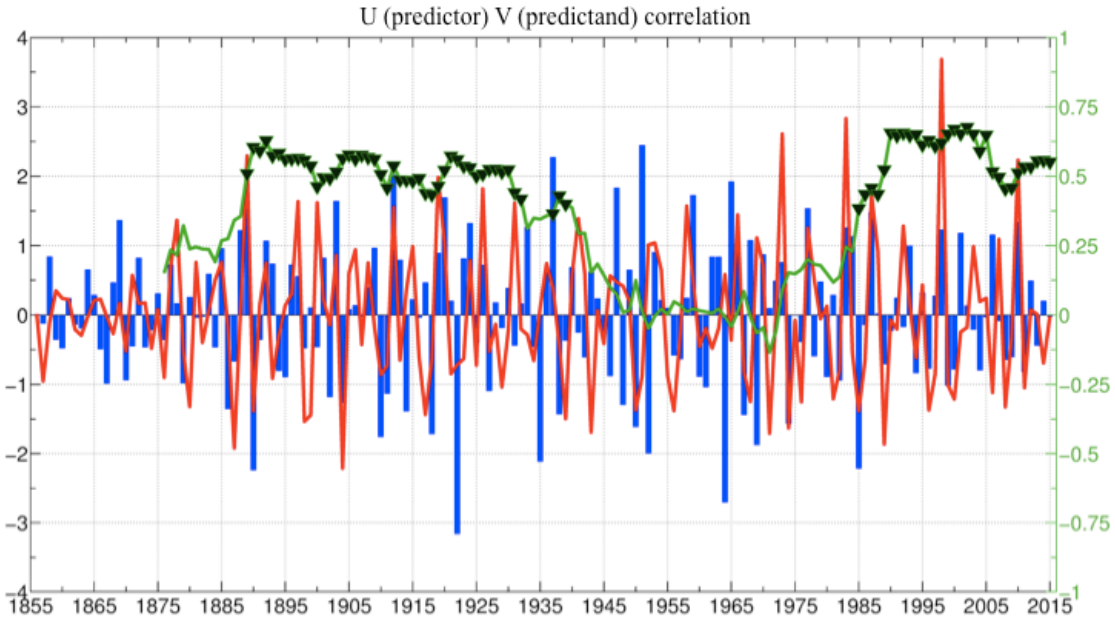

Fig. 7.7. 21 years moving correlation windows (green line) between the expansion coefficients U corresponding to tropical Atlantic SSTA (predictor, blue bars) and V corresponding to tropical Pacific SSTA (predictand, red line) obtained for the leading mode of co-variability from MCA analysis between predictor and predictand fields. Shaded triangles indicate significant correlation under a Montecarlo Test at 90%.

The leading MCA mode for the periods SC, NSC and EP explains 52%, 28% and 43% of co-variability respectively (Fig. 7.8). Regarding the SC and EP periods (Fig. 7.8; top and central panels repsectively), it is observed how a cooling (warming) in the tropical Atlantic is related to a warming (cooling). Thus the co-varibility pattern is defined by opposite sign anomalies between the predictor and predictand fields, although the magnitude of the anomalies is greater concerning the SC period. Considering the NSC period (Fig 7.8; bottom panels), a signal in tropical Pacific is not observed in response to the tropical Atlantic cooling (warming). These results are in agreement with former studies in which a similar tropical SSTA pattern defined by opposite SSTA between the

tropical Atlantic and Pacific has been documented to occur in the decades within the SC period (Rodríguez-Fonseca et al. 2009; Martín-Rey et al. 2012). Thus, Martín-Rey et al. (2014, 2015) point to a non-stationary relationship that seems to take place in the early 20th century and after the 1970s, confirming the correct determination of the leading co-variability modes by the model.

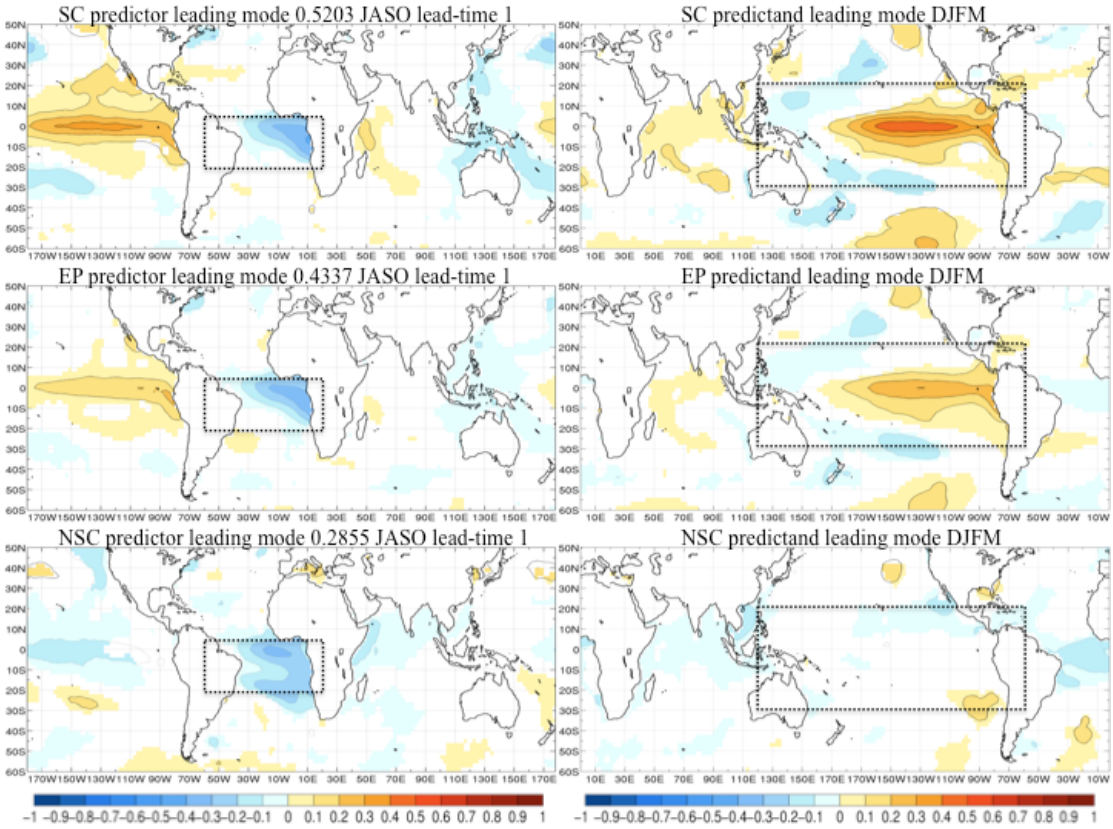

Fig. 7.8. Regression maps obtained for the leading mode by applying MCA between SSTA in the tropical Atlantic (predictor) and SSTA in the tropical Pacific (predictand). Left column represents the homogeneous regression map done by projecting the expansion coefficient U onto global SSTA (ºC) for predictor seasonal period. Right column represents the heterogeneous regression map done by projecting expansion coefficient U onto global SSTA (ºC std^{-1}) for predictand seasonal period. Period SC (top panels); EP (middle panels) and NSC (bottom panels). Rectangles show the selected regions for predictor and predictand fields considered in the MCA analysis. Values are plotted in regions where statistical significance under a Montecarlo test is higher than 90%.

The mechanism from which the teleconnection takes place, has been explained by Polo et al. (2015), who suggest that a cooling in the equatorial Atlantic results in enhanced equatorial convection, altering the Walker circulation and consequently enhancing subsidence and surface wind divergence over the equatorial Pacific during the period July-to-August (JASO). The anomalous wind piles up water in the western tropical Pacific, triggering a Kelvin wave eastward from autumn to winter, setting up the

conditions for a cold event in the equatorial east Pacific during the period December-to-March (DJFM). Considering a cooling in the tropical Atlantic, the opposite sequence takes place.

The skill of the model in reproducing tropical Pacific SSTA (Fig 7.9) is also restricted to stationary conditions. Thus, depending on the considered sequence of decades within the period EP (figure 9; middle panels), the model provides better results for period SC (figure 9; top panels), while it is not able to produce reliable estimations when period NSC (figure 9; bottom panels) is taken into account. These results highlight the need to consider different periods and possible modulations when tackling seasonal predictability of tropical Pacific SSTA, in agreement with recent results of Martín-Rey et al. (2015).

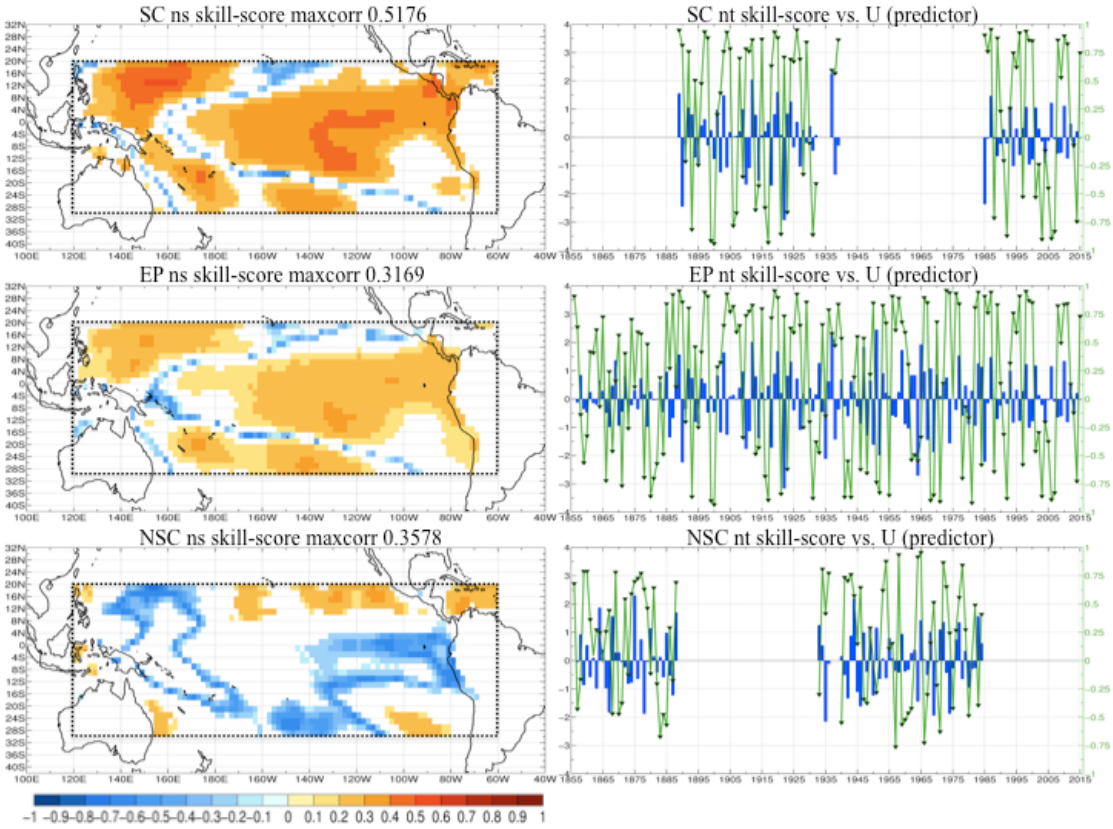

Fig. 7.9. Skill-score validation using Pearson correlation coefficients between observations and hindcasts. Left column corresponds to the spatial validation for each point in space. Right column corresponds to validation time series (green line) between hindcasts and observations considering only the regions indicated by positive significant spatial correlation. Period SC (top panels); EP (middle panels); NSC (bottom panels). Significant correlation values for time series are indicated by shaded triangles. Blue bars correspond to the expansion coefficient (U) of the SSTA (predictor). Significant values are plotted from a 90% statistical significance under a Montecarlo test.

7.4.3 Case study III: Tropical Pacific SST – Sahel rainfall

The influence of the ENSO on the variability of WAM at interannual time scales has been documented using observations (Folland et al. 1986; Palmer 1986; Fontaine et al. 1998; Janicot et al. 1998, 2001) and GCMs (Mohino et al. 2011b, 2011c; Rodríguez-Fonseca et al. 2011, 2015; Rowell 2001; Joly and Voldoire 2009; Losada et al. 2012). From these, a consensus emerged in that rainfall decrease in the region is linked to the positive phase of the ENSO.

Regarding the physical mechanisms involved in the observed ENSO-WAM link (Janicot et al. 2001; Giannini et al. 2005; Cook and Vizy 2006), several studies based on sensitivity experiments suggest that, during El Niño events, the high-tropospheric heating over the warm SST region in the tropical Pacific triggers a Kelvin wave throughout the African Atlantic sector, which is associated with anomalous subsidence over West Africa. Such a mechanism describes an anomalous Walker-type circulation that remotely connects the tropical Pacific and West Africa (Joly and Voldoire 2009; Mohino et al. 2011c; Losada et al. 2012; Rodríguez-Fonseca et al. 2015), thus reducing rainfall. In addition, a connection with the anomalies of the large-scale gradient between the SST from the west Pacific to the eastern Indian Ocean has also been proposed, by which a stationary equatorial Rossby wave propagating westward induces anomalous subsidence over West Africa (Rowell 2001).

Some works have put forward the non-stationary relationship in time between the ENSO and WAM variability (Mohino et al. 2011b; Rodríguez-Fonseca et al. 2011; Janicot et al. 1996, 2001; Fontaine et al. 1998; Losada et al. 2012). From the 1970s to the early 2000s, the negative correlation between Sahelian rainfall and tropical Pacific SST anomalies has strengthened in comparison to the previous decades (Janicot et al. 2001), as supported by sensitivity experiments done with GCMs (Mohino et al. 2011c). Nevertheless, observational studies do not show this increment (Rodríguez-Fonseca et al. 2011), maybe because during this period the Pacific acts together with the Atlantic, being anti-correlated during summer (Rodríguez-Fonseca et al. 2009). With this configuration, the Atlantic counteracts the effect of the Pacific on the Sahel, diminishing the observed impact, a theory that has been further supported through the use of sensitivity experiments (Losada et al. 2012).

In order to analyze the non-stationary link between the ENSO and Sahel rainfall and its impact on seasonal predictability, the S^{4}CAST model is applied between SSTA in the tropical Pacific sector (120ºE-60ºW; 30ºS-20ºN) and anomalous rainfall in the Sahel (18ºW-10ºE; 12ºN-18ºN) during JAS (July-August-September). Each mode of co-variability is defined by two spatial structures (for the predictand and predictor variables) and two time series (expansion coefficients) indicating the amplitude of the spatial pattern in each of the time steps. The variability of the expansion coefficients reveals changes in the standard deviation and changes in the correlation between both time series (Fig. 7.10). Indeed, the 21 year-sliding window correlations between the expansion coefficients of the leading mode (green line) indicate that the relationship changes over time in a significant way. In this way, three different steady periods are determined, namely, the EP, SC and NSC periods. By repeating the MCA for each individual period, the leading co-variability mode shows a percentage of explained variance of 46%, 48% and 37%, respectively. As a remarkable result, the SC period is mainly restricted to the period from 1950s onwards (Fig. 7.10, top panel), consistent with the previously mentioned works. The leading co-variability mode in terms of regression maps for the same SC period shows a heating in the tropical Pacific related to a decrease in rainfall in the Sahel, as pointed out by several authors (e.g., Mohino et al. 2011b; Rodríguez-Fonseca et al. 2011; Losada et al. 2012). A cross-validated hindcast for the three periods is done and the correlation between the hindcast rainfall and the observations is shown as a measure of the reliability of the mode in predicting Sahelian rainfall. According to these results, the ability of the leading mode in reproducing rainfall impacts due to ENSO is stronger during the SC period; it decreases during EP, and virtually vanishes for the NSC period.

The correlation curve in Figure 7.10 evolves as a multidecadal oscillation and indicates the periods in which ENSO teleconnection is stronger over the Sahel. Looking at the ENSO signal, there is no change in its spatial configuration, so it is plausible to think that the slowly varying background state could be modifying the teleconnection mechanism. This result has also been pointed out in Rodríguez-Fonseca et al. (2015), where the authors encourage further exploration of the multidecadal modulation of teleconnections. The present study confirms the absence of stationarity and its impact on seasonal predictability.

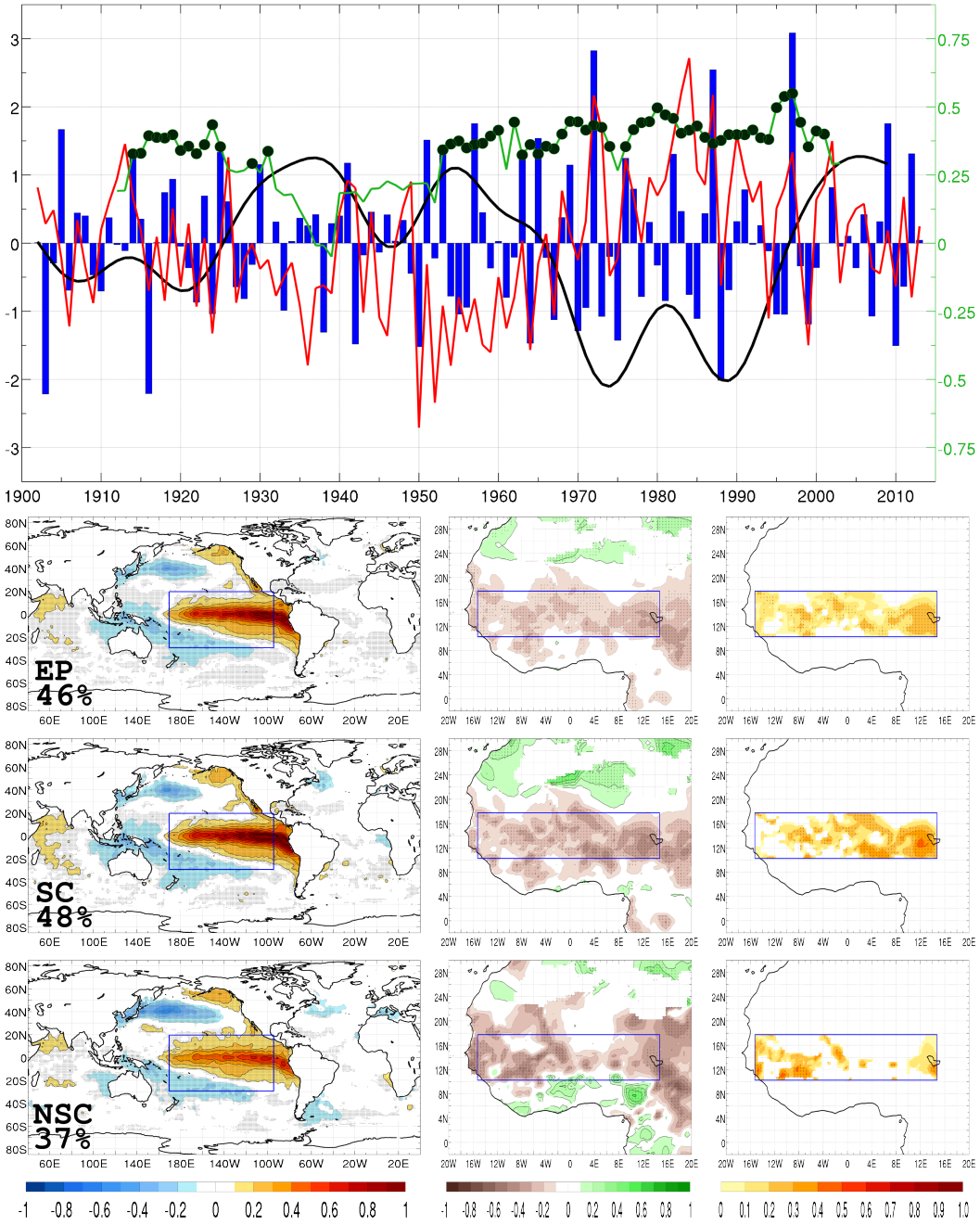

Fig. 7.10. (Top Panel) Expansion coefficients of the leading MCA mode calculated between the anomalies of tropical Pacific SST (blue bars, left axis) and the anomalous Sahelian rainfall (red line, left axis) in JAS. Superimposed, the 21-year centered moving correlation windows (green line, right axis) and significant correlation (black filled circles) between both expansion coefficients; (Bottom Panels): (First) Regression maps of the SST expansion coefficient of the leading MCA mode onto the SST (left) and rainfall (center). The black curve corresponds to the AMO index. Correlation maps (right) between the cross-validated hindcast of rainfall performed only with the leading MCA mode. The whole time period is used for the analysis. (Second) As (first) but using the years corresponding to the center of the significant correlation windows (green dots in the green curve). (Third) As (first) and (second) but using the years corresponding to the center of the non-significant correlation windows. The percentage of squared covariance fraction is indicated in the left bottom corner of the figure. (From Rodríguez-Fonseca et al. 2016).

7.4.4 Case study IV: Tropical Pacific SST – Euro-Mediterranean rainfall

Regardless of the mechanisms through which ENSO teleconnection is established over the extratropics, the ENSO signature on the European and Mediterranean rainfall has changed along the 20th century (Mariotti et al. 2002; Knippertz et al. 2003), a feature that confirms the absence of stationarity in the ENSO forcing. Some authors have attributed this changing impact to the influence of well-known multidecadal SST modes such as the AMO and the Interdecadal Pacific Oscillation (López-Parages and Rodríguez-Fonseca 2012, 2015; Zanchettin et al. 2008) on the atmospheric mean state.

This seems to be crucial for those regions where the skill of seasonal forecasting systems is still poor, as is the case of Europe and the Mediterranean region. As a consequence, windows of opportunity for the enhancement of these currently complicated seasonal predictions could be opened, at least, for certain decades.

To illustrate this point, the S^4CAST model has been applied during late winter and early spring (FMA) to determine the reliability of the tropical Pacific for seasonal predictability of European rainfall. In this way, Figure 7.11 depicts the leading co-variability mode between Pacific SST and European rainfall. The correlation between the expansion coefficients identifies a change in the teleconnection, with periods of strong rainfall response and positive correlation between the Niño 3.4 index and rainfall (SC periods: 1900-1940/1965-1984; consistent with López-Parages et al. (2015) and periods when this signal is weak and not statistically significant (NSC period: 1944-1964/2003-2008).

The evolution of the correlation exhibits some similarities to that found for the influence of the ENSO on Sahel rainfall variability in summer. The capability of the rainfall hindcast is plotted in terms of regression maps, showing that it significantly increases in the same periods in which the ENSO response over the Sahel is stronger.

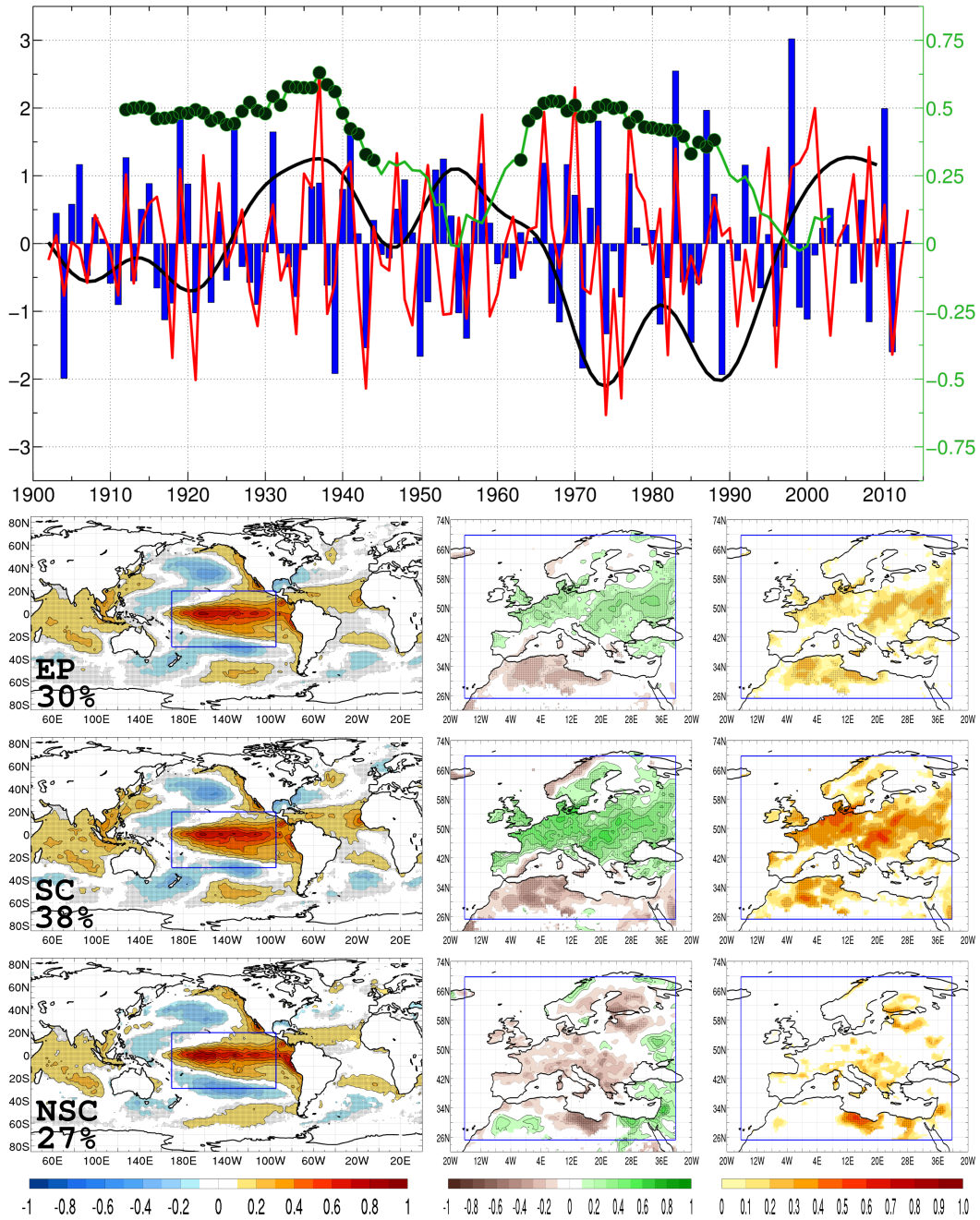

Fig. 7.11. (Top Panel) Expansion coefficients of the leading MCA mode calculated between the anomalies of tropical Pacific SST (blue bars, left axis) and the anomalous Euro-Mediterranean rainfall (red line, left axis) in FMA. Superimposed, the 21-year centered moving correlation windows (green line, right axis) and significant correlation (black filled circles, right axis) between both expansion coefficients. The black curve corresponds to the AMO index; (Bottom Panels) (First) Regression maps of the SST expansion coefficient of the leading MCA mode onto the SST (left) and rainfall (center); Correlation maps (right) between the cross-validated hindcast of rainfall performed only with the leading MCA mode. The whole time period is used for the analysis. (Second) As (first) but using the years corresponding to the center of the significant correlation windows (green dots in the green curve). (Third) As (first) and (second) but using the years corresponding to the center of the non-significant correlation windows. The percentage of squared covariance fraction is indicated in the left bottom corner of the figure. (From Rodríguez-Fonseca et al. 2016).

7.5 Discussion

It is well known how dynamical models are far to produce reliable seasonal climate forecasts for non-ENSO events, partly due to the presence of strong biases in some regions, noticeably the tropical Atlantic (Barnston et al. 2015). In contrast, statistical models, despite being a useful supplement, they are mostly unable to reproduce the non-linearity in the ocean-atmosphere system, exceptions include neural networks and Bayesian methods. Attempts to implement new statistical models constitute a fundamental contribution aimed to enhance and complement the dynamical models. Anyway, statistical models have evolved linked to dynamical models, either as an alternative or within them as a hybrid model.

Following this reasoning, the first part of this thesis introduces the S^{4}CAST model, which was created from a preliminary version developed as the main part of a cooperation project between the *Laboratoire de Physique de l'Atmosphère et de l'Océan Siméon Fongang* (LPAOSF) of the University Cheik Anta Diop (UCAD) in Dakar (Senegal) and the Complutense University of Madrid (UCM) within the VIII UCM Call for Cooperation and Development projects (VR: 101/11) and was named "Creation and Donation of a statistical seasonal forecast model for West African rainfall". Thereby, the version presented herein has been published as version 2.0 (S^{4}CAST v2.0; **Suárez-Moreno and Rodríguez-Fonseca 2015**). As a brief explanation on the history, the original model was restricted to study the predictability of West African rainfall from tropical global SSTA under some input parameters much more limited with respect to version 2.0. Thus, the reason for developing and improve the model for publication is the motivation arising from colleagues in different institutions along Africa and Europe to expand the model and use it as an alternative tool to look for SST-related predictability due to the strong SST bias that coupled dynamical models exhibit nowadays.

The model is based on the predictive power of the SST. Concerning the association along time between SSTA and any climate-related variable susceptible of being predicted from it, the concept of stationarity is raised as one of the motivating factors in creating the S^{4}CAST model. The stationarity refers to changes in the co-variability patterns between the predictor and the predictand fields along a given sequence of decades, so

that it can be kept invariant (stationary) or changing (non-stationary). This concept has been addressed by different authors (e.g., Janicot et al. 1996; Fontaine et al. 1998; Rodríguez-Fonseca et al. 2009, 2011; Mohino et al. 2011b; Martín-Rey et al. 2012; Losada et al. 2012; López-Parages and Rodríguez-Fonseca 2012; López-Parages et al. 2015) and becomes the main novelty and contribution introduced by the S^{4}CAST to be considered as a key factor to complement the seasonal forecasting provided by current prediction models, either dynamical or statistical. Thus, the S^{4}CAST model is an alternative to enhance and complement the estimates made by dynamical models, which exhibit a number of systematic biases to adequately reproduce the tropical climate variability (Biasutti et al. 2006; Richter and Xie 2008; Wahl et al. 2011; Doi et al. 2012; Richter et al. 2012; Bellenguer et al. 2013; Brown et al. 2013; Li and Xie 2013; Toniazzo and Woolnough 2014; Vanniere et al. 2013; Xue et al. 2013).

Strictly, the S^{4}CAST model cannot be applied in operational forecasting for the time being, although its application in determining stationary relationships between two fields and their co-variability patterns can be crucial for improving the estimates provided by the operating prediction models currently used. Thereby, the model is proposed for use in two areas: the study of seasonal predictability and the study of teleconnections, both based on the influence of SST. On the one hand, we refer to predictability when predictor is considered from a lead-time equal to 0 months (medium-range forecast) in advance (long-range forecast). On the other hand, we speak about the study of teleconnections when predictor seasonal selection partially or totally overlaps (synchronous) the forecast period, meaning that one cannot speak about lead-time, instead we speak about a monthly lag between the last month in the forecast period and the last month comprising the predictor monthly period.

In addition to previous considerations, the model always provides the predictions in hindcast mode for the different periods of stationarity (SC, NSC and EP), while the forecast mode depends on input parameters and data files used for predictor and predictand fields. For instance, considering the year of writing this thesis (the first half of 2017), to make a forecast of any climate-related variable for September-October-November (SON) by selecting a lead- time of two months for the prediction, which means taking the predictor (SST) two months before September (from April to June; AMJ), the prediction for SON 2017 will be performed if the predictand field is available

at least until November 2016 and predictor is available at least until June 2017. Thus, the model constructs the regression coefficients by using the common period until November 2016. Accordingly, the regression coefficients along with predictor data (AMJ 2017) will provide the forecast for SON 2017. In this way, the model firstly checks data availability related to the input parameters and shows by screen if future forecast is enabled. If enabled, the model performs three types of forecast by computing the regression coefficient respectively for each period (SC, NSC, EP). Finally, the user should determine the best forecast by a study of the modulations of each stationary period and the sequence of hindcasts immediately preceding the present.

In the applications shown in this paper we have focused in the results from MCA. This statistical methodology, along with Canonical Correlation Analysis (CCA), have been widely used in studies of predictability during the last decades (e.g., Barnston and Ropelewski 1992; Bretherton et al. 1992; Wallace et al. 1992; Barnston and Smith, 1996; Fontaine et al. 1999; Korecha and Barnston 2007; Barnston and Tippet 2014; Recalde-Coronel et al. 2014). Integration of the methodology and intuitive use through a user interface are some of the main advantages of the S^{4}CAST model, allowing the selection of a big number of inputs. Future releases of the model will include other methodologies that are currently being introduced and tested.

Originally, the model was created to tackle the study of the predictability of anomalous rainfall associated with WAM, which co-varies in a different way with the tropical band of Atlantic and Pacific ocean basins, being an indicator of non-stationarity (Losada et al. 2012). The transition between SC and NSC periods, around the 1970s, has served as the starting point of many studies focusing on the influence of global SSTA before and after that period (e.g., Mohino et al. 2011b; Rodríguez-Fonseca et al. 2011, 2015; Losada et al. 2012) while being one of the motivations to create the S^{4}CAST.

The choice of the case study related to Sahelian rainfall predictability from tropical Atlantic SST is motivated by two main reasons: on the one hand, SST in the tropical Atlantic is well known to strongly influence the dynamics of the ITCZ (e.g., Fontaine et al. 1998) which in turn determines the subsequent WAM. Nevertheless, dynamical models do not properly reproduce the influence of SST on the ITCZ (Lin 2007; Richter and Xie 2008; Doi et al. 2012; Tonniazzo and Woolnough 2013) becoming the statistical

prediction an alternative way to predict WAM variability. The second reason is related to the non-stationary influence of the tropical Atlantic on Sahel rainfall reported in several studies (Janicot et al. 1996, 1998; Ward 1998; Rodríguez-Fonseca et al. 2011; Mohino et al. 2011b; Losada et al. 2012).

The second case study has served as a benchmark to certify the ability of the S^{4}CAST model in the study of SSTA predictability by the corroboration of the tropical Atlantic SSTA as preditor of the ENSO. This is a recently discovered relationship (Rodríguez-Fonseca et al. 2009; Ding et al. 2012; Polo et al. 2015) that has been found to be non-stationary over time (Martín del Rey et al. 2014, 2015).

Otherwise, the non-stationarity of ENSO-related impacts have been reliably replicated by the model. Accordingly, both the ENSO impact on the Sahel (Mohino et al. 2011b; Rodríguez-Fonseca et al. 2011; Janicot et al. 1996, 2001; Fontaine et al. 1998; Losada et al. 2012) and on the Euro-Mediterranean rainfall (López-Parages and Rodríguez-Fonseca 2012; López-Parages et al. 2015) exhibit a robust non-stationary link.

The application of moving correlation windows between expansion coefficients obtained from MCA analysis results in three periods of stationarity depending on the statistically significant correlation: entire period (EP), significant correlation period (SC) and no-significant correlation period (NSC). For the case in which non-stationarity is considered we refer to EP period, assuming changes in co-variability patterns. Stationarity is referred to SC and NSC periods. These periods may slightly vary depending on the type of moving correlation windows: advanced, centered or delayed. Stationary analysis to determine the three different work periods (SC, NSC, EP) is limited to the selection of a single mode of co-variability. When selecting a set of modes, the stationarity analysis is not applied so that simulations are only developed for EP period, whereby the whole time series is considered for both the predictor and predictand fields.

Three conditions may enhance the degree of confidence in a given predictor. The first has to do with the COI index (see section 7.2) used to determine the working scenarios (SC, NSC, EP). Delayed moving correlation windows can help in this task. Thus, if correlation coefficients between the expansion coefficients (U and V) exhibit significant values for the present year and the previous 21 study years, greater confidence is

assumed for the predictor. The second condition is determined by the value of the expansion coefficient (*U*) for the current year so that the higher its value, the better the forecast. The last condition has to do with the percentage of variance explained by the selected co-variability mode, the higher its value, the better the forecast. Nevertheless, despite previous conditions, the influence of other remote and nearby oceanic predictors must be considered in order to provide a full and reliable predictability study.

The data files used as predictor and predictand fields correspond to observations and reanalysis from several institutions. The use of new data files is simple and can be performed according to user needs. The upgrade of data files from respective websites must be checked periodically to strengthen the results. In addition, it is also advisable to launch the same simulations using different data files in order to compare the results and assess the robustness of the forecast. The results shown in this work for different selections have been verified by following these criteria.

The results obtained by using the S^{4}CAST model put forward the consideration of non-stationarities in the co-variability patterns and therefore in atmospheric teleconnections. Thus, it is important to determine the multidecadal modulator of the interannual variability in order to know which predictor is the one affecting in particular periods and regions (Rodríguez-Fonseca et al. 2015).

7.6 Code availability

The model consists of a software package organized in folders containing libraries, functions and scripts developed as a MATLAB® toolbox from version R2010b onwards. Two of the folders, named as *mexcdf* and *netcdf_toolbox*, corresponds to libraries needed for working with NetCDF files and have been downloaded from *www.mexcdf.sourceforge.net* and built-in into the model. The file containing the model core with the executable code is named *S4core*. Once the toolbox has been added to the MATLAB® path and by simply typing '*S4cast*' in the command window, the user is prompted to enter a number of input parameters required to launch a simulation. The software package *S4plot* dedicated to plot figures, has been added so that the user can use this software by typing *'figures'* in the command window. Note that figures presented in this work have been further improved

manually. The code is Open Access and can be downloaded from the Zenodo repository (DOI 10.5281/zenodo.15985) in the URL *https://zenodo.org/record/15985*. To facilitate the execution of the model leading to the results shown in this paper, used data files that have been previously defined in Section 4, are included in the directories */S4CAST_v2.0/data_files/predictand* and */S4CAST_v2.0/data_files/predictor*. The second case study requires NOAA ERSST as predictor and predictand. The code has been thoroughly analyzed by using several data files and input parameters. However, the emergence of software bugs is not ruled out, being mostly associated with problems to adapt and use NetCDF files.

CHAPTER VIII

8 Interdecadal changes in the SST-driven teleconnections with the Sahel

As stated, the potential causes of alterations in the seasonal cycle of the WAM are mainly related to anthropogenic and natural forcing (Giannini et al. 2008) (see section 2.2). As part of the results of this thesis, the present section focuses on the latter, with the SST historically playing the dominant role (Folland et al. 1986; Palmer 1986; Xue and Shukla 1998; Fontaine et al. 1998; Ward 1998; Bader and Latif 2003; Giannini et al. 2003; Lu and Delworth 2005; Mohino et al. 2011a; Rodríguez-Fonseca et al. 2011, 2015; Losada et al. 2012; Rowell 2013).

As a reminder of what is described in section 2.4, the influence of global SSTA on Sahel rainfall ranges from interannual to multidecadal time scales (Giannini et al. 2003; Dieppois et al. 2015). On the one hand, several studies have addressed the influence of global SSTA on the interannual variability of Sahel rainfall, addressing robust impacts from the ENSO (Janicot et al. 2001; Rowell 2001; Giannini 2005; Joly and Voldoire 2009; Mohino et al. 2011c), the AEM (Janicot et al. 1998; Giannini et al. 2003; Kushnir et al. 2003; Polo et al. 2008; Joly and Voldoire 2010; Losada et al. 2010; Nnamchi and Li 2011) and the Mediterranean Sea (Rowell 2003; Jung et al. 2006; Fontaine et al. 2010, 2011a; Gaetani et al. 2010), all of them influencing the WAM system and its predictability. On the other hand, the leading patterns of multidecadal SST variability are linked to the rainfall trend in West Africa. In this framework, the Atlantic Multidecadal Variability (AMV), Interdecadal Pacific Oscillation (IPO) and Global Warming (GW) exert a prominent influence on the variability of WAM (Bader and Latif 2003; Lu and Delworth 2005; Chung and Ramanathan 2006; Knight et al. 2006; Zhang and Delworth 2006; Lu 2009; Shanahan et al. 2009; Findell and Delworth 2010; Mohino et al. 2011a; Biasutti 2013; García-García and Ummenhofer 2015).

When treated separately, the dynamical mechanisms linking those modes of SST variability aforementioned with the WAM system are consistently described. However, when it comes to interannual variability, there are observational evidences that oceanic impacts may be far from stable on decadal time scales. This feature has been addressed in terms of strengthened or weakened teleconnections and associated impacts depending on the decadal periods considered (Janicot et al. 1996; Fontaine et al. 1998; Mohino et al. 2011b; Rodriguez-Fonseca et al. 2011, 2015, 2016; Losada et al. 2012; Diatta and Fink 2014). Nevertheless, this evidence, despite being consistent, remains almost entirely observational, and dynamical factors have been scarcely proposed so far.

The present study considers the instability (non-stationarity) of the SST-forced response of Sahel rainfall to be primarily related with (*i*) changes in interannual SST variability patterns and (*ii*) interactions between interannual and multidecadal modes of SST variability. The dynamical mechanisms associated with both potential causes are therefore explored. The non-stationarities in the interannual SST-Sahel rainfall links are statistically analyzed by using the S^4CAST model (Suárez-Moreno and Rodríguez-Fonseca 2015). The period under investigation is 1921-2010 and the non-stationarity of teleconnections forced on interannual time scales by the tropical Pacific and Atlantic Oceans, and the Mediterranean Sea are investigated. Being previously suggested by Diatta and Fink (2014), the results obtained in this study corroborate the need for considering the non-stationary nature of the interannual teleconnections in order to improve the seasonal predictability of rainfall in the Sahel. The major novelties introduced herein are (*i*) the analysis of the dynamical processes explaining the non-stationarities and (*ii*) linking them statistically to multidecadal changes of the global-scale SST background.

The robustness of the results, noticeably those related to the evaluation of non-stationarity in the teleconnections, is based on the use of the rain-gauge station data described in section *5.1.1.1*, along with the CRU rainfall dataset.

8.1 Data and methodology

This study is based on the use of both observations and reanalysis data. While the former serves to explore co-variability patterns between SSTA and anomalous rainfall, the latter is used to examine the dynamical mechanisms underlying the teleconnections. A detailed description of both databases along with the experimental setup with the S^{4}CAST model is presented in the next sections.

8.1.1 Experimental setup with the S^{4}CAST model

The S^{4}CAST model is used to assess the predictability of anomalous seasonal rainfall over the Sahel considering the SSTA as potential predictor. As mentioned above, both station and gridded datasets have been used in the different experiments to assess the robustness of the results as well as to validate the use of gridded rainfall data.

In this study, the anomalies are calculated by subtracting the seasonal long-term mean from each of the three months season fields (July-August-September). Rainfall anomalies are standardized. A high-pass Butterworth filter (see section *6.1.2.1*) of 10th order with a cutoff frequency ($f_c = 2 \cdot dt/T$) set to 2/7 years^{-1} is applied to both rainfall and SST anomalous fields in order to extract the purely interannual variability, thus isolating the high-frequency influence of SSTA on the rainfall, including that associated with the leading modes of interannual SST variability such as the AEM (Polo et al. 2008) or the ENSO (Clarke 2014; Wang et al. 2017).

The S^{4}CAST model is applied herein to statistically evaluate periods of potential stability (stationarity) in the relationship between **Y** and **Z** based on the leading mode ($n = 1$) of co-variability. These periods are determined by means of 21-year sliding windows correlation between the time series expansion coefficients of **Y** and **Z** (**U** and **V** respectively). Thus, stationary (stable) periods correspond to those years in which the association between **U** and **V** remains invariant in terms of significant or non-significant correlation scores between both time series. In this study, the correlation index (hereinafter **COI**) between **U** and **V** for each time step (i) within the temporal dimension (n_i) is defined as in eqn (7.1) (see section 7.2).

Accordingly, a significance test is applied to determine the significant correlation period (SC) along which **COI** scores are statistically significant at a given level. Likewise, the non-significant correlation period (hereinafter NSC) corresponds to the remaining **COI** scores below the same significance level. The S^{4}CAST model performs a significance test according to the non-parametric Monte Carlo method under 1000 permutations. The significance level has been set in this study at 95% ($\alpha = 0.05$).

The S^{4}CAST model is used herein to explore the potential stationarity (stability) in the interannual SST-forced response of Sahel rainfall. In this framework, the model is applied to three different ocean basins: eMED, tATL and tPAC. The robustness of the stationarity analysis is based on the use of both gridded and station data as predictand field. Thus, six configurations are performed, two for each oceanic predictor. Moreover, for each configuration, the statistical methodology is applied under three assumptions: the extended period (EP, 1921-2010) during which **Y**-**Z** co-variability is assumed to be non-stationary (non-stable), and periods SC and NSC of distinct but stable co-variability. The forecast period for analysis is selected to cover the peak of the monsoon season in the Sahel, from July to September (JAS).

The atmospheric dynamics explaining the SST-driven teleconnections is explored in terms of seasonal composites (see section 6.5). These composites are based on anomalies of those atmospheric variables from the ERA-20C reanalysis presented in section 5.1.3. In this context, H refers to values of the predictor expansion coefficient (**U**) exceeding one positive standard deviation, whereas L corresponds to values of **U** below one negative standard deviation. Composites are independently calculated for SC and NSC periods to compare the changing atmospheric response under a potentially different SST-forcing. To evaluate the statistical significance of composite maps, a T-test of difference between two means (see section *6.3.1.1*) is applied, setting the confidence level to 90%.

8.2 Non-stationary interannual teleconnections

The results presented in this section are separated in different subsections. Firstly, the SSTA-Sahel rainfall co-variability patterns (eMED, tATL, tPAC) are analyzed from its corresponding leading MCA modes. To this aim, both gridded and station rainfall data are used in this analysis. Assuming that such patterns and associated atmospheric teleconnections will be found to be potentially non-stationary, the dynamical factors causing these instabilities are subsequently analyzed, being related with changes in the predictability of Sahel rainfall.

8.2.1 Leading SSTA-Sahel rainfall co-variability modes

In this section, an analysis of the leading MCA modes between SSTA and anomalous Sahel rainfall is presented, taking into account those two periods statistically evaluated from **COI**, namely, the SC and NSC terms. Note that the analysis is performed by the use of both gridded and station rainfall datasets. Thus, the expansion coefficients time series (**U**) along with **COI** indices are shown in Figure 8.1 for the HadISST-CRU (blue bars and lines) and HadISST-station (red bars and lines) analysis. For the Mediterranean (Fig. 8.1*A*), the co-variability pattern between the predictor and predictand anomalous fields is highly correlated before the 1960s and after the 1990s, thus setting the corresponding SC period. By construction, the complementary NSC period lies in the years in between. Regarding the tropical Atlantic (Fig. 8.1*B*), the SC period extends up to the end of the 1980s, with the NSC period lying in recent decades. For the tropical Pacific (Fig. 8.1*C*), SC ranges from the 1960s onwards, so that NSC is restricted to the 1940s and 1950s. An overview of the three oceanic predictors and its associated **COIs** reveals three different stages: up to the 1950s, the interannual variability of Sahel rainfall significantly co-varies with the eMED and tATL. Throughout a second stage (1960s-1990s), rainfall variability is strongly influenced from tropical SSTA (tATL, tPAC). The last stage, from the 1990s up to the present is characterized by a growing influence from eMED and a statistically less robust association with the tPAC. Interestingly, each stage exhibits the significant influence of two oceanic predictors, whilst the remaining one decays.

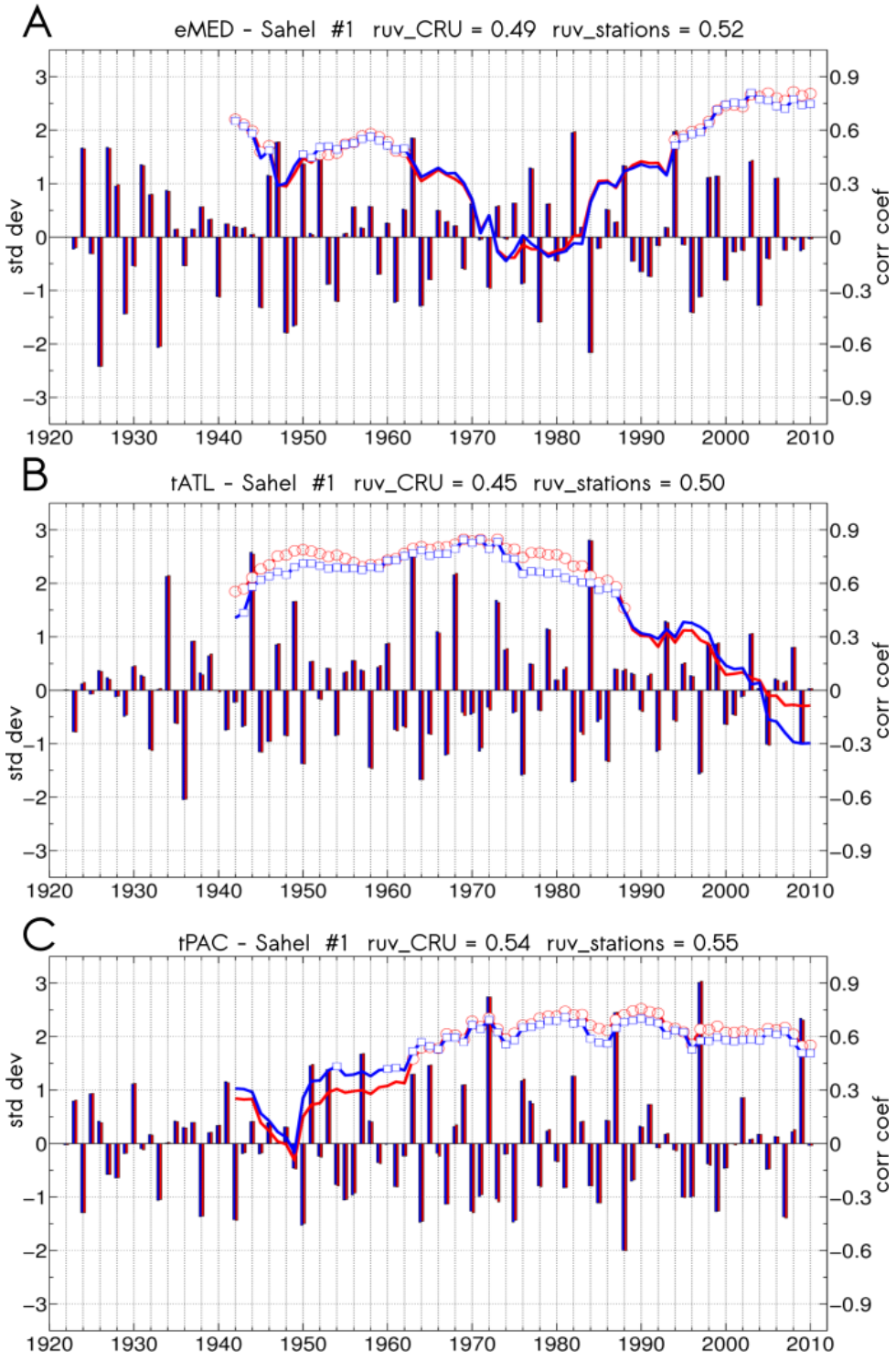

Fig. 8.1. Expansion coefficients time series and COI indices. SST expansion coefficients (U) for the leading MCA mode between observed SSTA (HadISST) and observed standardized anomalous JAS rainfall calculated from CRU (blue bars) and stations (red bars) in the Sahel (15ºW-15ºE, 10ºN-18ºN). COI indices are calculated as indicated in the text for the HadISST-CRU analysis (blue line) and the HadISST-station analysis (red line). The expansion coefficients and COIs are presented for (A) eMED, (B) tATL and (C) tPAC. Statistical significance for COI indices is set at 95% under the Monte Carlo method (1000 permutations) for the HadISST-CRU analysis (blue contoured boxes) and the HadISST-station analysis (red contoured circles). The correlation score between U and rainfall expansion coefficients (V, not shown) is included in figure titles for the CRU (ruv_CRU) and stations (ruv_stations) analysis. (From Suárez-Moreno et al. 2017a).

The SST-rainfall co-variability pattern for eMED is depicted in Figure 8.2. Positive (negative) SSTA in the Mediterranea Sea is related with increased (decreased) Sahel rainfall in the SC period (Fig. 8.2*A*). Note that the station data indicate less coherence that is unlikely to be explicable by errors in the station data, but smoothing effects and perhaps fewer/other stations used in the CRU analysis. The overall result is coherent with previous works that relate rainfall increase with enhanced southward moisture advection by the mean flow from the Mediterranean across the Sahara desert, causing an intensified low-level convergence with the southwesterly monsoon flow over the central-eastern Sahel (Rowell 2003; Jung et al. 2006; Fontaine et al. 2010, 2011; Gaetani et al. 2010). In contrast, a similar Mediterranean warming (cooling) is not associated with remarkable rainfall anomalies over the Sahel during the NSC period (Fig. 8.2*B*). This could be related with an additional forcing from significant cold SSTA in the eastern North Atlantic that will be discussed later.

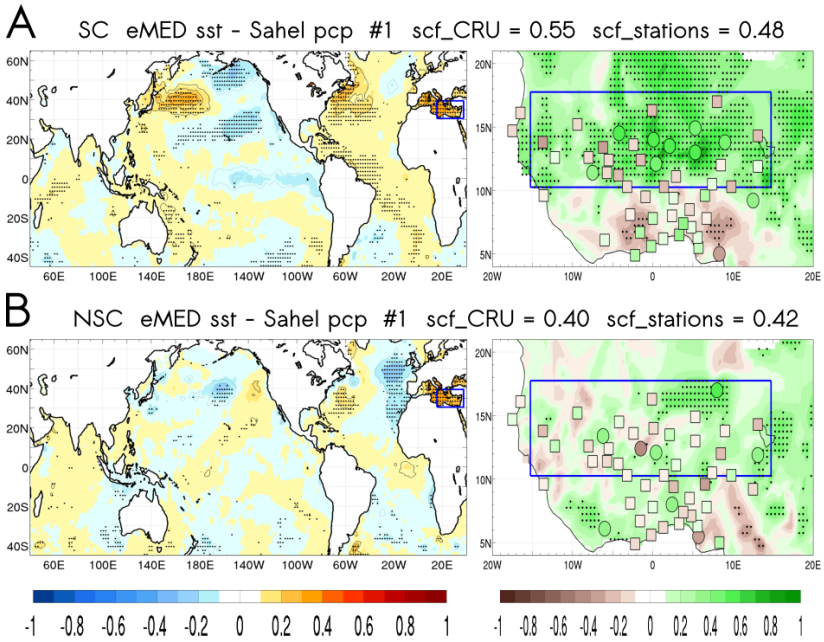

Fig. 8.2. Regression maps for the leading MCA mode between eMED SSTA and anomalous Sahel rainfall for (A) the SC period and (B) the NSC period. (Left column) Homogeneous SSTA (K std^{-1}) maps obtained by regression of SST expansion coefficient (U) onto global SSTA. Colored-shaded values correspond to HadISST-station analysis; contoured values denote results from HadISST-CRU analysis. (Right column) Heterogeneous anomalous rainfall (mm day^{-1} std^{-1}) maps obtained by regression of SST expansion coefficient (U) onto regional anomalous rainfall. Circles and squares denote significant and no-significant values respectively for HadISST-stations analysis. Colored-shaded values correspond to HadISST-CRU analysis with the significant interval in stippling. The squared-covariance fraction (scf) and correlation coefficients between expansion coefficients (ruv) are shown in figure titles for both (CRU and stations) analyses. Significance level is set at 95% under the Monte Carlo method (1000 permutations). (From Suárez-Moreno et al. 2017a).

For tATL (Fig. 8.3), a widespread tropical warming that resembles the positive phase of the AEM is related to negative rainfall anomalies in the Sahel and increased rainfall over the Guinea Coast during the SC period (Fig. 8.3*A*), the latter coherently confirmed by the station data. The WAM response to the positive AEM has been addressed in previous studies, showing a southward shift of the ITCZ in response to a reduced land-ocean thermal contrast (e.g., Chiang et al. 2002). This equatorward location of the ITCZ is associated with increased convective activity in the Gulf of Guinea and dry conditions over the Sahel, resulting in a rainfall dipole over West Africa (Janowiak 1988; Fontaine and Janicot 1996; Janicot et al. 1998; Giannini et al. 2003; Joly and Voldoire 2010; Losada et al. 2010a; Mohino et al. 2001b; Rodríguez-Fonseca et al. 2011). Considering the linear nature of the MCA, the rainfall dipole reverses its sign under a negative AEM-like pattern. A different pattern is observed in the NSC period (Fig. 8.3*B*), along which no dipolar rainfall structure appears in response to a tropical Atlantic warming. While the CRU data insinuate a monopole response over the WAM region, the station data by far do not show this coherence. As for the eMED case, the CRU signal suggests a "simpler" response than the station network. In any case, the NSC results point to the possibility that other mechanisms may be undermining the influence of the tropical Atlantic in the last 20 years. Notably, a significant, opposite SSTA pattern appears in the eastern equatorial Pacific. Indeed, the counteracting effect between both tropical basins and resulting impact on Sahel rainfall has been addressed in observational studies. Rodríguez-Fonseca et al. (2011, 2015) point out the Pacific counterpart as responsible for the non-stationary Atlantic SSTAs-induced variability of rainfall in West Africa. A dynamical explanation on this intricate teleconnection is presented later.

Regarding tPAC (Fig. 8.4), in both SC and NSC periods (Figs. 8.4*A* and 8.4*B* respectively), ENSO warm (cold) events are related to decreased (increased) rainfall in the Sahel, even though in SC ENSO significantly impacts on Sahel rainfall while the impact is not significant during NSC. Previous studies have suggested how the upper tropospheric heating over the tropical Pacific generates an atmospheric Kelvin wave that propagates eastward along the equatorial Atlantic sector. Consequently, the Walker-type circulation is altered, inducing anomalous subsidence over West Africa with the associated decrease in rainfall (Janicot et al. 2001; Rowell 2001; Giannini 2005; Joly and Voldoire 2009; Mohino et al. 2011c; Rodríguez-Fonseca et al. 2015). The different

amplitude of the SSTA when comparing SC to NSC may partially explain the observed changes in the rainfall response, hence being responsible for the non-stationary teleconnection. The dynamics associated with each period will be analyzed later, addressing whether other factors beyond the observed differences in the ENSO amplitude, are causing teleconnection instability.

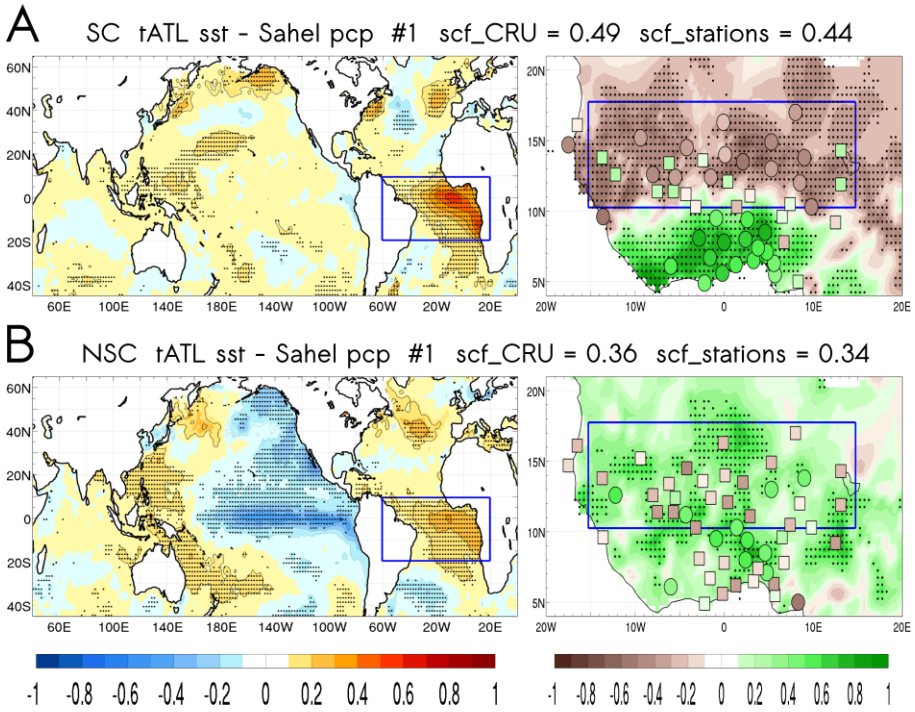

Fig. 8.3. Regression maps for the leading MCA mode between tATL SSTA and anomalous Sahel rainfall for (A) the SC period and (B) the NSC period. Same as Figure 3 but for the tropical Atlantic. (From Suárez-Moreno et al. 2017a).

The mechanisms aforementioned for each oceanic predictor, specifically those for the SC periods, mostly conform to what is known about the leading SST-forced teleconnections driving interannual variability of rainfall in the Sahel. However, enough evidence is shown to consider that these teleconnections are potentially unstable along the observational record. The results presented in the following sections shed light on this feature, analyzing the dynamical factors associated with SC and NSC periods and each oceanic predictor. As stated, seasonal (JAS) composites are used to explore these dynamical factors. Accordingly, H (high) and L (low) events are selected for SC and NSC periods from its respective SST expansion coefficient time series (U), which are depicted for each ocean predictor in Figure 8.5.

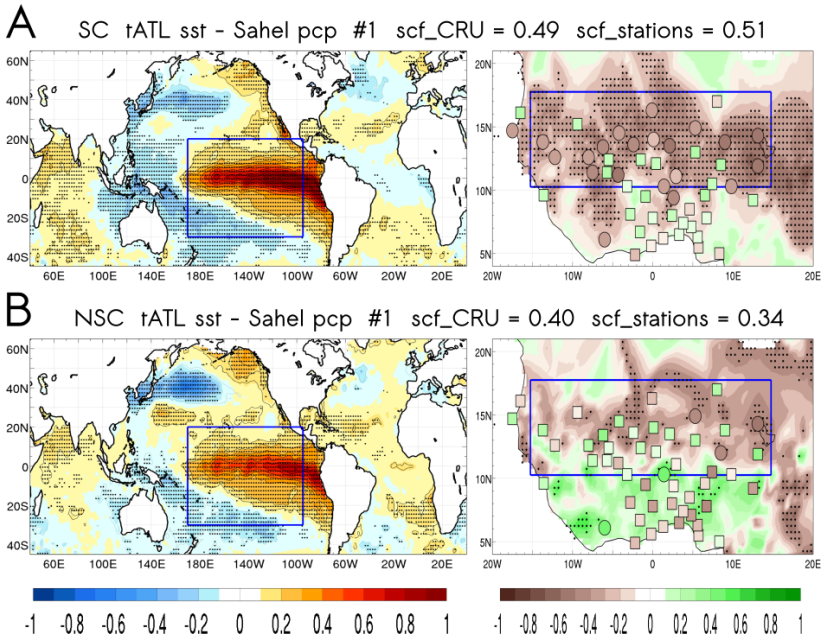

Fig. 8.4. Regression maps for the leading MCA mode between tPAC SSTA and anomalous Sahel rainfall for (A) the SC period and (B) the NSC period. Same as Figure 3 but for the tropical Pacific. (From Suárez-Moreno et al. 2017a).

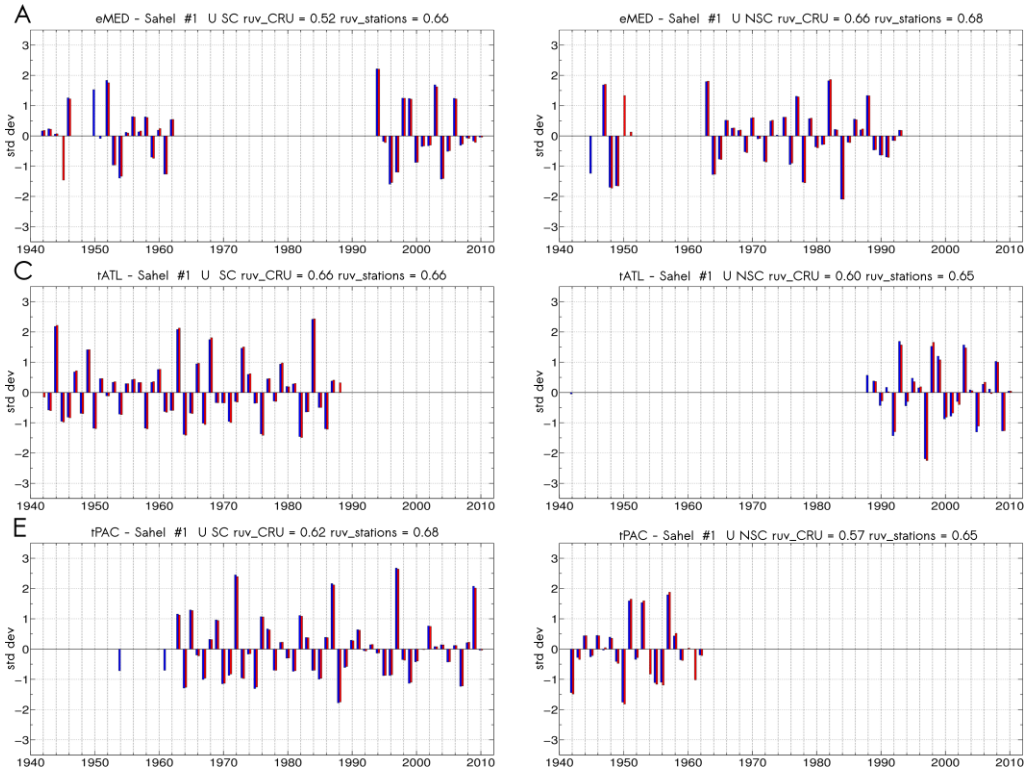

Fig. 8.5. SST expansion coefficients time series (U) for the leading MCA mode between observed SSTA (HadISST) and observed standardized anomalous JAS rainfall calculated from CRU (blue bars) and stations (red bars) in the Sahel (15ºW-15ºE, 10ºN-18ºN). (Left column) SST expansion coefficient for the SC periods. (Right column) SST expansion coefficient for the NSC periods. (A) eMED-Sahel, (B) tATL-Sahel, (C) tPAC-Sahel. (From Suárez-Moreno et al. 2017a).

8.2.2 Mediterranean – Sahel

During the SC period, the Mediterranean warming (see Fig. 8.2A) leads to a wetter central Sahel (Fig 8.6*A*), a region in which seasonal composites coincide for both CRU and station rainfall data. This positive rainfall anomaly may be related to the convergence of low-level anomalous winds (Fig. 8.6*B*), feeding convergence over the Sahel. Thus, an anomalous northeasterly wind would provide increased low-level moisture from a warmer Mediterranean that converges over the Sahel with the anomalous southwesterly monsoon flow inland (e.g., Rowell 2003; Gaetani et al. 2010). Moreover, an anomalous westerly flow from the tropical North Atlantic, penetrating the coast of Senegal, can be identified as a reinforcement of the low-level African Westerly Jet (AWJ), being associated to wet years in the Sahel during JAS (Grist and Nicholson 2001; Nicholson 2013) with its maximum in the monsoon layer at about 925 hPa. This region of enhanced convergence suggests a northward migration of the ITCZ, as indicated by the anomalous southerly monsoon flow inland. The anomalous cyclonic circulation expanding over the Mediterranean and eastern North Atlantic is concomitant with the negative *slp* anomalies observed in these regions (Fig. 8.6*B*). Furthermore, the low-level atmospheric thickness (*z700-z925*) does not reflect a significant interannual strengthening of the SHL over the Saharan location where it is typically stationary during boreal summer months (Fig. 8.6*C*) (e.g., Lavaysse et al. 2009, 2010).

Contrarily, during the NSC period, there are no significant precipitation anomalies over the Sahel (Fig. 8.7*A*). The anomalous low-level wind from the Mediterranean vanishes, leading to a weakening in the convergence with the southwesterly monsoon flow that is in turn reduced by the northerly component from the North Atlantic (Fig. 8.7*B*). The anomalous northerly wind establishes as a result of the geostrophic low-level wind associated with a *slp* dipole of anomalous high pressures over the Atlantic ocean side and an opposite sign lobe to the east (Fig. 8.7*B*). This anomalous northerly flow may be responsible for inhibiting the northward migration of the Atlantic ITCZ and associated monsoon flow inland, keeping maximum precipitation over the coast in the Guinean Gulf. Moreover, a significant component of this northerly low-level anomalous flow penetrates through Western Sahara and Mauritania, accompanying a strengthening of the SHL (Fig. 8.7*C*). In principle, a strengthened SHL has been related to increased convective activity over West Africa (Lavaysse et al. 2010), even though the threshold for

convection should be determined by additional factors, namely, the southwesterly monsoon flow that appears to be inhibited due to the equatorward position of the ITCZ. Additionally, the stronger SHL might also inhibit the ventilation from the Mediterranean at its eastern flank.

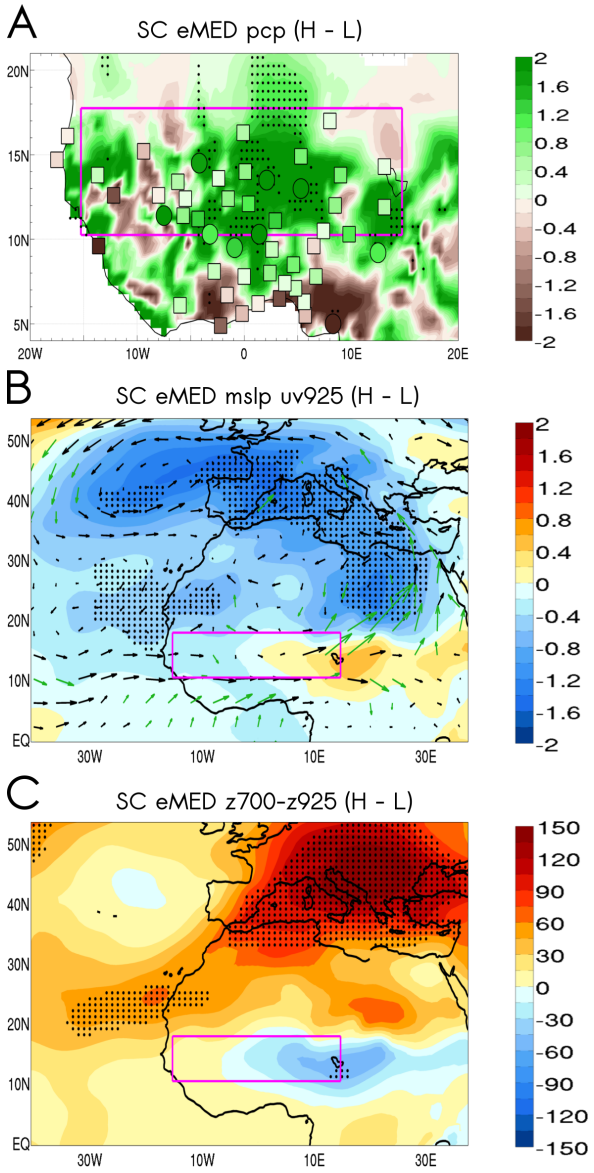

Fig. 8.6. Dynamical mechanism associated with the eMED SSTA-anomalous Sahel rainfall teleconnection for the SC period in terms of high (H) minus low (L) composite maps for different atmospheric variables. H and L events correspond to values of the SST expansion coefficient (U) above 1 std dev and below -1 std dev respectively (see Fig 8.5*A*, left panel). U is obtained from the leading MCA mode. (A) Anomalous rainfall (mm day^{-1} std^{-1}) using CRU (colored-shaded) and station (circles-squares) databases. Significant values are denoted in stippling and circles. (B) Anomalous horizontal wind (m s^{-1}) at 925 hPa (*uv925*, arrows) and mean sea level pressure (*slp,* hPa) anomalies. Significant values are indicated in stippling and green arrows. (C) Atmospheric thickness in terms of *z700* hPa – *z900* hPa (m^2 s^{-2}). Significant values denoted in stippling. The confidence level is set at 90% under a T-test. (From Suárez-Moreno et al. 2017a).

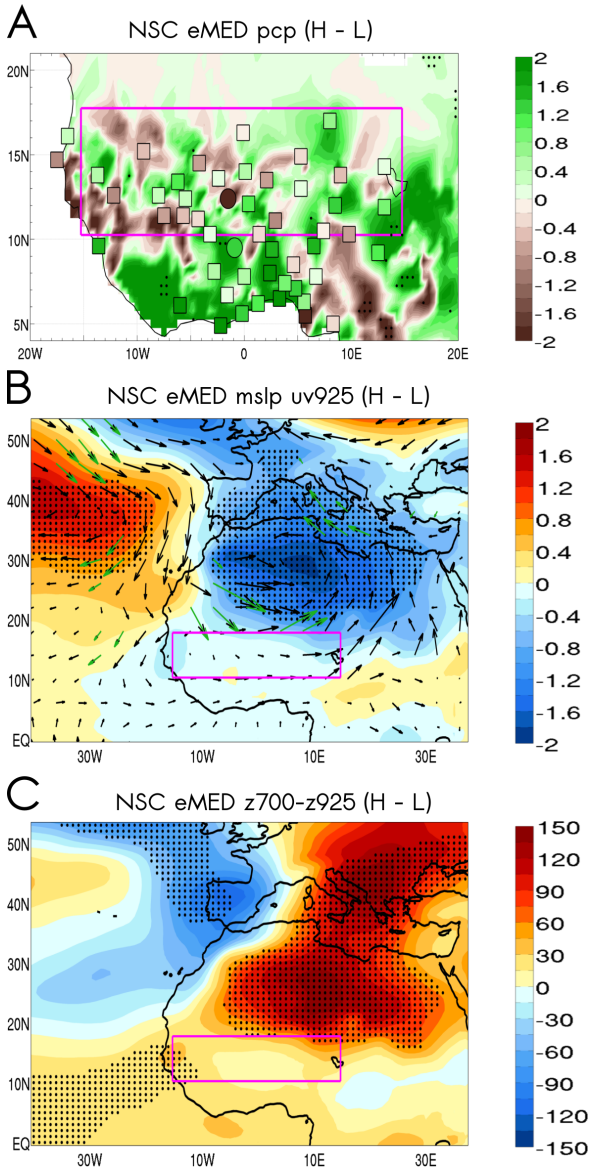

Fig. 8.7. Same as Figure 8.6 but for the NSC period. H and L events are shown in Figure 8.5*A* (right panel). (From Suárez-Moreno et al. 2017a).

8.2.3 Tropical Atlantic – Sahel

Significant changes are evident between NSC and SC periods concerning tATL. As stated, some authors have addressed a dipolar rainfall pattern occurring in response to positive SSTA during some particular decades coinciding with the SC period addressed here (e.g., Mohino et al. 2011b; Rodríguez-Fonseca et al. 2011; Losada et al. 2012). Nevertheless, positive SSTA can also be observed over the Atlantic during the NSC period, in this case being associated with increased rainfall in both the Gulf of Guinea and Sahel regions, so the precipitation dipole is absent. In this context, Losada et al.

(2012) conducted a set of sensitivity experiments showing this changing rainfall response to a tropical Atlantic warming depending on the sequence of decades under study. Otherwise, Diatta and Fink (2014) have documented a similar non-stationary relationship by means of statistical-observational analysis.

The positive AEM (Atlantic Niño) influence on the West African monsoon is characterized by an alteration of the whole monsoon-system components. In this way, the positive AEM-like pattern characterizing the SC period results in a well-defined dipole of anomalous precipitation (Fig. 8.8*A*), with negative anomalies over the Sahel, whilst wetter conditions are located over the Guinean Gulf. During a warm AEM event, the meridional pressure gradient induced by the differential land-ocean heating weakens (Fig. 8.8*B*), thus reducing the monsoon flow and keeping the ITCZ equatorward (Chiang et al. 2002). The anomalous zonal wind (Fig. 8.8*C*), reveals a weakening of both, the Tropical Easterly Jet (TEJ) and the African Easterly Jet (AEJ) and reduced southwesterly monsoon flow associated with a weakened African Westerly Jet (AWJ). All these atmospheric features are described under conditions of reduced rainfall in the Sahel (e.g., Nicholson 2013). In addition, the anomalous vertical wind component (Fig. 9*D*) exhibits a southward-located ITCZ around 0-5ºN in terms of enhanced upward motions related to deep convection over a warmer tropical Atlantic ocean (see Fig. 8.3*A*). Moreover, anomalous subsidence over the Sahel (i.e., anomalous downward motions of air masses) is concomitant with that southward position of the ITCZ, even weakening the dry shallow convection associated with the SHL. Those enhanced upward motions aforementioned are in turn observed in a zonal cross-section of meridional averages of w (Fig. 8.8*E*).

The dynamical features previously detailed for the SC period are disrupted during NSC (Fig. 8.9). In this case, the anomalous rainfall dipole vanishes (Fig. 8.9*A*). The emergence of a colder tropical Pacific induces anomalous Walker circulation, weakening local upward motions that remotely induce instability over the Sahelian troposphere (Fig. 8.9*E*). As a result subsidence over the Sahel weakens when compared to SC (Fig. 8.9*D*). Significant alterations in the zonal jets are not observed (Fig. 8.9*C*). Moreover, the SSTA forcing from the eastern equatorial Pacific counteracts the anomalous southward position of the ITCZ induced by a warmer tropical Atlantic, which is observed in reduced anomalous monsoon flow to the south (Fig. 8.9*B*). Thus, the tropical Pacific

balances the drying impact of a warmer tropical Atlantic, even leading to a relative increase of rainfall in the Sahel (Fig. 8.9*A*).

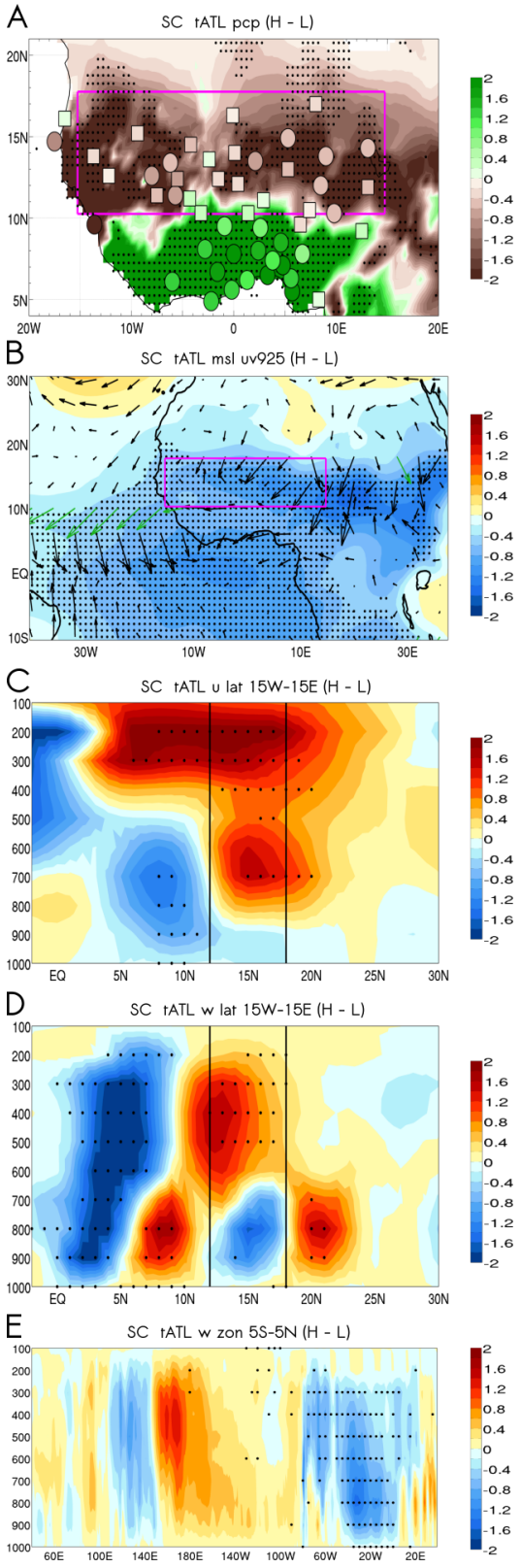

Fig. 8.8. Dynamical mechanism associated with the tATL SSTA-anomalous Sahel rainfall teleconnection for the SC period in terms of high (H) minus low (L) composite maps for different atmospheric variables. H and L events correspond to values of the SST expansion coefficient (U) above 1 std dev and below -1 std dev respectively (see Fig 8.5*B*, left panel). U is obtained from the leading MCA mode. (A) Anomalous rainfall (mm day^{-1} std^{-1}) using CRU (colored-shaded) and station (circles-squares) databases. Significant values are denoted in stippling and circles. (B) Anomalous horizontal wind (m s^{-1}) at 925 hPa (*uv925*, arrows) and mean sea level pressure (*slp*, hPa) anomalies. Significant values are indicated in stippling and green arrows. (C) Zonally averaged (15°W-15°E) latitudinal cross-section of zonal wind (*u*, m s^{-1}). (D) Zonally averaged (15°W-15°E) latitudinal cross-section of vertical wind (w, 10^{-2} Pa s^{-1}). (E) Meridionally averaged (5°S-5°N) longitudinal cross-section of vertical wind (w, 10^{-2} Pa s^{-1}). Cross-sections are depicted from 1000 to 100 hPa. Significant values from (C) to (D) are indicated in stippling. The confidence level is set at 90% under a T-test. (From Suárez-Moreno et al. 2017a).

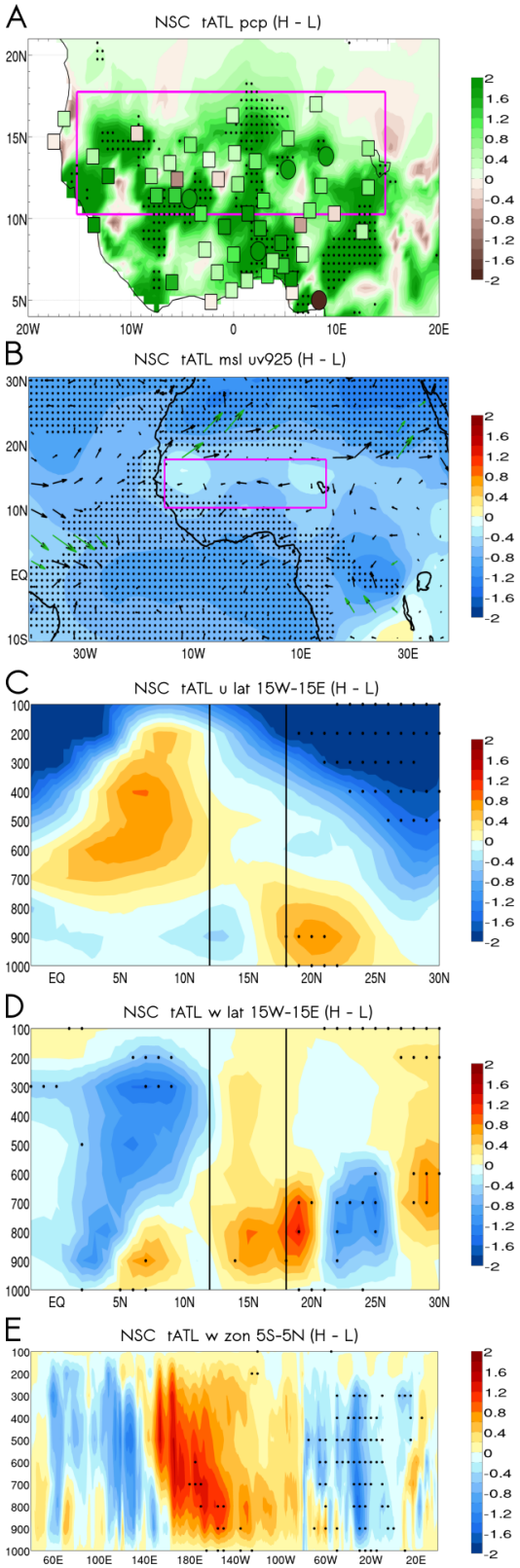

Fig. 8.9. Same as Figure 8.8 but for the NSC period. H and L events are shown in Figure 8.5*B* (right panel). (From Suárez-Moreno et al. 2017a).

8.2.4 Tropical Pacific – Sahel

A positive ENSO-like (El Niño) pattern is found in the SC period, accompanying drought conditions in the Sahel (Figs. 8.10*A*). Deep convection is enhanced over the equatorial eastern Pacific in terms of anomalous upward motions, which transport heat to the upper-troposphere, triggering an equatorial Kelvin wave throughout the African-Atlantic sector that results in anomalous subsidence over West Africa (Rowell 2001). Such a mechanism describes an anomalous Walker-type circulation that remotely connects the eastern equatorial Pacific and West Africa (Figs. 8.10B-8.10*C*). This anomalous circulation pattern is observed in the upper-level divergent and rotational circulations (Figs. 8.10*D* and 8.10*E* respectively). The direct response to the tropical Pacific heating in a baroclinic atmosphere results in anomalous upper-level convergence (subsidence) over West Africa (Jin and Hoskins 1995) (Fig. 8.10*E*), inducing anomalous low-level divergence in the region (not shown). Hence, a Gill-Matsuno type response (Matsuno 1966; Gill 1980) connects the large-scale anomalous circulation between the eastern equatorial Pacific and Atlantic ocean basins (Fig. 8.10*D*), inducing stability (instability) over West Africa under a heating (cooling) of the eastern equatorial Pacific. The Sahel rainfall response to this teleconnection pattern agrees with previous studies in the subject (e.g., Joly and Voldoire 2009; Mohino et al. 2011c; Losada et al. 2012; Rodríguez-Fonseca et al. 2015).

As for the NSC period (Fig. 8.11), the SST-forcing from a warmer tropical Pacific resembles that previously described for the SC period. Nevertheless, the widespread negative rainfall anomalies observed in SC, are barely significant over the Sahel during NSC (Fig. 8.11*A*), even being positive southward. These differences in the rainfall response may be related to a similar, although somewhat weaker El Niño signal during SC compared to NSC (see Fig. 8.4). However, some differences are apparent, such as those in the vertical wind component (Fig. 8.11*B*), indicating a weakening of the anomalous subsidence over the Sahel. When compared to SC, this weakening in the atmospheric response can also be observed by analyzing the remaining variables treated in the study (Figs. 8.11*C*-8.11*D*-8.11*E*).

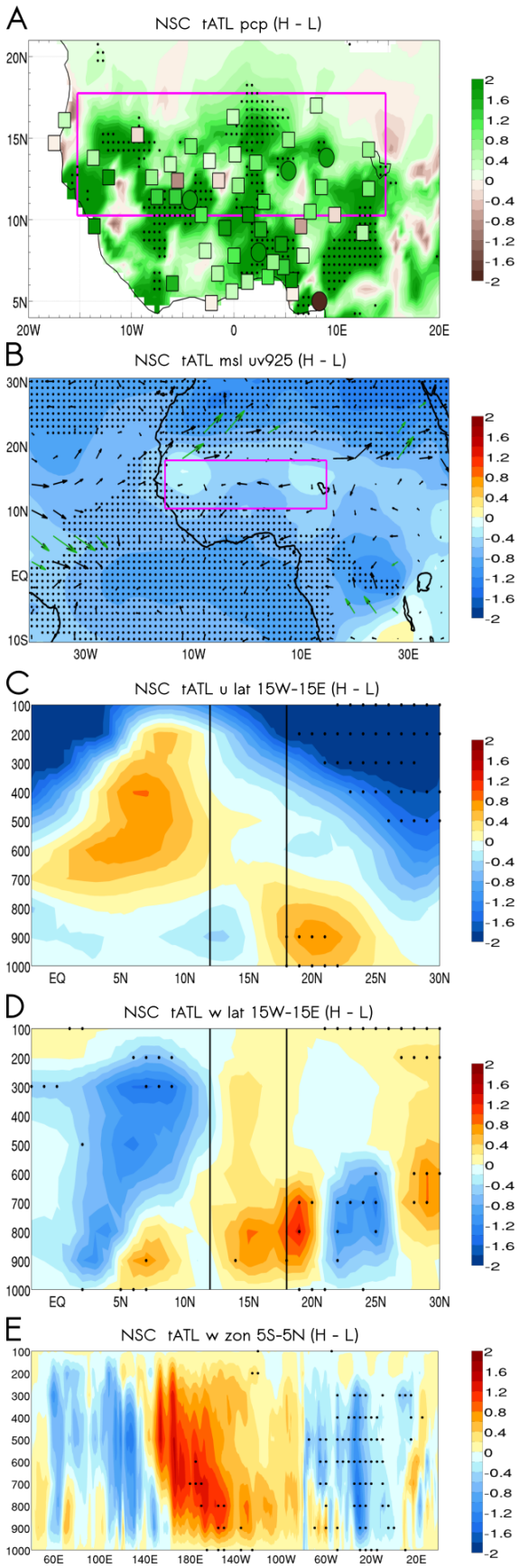

Fig. 8.10. Dynamical mechanism associated with the tPAC SSTA-anomalous Sahel rainfall teleconnection for the SC period in terms of high (H) minus low (L) composite maps for different atmospheric variables. H and L events correspond to values of the SST expansion coefficient (U) above 1 std dev and below -1 std dev respectively (see Fig 8.5*C*, left panel). U is obtained from the leading MCA mode. (A) Anomalous rainfall (mm day^{-1} std^{-1}) using CRU (colored-shaded) and station (circles-squares) databases. Significant values are denoted in stippling and circles. (B) Zonally averaged (15°W-15°E) latitudinal cross-section of zonal wind (*u*, m s^{-1}). (C) Meridionally averaged (5°S-5°N) longitudinal cross-section of vertical wind (w, 10^{-2} Pa s^{-1}). (D) Anomalous stream function (x10^{6} m^{2} s^{-1}) at 200 hPa. (E) Anomalous velocity potential (x10^{6} m^{2} s^{-1}) at 200 hPa. Cross-sections are depicted from 1000 to 100 hPa. Significant values from (B) to (E) are indicated in stippling. The confidence level is set at 90% under a T-test. (From Suárez-Moreno et al. 2017a).

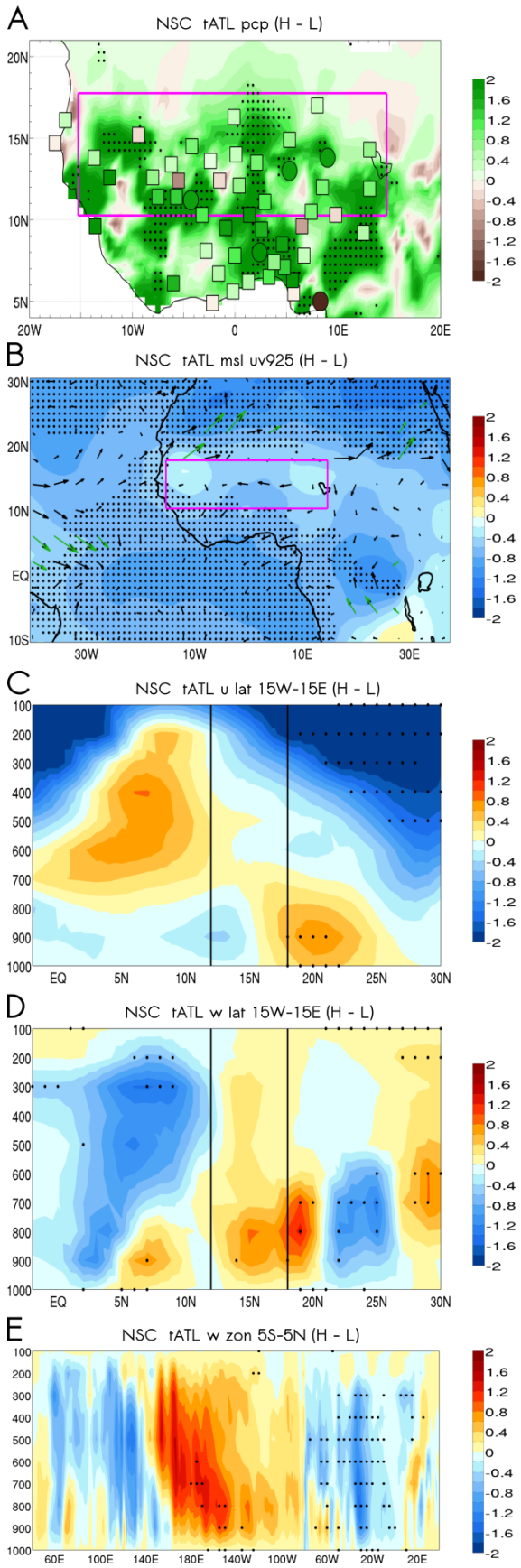

Fig. 8.11. Same as Figure 8.10 but for the NSC period. H and L events are shown in Figure 8.5*C* (right panel). (From Suárez-Moreno et al. 2017a).

Despite the similarity in the SSTA-forcing and associated dynamics in the SC and NSC periods, the remarkable difference in the Sahel rainfall response put forward the non-stationary behavior of the teleconnection throughout the observational record (1922-2010). Nevertheless, additional factors may be the cause for the weakened ENSO signal and associated rainfall response in NSC, being in turn responsible for the modulation of the teleconnection. The existence of a potential large-scale modulating mechanism will be further explored later, suggesting that multidecadal changes in the SST background could affect the interannual teleconnections.

8.3 Implications in predictability

Those changes in the dynamical mechanisms previously described could determine the SST-driven predictability of anomalous rainfall events in the Sahel. Indeed, it will be shown in this section how the SST-forced teleconnections associated with the SC periods are related to improved predictability whatever the oceanic predictor. To this aim, an analysis is carried out by means of cross-validated hindcasts ($\hat{Z}$) calculated as posed in the methodology (see section *6.2.1.2*) for SC and NSC periods separately. Note that, in each time step within the independent temporal dimensions of SC and NSC, the regression coefficients are calculated as in eqn (6.17). The correlation skill-scores between observations and hindcasts are likewise independently calculated for both periods. In this way, using eqn (6.18) it follows that:

$$\rho_{SC} = \frac{\mathrm{cov}(\hat{Z}_{SC}, Z_{SC})}{\sigma_{\hat{Z}}^{SC}\sigma_{Z}^{SC}} \tag{8.1}$$

$$\rho_{NSC} = \frac{\mathrm{cov}(\hat{Z}_{NSC}, Z_{NSC})}{\sigma_{\hat{Z}}^{NSC}\sigma_{Z}^{NSC}} \tag{8.2}$$

Accordingly, ρ_{SC} and ρ_{NSC} are depicted in Figure 8.12 (left and right columns respectively). As it can be observed, whatever the oceanic predictor, the skill-score of the statistical model in reproducing the anomalous rainfall response is clearly higher during the SC periods. Focusing on eMED (Fig. 8.12*A*), those changes in the teleconnection mechanisms between SC and NSC lead to notably enhanced skill-score during the

former period. Regarding tATL (Fig. 8.12*B*), the skill-score significantly improves during SC, when the teleconnection is driven by an isolated SST signal in the tropical Atlantic (SC) against the counteracting tATL-tPAC effect (NSC). Concerning tPAC (Fig. 8.12*C*), the skill-score is barely significant in NSC, whereas the improvement during SC could be related to the stronger ENSO-like signal associated to this period.

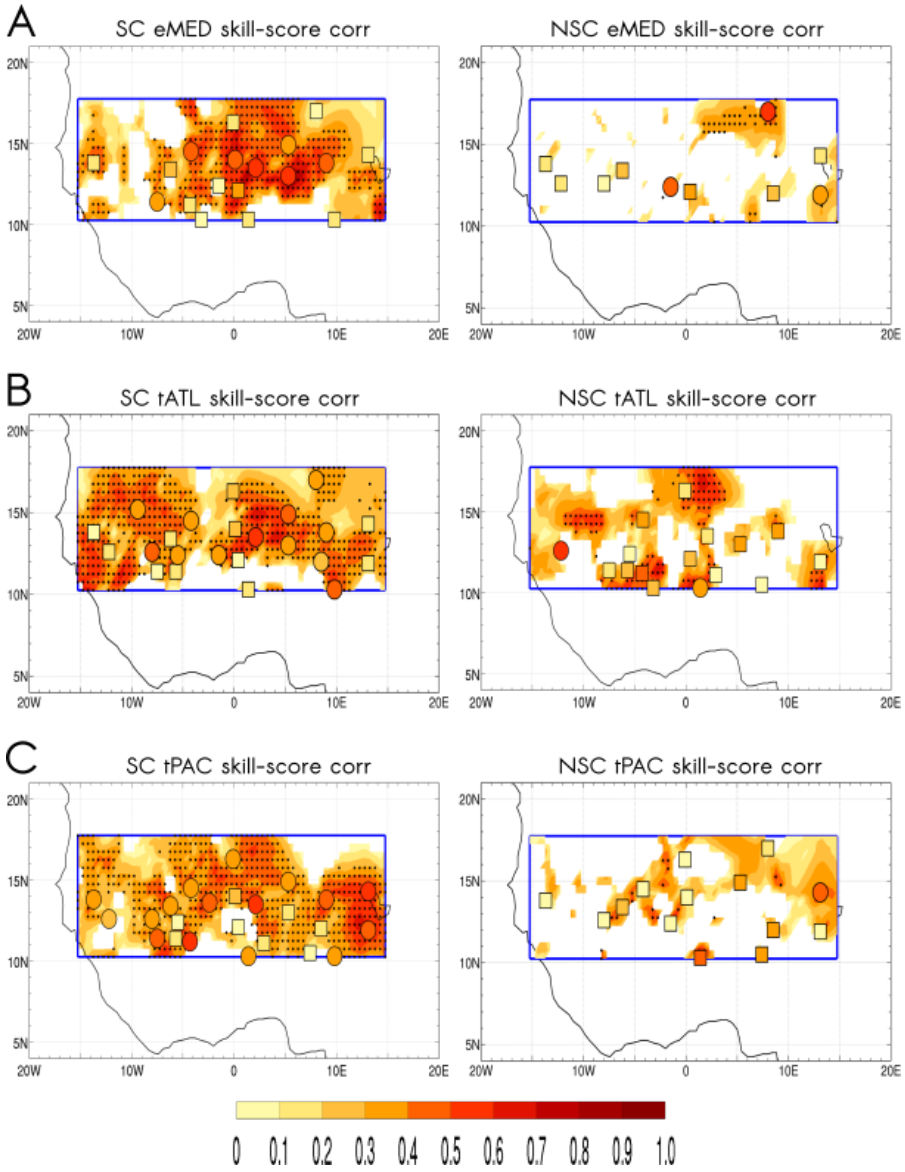

Fig. 8.12. Skill-score between cross-validated hindcasts and observations of rainfall calculated in terms of Pearson correlation coefficients for each grid point in the Sahel (15ºW-15ºE, 10ºN-18ºN). The analysis is based on the leading MCA modes as indicated in the text. Colored-shaded values correspond to HadISST-CRU analysis. Squares and circles correspond to HadISST-station analysis. Black flecked regions are statistically significant at 95% according to a Monte Carlo test (1000 permutations). Circles (squares) indicate significant (non-significant) values for HadISST-stations analysis at 95% under a Monte Carlo test (1000 permutations). Cross-validation is applied from the MCA between JAS Sahel rainfall and JAS SSTA for (A) eMED, (B) tATL, (C) tPAC. (Left column) Skill scores for the SC periods. (Right column) Skill-score for the NSC periods. (From Suárez-Moreno et al. 2017a).

In all cases, the changing skill-score between the SC and the NSC periods is potentially related to the different dynamics underlying the interannual teleconnection in each period. To some extent, an additional factor contributing to these changes in interannual teleconnections, and thus to predictability, may be the varying multidecadal SST background. Nevertheless, to qualify and quantify this contribution is a key factor that requires further study. A statistical-observational analysis is conducted in the next section to shed light on this matter, posing some reasonable hypotheses.

8.4 The potential role of multidecadal SST variability

When analyzing the **COI** indices (see Fig. 8.1), it was shown that the significant interannual impact of the tropical Atlantic SSTA on the anomalous Sahel rainfall declines during recent decades, whereas the tropical Pacific fits into an increasing trend. The case of the Mediterranean **COI** is different, showing an oscillatory evolution with two peaks, noticeably the second during recent decades. Now, these indices are tackled as climate indices, so that the **COIs** are averaged and standardized to be transformed into multidecadal variability indices (hereinafter **MVIs**):

$$COI' = COI - \overline{COI} \tag{8.3}$$

$$MVI = \frac{COI'}{std(COI')} \tag{8.4}$$

Moreover, a low-pass Butterworth filter of 10th order with a 13-year cutoff period is applied to remove the high-frequency variability (e.g., Mohino et al. 2011a). These **MVIs** corresponding to eMED, tATL and tPAC are depicted in Figure 8.13*A*. The positive phase of the **MVIs** time-series closely coincides with the SC periods (significant correlation scores of **COIs**), while the negative phase matches the NSC periods (non-significant correlation scores of **COIs**). In the same way as it was introduced in section 8.2.1, three different periods are distinguished: a first period (P1), from 1942 to 1964, is related to enhanced Sahel rainfall predictability associated to eMED and tATL interannual impacts; a second period (P2), from 1965 to 1987, during which the interannual predictability of Sahel rainfall improves if tropical oceanic predictors (tATL, tPAC) are considered; and a third period (P3), from 1988 to 2010, along which the

interannual impact from eMED becomes crucial in improving seasonal predictability of Sahel rainfall, even though tPAC influence cannot be neglected. The next step is to identify each of these periods by its underlying SSTA climatology (Figs. 8.13*B*-8.13*C*-8.13*D*), which in turn is associated with the corresponding interannual teleconnections aforementioned.

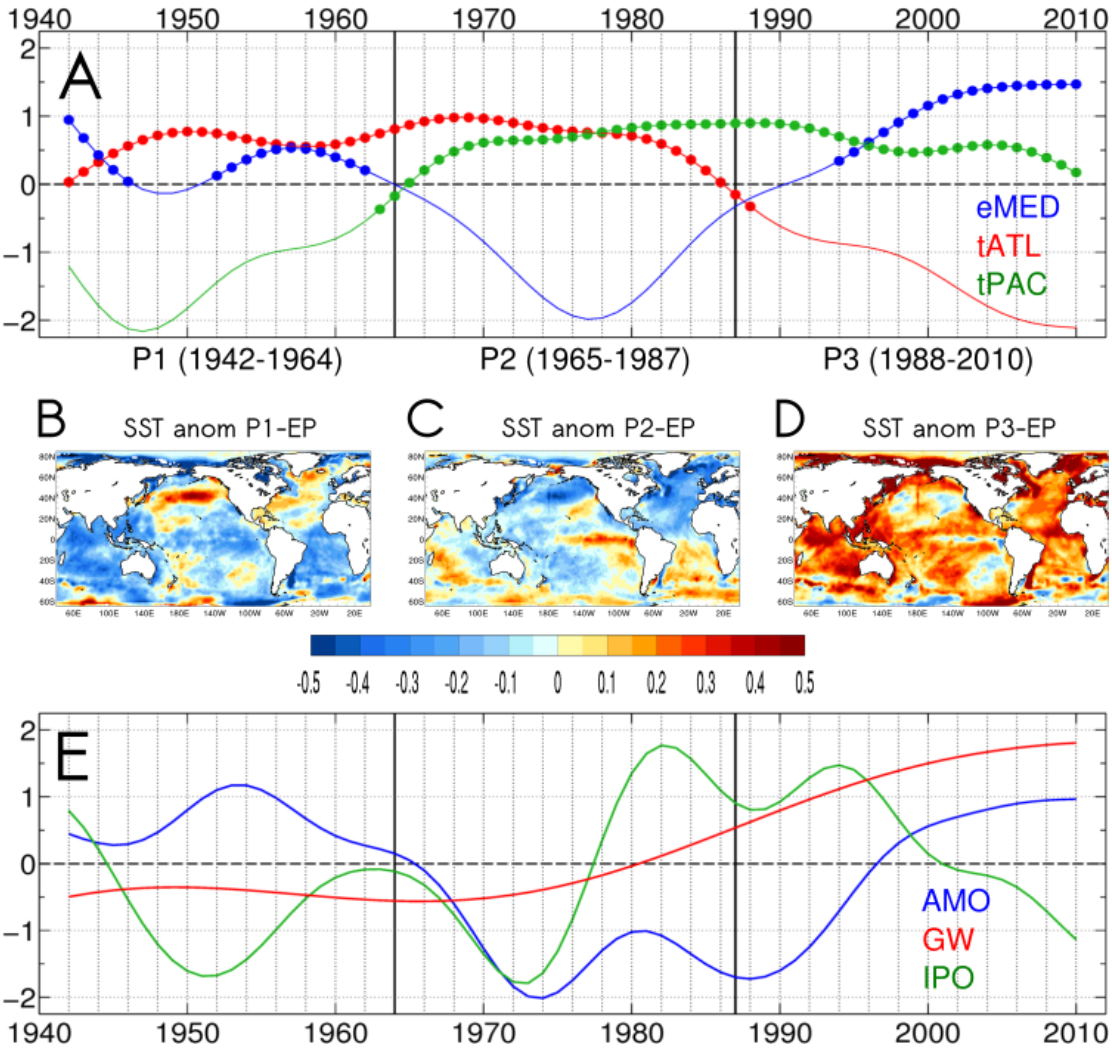

Fig. 8.13. Multidecadal variability indices (MVIs) and global SSTA patterns. (A) MVIs calculated as the 13-year low-pass filtered (solid lines) of the averaged-standardized correlation indices (COIs). Significant correlation periods (SC) are indicated by colored circles. Three different periods (P1, P2 and P3) are identified. (B to D) SSTA maps calculated from HadISST as global JAS SST climatologies minus the JAS SST climatology along the whole period for (B) P1, (C) P2 and (D) P3. (E) Multidecal indices of AMO, IPO and GW calculated from HadISST as indicated in the text. (From Suárez-Moreno et al. 2017a).

To some extent, **MVIs** could keep a link with the most prominent indices of multidecadal SST variability (Fig. 8.13E), namely, the AMV, IPO and GW, whose associated SST patterns are known to robustly influence the WAM variability on multidecadal time scales (Mohino et al. 2011a). These indices are calculated from the

HadISST database following the same procedure as in Mohino et al. (2011a). Overall, in the methodology, GW trend is removed from yearly SST and the Empirical Orthogonal Function (EOF) analysis is applied for Atlantic and Pacific basins, in decadal frequencies, being AMV and IPO indices the leading PCs respectively. The GW index is based on yearly averaged global SST, being a good approximation for the observed forced signal (Ting et al. 2009).

In order to quantify the potential link between the **MVIs** and the AMV, IPO and GW indices, a multilinear regression model is applied. All possible linear combinations between GW, AMV and IPO are taken into account in the model construction, their corresponding regression coefficients being α , β and γ respectively. Thus, each combination is named as follows:

$$GAI = \alpha \cdot GW + \beta \cdot AMV + \gamma \cdot IPO \quad (8.5)$$

$$GA = \alpha \cdot GW + \beta \cdot AMV \quad (8.6)$$

$$GI = \alpha \cdot GW + \gamma \cdot IPO \quad (8.7)$$

$$AI = \beta \cdot AMV + \gamma \cdot IPO \quad (8.8)$$

$$G = \alpha \cdot GW \quad (8.9)$$

$$A = \beta \cdot AMV \quad (8.10)$$

$$I = \gamma \cdot IPO \quad (8.11)$$

The statistics from the multilinear regression model to estimate **MVIs** from each possible combination (eqns 8.5-8.11) and each oceanic predictor are shown in Figure 8.14 in terms of Taylor diagrams (Taylor 2001), whereas the corresponding regression coefficients are collected in Table 8.1. The Mediterranean **MVI** (Fig. 8.14*A*) is reliably reproduced by a linear combination of GW and AMO, both presenting similar positive contributions (* in Table 8.1). The corresponding **MVI** to the tropical Atlantic (Fig. 8.14*B*) is almost entirely explained by the GW signal, both indices being highly anticorrelated (** in Table 8.1). Concerning the tropical Pacific (Fig. 8.14*C*), estimates of **MVI** do not show a link as clear as in previous cases, even though a positive and negative contributions of the GW and AMV respectively, both with similar amplitudes, provide the best estimates (*** in Table 8.1).

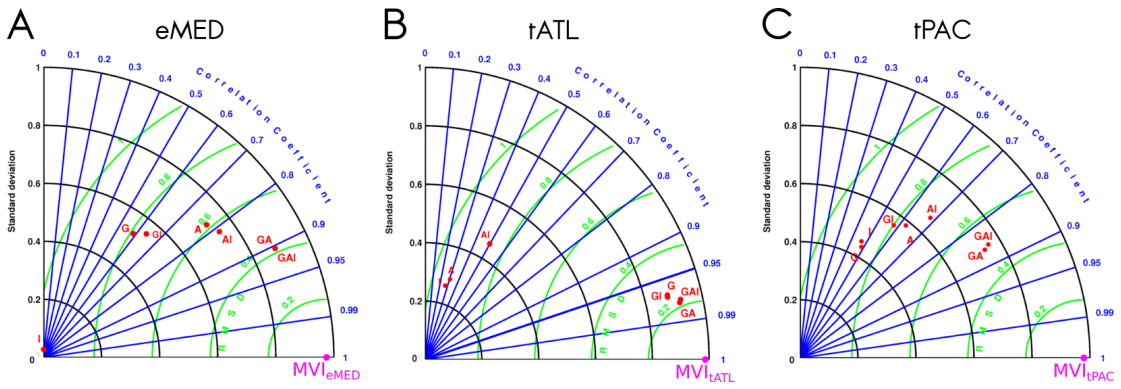

Fig. 8.14. Taylor diagrams representing the statistics from a multilinear regression model applied to estimate the MVIs for (A) eMED, (B) tATL, (C) tPAC. (From Suárez-Moreno et al. 2017a).

The positive phase of the AMV (P1, P3) seems to favor the eMED-Sahel interannual teleconnection, which is even more enhanced under the GW trend of recent decades (P3). Otherwise, the significant tATL SST-forced response of Sahel rainfall is fostered under a weak, negative GW signal (P1), whilst the increasing GW trend in the recent period (P3) characterizes a declining of the interannual tATL-Sahel teleconnection. Regarding tPAC, the negative AMO signal (P2) and GW trend (P3) seem to favor an enhanced interannual teleconnections with the Sahel rainfall.

To hypothesize, the common northern-hemispheric differential warming between P1 and P3 (see Figs, 8.13*B* and 8.13*D*) may exert a major role in the enhanced interannual teleconnection from eMED. In these periods, it is also observed an intrinsic warming component to the Mediterranean, which in turn could strengthen the interannual impact from an anomalously warmer eMED, whereas the impact from the negative phase (cooling) of the interannual co-variability mode would be damped. Meanwhile, the weakening in the south-north positive SST gradient (P3), or even the inversion thereof (P2), accompany a stronger influence from tPAC. In these cases, the relative multidecadal warming of the tropical Pacific would reinforce the drying of the Sahel under a positive ENSO-like pattern, the wetting impact associated to the negative ENSO phase being otherwise weakened. When it comes to tATL, the northern (southern)-hemispheric SSTA gradient, characterizing the underlying SSTA background in P1 (P2) is related to enhanced interannual impact. The wetting (drying) impact from a negative (positive) AEM-like pattern would be increased during P1 (P2) under a colder (warmer) tropical Atlantic.

Table 8.1. Regression coefficients of the multilinear regression model

		eMED	tATL	tPAC
GAI	α	*0.63**	*-0.99***	*0.54****
	β	*0.57**	*-0.22*	*-0.58****
	γ	*0.04*	*-0.06*	*0.12*
GA	α	*0.54**	*-1.02***	*0.59****
	β	*0.56**	*-0.20*	*-0.62****
GI	α	*0.70*	*-1.05***	*0.39*
	γ	*-0.21*	*0.02*	*0.33*
AI	β	*0.78*	*-0.40*	*-0.48*
	γ	*0.21*	*-0.37*	*0.29*
G	α	*0.62*	*-1.04***	*0.51*
A	β	*0.71*	*-0.28*	*-0.57*
I	γ	*-0.03*	*-0.25*	*0.48*

The first column indicates different combinations between GW, AMO and IPO as stated in expressions (8.5)-(8.11). Regression coefficients from the model are shown in second column. The regression coefficient values for eMED, tATL and tPAC are shown from third to fifth column respectively. (*) Represent the best estimates for eMED. (**) Represent the best estimates for tATL. (***) Represent the best estimates for tPAC. (From Suárez-Moreno et al. 2017a).

Another key factor is the influence of the interhemispheric SSTA gradients, inducing meridional shifts of the ITCZ that would also influence interannual teleconnections. In this framework, the impact of Atlantic interhemispheric SSTA gradients and the remote influence of the tropical Pacific on the ITCZ have been documented in previous works (e.g., Chiang et al. 2000). Accordingly, the spatial configuration of the SSTA patterns in each of the periods (P1, P2, P3) (Figs. 8.13*B*-8.13*C*-8.13*D*) suggests a potential link between the changing climatological SST background and fluctuations in the ITCZ location. The mean global ITCZ position is explored herein by means of the latitude at which the vertically integrated moist static energy (MSE) transport by the mean meridional circulation changes its sign (i.e., the energy flux equator δ) (Broccoli et al. 2006) (see eqn 4.18 and section 4.2.1). In this way, the meridional excursions of the

ITCZ may be determined by the cross-equatorial energy flux (F_0) (e.g., Kraus 1977; Donohoe et al. 2013; Adam et al. 2016a, 2016b).

As a reminder, the cross-equatorial energy flux F_0 is expected to be stronger the farther north is the ITCZ. Thus, the northernmost climatological position of the ITCZ is observed in P1, while it is closely similar in P2 and P3 (Fig. 8.15*A*). Nevertheless, a zoom over subtropical latitudes (Fig. 8.15*B*) reveals an ITCZ located around 15ºN in P2, whereas it lies slightly further north in P1 and P3. Despite the small amplitude (~ 0.6ºN), this difference is found to be statistically significant. By contrast, the difference between P1 and P3 (~ 0.1ºN) is not significant.

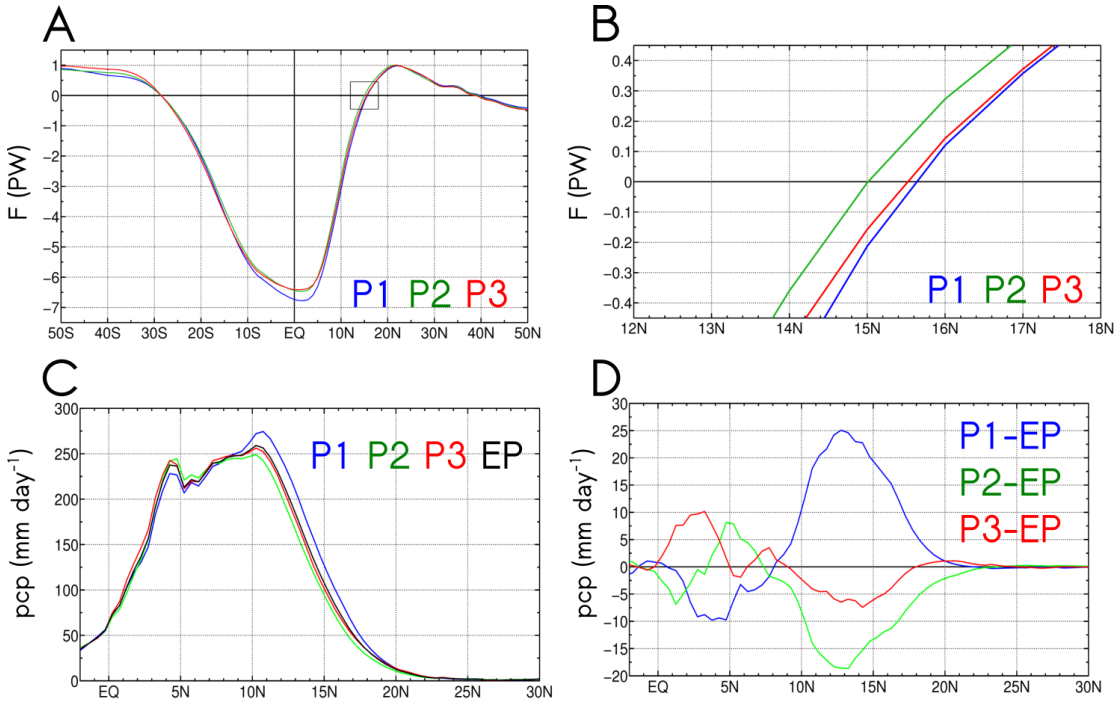

Fig. 8.15. Atmospheric meridional moist static energy (MSE) flux and latitudinal profiles of rainfall averaged in JAS. (A) Latitudinal profile of the vertically integrated MSE flux (PW) for the three periods (P1, P2 and P3) identified in Figure 14. MSE is zonally and globally averaged. (B) Zoom in the squared region marked on (A). (C) Latitudinal profile of climatological rainfall amounts (mm day^{-1}) for the three periods (P1, P2 and P3) and the entire period (EP). (D) Anomalous rainfall amounts calculated by subtracting the EP rainfall climatology to each one of the three periods (P1, P2 and P3). Each period is identified by a different color as indicated in figures. (From Suárez-Moreno et al. 2017a).

The climatological position of the ITCZ accompanies the location of the maximum tropical rain belt. The zonally averaged amount of rainfall in the Sahel (Fig. 8.15*C*) is shown to increase in P1, decreasing in P2 and being halfway to both periods in P3. This behavior is further supported by anomalous rainfall in each period taking as reference the entire record (EP, 1922-2010) (Fig. 8.15*D*). Thus, positive rainfall anomalies are found in

P1, meaning a wetter period, followed by a big drought during P2. The last period (P3) is characterized by dry anomalies, although a recovery trend is observed over the preceding period. Consequently, the link between the calculated climatological position of the ITCZ and multidecadal variability of rainfall seems to be consistent. Moreover, the chronological evolution P1-P2-P3 agrees with what is known from observations, namely, a wet period of positive rainfall anomalies, followed by the big drought in the Sahel and the apparent trend towards increased rainfall in the recent period (e.g., Le Barbè et al. 2002; Dai et al. 2004; Hagos and Cook 2008).

8.5 Discussion.

This study deals up with the non-stationary SST-forced interannual teleconnections with the Sahel. Up to now, the unstable character of these teleconnections has been shown in terms of observational analysis (Janicot et al. 1996; Fontaine et al. 1998; Mohino et al. 2011b; Rodriguez-Fonseca et al. 2011, 2015; Losada et al. 2012; Diatta and Fink 2014). However, no physical hypotheses have been explored to explain the dynamical causes of these instabilities. On the one hand, the counteracting effects between the different oceanic forcing operating at the same time in some periods (e.g., Atlantic and Pacific during P3) but not in others, are partly responsible for these instabilities. On the other hand, the interannual teleconnections could be modulated at multidecadal time scales by the changing ocean background state and associated fluctuations in the climalogical atmospheric circulation. Nevertheless, while the first cause seems to be robust, further analysis should be conducted in order to analyze the role of the ocean background state in modulating the teleconnections. In this way, sensitivity experiments with AGCMs would be particularly relevant.

On interannual time scales, the analysis of the underlying dynamics reveals changes in the SST-forced response of Sahel rainfall depending on the considered sequence of decades (SC against NSC). These periods are robustly assessed by the use of a network of in-situ rainfall measurements used for the first time in this thesis to this aim. A step forward is done in order to sort out the intricate teleconnections that determine the rainfall variability in the Sahel on interannual time scales. The presence of non-stationary interannual teleconnections with the Sahel is observed for the Mediterranean Sea,

tropical Atlantic and tropical Pacific oceans. Thus, unstable teleconnections are potentially due to variations in the leading SSTA variability patterns at interannual time scales. For the eMED, a cooling in the eastern North Atlantic is observed in NSC that may be responsible for inducing a more southern position of the ITCZ associated with a decreased rainfall in the Sahel despite a warm Mediterranean. By contrast, the absence of such cooling in SC allows the development of the classical teleconnection mechanism (i.e., moisture advection) to unfold without being disrupted. When it comes to the tATL, the different mechanisms between SC and NSC periods are based on the damping effect of the tropical Pacific observed in the latter period. Regarding the tPAC, the non-stationarity of the teleconnection is likely due to the varying amplitude of the ENSO signal between SC and NSC.

The skill-score of the statistical model further supports the hypotheses about non-stationary teleconnections, reproducing enhanced SSTA impacts on anomalous Sahel rainfall during some periods against others (see section 8.3). Indeed, during SC periods, the rainfall response enhances over the study region in terms of cross-validated skill-scores, whilst for the NSC periods the absence of skill is related to ineffective teleconnections. However, although non-stationarity is consistent, its cause remained unclear.

The multidecadal SST variability is hypothesized to play a major role in the varying nature of the teleconnections. Thus, the climatological SSTA could exert an influence not only on the decadal trends of Sahel rainfall, but also on defining the prevailing interannual SST-driven teleconnections with this region. On the one side, the AMV plays a crucial role in the interdecadal shifts of the ITCZ (Chiang et al. 2000), whose Atlantic branch determines the climatological location of the tropical rain belt within West Africa. Moreover, several works describe the AMV impact on the WAM system, with its negative phase underlying the Sahel big drought in the 1970s-1980s, whereas the positive phase is related to increased rainfall (Knight et al 2006; Shanahan et al. 2009; Mohino et al. 2011a; Ting et al. 2011; Martin et al. 2013; Martin and Thorncroft 2014). In this way, a northern (southern)-hemispheric differential SST warming is related to a northward (southward) shift of the ITCZ, inducing wetter (drier) conditions in the Sahel. This feature of the atmospheric general circulation has been evaluated in this work for three different periods (P1, P2, P3) through an analysis of the northward MSE transport,

suggesting a potential link between the climatological position of the ITCZ and multidecadal changes of the interannual teleconnection patterns. Hence, during P1 (1942-1964), a positive AMO-like pattern occurs coinciding with the northernmost position of the ITCZ, which seems to foster the interannual impacts from the Mediterranean and tropical Atlantic. Otherwise, under the negative phase of the AMO in P2 (1965-1987), tropical oceans seem to interact together, prevailing over the extratropical influence of the Mediterranean, whose impact gets weaker. Conversely, the underlying GW and positive AMO of recent decades P3 (1988-2010) seem to promote the Mediterranean interannual teleconnection, even though the tropical Pacific impact is also significant. These results suggest the relevant role of interhemispheric SST gradients, noticeably in the Atlantic, in the modulation of interannual teleconnections. In addition, the GW trend appears to be responsible for increasing the Mediterranean impact on the Sahel. Although the GW signal has been linked to a weakened monsoon circulation, causing drought conditions (Dai et al. 2013) as a response to the GW-induced stabilization of the tropical troposphere (Gaetani et al. 2016), the wetting impact of anthropogenic Mediterranean warming has been proposed as the main responsible for the recent trend of increasing precipitation in the Sahel (Park et al. 2016). Moreover, the northern-hemispheric differential warming has been addressed by its role in increasing precipitation, becoming a key factor in the projected Sahel rainfall (Munemoto and Tachinaba 2012; Park et al. 2015). Note that the influence of the IPO, which has been recently identified by negatively impacting on Sahel rainfall anomalies under its positive phase (Villamayor and Mohino 2015), does not seem to play a relevant role in modulating the interannual teleconnections. Anyway, further study is needed to explore this matter.

Concerning the important subject of the seasonal predictability of Sahel rainfall, the focus should be on the last period analyzed in this study (P3). In recent decades, the growing impact from the Mediterranean seems to prevail over the SST-forcing from tropical oceans. It is shown that this trend could keep a link with the underlying GW signal and positive phase of the AMV, both multidecadal SST patterns being related to each other by a warmer North Atlantic and a northern-hemispheric differential warming. Therefore, the ocean modeling of the Mediterranean and Atlantic ocean basins becomes crucial to improve the seasonal predictability of rainfall in the West African Sahel.

CHAPTER IX

9 Modulation of the non-stationary Mediterranean-Sahel teleconnection

The SST has been identified as driver of interannual to multidecadal Sahel rainfall variability (e.g., Bader and Latif 2003; Mohino et al. 2011a), thus becoming a key factor in the predictability of West African droughts (Rodríguez-Fonseca et al. 2015). One of these drivers is the Mediterranean Sea. At multidecadal time scales, the wetting impact of anthropogenic Mediterranean warming has been recently presented by its dominant role on projected Sahel rainfall, prevailing over the tropical Atlantic and Indo-Pacific oceans, which historically were the main drivers of Sahel drought (Park et al. 2016). Otherwise, the impact of Mediterranean SSTA on the Sahel also comprises interannual time scales. Thereby, warm events in the Mediterranean enhance low-level moisture transport across the Sahara to the south, converging in the Sahel with the southwesterly monsoonal flow to increase precipitation. Conversely, cold Mediterranean events are associated to decreased rainfall. Although this teleconnection has been widely described (Rowell 2003; Jung et al. 2003; Fontaine et al. 2010, Gaetani et al. 2010), it has been suggested to be non-stationary over time, getting stronger in some decades compared to others (Fontaine et al. 2011a; Rodríguez-Fonseca et al. 2011). Nevertheless, underlying causes for this instability have not yet been found and its clarification would be crucial to improve seasonal predictability of rainfall in the Sahel, with consequent socio-economic benefits to the region.

To some extent, non-stationarity in the Mediterranean-Sahel teleconnection could be determined by the multidecadal SST variability, which could exert not only an influence on the decadal trend of rainfall, but also in modulating the interannual impact of the Mediterranean. In this context, fluctuations in the West African rainfall trend have been attributed to changing Atlantic SST (Martin et al. 2013; Martin and Thorncorft 2014; Knight et al. 2006; Shanahan et al. 2009). Specifically, the Atlantic Multidecadal

Variability (AMV) plays a major role in interdecadal shifts of the Inter-tropical Convergence Zone (ITCZ) (Chiang et al. 2000). Likewise, the northern-hemispheric differential SST warming has been proposed as responsible for the recovery trend of precipitation in the Sahel (Munemoto and Tachinaba 2012; Park et al. 2015). In fact, even though the warming of the tropical oceans increases the threshold for triggering convention over West Africa (Sheffield and Wood 2008; Dai 2013; Hagos and Cook 2008), a warming of the North Atlantic and the Mediterranean could provide sufficient moisture in the monsoon flow to meet this threshold, thus resulting in a positive rainfall trend (Giannini et al 2013). Anyway, despite some uncertainties, the trend towards rainfall recovery in the Sahel is now a matter of fact (Dai et al. 2004; Nicholson 2005; Lebel and Ali 2009), with no shortage of work aiming to identify both drought and recovery background conditions, as well as to disentangle anthropogenic and natural forcing (Giannini et al. 2008; Greene et al. 2009; Ting et al. 2009).

In this section, a mechanism involving interactions between interannual and multidecadal SST variability is found to be responsible for the non-stable Mediterranean SST-forced response of Sahel rainfall. Using an AGCM, a set of numerical experiments is conducted to demonstrate how the multidecadal SST variability in the North Atlantic determines the consistency of the year-to-year Mediterranean-Sahel teleconnection. Evidence is shown on how this mechanism involves a key player of the WAM system, the Saharan heat low (SHL), which has been recently demonstrated to be connected with the interannual variability and recovery trend of precipitation in the central and eastern Sahel (Biasutti et al. 2009; Lavaysse et al. 2010, 2016; Engelstaedter et al. 2015; Evan et al. 2015).

This study is carried out in two distinct parts. Firstly the S^{4}CAST model (see section 7) is applied to assess the non-stationary teleconnection between Mediterranean SSTA and Sahel rainfall (section 9.2). This link is found to comply with the results obtained in previous sections for the same teleconnection (see section 8.2.1), taking into account that different databases have been used herein. Then, the statistical results from the S^{4}CAST application are treated as working hypothesis to design a set of numerical experiments (section 9.3). The results of this section are included in Suárez-Moreno et al. (2017b).

9.1 Observational data

Regarding SST, Extended Reconstructed Sea Surface Temperature (ERSST v3b) has been used. Precipitation data corresponds to high-resolution monthly values from the Climatic Research Unit (CRU). These databases are described in section 5.1.

9.2 Statistical approach with the S^{4}CAST model

In the same way that has been shown in previous sections, the S^{4}CAST is used here to construct a preliminary hypothesis on the existence of the non-stationarity in the Mediterranean-Sahel interannual teleconnection. This hypothesis is used later to define a series of numerical experiments to be conducted with the LMDZ model.

As mentioned, the changes in the Mediterranean SST-forced response of Sahel rainfall are studied by applying the S^{4}CAST model. In this way, the study period is set to July-August-September (JAS) regarding both Mediterranean SSTA and anomalous Sahel rainfall, coinciding with the maximum activity of the monsoon season in West Africa. The anomalies are calculated with reference to the climatology of the observational 1902-2013 record. The decadal-to-multidecadal variability is removed from the time series of both anomalous fields by applying a high-pass Butterworth filter (cutoff frequency > 2/7 years^{-1}). A first MCA is applied by selecting the leading MCA mode. Next, 21-years delayed sliding window correlation is applied in order to compute **COI** (see section 7.2), thus determining two periods significantly correlated (SC_1 and SC_2) and a non-significant period (NSC). From these periods the model calculates cross-validate hindcasts for each one separately by using the leave-one-out method (see section *6.2.1.2*). In order to examine the predictability, the model provides co-variability patterns in terms of regression maps and time-series of the expansion coefficients. The skill-score of the model is assessed between cross-validated hindcasts and observations by means of Pearson correlation coefficients (see section *6.2.1.2*). The level of statistical significance has been set here at 95%, and it is assessed by the Monte Carlo method (see section 6.3.2).

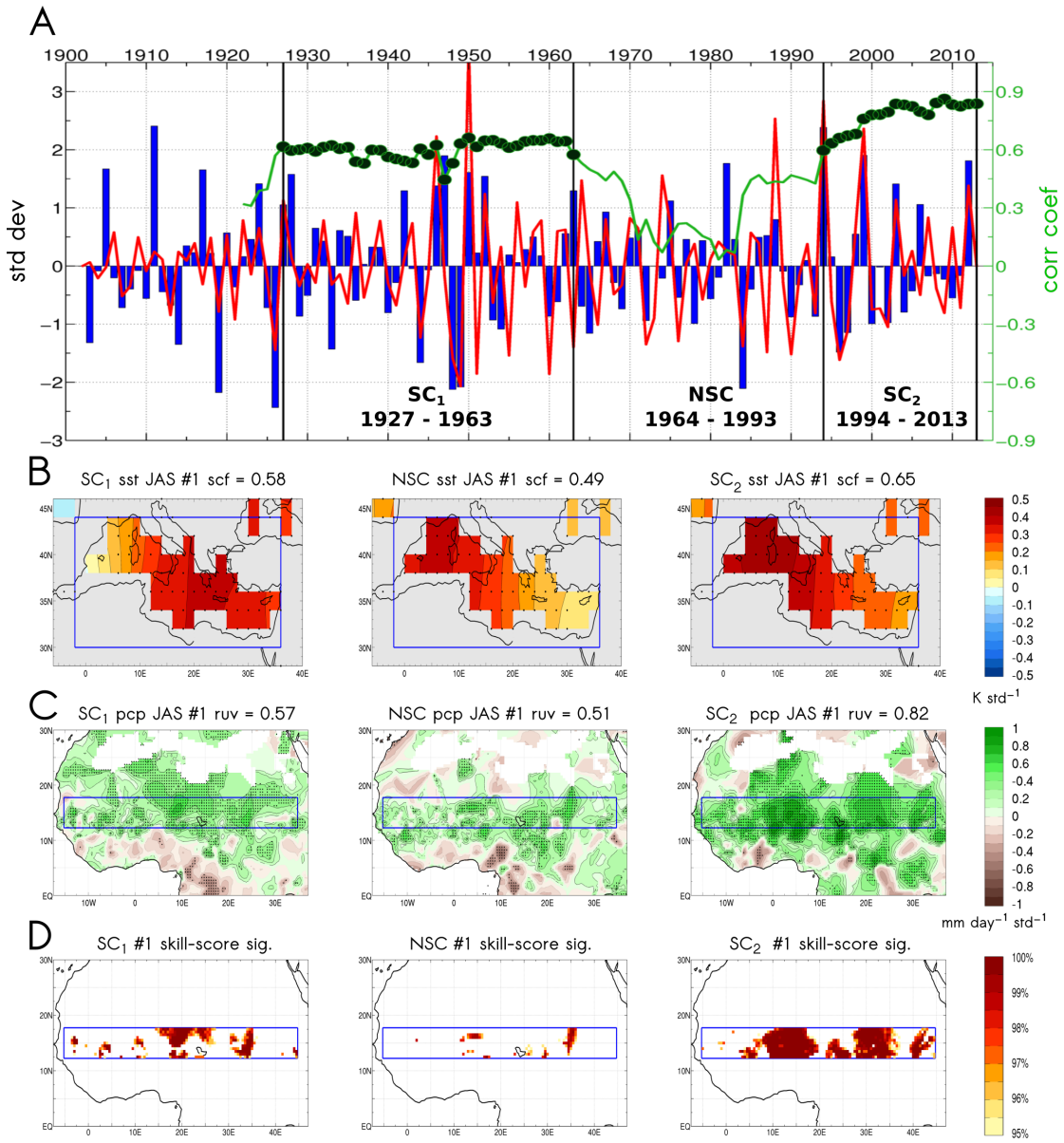

Fig. 9.1. July-to-September (JAS) leading MCA mode calculated from Mediterranean SSTA defined in 2ºW-36ºE; 30ºN-44ºN and standardized anomalous Sahel rainfall defined in 15ºW-35ºE; 12ºN-18ºN. (A) Time series of the standardized expansion coefficients for SSTA (U, blue bars) and anomalous rainfall (V, red line) corresponding to the whole 1902-2013 period (values on the left vertical axis). 21-years (for each year and the previous twenty) sliding window correlation scores between U and V (green line) and corresponding statistically significant values (green shaded circles) (values on the right vertical axis). From this figure, three different periods are identified: the first significant correlation period (SC_1, 1927-1963), a non-significant correlation period (NSC, 1964-1993) and the second significant correlation period (SC_2, 1994-2013). (B) Homogeneous SSTA (K std^{-1}) maps calculated by regressing U onto the Mediterranean SSTA. (C) Heterogeneous anomalous rainfall (mm day^{-1} std^{-1}) maps obtained by regressing U onto regional anomalous Sahel rainfall (D) Skill-score in terms of Pearson correlation coefficient score between cross-validated hindcasts and observations for anomalous rainfall in the Sahel. Shaded values denote the significance level (%) in the regions of positive skill. From (B) to (C): Leading MCA mode and skill-score for SC_1 period (left column), NSC period (central column) and SC_2 (right column). The squared-covariance fraction (*scf*) and correlation between expansion coefficients (*ruv*) are shown in figure titles. Blue contoured boxes indicate the selected spatial domains in the MCA analysis. Stippling denotes statistical significance at 95% assessed using the Monte Carlo method (1000 permutations). (From Suárez-Moreno et al. 2017b).

It is found that the interannual Mediterranean-Sahel teleconnection pattern varies according to SC_1 (1927-1963), NSC (1964-1993) and SC_2 (1994-2013) (Fig. 9.1*A*). For the three periods, the leading MCA mode exhibits a widespread warming over the Mediterranean (Fig. 9.1*B*) accompanying positive rainfall anomalies in the Sahel (Fig. 9.1*C*), the signal being stronger for SC_1 and SC_2 compared to NSC. The robustness of the impact associated with this changing teleconnection is further assessed by the model skill to reproduce the observed rainfall (Fig. 9.1*D*), the skill-score (see section *6.2.1.2*) improving for those periods of significant correlation (SC_1 and SC_2). Results for the extended period (1902-2013) are consistent with the co-variability patterns aforementioned (Fig. 9.2).

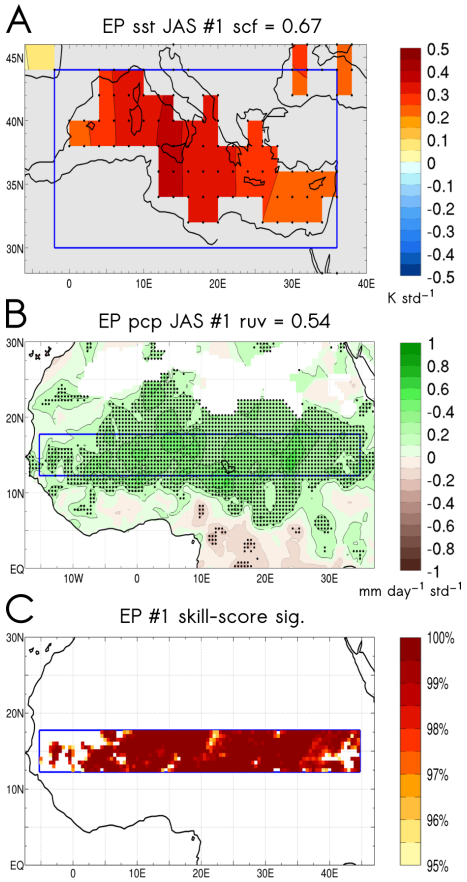

Fig. 9.2. July-to-September (JAS) leading MCA mode for the extended 1922-2013 period between Mediterranean SSTA defined in 2ºW-36ºE; 30ºN-44ºN and standardized anomalous Sahel rainfall defined in 15ºW-35ºE; 12ºN-18ºN. (A) Homogeneous SSTA (K std^{-1}) map calculated by regressing U (see Fig. 9.1*A*) onto the Mediterranean SSTA. (B) Heterogeneous anomalous rainfall (mm day^{-1} std^{-1}) map obtained by regressing U onto anomalous Sahel rainfall. (D) Skill-score in terms of Pearson correlation coefficient between cross-validated hindcasts and observed anomalous Sahel rainfall. Shaded values denote the significance level (%) in the regions of positive skill. The squared-covariance fraction (*scf*) and correlation between corresponding expansion coefficients (*ruv*) are shown in figure titles. Blue boxes indicate the selected spatial domains in the MCA analysis. Stippling denotes statistical significance at 95% assessed by the Monte Carlo method (1000 permutations). (From Suárez-Moreno et al. 2017b).

9.3 Numerical experiments with the LMDZ model

The identification of those well-defined multidecadal periods (SC_1, NSC, SC_2) set in the statistical hypothesis, during which the interannual impact of the Mediterranean on the Sahel shifts from weak to strong, suggests the possibility of a large-scale modulation of the teleconnection. In this way, the multidecadal SST variability is hypothesized to be a key factor, modulating the impact of a warm Mediterranean event on the monsoonal rainfall in the Sahel. To verify this, we conduct a set of numerical experiments with the LMDZ AGCM (see section 5.2.1).

In this study, the LMDZ model (section 5.2.1) runs on a regular grid at 2.50°×1.27° longitude-latitude resolution, with 19 vertical levels. Each experiment consists of 20 members, initialized on the 1 January, from 1980 to 1999. Aerosol concentration is prescribed, imposing the 1860-1870 climatology for the natural aerosols and the 1995-2005 climatology for anthropogenic emissions. Solar constant is set at the present day value (1366 W/m2) and the CO2 concentration is set at the year 2000 value (369 ppm). Vegetation in ORCHIDEE is not interactive, and the PFTs map is set at the year 2000.

Each experiment consists of an ensemble of 20-year integrations, running from January to December and forced with prescribed climatological SST. Thereby, the ERSST data have been used. We first simulate the atmospheric response to globally prescribed SST climatology for the period 1922-2013, comprising SC1, NSC and SC2 (Fig. 9.3). This simulation is defined as the control experiment (CTL). Then, three simulations are conducted by prescribing climatological SST corresponding to the three periods statistically defined (see Fig. 9.1). Compared to CTL, SC_1 (1927-1963) exhibits warm anomalies in the North Atlantic and the North Pacific contrasting with cooler southern oceans, resulting in a northern-hemispheric differential warming. Conversely, NSC (1964-1993) is dominated by the cooling of the North Atlantic and the North Pacific, and a southern-hemispheric differential warming, predominating in the Atlantic sector. Lastly, SC_2 (1994-2013) is broadly dominated by the GW signal of recent decades.

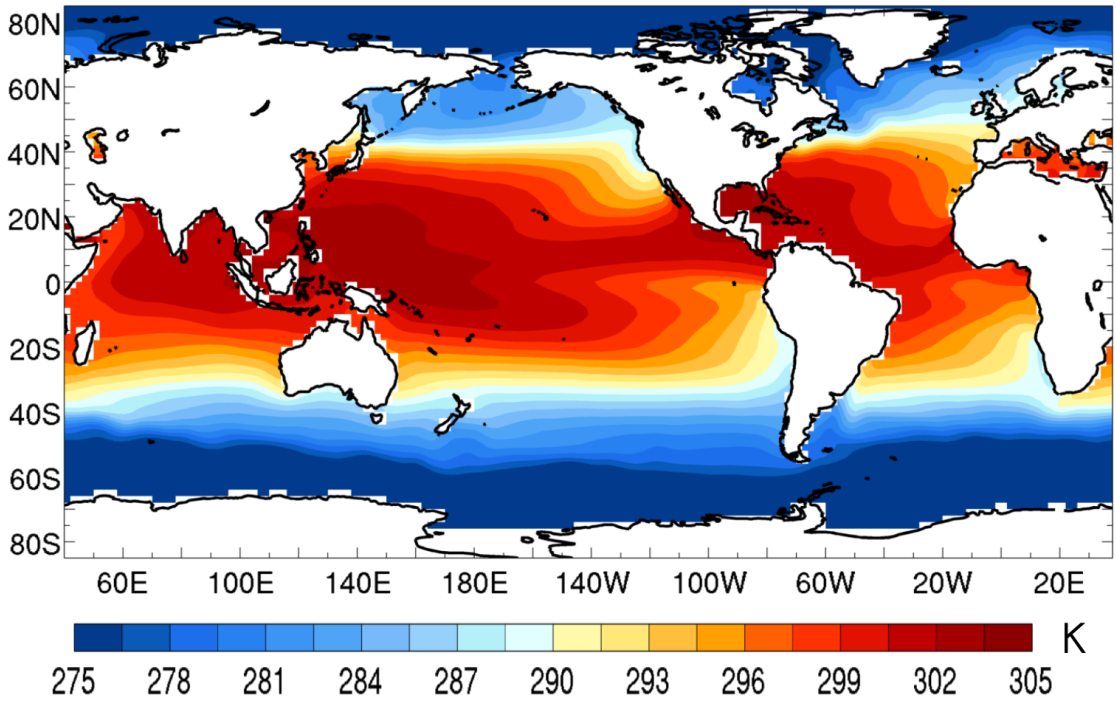

Fig. 9.3. Global climatological SST (1922-2013) prescribed in the CTL experiment. (From Suárez-Moreno et al. 2017b).

It is remarkable that, when comparing those periods in which the Mediterranean-Sahel link is statistically stronger (SC_1 and SC_2), the SSTA patterns are characterized by a warm SSTA in the North Atlantic. On the basis of this evidence, and to assess the impact of the stand-alone North Atlantic basin, we have implemented two additional simulations in which global SST climatology is prescribed as in CTL, and SSTA are solely superimposed in the North Atlantic. Therefore, additional simulations are defined a by North Atlantic warming (NAW) and a North Atlantic cooling (NAC) respectively. The NAW experiment is driven by the SST climatology of the CTL period (see Fig. 9.3), adding a warm anomaly limited to the North Atlantic (80ºW-40ºE; 25ºN-80ºN), obtained as the average SST climatology between SC_1 and SC_2, and excluding the Mediterranean Sea. In the NAC experiment, the North Atlantic cold anomaly added to the CTL climatology is obtained as the opposite of NAW. Table 9.1 contains information on the SST-forcing in all experiments.

To assess the climate sensitivity to interannual warming in the Mediterranean (hereinafter MED), we conduct a second set of experiments by adding to the climatological SST this warm SSTA in the Mediterranean (Fig. 9.4). The MED forcing is computed as 2 times the composite anomaly of the warm years in the Mediterranean, selected as those years exceeding 1 standard deviation in the time series of the CTL experiment (from Fig. 9.1*A*:

1928, 1942, 1946, 1947, 1950, 1952, 1963, 1975, 1982, 1994, 1999, 2003, 2006, 2012). In the following, climatological experiments refer to those simulations exclusively forced with SST climatologies (CTL, SC_1, NSC, SC_2, NAW and NAC), whereas sensitivity experiments are defined by the MED forcing superimposed to SST climatologies (CTL_{MED}, SC_{1MED}, NSC_{MED}, SC_{2MED}, NAW_{MED} and NAC_{MED}). A schematic description of the experiments is given in Table 9.2.

Table 9.1. Summary table on the definition of SSTA with respect to CTL

SSTA definition	SSTA pattern	SSTA key features
SC_1 = SST(SC_1) – SST(CTL)	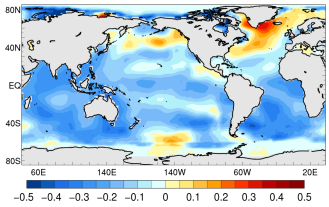	Warming in the North Atlantic Northern positive SST gradient
NSC = SST(NSC) – SST(CTL)	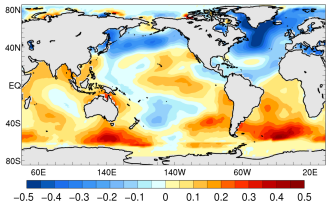	Cooling in the North Atlantic Southern positive SST gradient
SC_2 = SST(SC_2) – SST(CTL)	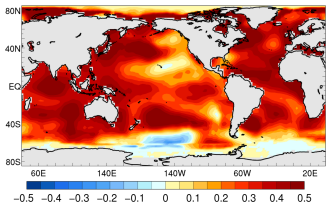	Atlantic inter-hemispheric SST gradient GW-like pattern
NAW = SST(NAW) – SST(CTL)	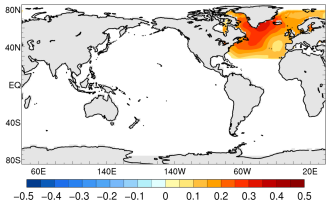	North Atlantic warming
NAC = -NAW	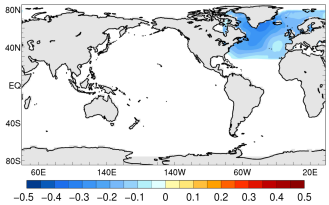	North Atlantic cooling

The first column shows SSTA with respect to CTL as defined in each climatological experiment. The second column displays SSTA (K) patterns in terms of July-to-September (JAS) means. A description of the main SSTA features is given in column 3. (From Suárez-Moreno et al. 2017b).

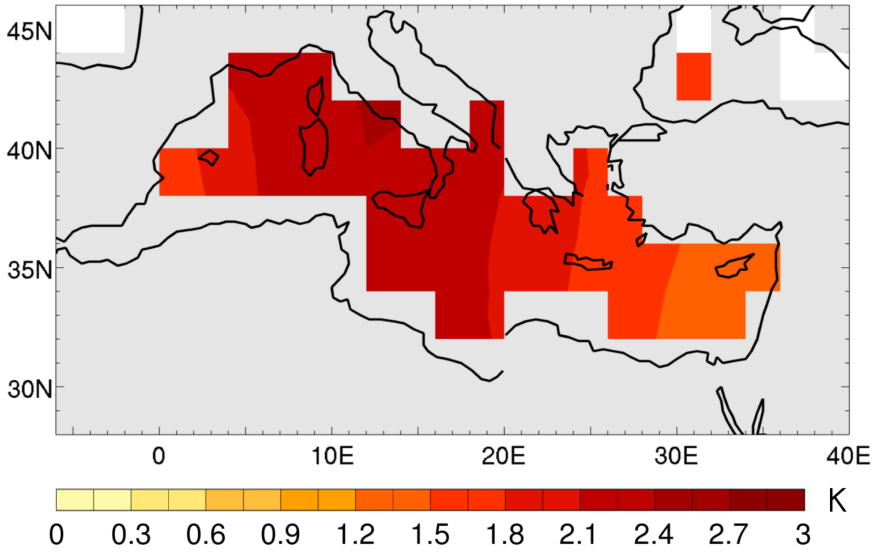

Fig. 9.4. Mediterranean SSTA used to prescribe a warm interannual event (MED) in sensitivity experiments. SSTA is computed as 2 times the composite anomaly of the warm years in the Mediterranean (see time series in Fig. 9.1*A*). Warm years are selected as those exceeding one standard deviation of the whole time series of the CTL period: 1928, 1942, 1946, 1947, 1950, 1952, 1963, 1975, 1982, 1994, 1999, 2003, 2006, 2012. (From Suárez-Moreno et al. 2017b).

Table 9.2. Summary table on the description of the experiments by prescribed SST

Experiment	Global SST climatology	North Atlantic SSTA	Mediterranean event (MED)
CTL	1922 – 2013		
SC_1	1927 – 1963		
SC_{1MED}	1927 – 1963		*warm*
NSC	1964 – 1993		
NSC_{MED}	1964 – 1993		*warm*
SC_2	1994 – 2013		
SC_{2MED}	1994 – 2013		*warm*
NAW	1922 – 2013	*warm*	
NAW_{MED}	1922 – 2013	*warm*	*warm*
NAC	1922 – 2013	*cold*	
NAC_{MED}	1922 – 2013	*cold*	*warm*

The first column shows the experiments as defined throughout the text. Climatological periods for prescribed SST are shown in column 2. The third column indicates idealized experiments with prescribed SSTA in the North Atlantic. The fourth column denotes sensitivity experiments where a warm Mediterranean event (MED) is superimposed on the SST climatologies. (From Suárez-Moreno et al. 2017b).

As expected, increased rainfall in the Sahel results from MED, whatever the underlying SST climatology is (Fig. 9.5, left column). Nevertheless, the precipitation response

enhances (weakens) in terms of intensity and spatial extension under a warmer (colder) North Atlantic. Indeed, for warmer North Atlantic scenarios (SC_{1MED}, SC_{2MED}, NAW_{MED}) the significant rainfall response to MED extends over the whole Sahel (Figs. 9.5*A*-9.5*E*-9.5*G*, left panels), while it is limited to the central and eastern regions (Figs. 9.5*C* and 9.5*I*, left panels) for cold scenarios (NSC_{MED}, NAC_{MED}). The different MED impact in the diverse periods is discussed in the context of the corresponding SST climatology (Fig. 9.5, central column). The SC_1 scenario, where the SSTA pattern resembles the positive phase of the AMV, is associated with an increase of rainfall in the Sahel (Fig. 9.5*A,* right panel). By contrast, in the NSC experiment, the SSTA pattern is almost opposite to the previous one, inducing a widespread decrease of rainfall over West Africa (Fig. 9.5*C,* right panel). These results are in line with previous studies that describe the impact of the AMV on the WAM, the negative phase underlying the Sahel big drought in the 70s-80s, whereas a positive AMV is related to increased rainfall (Martin et al. 2013; Martin and Thorncorft 2014; Knight et al. 2006; Shanahan et al. 2009). Moreover, there is a barely significant decrease in Sahel rainfall in response to the GW-like pattern in the SC_2 experiment, with a robust increase in the Guinea Gulf region instead (Fig. 9.5*E,* right panel). The southward shift of the precipitation belt is the response to the GW-induced stabilization of the tropical troposphere, which weakens the monsoonal circulation (Gaetani et al. 2016). The multidecadal evolution of the simulated precipitation, from SC_1 to SC_2 through NSC, shows the main features of the observed variability: namely, a wet period in the first half of the 20th century, the big drought in the 70s-80s, and the recent partial recovery (Figs. 9.5*A*-9.5*C*-9.5*E*, right panels). Noticeably, an isolated SST forcing in the North Atlantic, either NAW or NAC, does not cause a significant rainfall response in the Sahel (Figs. 9.5*G*-9.5*I*, right panels).

When comparing the MED impact in different periods, it is clearly stronger when associated with North Atlantic warm SSTA (SC_{1MED}, SC_{2MED}) than in NSC_{MED}, when the North Atlantic is colder (Figs. 9.6*B*-9.6*C*-9.6*E*-9.6*F*). The comparison between those periods sharing a North Atlantic warming (SC_{1MED} compared to SC_{2MED}) shows a stronger MED impact in the presence of an inter-hemispheric SSTA dipole, i.e. SC_{1MED} (Figs. 9.6*H*-9.6*I*). The positive contribution of MED to the Sahel precipitation is therefore non-linear, being dependent on the underlying SST climatology, specifically to the thermal anomalies in the North Atlantic and the inter-hemispheric SSTA dipole. In

all cases, the non-linear positive MED contribution is stronger on the eastern and central Sahel than on the western part (Figs. 9.6*B*-9.6*C*-9.6*E*-9.6*F*-9.6*H*-9.6*I*).

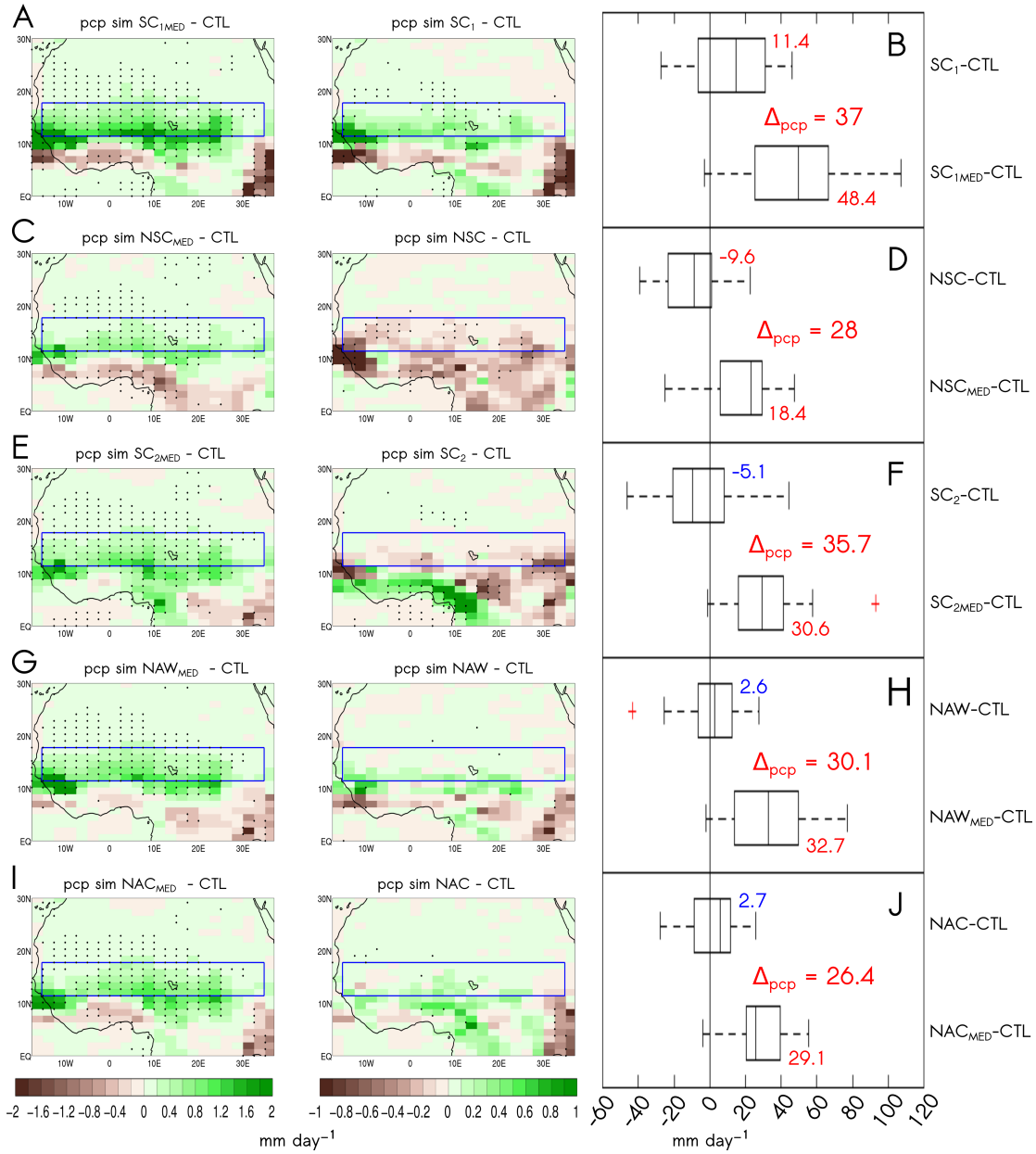

Fig. 9.5. Simulated differences in JAS rainfall response (mm day^{-1}) defined as twenty-member ensemble mean in each simulation minus twenty-member ensemble mean in CTL run (see Table 2). Left column: differences from sensitivity experiments. Central column: differences from climatological experiments. Right column: Box-plot of the anomalous amount of rainfall calculated by members in each simulation. Rainfall differences averaged in the Sahel (blue boxes) are shown beside each box-plot, along with the rainfall increase (Δ_{pcp}) associated with the MED forcing, calculated as the sensitivity minus climatological experiment. Values in red are statistically significant and non-significant values are shown in blue. Results are shown according to experiments: SC_1 (A and B), NSC (C and D), SC_2 (E and F), NAW (G and H), NAC (I and J). The level of statistical significance has been set at 90% under a t-test. (From Suárez-Moreno et al. 2017b).

Note that, under North Atlantic warm scenarios, the precipitation increase induced by MED forcing is stronger (Figs. 9.5*B*-9.5*F*-9.5*H*) compared to that resulting from the cold

scenarios (Figs. 9.5*D*-9.5*J*), suggesting that the North Atlantic warming is the key factor for the amplification of the Mediterranean impact on the Sahel. Moreover, chronologically, the transition SC_1-NSC-SC_2 is characterized by a significantly wet period of enhanced Mediterranean impact (Figs. 9.5*A*-9.5*B*), followed by a drought stage and a less marked effect of the Mediterranean (Figs. 9.5*C*-9.5*D*), ending with a period of reduced drought where the Mediterranean regains a more prominent role (Figs. 9.5*E*-9.5*F*).

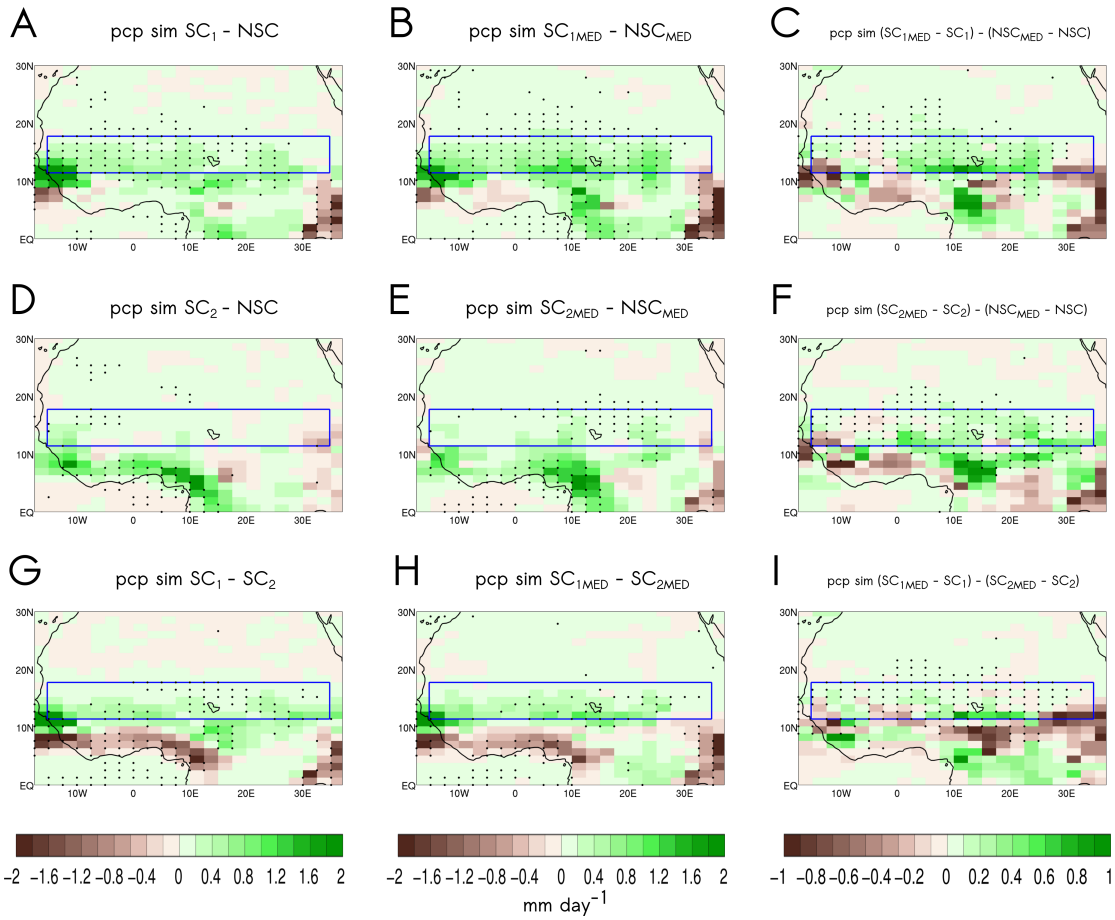

Fig. 9.6. Simulated differences in JAS rainfall response (mm day^{-1}) defined as twenty-member ensemble mean. Left column: differences from climatological experiments. Central column: differences in sensitivity experiments. Right column: non-linearity of the MED forcing when superimposed to different climatological experiments. Stippling denotes statistical significance. From (A) to (B): differences between SC_1 and NSC. From (D) to (F): differences between SC_2 and NSC. From (G) to (I): differences between SC_1 and SC_2. The level of statistical significance has been set at 90% under a t-test. (From Suárez-Moreno et al. 2017b).

In the climatological context, interdecadal variations in the location of the tropical rain belt are highly sensitive to the position of the ITCZ, which is in turn controlled by the underlying SSTA patterns. Consequently, we analyze the impact of the prescribed Atlantic SST climatology on the Atlantic branch of the ITCZ, which position is explored

by the minimum OLR at the top of the atmosphere (TOA), indicating high concentration of deep convective clouds (Fig. 9.7*B*). Atlantic SSTA profiles characterized by a warmer North Atlantic and a positive meridional slope (SC_1, SC_2, NAW) are associated with a northward displacement of the ITCZ, compared to those profiles with a colder North Atlantic and a negative slope (NSC, NAC) (Figs. 9.7A and 9.7*B*). Thus, the inter-hemispheric SSTA gradient sets the mean position of the ITCZ in the tropical Atlantic (Fig. 9.7C), where the precipitation belt shifts farther north under a positive south-north slope.

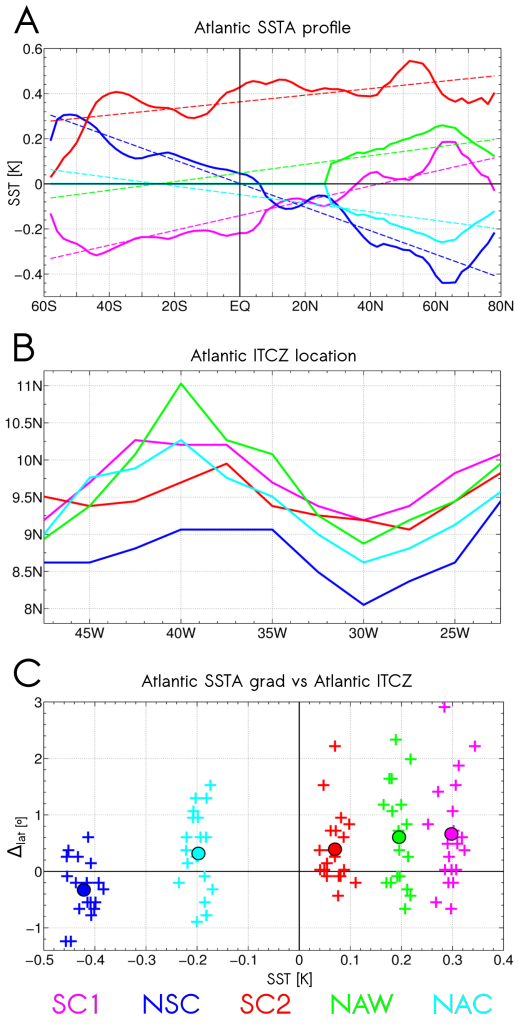

Fig. 9.7. JAS Atlantic SSTA latitudinal profiles and ITCZ location in the climatological experiments. (A) Atlantic SSTA latitudinal profiles averaged in 60°W-10°E. SSTA is defined as the difference between the SST prescribed in the climatological experiments and the CTL simulation. (B) ITCZ location over the tropical Atlantic determined as the position of the minimum outgoing long wave-radiation (OLR) at the top of the atmosphere (TOA). (C) Scatter-plot representing the ITCZ meridional deviation (Δ_{lat}) from the CTL simulation for each one of the 20 members versus the Atlantic inter-hemispheric SSTA gradient (defined as AIG = SSTA (60°W-20°W, 30°N-60°N) – SSTA (40°W-10°E, 30°S-EQ). Shaded circles represent the ensemble mean. Each color indicates an experiment: SC_1 (purple), NSC (blue), SC_2 (red), NAW (green), NAC (cyan). (From Suárez-Moreno et al. 2017b).

This confirms the global SSTA in general, and the Atlantic basin in particular, as the main factor to interpret the precipitation anomalies in the climatological experiments via the meridional displacement of the tropical rain belt. Noticeably, in SC_2, the positive SSTA gradient to the north leads to a northern ITCZ but dry anomalies in the Sahel (see Fig. 9.7*E*). This can be explained with the warming of the tropical Atlantic taking place in SC_2 but not in SC_1, which induces a widespread surface warming over West Africa that reduces the meridional temperature gradient over land (Fig. 9.8), keeping the precipitation belt on the coast (Gaetani et al. 2016).

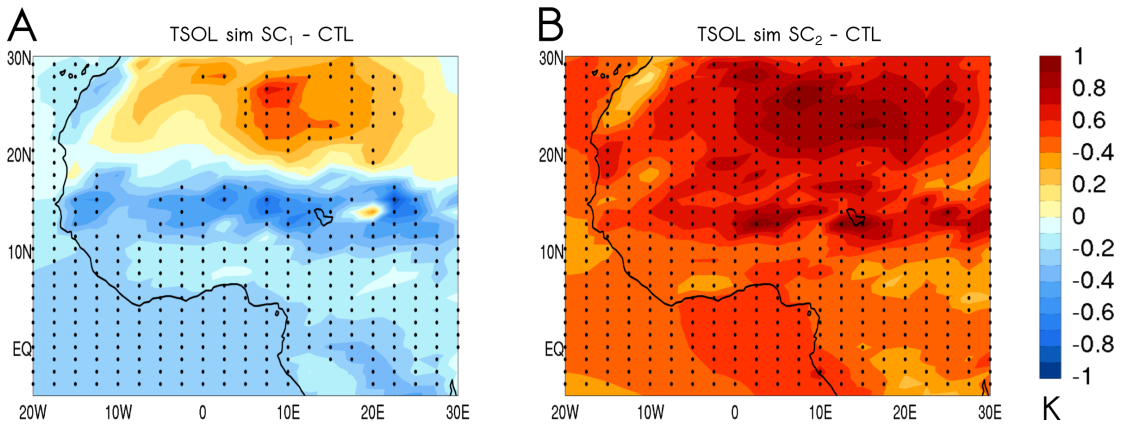

Fig. 9.8. Simulated differences in JAS surface temperature (TSOL, K) defined as twenty-member ensemble mean in each simulation minus twenty-member ensemble mean in CTL run. Differences are shown from climatological experiments corresponding to SC_1 (A), SC_2 (B). Stippling denotes statistically significant values at 90% under a t-test. (From Suárez-Moreno et al. 2017b).

To understand the underlying dynamics, the low-level atmospheric thickness and moisture flows are explored in response to different SST climatologies (Fig. 9.9, left column). A lobe of positive anomalous low-level atmospheric thickness appears over the Sahara, indicating a strengthening of the SHL (Lavaysse et al. 2009). Interestingly, the strongest SHL anomalies are simulated in those experiments defined by a warmer North Atlantic (SC_1, SC_2, NAW), in which the associated enhanced cyclonic circulation in the lower troposphere favors a moisture flux from the subtropical North Atlantic into the Sahel (Lavaysse et al. 2010). In two of these three cases (SC_1, NAW), the southwesterly monsoon flow is also strengthened, converging in the Sahel with the northwesterly flow (Figs. 9.9*A*-9.9*G*). In the remaining case (SC_2), the SST warming in the tropical Atlantic weakens the meridional temperature gradient (Fig. 9.8*B*), significantly reducing the southwesterly inflow. However, dry conditions in the Sahel are dampen by the enhanced moisture supply associated with the climatological warming of the Mediterranean (Fig.

9.9*E*, see also the SSTA pattern in Table 9.2). Consistently, negative sea level pressure (SLP) anomalies result from the reinforced SHL (Figs. 9.10*A*-9.10*C*-9.10*D*).

On the contrary, the strengthening of the SHL weakens under a North Atlantic cooling (NAC), with no significant moisture flux anomalies associated, and no alterations in the southwesterly monsoon flow (Fig. 9.9*I*). This idealized experiment illustrates that, under a negative AMV-like pattern (NSC), the SHL signal vanishes and the associated moisture transport is not redirected into the Sahel, thus preventing convergence with the southwesterly monsoon flow (Fig. 9.9*C*). Noticeably, for these scenarios (NSC, NAC), the key factor lies in the anomalous SLP pattern over the North Atlantic, which resembles a multidecadal strengthening of the positive North Atlantic oscillation (NAO) (Figs. 9.10*C*-9.10*I*). Accordingly, the associated anticyclonic anomaly in the subtropical North Atlantic results in a weakening of the moisture flux into West Africa.

In all sensitivity experiments, the atmospheric response to MED exhibits a strengthening of the SHL, an anomalous cyclonic circulation encircling the Mediterranean and the Sahara, accompanied by enhanced low-level moisture transport from the subtropical North Atlantic into the Sahara, and a reinforced southwesterly monsoonal flow (Fig. 9.9, right column). Moreover, the circulation pattern described above intensifies under a warmer North Atlantic (SC_{1MED}, SC_{2MED}, NAW_{MED}), where the low-level cyclonic circulation associated with the MED forcing is amplified, extending more into Europe and the subtropical North Atlantic (Figs. 9.9*B*-9.9*F*-9.9*H*). Fed by the moisture flux, the SHL dry convection is thus strengthened (Gaetani et al. 2010; Evan et al. 2015), as well as the associated cyclonic circulation, which in turn reinforces the westerly flow from the tropical Atlantic into the Sahel. Conversely, for cooling scenarios in the North Atlantic (NSC_{MED}, NAC_{MED}), the occurrence of a positive NAO-like pattern induces an atmospheric blocking located over the Atlantic offshore western Europe, inhibiting the expansion of the low-level cyclonic circulation associated with the MED forcing. Under these conditions, the moisture transport into the SHL is reduced, with no additional inflow from the subtropical North Atlantic, and the intensification of the SHL convection is limited (Figs. 9.9*D*-9.9*J*).

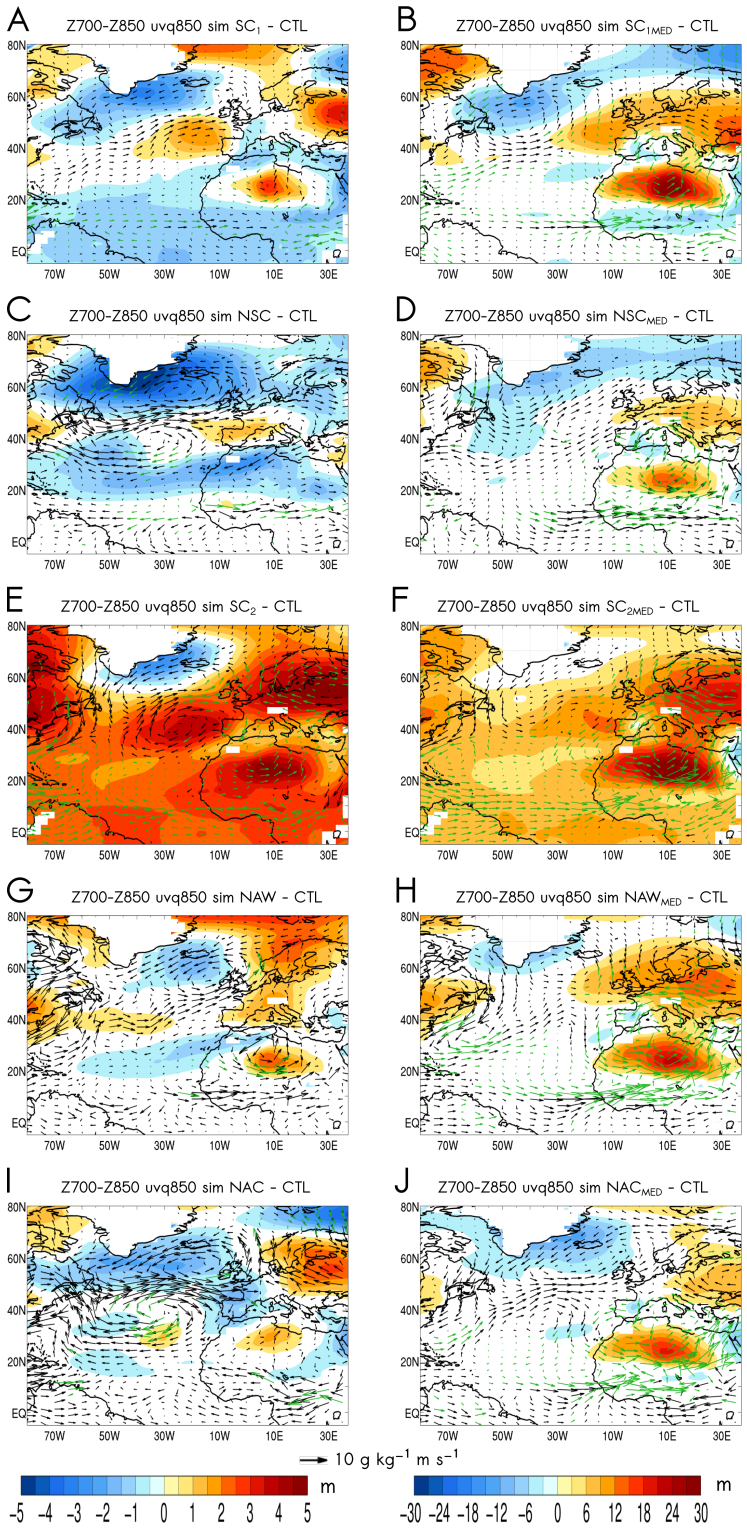

Fig. 9.9. Simulated differences in JAS low-level atmospheric thickness (m) and moisture transport (g kg m s^{-1}) defined as twenty-member ensemble mean in each simulation minus twenty-member ensemble mean in the CTL run (see Table 9.2). The atmospheric thickness in low levels (shaded) is calculated as the difference between geopotential heights at 700 and 925 hPa (Z700-Z925). The moisture transport at 925 hPa (uvq925, vectors) is shown through its zonal and meridional components (u925*q925 and v925*q925 respectively). Left column: differences from climatological experiments. Right column: differences from sensitivity experiments. Results are shown according to experiments: SC_1 (A and B), NSC (C and D), SC_2 (E and F), NAW (G and H), NAC (I and J). Shaded values and green vectors are statistically significant at 90% under a t-test. (From Suárez-Moreno et al. 2017b).

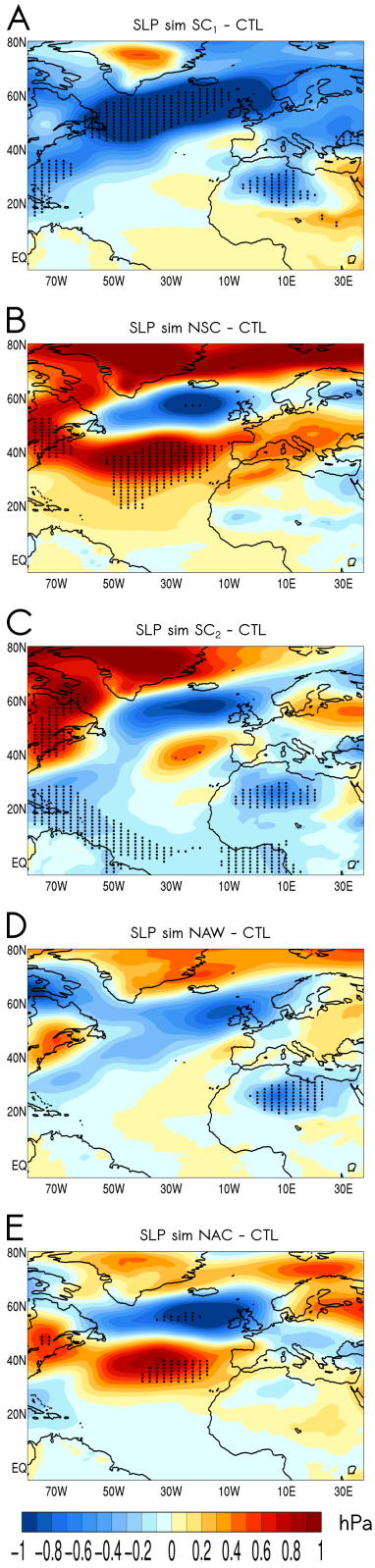

Fig. 9.10. Simulated differences in JAS sea level pressure (SLP, hPa) defined as twenty-member ensemble mean in each simulation minus twenty-member ensemble mean in CTL run. Differences from climatological experiments corresponding to SC_1 (A), NSC (B), SC_2 (C), NAW (D), NAC (E). Stippling denotes statistically significant values at 90% under a t-test. (From Suárez-Moreno et al. 2017b).

9.4 Discussion

The mechanism by which warm (cold) anomalies in the Mediterranean are related to increased (decreased) rainfall in the Sahel has been widely described (Rowell 2003; Jung et al. 2003; Fontaine et al. 2010; Gaetani et al. 2010). More recently, the anthropogenic Mediterranean warming has been presented as an essential driver for present and future Sahel rainfall (Park et al. 2016). Nevertheless, changes in the impact of the Mediterranean on the Sahel over the last 100 years have been barely suggested (Fontaine et al. 2011a; Rodríguez-Fonseca et al. 2011). Therefore, the underlying causes of instability in the Mediterranean-Sahel link have been overlooked up to now.

Here, it is shown that multidecadal variability of SST plays a pivotal role in switching on the Mediterranean-Sahel teleconnection. Statistical-observational analysis reveals that, given a warm event in the Mediterranean, the rainfall response in the Sahel changes depending on the decades under study. Indeed, from the beginning of the 20th century, three periods are identified. Namely, during SC_1 (1927-1963) and SC_2 (1994-2013) the impact was significant, being weaker during NSC (1964-1993).

Evidence is shown on how the underlying SST climatology in the North Atlantic is the leading factor to enhance or weaken the Mediterranean impact on the Sahel by means of a three-stage process. Firstly, the multidecadal SST variability determines the climatological position of the ITCZ and therefore the tropical rain belt. Secondly, North Atlantic SSTA is able to induce a blocking-type mechanism that interacts with the cyclonic low-level moisture transport from the Mediterranean. Lastly, the water vapor transported over the Sahara leads to a greenhouse effect, determining the intensity of the SHL, which in turn impacts convergence in the Sahel with the southwesterly monsoon flow.

The multidecadal SST variability affects the general atmospheric circulation. The experiments conducted in this work have shown that changes in the Atlantic branch of the ITCZ and associated rainfall in West Africa are strongly influenced by the underlying climatological SSTA (Fig. 9.5, central column and Fig. 9.6), particularly by that on the North Atlantic. Thus, under a well-defined inter-hemispheric Atlantic SSTA gradient (SC_1 and NSC), the rain belt is located northward (southward) when the gradient is

positive (negative) to the north, resulting in a significantly wetter (drier) Sahel. These results are consistent with those found in previous studies on the AMV impact on the WAM (e.g., Chiang and Friedman 2012; Martin and Thorncroft 2014). Moreover, meridional shifts of the ITCZ are less pronounced under a weakening of the inter-hemispheric Atlantic SSTA gradient (NAW, NAC), with no significant rainfall response observed in the Sahel. In relation to a GW-like SSTA pattern (SC_2), maximum rainfall moves equatorward, being consistent with the GW signature in the WAM (e.g., Gaetani et al. 2016).

Beyond the influence of the AMV on Sahel rainfall via the ITCZ, we find alterations in the SHL intensity linked to North Atlantic SSTA (Fig. 9.9, left column). Specifically in SC_2, a warmer Mediterranean enhances the low-level moisture, accompanying a cyclonic anomaly, which is added to the westerly flow from the tropical Atlantic inland (Fig. 9.9*E*). This input of water vapor leads to enhanced greenhouse effect and warming over the Sahara, resulting in an intensification of the SHL (Evan et al. 2015). Consequently, this warming of the Mediterranean dampens the GW-driven drying of the Sahel via increased low-level moisture, which is transported by the mean flow across the Sahara to the south, in turn strengthening the SHL. This scenario takes place after a consistent drought period (NSC), supporting the theory that the anthropogenic warming of the Mediterranean is playing a relevant role in the recent positive trend of rainfall in the Sahel (Park et al. 2015). Surprisingly, the SHL and associated moisture transport appear to be strengthened even under attenuated (SC_1) or absent (NAW) warming in the Mediterranean (see Table 9.1 and Figs. 9.9*A* and 9.9*G*), highlighting the pivotal role of a warmer North Atlantic in the reinforcement of the SHL. Conversely, a colder North Atlantic (NSC, NAC) promotes the weakening of the SHL and associated moisture supply to the Sahel (Figs. 9.9*C*-9.9*I*).

Whatever the underlying SST climatology, when an anomalously warm event occurs in the Mediterranean, Sahel precipitation significantly increases (Fig. 9.5, left column). Nevertheless, the rainfall response to MED enhances under warm scenarios in the North Atlantic (Figs. 9.5*A*-9.5*E*-9.5*G*). In these cases, the cyclonic circulation associated with the Mediterranean forcing enlarges, advecting the additional moisture available in the subtropical North Atlantic into West Africa. Thus, these warm scenarios induce a strengthening of the SHL, which is in turn reinforced by the warming of the

Mediterranean (Figs. 4*B*-4*F*-4*H*). In other words, when MED occurs under a warmer North Atlantic, the moisture transport into West Africa is fed from both the Mediterranean and the subtropical North Atlantic, causing an intensification of the SHL that fosters a wetter Sahel. By contrast, this situation does not occur under a colder North Atlantic. A mechanism is evidenced by which, under cooling scenarios in the North Atlantic (NSC, NAC), a strengthening of the positive North Atlantic oscillation (NAO)-like pattern generates a blocking-type mechanism associated with the reinforcement of the Azores High (Figs. 9.10*C*-9.10*I*). This kind of atmospheric blocking over the North Atlantic, mainly influences the circulation over the upper ocean by affecting wind patterns (Häkkinen et al. 2011). In this context, the enhanced cyclonic moisture flow associated with MED is inhibited, weakening the northwesterly moisture input from the subtropical North Atlantic, in turn reducing the intensification of the SHL (Figs. 9.9*D*-9.9*J*). Therefore, whether warm or cold SSTA are present in the North Atlantic, the role of the SHL is demonstrated to be overriding in driving moisture flux across the Sahara, thus affecting convection over the Sahel.

CHAPTER X

10 Concluding remarks

The main conclusions of this thesis as well as the potential lines of future work are addressed in this section.

10.1 Main conclusions

In the same way that the objectives are presented (see section 3), the conclusions of this thesis can be posed in a logical order:

1. The **S^{4}CAST model** has been designed and created as **a tool to conduct predictability studies** based on **the potential influence of changes in SST on teleconections.** The model is based on Maximum Covariance Analysis **methodology** and isolate co-variability coupled patterns in climate for different frequencies and regions. S^{4}CAST evaluates potential **instabilities in teleconnections**, being this the main novelty of this statistical tool. These instabilities are understood in terms of **non-stationary links** between a predictor field (SST) and a particular variable to be predicted (e.g., Sahel rainfall). The SST-forced teleconnections can be studied along the observational record in order to analyze whether the impacts associated with a given oceanic predictor have changed (non-stationary) or remain unaltered (stationary). Under non-stationarity conditions, the model analyzes the changes in teleconnections and the consequent **implications in predictability**. S^{4}CAST performs a hindcast of the variable to be predicted for the different considered periods, evaluating its potential predictability. Finally, the model has been configured for providing forecast with different lead times and forecast times.

2. A **benchmarking** carried out with the S^{4}CAST model confirms the use of this tool for evaluating predictability and associated regimen shifts. In particular, both, the change in **the influence of ENSO on Euro-Mediterranean rainfall** and the change in the **impact of tropical Atlantic SSTA on ENSO** have been reproduced using this tool.

3. **S^{4}CAST model** has been used to **study the SST-forced teleconnections with Sahelian rainfall**, and to pose the **working hypotheses** leading to the results obtained in this thesis.

4. The leading modes of co-variability between SSTA and Sahel rainfall have been computed using the S^{4}CAST model, and their fluctuations on time have been assessed with the S^{4}CAST. The model has been applied for those ocean regions with a strong impact on the Sahel at interannual timescales: **Mediterranean sea**, **tropical Atlantic** and **tropical Pacific**. Enhanced impacts are detected during some periods (named as SC) compared to others (named as NSC).

5. The non-stationarities in SST-Sahel rainfall teleconnections have been validated for the first time using **a network of in-situ rainfall measurements**, confirming the presence of periods for which the teleconnections are enhanced in terms of a more robust rainfall response.

6. The atmospheric dynamics associated with the forcing of each of the ocean predictors and for each of the stable periods has been analyzed. For each ocean basin, the key findings are, in summary:

    - **Mediterranean.** The periods with enhanced impacts (SC) are characterized by a strong, widespread SST warming (cooling) of the Mediterranean, with no significant remote SSTA signals. Under these conditions, the classic teleconnection mechanism **relates a warming (cooling) of the Mediterranean with** increased (decreased) rainfall in the Sahel. This effective impact is disrupted in some other periods (NSC) when a cold (warm) SST anomaly over the eastern North Atlantic coast accompanies the

Mediterranean warming (cooling), counteracting the classic teleconnection mechanism by influencing the ITCZ location.

- **Tropical Atlantic.** Strong teleconnections (SC) are identified relating the Atlantic Equatorial mode with a Sahel-Guinean Gulf rainfall dipole. The mechanism is explained by a strong (weak) land-ocean temperature and pressure gradient that shifts northward (equatorward) the ITCZ. The teleconnection is disrupted in recent decades (NSC), when a counteracting effect appears from opposite-sign SST anomalies in the tropical Pacific.

- **Tropical Pacific.** The teleconnection is characterized by a significant SST warming (cooling) in the tropical Pacific, inducing decreased (increased) rainfall over the Sahel. This is due to enhanced (weakened) subsidence in response to alterations of the upper-level Walker circulation from a Gill-Matsuno type response. The rainfall response is stronger in recent decades (SC), a feature that could be in part related to and increase in the SSTA amplitude compared to the remaining decades (NSC).

7. **It has been found how changes in the climatological SST background at multidecadal timescales can modulate the interannual teleconnections**. Thus, the SST climatology induces alterations in the atmospheric circulation which in turn interacts with the underlying dynamics associated with each interannual teleconnection. In this context, three different periods are found during which distinct teleconnections are enhanced:

   - **A first period (1942-1964)** dominated by a **positive AMO-like** pattern that promotes a northward shift of the ITCZ and associated wetter conditions in the Sahel. Under this scenario, the teleconnections from **tropical Pacific and Mediterranean** are fostered.

   - **A second period (1965-1987)** during which the **AMO turns into its negative phase**, mostly dominating the multidecadal SST variability. Consequently, the southern-hemispheric SST gradient induces the equatorward position of the ITCZ, favoring tropical teleconnections

associated with **tropical Atlantic and Pacific** basins. The Mediterranean influence on the Sahel becomes unsignificant.

- **A third period (1988-2010)** along which the **global SST warming and positive Atlantic Multidecadal Oscillation** promote the interannual teleconnection from the **Mediterranean**. On the one hand, the SST gradient shifts the ITCZ northward, whereas de GW component dampens this shift to the north as a response to the GW-induced stabilization of the tropical troposphere. Morover, wetter conditions in the Sahel are related to the anthropogenic warming of the Mediterranean, which in turn enhances the rainfall response to an interannual warm event.

8. Observations reveal that the interannual impact of the **Mediterranean is found to prevail over tropical oceans** during recent decades and in the 1942-1964 period, playing this basin a major role in the projected Sahel rainfall variability. This trend has been linked to the underlying GW signal and positive phases of the AMO, both being connected by a **warmer North Atlantic inducing a northward shift of the ITCZ. The results** put forward that the ocean modeling of this basin together with the Mediterranean becomes crucial to improve the seasonal forecast of rainfall in the Sahel.

9. **Sensitivity experiments** with an atmospheric general circulation model reveal a clear **dependence between the multidecadal SST variability in the North Atlantic and the year-to-year impact of the Mediterranean on the Sahel**. Concretely, it is described how under **warming scenarios in the North Atlantic** related either to the positive AMO, the GW, or both, **the impact of a warm Mediterranean event on the Sahel is amplified**, substantially increasing rainfall. Furthermore, the GW trend of recent decades underlies the strongest impact from the Mediterranean. Thus, **the inter-hemispheric SSTA gradient** becomes crucial for present and future Sahel rainfall. Specifically, the SSTA gradient in the Atlantic basin **modulates the position of the ITCZ** within West Africa, defining the impact from a warm Mediterranean, which in turn is boosted by the anthropogenic warming.

The results from this thesis imply **an advance in the seasonal predictability of rainfall in the Sahel**, determining the decades in which the different ocean basins are key predictors of anomalous rainfall in the region. The position of the climatological ITCZ in each of the periods determines the prevalence of particular dynamics in the increase of rainfall variability. In fact, when the **North Atlantic SST is anomalously warm, the Mediterranean becomes a confident predictor** for the Sahel rainy season. Accordingly, in the perspective of a future warming of the North Atlantic and the Mediterranean, the ocean modeling of the latter will be crucial to provide a reliable forecast of rainfall in the Sahel.

10.2 Future work

The results of this thesis represent a step forward in the study of interannual rainfall variability and predictability in the Sahel. Nevertheless, reaching a consensus on the reasons for the non-stationary behavior of the links between Sahel rainfall and global SSTA becomes a difficult task that has not been successfully addressed so far. Such non-stationarities could be attributed to different causes.

Multidecadal variability of the ocean implies changes in the teleconnection patterns, which in turn can enhance interactions in some periods and not in others. For example, the counteracting effects between different oceanic forcing, operating at the same time in some periods, but not in others, are partly responsible for these instabilities. But, without any counteracting effect, the different configuration of the general circulation under different differential warming of the global oceans, implies changes in the location of the ITCZ and, thus, of the west African monsoon.

From the original hypothesis and results achieved during this thesis, a future work strategy is raised:

- To use the statistical seasonal forecast model (S^4CAST) for analyzing the optimum forecast lead-time of each oceanic predictor, trying to produce an operational forecast tool. In this context, the S^4CAST has served to provide results that have already been included in a **Forecasters´ Handbook for West**

Africa (see Colman et al. 2017).

- To further explore the role of the ocean SST background in changing the teleconnections and other potential causes that could determine the equatorward shift of the ITCZ. In particular, the role of the extratropical non-linear dynamics associated with changes in the Ferrell circulation and, thus, on the global circulation will be explored. Also, the role of changes in the Atlantic Meridional Overturning Circulation (AMOC) on abrupt shifts of the ITCZ and, therefore, on global SST-forced teleconnections will be analyzed. Finally, the role of extratropical SST warming (cooling) associated with the increase (decrease) in cloudiness (see Mechoso et al. 2015) will be also addressed.

- To analyze the IPCC GCM CMIP5 PI-control simulations, historical simulations and those associated with future scenarios with the aim of relating the bias in climate models with the multidecadal modulation of the teleconnections found in this thesis.

- To extend the analysis done with AGCM sensitivity experiments for the Mediterranean to the tropical Atlantic and tropical Pacific oceans. Thus, a warming or cooling over the Atlantic will be imposed. In this context, the simulations performed by López-Parages et al. (2016) for different types of El Niño configurations and different climatological backgrounds, will be use to further explore fluctuations in ENSO teleconnections.

List of publications

The results presented throughout this thesis are partially or totally reflected in the following publications:

- **Suárez-Moreno R** and Rodríguez-Fonseca B (2015) S^4CAST v2.0: sea surface temperature based statistical seasonal forecast model. Geoscientific model development 8 (11) 3639-3658.

- Rodríguez-Fonseca B, **Suárez-Moreno R**, Ayarzagüena B, López-Parages J, Gómara I, Villamayor J, Mohino E, Losada T and Castaño-Tierno A (2016) A review of ENSO influence on the North Atlantic. A Non-Stationary Signal. Atmosphere 7(7), 87.

- Colman A, Rowell D, Foamouhoue AK, Ndiaye O, Rodríguez-Fonseca B, **Suárez-Moreno R**, Yaka P, Parker DJ and Diop-Kane M (2017) Seasonal Forecasting in Meteorology of Tropical West Africa: The Forecasters' Handbook (eds D. J. Parker and M. Diop-Kane), John Wiley & Sons, Ltd, Chichester, UK.

- **Suárez-Moreno R**, Rodríguez-Fonseca B, Barroso JA and Fink AH (2017a) Interdecadal changes in SST-driven teleconnections with Sahel rainfall. Dynamical factors and implications in predictability (submitted)

- **Suárez-Moreno R**, Rodríguez-Fonseca B, Gaetani M and Flamant C (2017b) The North Atlantic Key role in driving the Mediterranean impact on the Sahel (submitted)

Acronym Index

H

I

J

L

M

N

O

P

S

T

U

W

References

Adam O, Bischoff T and Schneider T (2016) Seasonal and Interannual Variations of the Energy Flux Equator and ITCZ. Part II: Zonally Varying Shifts of the ITCZ. Journal of Climate 29 20 7281-7293

Adam O, Bischoff T and Schneider T (2016) Seasonal and Interannual Variations of the Energy Flux Equator and ITCZ. Part I: Zonally Averaged ITCZ Position. Journal of Climate 29 9 3219-3230

Alexander MA, Bladé I, Newman M, Lanzante JR, Lau N-C and Scott JD (2002) The Atmospheric Bridge: The Influence of ENSO Teleconnections on Air–Sea Interaction over the Global Oceans. Journal of Climate 15 16 2205-2231

Alexander MA and Scott JD (1997) Surface Flux Variability over the North Pacific and North Atlantic Oceans. Journal of Climate 10 11 2963-2978

Ali A and Lebel T (2009) The Sahelian standardized rainfall index revisited. International Journal of Climatology 29 12 1705-1714.

An S-I (2011) Atmospheric Responses of Gill-Type and Lindzen–Nigam Models to Global Warming. Journal of Climate 24 23 6165-6173

Ashok K, Guan Z and Yamagata T (2001) Impact of the Indian Ocean dipole on the relationship between the Indian monsoon rainfall and ENSO. Geophysical Research Letters 28 23 4499-4502

Ault TR, Cole JE and St. George S (2012) The amplitude of decadal to multidecadal variability in precipitation simulated by state-of-the-art climate models. Geophysical Research Letters 39 21.

Bader J and Latif M (2003) The impact of decadal-scale Indian Ocean sea surface temperature anomalies on Sahelian rainfall and the North Atlantic Oscillation. Geophysical Research Letters 30 22.

Barnett TP (1995) Monte Carlo Climate Forecasting. Journal of Climate 8 5 1005-1022

Barnston AG and Ropelewski CF (1992) Prediction of ENSO episodes using canonical correlation analysis. Journal of Climate 5 11 1316-1345.

Barnston AG (1992) Correspondence among the Correlation, RMSE, and Heidke Forecast Verification Measures; Refinement of the Heidke Score. Weather and Forecasting 7 4 699-709.

Barnston AG and van den Dool HM (1993) A Degeneracy in Cross-validated skill in regression-based forecasts. Journal of Climate 6 5 963-977.

Barnston AG, Thiao W and Kumar V (1996) Long-lead forecasts of seasonal precipitation in Africa using CCA. Weather and Forecasting 11 4 506-520.

Barnston AG and Smith TM (1996) Specification and prediction of global surface temperature and precipitation from global SST using CCA. Journal of Climate 9 11 2660-2697.

Barnston AG and Tippett MK (2014) Climate information, outlooks, and understanding–where does the IRI stand?. Earth Perspectives 1 1 20.

Barnston AG, Tippett MK, van den Dool HM and Unger DA (2015) Toward an Improved Multimodel ENSO Prediction. Journal of Applied Meteorology and Climatology 54 7 1579-1595.

Batterbury S and Warren A (2001) The African Sahel 25 years after the great drought: assessing progress and moving towards new agendas and approaches. Global Environmental Change 11 1 1-8.

Becker A, Finger P, Meyer-Christoffer A, Rudolf B, Schamm K, Schneider U and Ziese M

(2013) A description of the global land-surface precipitation data products of the Global Precipitation Climatology Centre with sample applications including centennial (trend) analysis from 1901-present. Earth System Science Data 5 1 71.

Bellenger H, Guilyardi E, Leloup J, Lengaigne M and Vialard J (2013) ENSO representation in climate models: from CMIP3 to CMIP5. Climate Dynamics 42 7-8 1999-2018.

Bengtsson L, Arkin P, Berrisford P, Bougeault P, Folland KC, Gordon C, Haines K, Hodges IK, Jones P, Kallberg P, Rauner N, Simmons JA, Stammer D, Thorne WP, Uppala S, Vose SR (2007) The need for a dynamical climate reanalysis. 88 American Meteorological Society 7

Berry GJ and Thorncroft C (2005) Case Study of an Intense African Easterly Wave. Monthly Weather Review 133 4 752-766

Berry G and Reeder MJ (2014) Objective identification of the Intertropical Convergence Zone: climatology and trends from the ERA-Interim. Journal of Climate 27 5 1894-1909.

Biasutti M, Battisti DS and Sarachik ES (2003) The Annual Cycle over the Tropical Atlantic, South America, and Africa. Journal of Climate 16 15 2491-2508

Biasutti M, Battisti DS and Sarachik ES (2005) Terrestrial Influence on the Annual Cycle of the Atlantic ITCZ in an AGCM Coupled to a Slab Ocean Model. Journal of Climate 18 1 211-228

Biasutti M, Sobel AH and Kushnir Y (2006) AGCM Precipitation biases in the tropical Atlantic. Journal of Climate 19 6 935-958.

Biasutti M, Held IM, Sobel AH and Giannini A (2008) SST forcings and Sahel rainfall variability in simulations of the twentieth and twenty-first centuries. Journal of Climate 21 14 3471-3486.

Biasutti M, Sobel AH and Camargo SJ (2009) The role of the Sahara Low in summertime Sahel rainfall variability and change in the CMIP3 Models. Journal of Climate 22 21 5755-5771.

Biasutti M (2013) Forced Sahel rainfall trends in the CMIP5 archive. Journal of Geophysical Research: Atmospheres 118 4 1613-1623.

Bijlsma SJ, Hafkenscheid LM and Lynch P (1986) Computation of the Streamfunction and Velocity Potential and Reconstruction of the Wind Field. Monthly Weather Review 114 8 1547-1551

Bischoff T and Schneider T (2014) Energetic Constraints on the Position of the Intertropical Convergence Zone. Journal of Climate 27 13 4937-4951

Bjerknes J (1921) The Meteorology of the Temperate Zone and the General Atmospheric circulation. Monthly Weather Review 49 1 1-3

Bjerknes J (1969) Atmospheric teleconnections from the equatorial Pacific. Monthly Weather Review 97 3 163-172.

Braconnot P, Hourdin F, Bony S, Dufresne JL, Grandpeix JY and Marti O (2007) Impact of different convective cloud schemes on the simulation of the tropical seasonal cycle in a coupled ocean–atmosphere model. Climate Dynamics 29 5 501-520

Bretherton C, Smith C and Wallace J (1992) An intercomparison of methods for finding coupled patterns in climate data. Journal of Climate 5 6 541-560.

Broccoli AJ, Dahl KA and Stouffer RJ (2006) Response of the ITCZ to Northern Hemisphere cooling. Geophysical Research Letters 33 1.

Brown JN, Sen Gupta A, Brown JR, Muir LC, Risbey JS, Whetton P, Zhang X, Ganachaud A, Murphy B and Wijffels SE (2013) Implications of CMIP3 model biases and uncertainties for climate projections in the western tropical Pacific. Climatic Change 119 1 147-161.

Bulic IH and Kucharski F (2012) Delayed ENSO impact on spring precipitation over North/Atlantic European region. Climate Dynamics 38 2593-2612.

Butterworth S (1930) On the theory of filter amplifiers. Experimental wireless and the wireless engineer 7 536-541

Camberlin P, Janicot S and Poccard I (2001) Seasonality and atmospheric dynamics of the teleconnection between African rainfall and tropical sea-surface temperature: Atlantic vs. ENSO. International Journal of Climatology 21 8 973-1005.

Carton JA and Huang B (1994) Warm events in the tropical Atlantic. Journal of Physical Oceanography 24 5 888-903.

Carton JA, Cao X, Giese BS and Da Silva AM (1996) Decadal and interannual SST variability in the Tropical Atlantic Ocean. Journal of Physical Oceanography 26 7 1165-1175

Cayan DR (1992) Latent and Sensible Heat Flux Anomalies over the Northern Oceans: Driving the Sea Surface Temperature. Journal of Physical Oceanography 22 8 859-881

Chen T-C, Tzeng R-Y and Yen M-C (1988) Development and Life Cycle of the Indian Monsoon: Effect of the 30–50 Day Oscillation. Monthly Weather Review 116 11 2183-2199

Cherry S (1996) Singular Value Decomposition Analysis and Canonical Correlation Analysis. Journal of Climate 9 9 2003-2009.

Cherry S (1997) Some comments on singular value decomposition analysis. Journal of Climate 10 7 1759-1761.

Chiang JCH and Kushnir Y (2000) Interdecadal changes in eastern Pacific ITCZ variability and its influence on the Atlantic ITCZ. Geophysical Research Letters 27 3687-3690

Chiang JCH, Kushnir Y and Giannini A (2002) Deconstructing Atlantic Intertropical Convergence Zone variability: Influence of the local cross-equatorial sea surface temperature gradient and remote forcing from the eastern equatorial Pacific. Journal of Geophysical Research: Oceans 107.

Chiang JCH, Biasutti M and Battisti DS (2003) Sensitivity of the Atlantic Intertropical Convergence Zone to Last Glacial Maximum boundary conditions. Paleoceanography 18 4.

Chiang JCH and Bitz CM (2005) Influence of high latitude ice cover on the marine Intertropical Convergence Zone. Climate Dynamics 25 5 477-496.

Chiang JCH and Friedman AR (2012) Extratropical cooling, interhemispheric thermal gradients, and tropical climate change. Annual Review of Earth and Planetary Sciences 40 1 383-412.

Chung CE and Ramanathan V (2006) Weakening of North Indian SST Gradients and the Monsoon Rainfall in India and the Sahel. Journal of Climate 19 10 2036-2045.

Clarke AJ (2014) El Nino physics and El Nino predictability. Annual review of marine science 6 79-99.

Colman A, Rowell D, Foamouhoue AK, Ndiaye O, Rodríguez-Fonseca B, Suárez-Moreno R, Yaka P, Parker DJ and Diop-Kane M (2017) Seasonal Forecasting in Meteorology of Tropical West Africa: The Forecasters' Handbook (eds D. J. Parker and M. Diop-Kane), John Wiley & Sons, Ltd, Chichester, UK.

Cook KH (1999) Generation of the African Easterly Jet and Its Role in Determining West African Precipitation. Journal of Climate 12 5 1165-1184

Cook KH (1999) Generation of the African Easterly Jet and Its Role in Determining West African Precipitation. Journal of Climate 12 5 1165-1184.

Cook KH and Vizy EK (2006) Coupled Model Simulations of the West African Monsoon System: Twentieth- and Twenty-First-Century Simulations. Journal of Climate 19 15 3681-3703

Cook KH and Vizy EK (2012) Impact of climate change on mid-twenty-first century growing seasons in Africa. Climate Dynamics 39 12 2937-2955

Cvijanovic I and Chiang JCH (2013) Global energy budget changes to high latitude North Atlantic cooling and the tropical ITCZ response. Climate Dynamics 40 5 1435-1452.

Dai A and Wigley TML (2000) Global patterns of ENSO-induced precipitation. Geophysical Research Letters 27 9 1283-1286.

Dai A, Lamb PJ, Trenberth KE, Hulme M, Jones PD and Xie P (2004) The recent Sahel drought is real. International Journal of Climatology 24 11 1323-1331.

Dai A (2013) Increasing drought under global warming in observations and models. Nature Climate Change 3 1 52-58.

Davey MK and Gill AE (1987) Experiments on tropical circulation with a Simple Moist Model. Quarterly Journal of the Royal Meteorological Society 113 478 1237-1269.

Dayan H, Vialard J, Izumo T and Lengaigne M (2014) Does sea surface temperature outside the tropical Pacific contribute to enhanced ENSO predictability?. Climate Dynamics 43 5 1311-1325.

Dee DP, Uppala SM, Simmons AJ, Berrisford P, Poli P, Kobayashi S, Andrae U, Balmaseda MA, Balsamo G, Bauer P, Bechtold P, Beljaars ACM, van de Berg L, Bidlot J, Bormann N, Delsol C, Dragani R, Fuentes M, Geer AJ, Haimberger L, Healy SB, Hersbach H, Hólm EV, Isaksen L, Kållberg P, Köhler M, Matricardi M, McNally AP, Monge-Sanz BM, Morcrette JJ, Park BK, Peubey C, de Rosnay P, Tavolato C, Thépaut JN and Vitart F (2011) The ERA-Interim reanalysis: configuration and performance of the data assimilation system. Quarterly Journal of the Royal Meteorological Society 137 656 553-597.

Delworth TL and Greatbatch RJ (2000) Multidecadal Thermohaline Circulation Variability Driven by Atmospheric Surface Flux Forcing. Journal of Climate 13 9 1481-1495

Delworth TL and Mann ME (2000) Observed and simulated multidecadal variability in the Northern Hemisphere. Climate Dynamics 16 661-676.

Deser C and Timlin MS (1997) Atmosphere–Ocean Interaction on Weekly Timescales in the North Atlantic and Pacific. Journal of Climate 10 3 393-408

Deser C, Alexander MA and Timlin MS (2003) Understanding the Persistence of Sea Surface Temperature Anomalies in Midlatitudes. Journal of Climate 16 1 57-72

Deser C, Phillips AS and Hurrell JW (2004) Pacific Interdecadal Climate Variability: Linkages between the Tropics and the North Pacific during Boreal Winter since 1900. Journal of Climate 17 16 3109-3124

Diatta S and Fink AH (2014) Statistical relationship between remote climate indices and West African monsoon variability. International Journal of Climatology 34 12 3348-3367.

Dieppois B, Rouault M and New M (2015) The impact of ENSO on Southern African rainfall in CMIP5 ocean atmosphere coupled climate models. Climate Dynamics 45 9 2425-2442

Ding H, Keenlyside NS and Latif M (2012) Impact of the Equatorial Atlantic on the El Niño Southern Oscillation. Climate Dynamics 38 9-10 1965-1972.

Dixon KW, Delworth TL, Spelman MJ and Stouffer RJ (1999) The influence of transient surface fluxes on North Atlantic overturning in a coupled GCM climate change experiment. Geophysical Research Letters 26 17 2749-2752.

Doi T, Vecchi GA, Rosati AJ and Delworth TL (2012) Biases in the Atlantic ITCZ in seasonal-interannual variations for a coarse-and a high-resolution coupled climate model. Journal of Climate 25 16 5494-5511.

Dong B and Sutton R (2015) Dominant role of greenhouse-gas forcing in the recovery of Sahel rainfall. Nature Climate Change 5 8 757-760.

Donohoe A, Marshall J, Ferreira D and McGee D (2013) The Relationship between ITCZ Location and Cross-Equatorial Atmospheric Heat Transport: From the Seasonal Cycle to the Last Glacial Maximum. Journal of Climate 26 11 3597-3618

Drobinski P, Sultan B and Janicot S (2005) Role of the Hoggar massif in the West African monsoon onset. Geophysical Research Letters 32 1

Drosdowsky W and Chambers LE (2001) Near-Global sea surface temperature anomalies as predictors of Australian seasonal rainfall. Journal of Climate 14 7 1677-1687.

Dufresne JL, et al. (2013) Climate Change projections using the IPSL-CM5 Earth System Model: from CMIP3 to CMIP5. Climate Dynamics 40 9 2123-2165.

Elsner JB and Schmertmann CP (1994) Assessing Forecast Skill through Cross Validation. Weather and Forecasting 9 4 619-624.

Enfield DB and Cid-Serrano L (2006) Projecting the risk of future climate shifts. International Journal of Climatology 26 7 885-895.

Engelstaedter S, Washington R, Flamant C, Parker DJ, Allen CJT and Todd MC (2015) The Saharan heat low and moisture transport pathways in the central Sahara—Multiaircraft observations and Africa-LAM evaluation. Journal of Geophysical Research: Atmospheres 120 10 4417-4442.

Evan AT, Flamant C, Lavaysse C, Kocha C and Saci A (2015) Water Vapor–Forced Greenhouse Warming over the Sahara Desert and the Recent Recovery from the Sahelian Drought. Journal of Climate 28 1 108-123.

Fasullo JT and Trenberth KE (2008) The Annual Cycle of the Energy Budget. Part II: Meridional Structures and Poleward Transports. Journal of Climate 21 10 2313-2325.

Feulner G, Rahmstorf S, Levermann A and Volkwardt S (2013) On the origin of the surface air temperature difference between the hemispheres in Earth's present-day climate. Journal of Climate 26 18 7136-7150.

Ferrel W (1856) Essay on the winds and ocean currents. Nashville J. Med. and Surg. 11 287–301375–301389

Findell KL and Delworth TL (2010) Impact of common sea surface temperature anomalies on global drought and pluvial frequency. Journal of Climate 23 3 485-503.

Fink AH, Engel T, Ermert V, van der Linden R, Schneidewind M, Redl R, Afiesimama E, Thiaw W, Yorke C and Evans M (2017) Mean climate and seasonal cycle. . In: "Meteorology of Tropical West Africa: The Forecasters' Handbook" D. J. Parker and M. Diop-Kane (Eds.), John Wiley & Sons, Ltd, Chichester, UK. 1-39

Folland C, Palmer T and Parker D (1986) Sahel rainfall and worldwide sea temperatures, 1091-85. 320 Nature Publishing Group

Fontaine B and Janicot S (1996) Sea surface temperature fields associated with West African rainfall anomaly types. Journal of Climate 9 11 2935-2940.

Fontaine B, Trzaska S and Janicot S (1998) Evolution of the relationship between near global and Atlantic SST modes and the rainy season in West Africa: statistical analyses and sensitivity experiments. Climate Dynamics 14 5 353-368.

Fontaine B, Philippon N and Camberlin P (1999) An improvement of June–September rainfall forecasting in the Sahel based upon region April–May moist static energy content (1968–1997). Geophysical Research Letters 26 14 2041-2044

Fontaine B, Garcia-Serrano J, Roucou P, Rodriguez-Fonseca B, Losada T, Chauvin F, Gervois S, Sijikumar S, Ruti P and Janicot S (2010) Impacts of warm and cold situations in the Mediterranean basins on the West African monsoon: observed connection patterns (1979–2006) and climate simulations. Climate Dynamics 35 1 95-114.

Fontaine B, Monerie P-A, Gaetani M and Roucou P (2011a) Climate adjustments over the African-Indian monsoon regions accompanying Mediterranean Sea thermal variability. Journal of Geophysical Research: Atmospheres 116 D23.

Fontaine B, Gaetani M, Ullmann A and Roucou P (2011b) Time evolution of observed July–September sea surface temperature-Sahel climate teleconnection with removed quasi-global effect (1900–2008). Journal of Geophysical Research: Atmospheres 116 D4.

Frankignoul C and Hasselmann K (1977) Stochastic climate models, Part II Application to sea-surface temperature anomalies and thermocline variability. Tellus 29 4 289-305

Frierson DMW and Hwang Y-T (2012) Extratropical Influence on ITCZ Shifts in Slab Ocean Simulations of Global Warming. Journal of Climate 25 2 720-733.

Frierson DMW, Hwang Y-T, Fuckar NS, Seager R, Kang SM, Donohoe A, Maroon EA, Liu X and Battisti DS (2013) Contribution of ocean overturning circulation to tropical rainfall peak in the Northern Hemisphere. Nature Geoscience 6 11 940-944.

Gaetani M, Fontaine B, Roucou P and Baldi M (2010) Influence of the Mediterranean Sea on the West African monsoon: Intraseasonal variability in numerical simulations. Journal of Geophysical Research: Atmospheres 115 D24 D24115.

Gaetani M, Flamant C, Bastin S, Janicot S, Lavaysse C, Hourdin F, Braconnot P and Bony S (2016) West African monsoon dynamics and precipitation: the competition between global SST warming and CO2 increase in CMIP5 idealized simulations. Climate Dynamics 48 3 1353-1373.

García-García D and Ummenhofer CC (2015) Multidecadal variability of the continental precipitation annual amplitude driven by AMO and ENSO. Geophysical Research Letters 42 2 526-535.

Gardner MW and Dorling SR (1998) Artificial neural networks (the multilayer perceptron)—a review of applications in the atmospheric sciences. Atmospheric Environment 32 14–15 2627-2636.

Giannini A, Chiang JCH, Cane MA, Kushnir Y and Seager R (2001) The ENSO Teleconnection to the Tropical Atlantic Ocean: Contributions of the Remote and Local SSTs to Rainfall Variability in the Tropical Americas*. Journal of Climate 14 24 4530-4544.

Giannini A, Saravanan R and Chang P (2003) Oceanic forcing of Sahel rainfall on interannual to interdecadal time scales. Science 302 5647 1027-1030.

Giannini A, Saravanan R and Chang P (2005) Dynamics of the boreal summer African monsoon in the NSIPP1 atmospheric model. Climate Dynamics 25 5 517-535.

Giannini A, Biasutti M, Held IM and Sobel AH (2008) A global perspective on African climate. Climatic Change 90 4 359-383.

Giannini A, Salack S, Lodoun T, Ali A, Gaye AT and Ndiaye O (2013) A unifying view of climate change in the Sahel linking intra-seasonal, interannual and longer time scales. Environmental Research Letters 8 2 024010.

Gill AE (1980) Some simple solutions for heat-induced tropical circulation. Quarterly Journal of the Royal Meteorological Society 106 449 447-462.

Gill AE (1982) Atmosphere-ocean dynamics. Academic press Vol. 30.

Glahn HR and Lowry DA (1972) The use of model output Statistics (MOS) in objective weather forecasting. Journal of Applied Meteorology 11 8 1203-1211.

Gorgas J, Cardiel N and Zamorano J (2009) Estadística Básica para Estudiantes de Ciencias, 206

Greatbatch RJ, Lu J and Peterson KA (2004) Nonstationary impact of ENSO on Euro-Atlantic winter climate. Geophysical Research Letters 31 2.

Greene AM, Giannini A and Zebiak SE (2009) Drought return times in the Sahel: A question of attribution. Geophysical Research Letters 36 12.

Grist JP and Nicholson SE (2001) A study of the dynamic factors influencing the rainfall variability in the West African Sahel. Journal of Climate 14 7 1337-1359.

Gu G and Adler RF (2004) Seasonal Evolution and Variability Associated with the West African Monsoon System. Journal of Climate 17 17 3364-3377

Guan B and Nigam S (2008) Pacific Sea Surface Temperatures in the Twentieth Century: An Evolution-Centric Analysis of Variability and Trend. Journal of Climate 21 12 2790-2809

Hadley G (1735) Concerning the cause of the general trade winds. Philosophical transactions Royal Society, London 29 58-62

Hagos SM and Cook KH (2008) Ocean warming and late-twentieth-century Sahel drought and recovery. Journal of Climate 21 15 3797-3814.

Häkkinen S, Rhines PB and Worthen DL (2011) Atmospheric Blocking and Atlantic Multidecadal Ocean Variability. Science 334 6056 655.

Hall NMJ, Kiladis GN and Thorncroft CD (2006) Three-Dimensional Structure and Dynamics of African Easterly Waves. Part II: Dynamical Modes. Journal of the

Atmospheric Sciences 63 9 2231-2245
Halley E (1686) An Historical Account of the Trade Winds, and Monsoons, observable in the Sea between and near the Tropicks, with an attempt to assign the Physical cause of the same Winds Philosophical transactions 16 153–168
Halpert MS and Ropelewski CF (1992) Surface temperature patterns associated with the Southern Oscillation. Journal of Climate 5 6 577-593.
Harris I, Jones PD, Osborn TJ and Lister DH (2014) Updated high-resolution grids of monthly climatic observations – the CRU TS3.10 Dataset. International Journal of Climatology 34 3 623-642.
Hasselmann K (1976) Stochastic climate models Part I. Theory. Tellus 28 6 473-485.
Hastenrath S (2012) Climate dynamics of the tropics. Springer Science & Business Media. 8.
Haylock MR, Peterson TC, Alves LM, Ambrizzi T, Anunciação YMT, Baez J, Barros VR, Berlato MA, Bidegain M, Coronel G, Corradi V, Garcia VJ, Grimm AM, Karoly D, Marengo JA, Marino MB, Moncunill DF, Nechet D, Quintana J, Rebello E, Rusticucci M, Santos JL, Trebejo I and Vincent LA (2006) Trends in total and extreme South American rainfall in 1960–2000 and links with sea surface temperature. Journal of Climate 19 8 1490-1512.
Held IM, Delworth TL, Lu J, Findell KL and Knutson TR (2005) Simulation of Sahel drought in the 20th and 21st centuries. Proceedings of the National Academy of Sciences of the United States of America 102 50 17891-17896.
Hirst AC (1986) Unstable and damped equatorial modes in simple coupled ocean-atmosphere models. Journal of the Atmospheric Sciences 43 6 606-632.
Hoerling M, Hurrell J, Eischeid J and Phillips A (2006) Detection and attribution of twentieth-century northern and southern African rainfall change. Journal of Climate 19 16 3989-4008.
Holton JR (2004) Introduction to Dynamical Meteorology. Elsevier Academic Press, 4th Edition.
Hourdin F, Musat I, Bony S, Braconnot P, Codron F, Dufresne J-L, Fairhead L, Filiberti M-A, Friedlingstein P, Grandpeix J-Y, Krinner G, LeVan P, Li Z-X and Lott F (2006) The LMDZ4 general circulation model: climate performance and sensitivity to parametrized physics with emphasis on tropical convection. Climate Dynamics 27 7 787-813.
Hourdin F, Foujols M-A, Codron F, Guemas V, Dufresne J-L, Bony S, Denvil S, Guez L, Lott F, Ghattas J, Braconnot P, Marti O, Meurdesoif Y and Bopp L (2013) Impact of the LMDZ atmospheric grid configuration on the climate and sensitivity of the IPSL-CM5A coupled model. Climate Dynamics 40 9 2167-2192.
Hsieh WW and Tang B (1998) Applying neural network models to prediction and data analysis in meteorology and oceanography. Bulletin of the American Meteorological Society 79 9 1855-1870.
Hsieh WW (2001) Nonlinear Canonical Correlation Analysis of the Tropical Pacific Climate Variability Using a Neural Network Approach. Journal of Climate 14 12 2528-2539
Huang B, Banzon VF, Freeman E, Lawrimore J, Liu W, Peterson TC, Smith TM, Thorne PW, Woodruff SD and Zhang H-M (2015) Extended Reconstructed Sea Surface Temperature version 4 (ERSST.v4). Part I: Upgrades and intercomparisons. Journal of Climate 28 3 911-930.
Hulme M (2001) Climatic perspectives on Sahelian desiccation: 1973–1998. Global Environmental Change 11 1 19-29.
Janicot S (1992) Spatiotemporal variability of West African rainfall. Part I: Regionalizations and typings. Journal of Climate 5 5 489-497.
Janicot S, Moron V and Fontaine B (1996) Sahel droughts and ENSO dynamics. Geophysical Research Letters 23 5 515-518.
Janicot S, Harzallah A, Fontaine B and Moron V (1998) West African Monsoon Dynamics

and Eastern Equatorial Atlantic and Pacific SST Anomalies (1970–88). Journal of Climate 11 8 1874-1882.

Janicot S, Trzaska S and Poccard I (2001) Summer Sahel-ENSO teleconnection and decadal time scale SST variations. Climate Dynamics 18 3 303-320.

Janicot S, Thorncroft CD, Ali A, Asencio N, Berry GJ, Bock O, Bourlès B, Caniaux G, Chauvin F, Deme A, Kergoat L, Lafore J-P, Lavaysse C, Lebel T, Marticoréna B, Mounier F, Nédélec P, Redelsperger J-L, Ravegnani F, Reeves CE, Roca R, De Rosnay P, Schlager H, Sultan B, Tomasini M and Ulanovsky A (2008) Large-scale overview of the summer monsoon over West Africa during the AMMA field experiment in 2006. Annales Geophysicae 26 2569-2595

Janowiak JE (1988) An Investigation of Interannual Rainfall Variability in Africa. Journal of Climate 1 3 240-255.

Jin F and Hoskins BJ (1995) The Direct Response to Tropical Heating in a Baroclinic Atmosphere. Journal of the Atmospheric Sciences 52 3 307-319

Joly M, Voldoire A, Douville H, Terray P and Royer JF (2007) African monsoon teleconnections with tropical SSTs: validation and evolution in a set of IPCC4 simulations. Climate Dynamics 29 1 1-20.

Joly M and Voldoire A (2009) Influence of ENSO on the West African Monsoon: Temporal Aspects and Atmospheric Processes. Journal of Climate 22 12 3193-3210.

Joly M and Voldoire A (2010) Role of the Gulf of Guinea in the inter-annual variability of the West African monsoon: what do we learn from CMIP3 coupled simulations?. International Journal of Climatology 30 12 1843-1856.

Jung T, Ferranti L and Tompkins AM (2006) Response to the summer of 2003 Mediterranean SST anomalies over Europe and Africa. Journal of Climate 19 20 5439-5454.

Kalnay E, Kanamitsu M, Kistler R, Collins W, Deaven D, Gandin L, Iredell M, Saha S, White G, Woollen J, Zhu Y, Leetmaa A, Reynolds R, Chelliah M, Ebisuzaki W, Higgins W, Janowiak J, Mo KC, Ropelewski C, Wang J, Jenne R and Joseph D (1996) The NCEP/NCAR 40-Year Reanalysis Project. Bulletin of the American Meteorological Society 77 3 437-471

Kang SM, Held IM, Frierson DMW and Zhao M (2008) The response of the ITCZ to extratropical thermal forcing: Idealized slab-ocean experiments with a GCM. Journal of Climate 21 14 3521-3532.

Kang SM, Frierson DMW and Held IM (2009) The Tropical Response to Extratropical Thermal Forcing in an Idealized GCM: The Importance of Radiative Feedbacks and Convective Parameterization. Journal of the Atmospheric Sciences 66 9 2812-2827

Kang SM, Held IM and Xie S-P (2014) Contrasting the tropical responses to zonally asymmetric extratropical and tropical thermal forcing. Climate Dynamics 42 7 2033-2043.

Kang I-S, No H-h and Kucharski F (2014) ENSO Amplitude Modulation Associated with the Mean SST Changes in the Tropical Central Pacific Induced by Atlantic Multidecadal Oscillation. Journal of Climate 27 20 7911-7920

Kiladis GN, Thorncroft CD and Hall NMJ (2006) Three-Dimensional Structure and Dynamics of African Easterly Waves. Part I: Observations. Journal of the Atmospheric Sciences 63 9 2212-2230

Klein WH and Glahn HR (1974) Forecasting local weather by means of model output statistics. Bulletin of the American Meteorological Society 55 10 1217-1227.

Knauss, JA (1997) Introduction to physical oceanography. Prentice Hall

Knight JR, Folland CK and Scaife AA (2006) Climate impacts of the Atlantic Multidecadal Oscillation. Geophysical Research Letters 33 17 L17706

Knippertz P, Ulbrich U, Marques F and Corte-Real J (2003) Decadal changes in the link between El Niño and springtime North Atlantic oscillation and European–North African rainfall. International Journal of Climatology 23 11 1293-1311.

Knutti R, Stocker TF, Joos F and Plattner GK (2003) Probabilistic climate change projections using neural networks. Climate Dynamics 21 3 257-272.

Korecha D and Barnston AG (2007) Predictability of june–september rainfall in Ethiopia. Monthly Weather Review 135 2 628-650.

Koutavas, A, Lynch-Stieglitz, J and Kovats RS (2000) El Niño and human health. Bulletin of the World Health Organization 78 1127-1135.

Kraus EB (1977) Subtropical Droughts and Cross-Equatorial Energy Transports. Monthly Weather Review 105 8 1009-1018

Krinner G, Viovy N, de Noblet-Ducoudré N, Ogée J, Polcher J, Friedlingstein P, Ciais P, Sitch S and Prentice IC (2005) A dynamic global vegetation model for studies of the coupled atmosphere-biosphere system. Global Biogeochemical Cycles 19.

Krishnamurti TN (1961) The subtropical jet stream of winter. Journal of Meteorology 18 2 172-191

Kucharski F, Bracco A, Yoo JH and Molteni F (2008) Atlantic forced component of the Indian monsoon interannual variability. Geophysical Research Letters 35 4 L04706

Kushnir Y, Barreiro M, Chang P, Chiang J, Lazar A and Malanotte-Rizzoli P (2003) The role of the south Atlantic in the Variability of the ITCZ White paper for CLIVAR/IAI/OOPC

Hagos SM and Cook KH (2008) Ocean Warming and Late-Twentieth-Century Sahel Drought and Recovery. Journal of Climate 21 15 3797-3814

Haimberger L, Tavolato C and Sperka S (2008) Toward Elimination of the Warm Bias in Historic Radiosonde Temperature Records—Some New Results from a Comprehensive Intercomparison of Upper-Air Data. Journal of Climate 21 18 4587-4606

Harris I, Jones PD, Osborn TJ and Lister DH (2014) Updated high-resolution grids of monthly climatic observations – the CRU TS3.10 Dataset. International Journal of Climatology 34 3 623-642

Hourdin F, Musat I, Bony S, Braconnot P, Codron F, Dufresne J-L, Fairhead L, Filiberti M-A, Friedlingstein P, Grandpeix J-Y, Krinner G, LeVan P, Li Z-X and Lott F (2006) The LMDZ4 general circulation model: climate performance and sensitivity to parametrized physics with emphasis on tropical convection. Climate Dynamics 27 7 787-813

Hourdin F, Foujols M-A, Codron F, Guemas V, Dufresne J-L, Bony S, Denvil S, Guez L, Lott F, Ghattas J, Braconnot P, Marti O, Meurdesoif Y and Bopp L (2013) Impact of the LMDZ atmospheric grid configuration on the climate and sensitivity of the IPSL-CM5A coupled model. Climate Dynamics 40 9 2167-2192

Huang B, Banzon VF, Freeman E, Lawrimore J, Liu W, Peterson TC, Smith TM, Thorne PW, Woodruff SD and Zhang H-M (2015) Extended Reconstructed Sea Surface Temperature Version 4 (ERSST.v4). Part I: Upgrades and Intercomparisons. Journal of Climate 28 3 911-930

Lavaysse C, Flamant C, Janicot S, Parker DJ, Lafore JP, Sultan B and Pelon J (2009) Seasonal evolution of the West African heat low: a climatological perspective. Climate Dynamics 33 2 313-330.

Lavaysse C, Flamant C and Janicot S (2010) Regional-scale convection patterns during strong and weak phases of the Saharan heat low. Atmospheric Science Letters 11 4 255-264.

Lavaysse C, Flamant C, Evan A, Janicot S and Gaetani M (2016) Recent climatological trend of the Saharan Heat Low and its impact on the West African climate. Climate Dynamics 47 11 3479-3498.

Le Barbé L, Lebel T and Tapsoba D (2002) Rainfall variability in West Africa during the years 1950–90. Journal of Climate 15 2 187-202.

Lebel T and Ali A (2009) Recent trends in the central and western Sahel rainfall regime (1990–2007). Journal of Hydrology 375 1–2 52-64.

Lebel T, Parker DJ, Flamant C, Bourlès B, Marticorena B, Mougin E, Peugeot C, Diedhiou A,

Haywood JM, Ngamini JB, Polcher J, Redelsperger JL and Thorncroft CD (2010) The AMMA field campaigns: multiscale and multidisciplinary observations in the West African region. Quarterly Journal of the Royal Meteorological Society 136 S1 8-33.

Lebel T, Diedhiou A and Laurent H (2003) Seasonal cycle and interannual variability of the Sahelian rainfall at hydrological scales. Journal of Geophysical Research: Atmospheres 108 D8

Li H, Wang H and Yin Y (2012) Interdecadal variation of the West African summer monsoon during 1979–2010 and associated variability. Climate Dynamics 39 12 2883-2894.

Li G and Xie S-P (2013) Tropical Biases in CMIP5 multimodel ensemble: The excessive Equatorial Pacific cold tongue and double ITCZ problems*. Journal of Climate 27 4 1765-1780.

Lin Y-L, Robertson KE and Hill CM (2005) Origin and Propagation of a Disturbance Associated with an African Easterly Wave as a Precursor of Hurricane Alberto (2000). Monthly Weather Review 133 11 3276-3298

Lin JL (2007) The double-ITCZ problem in IPCC AR4 coupled GCMs: Ocean-atmosphere feedback analysis. Journal of Climate 20 18 4497-4525.

Lindzen RS and Nigam S (1987) On the role of sea surface temperature gradients in forcing low-level winds and convergence in the tropics. Journal of the Atmospheric Sciences 44 17 2418-2436.

Ling J and Zhang C (2013) Diabatic heating profiles in recent global reanalyses. Journal of Climate 26 10 3307-3325.

Liu Z, Ostrenga D, Teng W and Kempler S (2012) Tropical Rainfall Measuring Mission (TRMM) Precipitation Data and Services for Research and Applications. Bulletin of the American Meteorological Society 93 9 1317-1325

Liu Y, Chiang JCH, Chou C and Patricola CM (2014) Atmospheric teleconnection mechanisms of extratropical North Atlantic SST influence on Sahel rainfall. Climate Dynamics 43 9 2797-2811.

Livezey RE and Chen WY (1983) Statistical field significance and its determination by Monte Carlo techniques. Monthly Weather Review 111 1 46-59.

López-Parages J and Rodríguez-Fonseca B (2012) Multidecadal modulation of El Niño influence on the Euro-Mediterranean rainfall. Geophysical Research Letters 39 2 L02704.

López-Parages J, Rodríguez-Fonseca B and Terray L (2015) A mechanism for the multidecadal modulation of ENSO teleconnection with Europe. Climate Dynamics 45 3 867-880.

López-Parages J, Rodríguez-Fonseca B, Dommenget D and Frauen C (2016) ENSO influence on the North Atlantic European climate: a non-linear and non-stationary approach. Climate Dynamics 47 7 2071-2084

Losada T, Rodríguez-Fonseca B, Janicot S, Gervois S, Chauvin F and Ruti P (2010a) A multi-model approach to the Atlantic Equatorial mode: impact on the West African monsoon. Climate Dynamics 35 1 29-43.

Losada T, Rodríguez-Fonseca B, Polo I, Janicot S, Gervois S, Chauvin F and Ruti P (2010b) Tropical response to the Atlantic Equatorial mode: AGCM multimodel approach. Climate Dynamics 35 1 45-52.

Losada T, Rodriguez-Fonseca B, Mohino E, Bader J, Janicot S and Mechoso CR (2012) Tropical SST and Sahel rainfall: A non-stationary relationship. Geophysical Research Letters 39 12 L12705.

Lothon M, Saïd F, Lohou F and Campistron B (2008) Observation of the Diurnal Cycle in the Low Troposphere of West Africa. Monthly Weather Review 136 9 3477-3500

Lu J and Delworth TL (2005) Oceanic forcing of the late 20th century Sahel drought. Geophysical Research Letters 32 22.

Lu J (2009) The dynamics of the Indian Ocean sea surface temperature forcing of Sahel

drought. Climate Dynamics 33 4 445-460.
Mahowald NM (2007) Anthropocene changes in desert area: Sensitivity to climate model predictions. Geophysical Research Letters 34 18.
Maia AHN, Meinke H, Lennox S and Stone R (2007) Inferential, nonparametric statistics to assess the quality of probabilistic forecast systems. Monthly Weather Review 135 2 351-362.
Majda AJ, Timofeyev I and Vanden Eijnden E (1999) Models for stochastic climate prediction. Proceedings of the National Academy of Sciences 96 26 14687-14691.
Mariotti A, Zeng N and Lau KM (2002) Euro-Mediterranean rainfall and ENSO—a seasonally varying relationship. Geophysical Research Letters 29 12 59-51.
Mariotti A and Dell'Aquila A (2012) Decadal climate variability in the Mediterranean region: roles of large-scale forcings and regional processes. Climate Dynamics 38 5 1129-1145.
Marshall J, Kushnir Y, Battisti DS, Chang P, Czaja A, Dickson RR, Hurrell JW, McCartney MS, Saravanan R and Visbeck M (2001) North Atlantic climate variability: phenomena, impacts and mechanisms. International Journal of Climatology 21 1863-1898
Marshall J, Donohoe A, Ferreira D and McGee D (2014) The ocean's role in setting the mean position of the Inter-Tropical Convergence Zone. Climate Dynamics 42 7 1967-1979.
Marti O, Braconnot P, Dufresne JL, Bellier J, Benshila R, Bony S, Brockmann P, Cadule P, Caubel A, Codron F, de Noblet N, Denvil S, Fairhead L, Fichefet T, Foujols MA, Friedlingstein P, Goosse H, Grandpeix JY, Guilyardi E, Hourdin F, Idelkadi A, Kageyama M, Krinner G, Lévy C, Madec G, Mignot J, Musat I, Swingedouw D and Talandier C (2010) Key features of the IPSL ocean atmosphere model and its sensitivity to atmospheric resolution. Climate Dynamics 34 1 1-26
Martin ER, Thorncroft C and Booth BBB (2013) The multidecadal Atlantic SST—Sahel rainfall teleconnection in CMIP5 simulations. Journal of Climate 27 2 784-806.
Martin ER and Thorncroft CD (2014) The impact of the AMO on the West African monsoon annual cycle. Quarterly Journal of the Royal Meteorological Society 140 678 31-46.
Martin ER, Thorncroft C and Booth BBB (2013) The Multidecadal Atlantic SST—Sahel Rainfall Teleconnection in CMIP5 Simulations. Journal of Climate 27 2 784-806
Martín-Rey M, Polo I, Rodríguez-Fonseca B and Kucharski F (2012) Changes in the interannual variability of the tropical Pacific as a response to an equatorial Atlantic forcing. Scientia Marina 76 S1 105-116.
Martín-Rey M, Rodríguez-Fonseca B, Polo I and Kucharski F (2014) On the Atlantic–Pacific Niños connection: a multidecadal modulated mode. Climate Dynamics 43 11 3163-3178.
Martín-Rey M, Rodríguez-Fonseca B and Polo I (2015) Atlantic opportunities for ENSO prediction. Geophysical Research Letters 42 16 6802-6810.
Marshall J, Donohoe A, Ferreira D and McGee D (2014) The ocean's role in setting the mean position of the Inter-Tropical Convergence Zone. Climate Dynamics 42 7 1967-1979
Marullo S, Artale V and Santoleri R (2011) The SST Multidecadal Variability in the Atlantic–Mediterranean Region and Its Relation to AMO. Journal of Climate 24 16 4385-4401.
Matsuno T (1966) Quasi-geostrophic motions in the equatorial area. Journal of Meteorological Society of Japan 44 25–43.
Mechoso CR, Losada T, Koseki S, Mohino-Harris E, Keenlyside N, Castaño-Tierno A, Myers TA, Rodriguez-Fonseca B and Toniazzo T (2016) Can reducing the incoming energy flux over the Southern Ocean in a CGCM improve its simulation of tropical climate? Geophysical Research Letters 43 20 11,057-011,063
Meehl GA, Covey C, Taylor KE, Delworth T, Stouffer RJ, Latif M, McAvaney B and Mitchell JFB (2007) THE WCRP CMIP3 Multimodel Dataset: A new era in climate change research. Bulletin of the American Meteorological Society 88 9 1383-1394.
Merle J (1980) Seasonal variation of heat-storage in the tropical Atlantic ocean. Oceanologica Acta 3 4 455-463.

Michaelsen J (1987) Cross-validation in statistical climate forecast models. Journal of Climate and Applied Meteorology 26 11 1589-1600.
Mitchell TP and Wallace JM (1992) The Annual Cycle in Equatorial Convection and Sea Surface Temperature. Journal of Climate 5 10 1140-1156
Mohino E, Janicot S and Bader J (2011a) Sahel rainfall and decadal to multi-decadal sea surface temperature variability. Climate Dynamics 37 3 419-440.
Mohino E, Rodríguez-Fonseca B, Losada T, Gervois S, Janicot S, Bader J, Ruti P and Chauvin F (2011b) Changes in the interannual SST-forced signals on West African rainfall. AGCM intercomparison. Climate Dynamics 37 9-10 1707-1725.
Mohino E, Rodríguez-Fonseca B, Mechoso CR, Gervois S, Ruti P and Chauvin F (2011) Impacts of the tropical Pacific/Indian Oceans on the seasonal cycle of the West African monsoon. Journal of Climate 24 15 3878-3891.
Mokhov II and Smirnov DA (2006) El Niño–Southern Oscillation drives North Atlantic Oscillation as revealed with nonlinear techniques from climatic indices. Geophysical Research Letters 33 3.
Moron V, Robertson AW and Ward MN (2006) Seasonal Predictability and Spatial Coherence of Rainfall Characteristics in the Tropical Setting of Senegal. Monthly Weather Review 134 11 3248-3262
Mortimore MJ and Adams WM (2001) Farmer adaptation, change and 'crisis' in the Sahel. Global Environmental Change 11 1 49-57.
Moura AD and Shukla J (1981) On the dynamics of droughts in northeast Brazil: Observations, theory and numerical experiments with a general circulation model. Journal of Atmospheric Sciences 38 12 2653-2675
Munemoto M and Tachibana Y (2012) The recent trend of increasing precipitation in Sahel and the associated inter-hemispheric dipole of global SST. International Journal of Climatology 32 9 1346-1353.
Namias J (1953) Thirty-day forecasting: A review of a ten-year experiment. Springer 2.
Namias J (1959) Recent seasonal interactions between north Pacific waters and the overlying atmospheric circulation. Journal of Geophysical Research 64 6 631-646.
Neelin JD and Held IM (1987) Modeling tropical convergence based on the moist static energy budget. Monthly Weather Review 115 1 3-12
Neelin JD (1989) On the interpretation of the Gill model. 46 American Meteorological Society 3.
Newman M and Sardeshmukh PD (1995) A caveat concerning Singular Value Decomposition. Journal of Climate 8 2 352-360.
Newman M (2007) Interannual to Decadal Predictability of Tropical and North Pacific Sea Surface Temperatures. Journal of Climate 20 11 2333-2356
Nicholson SE and Palao IM (1993) A re-evaluation of rainfall variability in the sahel. Part I. Characteristics of rainfall fluctuations. International Journal of Climatology 13 4 371-389.
Nicholson SE, Some B and Kone B (2000) An analysis of recent rainfall conditions in West Africa, including the rainy seasons of the 1997 El Niño and the 1998 La Niña Years. Journal of Climate 13 14 2628-2640.
Nicholson SE and Grist JP (2003) The seasonal evolution of the atmospheric circulation over West Africa and equatorial Africa. Journal of Climate 16 7 1013-1030.
Nicholson S (2005) On the question of the "recovery" of the rains in the West African Sahel. Journal of Arid Environments 63 3 615-641.
Nicholson SE and Webster PJ (2007) A physical basis for the interannual variability of rainfall in the Sahel. Quarterly Journal of the Royal Meteorological Society 133 629 2065-2084.
Nicholson SE (2009) A revised picture of the structure of the "monsoon" and land ITCZ over West Africa. Climate Dynamics 32 7 1155-1171
Nicholson SE (2013) The West African Sahel: A review of recent studies on the rainfall

regime and its interannual variability. ISRN Meteorology 1-32.
Nnamchi H and Li J (2011) Influence of the South Atlantic Ocean Dipole on West African Summer precipitation. Journal of Climate 24 4 1184-1197.
Nobre P and Shukla J (1996) Variations in sea surface temperature, wind stress, and rainfall over the tropical Atlantic and South America. Journal of Climate 9 2464-2479.
Nonaka M, Nakamura H, Tanimoto Y, Kagimoto T and Sasaki H (2006) Decadal Variability in the Kuroshio–Oyashio Extension Simulated in an Eddy-Resolving OGCM. Journal of Climate 19 10 1970-1989
North GR, Bell TL, Cahalan F and Moeng FJ (1982) Sampling errors in the estimation of empirical orthogonal function. Monthly Weather Review 110 699–706.
Okumura Y and Xie S-P (2004) Interaction of the Atlantic Equatorial Cold Tongue and the African Monsoon. Journal of Climate 17 18 3589-3602
Oort AH and Yienger JJ (1996) Observed Interannual Variability in the Hadley Circulation and Its Connection to ENSO. Journal of Climate 9 11 2751-2767
Palmer TN (1986) Influence of the Atlantic, Pacific and Indian Oceans on Sahel rainfall. Nature 322 6076 251-253.
Park J-Y, Bader J and Matei D (2015) Northern-hemispheric differential warming is the key to understanding the discrepancies in the projected Sahel rainfall. Nature Communications 6 5985.
Park J-Y, Bader J and Matei D (2016) Anthropogenic Mediterranean warming essential driver for present and future Sahel rainfall. Nature Climate Change 6 10 941-945.
Parker DJ, Thorncroft CD, Burton RR and Diongue-Niang A (2005a) Analysis of the African easterly jet, using aircraft observations from the JET2000 experiment. Quarterly Journal of the Royal Meteorological Society 131 608 1461-1482.
Parker DJ, Burton RR, Diongue-Niang A, Ellis RJ, Felton M, Taylor CM, Thorncroft CD, Bessemoulin P and Tompkins AM (2005b) The diurnal cycle of the West African monsoon circulation. Quarterly Journal of the Royal Meteorological Society 131 611 2839-2860.
Parker D, Folland C, Scaife A, Knight J, Colman A, Baines P and Dong B (2007) Decadal to multidecadal variability and the climate change background. Journal of Geophysical Research: Atmospheres 112 D18 D18115.
Pauluis O (2004) Boundary layer dynamics and cross-equatorial Hadley Circulation. Journal of the Atmospheric Sciences 61 10 1161-1173.
Pedlosky J (1987) An Inertial Theory of the Equatorial Undercurrent. Journal of Physical Oceanography 17 11 1978-1985
Peixoto JP and Oort AH (1992) Physics of climate. New York, NY (United States); American Institute of Physics
Penland C and Sardeshmukh PD (1995) The optimal growth of tropical Sea Surface Temperature anomalies. Journal of Climate 8 8 1999-2024.
Penland C and Matrosova L (1998) Prediction of tropical Atlantic Sea Surface temperatures using linear inverse modeling. Journal of Climate 11 3 483-496.
Philander SHG (1990) El Niño, La Niña, and the Southern Oscillation. International Geophysics Series, Academic Press 46 293.
Philander SHG, Yamagata T and Pacanowski RC (1984) Unstable air-sea interactions in the tropics. Journal of Atmospheric Sciences 41 4 604-613.
Poli P, Hersbach H, Dee DP, Berrisford P, Simmons AJ, Vitart F, Laloyaux P, Tan DGH, Peubey C, Thépaut J-N, Trémolet Y, Hólm EV, Bonavita M, Isaksen L and Fisher M (2016) ERA-20C: An Atmospheric Reanalysis of the Twentieth Century. Journal of Climate 29 11 4083-4097
Polo I, Martin-Rey M, Rodriguez-Fonseca B, Kucharski F and Mechoso C (2015) Processes in the Pacific La Niña onset triggered by the Atlantic Niño. Climate Dynamics 44 1 115-131.

Polo I, Rodríguez-Fonseca B, Losada T and García-Serrano J (2008) Tropical Atlantic variability Modes (1979–2002). Part I: Time-evolving SST modes related to West African rainfall. Journal of Climate 21 24 6457-6475.

Power S, Casey T, Folland C, Colman A and Mehta V (1999) Inter-decadal modulation of the impact of ENSO on Australia. Climate Dynamics 15 5 319-324.

Preisendorfer RW and Mobley C (1988).) Principal component analysis in meteorology and oceanography. Elsevier Science Ltd. 17

Qin H, Kawamura H and Kawai Y (2007) Detection of hot event in the equatorial Indo-Pacific warm pool using advanced satellite sea surface temperature, solar radiation, and wind speed. Journal of Geophysical Research: Oceans 112 C7

Ramel R, Gallée H and Messager C (2006) On the northward shift of the West African monsoon. Climate Dynamics 26 4 429-440

Rasmusson EM and Carpenter TH (1983) The relationship between eastern equatorial Pacific sea surface temperatures and rainfall over India and Sri Lanka. Monthly Weather Review 111 3 517-528.

Rayner NA, Parker DE, Horton EB, Folland CK, Alexander LV, Rowell DP, Kent EC and Kaplan A (2003) Global analyses of sea surface temperature, sea ice, and night marine air temperature since the late nineteenth century. Journal of Geophysical Research: Atmospheres 108 D14 4407.

Recalde-Coronel GC, Barnston AG and Muñoz ÁG (2014) Predictability of december–april rainfall in coastal and Andean Ecuador. Journal of Applied Meteorology and Climatology 53 6 1471-1493.

Redelsperger J-L, Thorncroft CD, Diedhiou A, Lebel T, Parker DJ and Polcher J (2006) African Monsoon Multidisciplinary Analysis: An International Research Project and Field Campaign. Bulletin of the American Meteorological Society 87 12 1739-1746

Reed RJ, Norquist DC and Recker EE (1977) The Structure and Properties of African Wave Disturbances as Observed During Phase III of GATE. Monthly Weather Review 105 3 317-333

Richter I and Xie SP (2008) On the origin of equatorial Atlantic biases in coupled general circulation models. Climate Dynamics 31 5 587-598.

Richter I, Xie SP, Wittenberg A and Masumoto Y (2012) Tropical Atlantic biases and their relation to surface wind stress and terrestrial precipitation. Climate Dynamics 38 5-6 985-1001.

Riehl H (1945) Waves in the easterlies and the polar front in the tropics. University of Chicago Press.

Rimac A, Storch J-Sv and Eden C (2016) The total energy flux leaving the ocean's mixed layer. Journal of Physical Oceanography 46 6 1885-1900.

Rimbu N, Lohmann G, Felis T and Pätzold J (2003) Shift in ENSO teleconnections recorded by a northern red sea coral. Journal of Climate 16 9 1414-1422.

Roe GH and Steig EJ (2004) Characterization of Millennial-Scale Climate Variability. Journal of Climate 17 10 1929-1944

Rodó X, Pascual M, Fuchs G and Faruque ASG (2002) ENSO and cholera: A nonstationary link related to climate change? Proceedings of the National Academy of Sciences 99 20 12901-12906

Rodríguez-Fonseca B (2001) Relación entre el Régimen de precipitación anómalo en la Península Ibérica y la variabilidad de baja frecuencia del sistema climático en el Atlántico Norte, Ph.D. thesis, University Complutense of Madrid.

Rodríguez-Fonseca B, Polo I, García-Serrano J, Losada T, Mohino E, Mechoso CR and Kucharski F (2009) Are Atlantic Niños enhancing Pacific ENSO events in recent decades?. Geophysical Research Letters 36 20 L20705.

Rodríguez-Fonseca B, Janicot S, Mohino E, Losada T, Bader J, Caminade C, Chauvin F,

Fontaine B, García-Serrano J, Gervois S, Joly M, Polo I, Ruti P, Roucou P and Voldoire A (2011) Interannual and decadal SST-forced responses of the West African monsoon. Atmospheric Science Letters 12 1 67-74.

Rodríguez-Fonseca B, Mohino E, Mechoso CR, Caminade C, Biasutti M, Gaetani M, Garcia-Serrano J, Vizy EK, Cook K, Xue Y, Polo I, Losada T, Druyan L, Fontaine B, Bader J, Doblas-Reyes FJ, Goddard L, Janicot S, Arribas A, Lau W, Colman A, Vellinga M, Rowell DP, Kucharski F and Voldoire A (2015) Variability and predictability of West African Droughts: A review on the role of sea surface temperature anomalies. Journal of Climate 28 10 4034-4060.

Rodríguez-Fonseca B, Suárez-Moreno R, Ayarzagüena B, López-Parages J, Gómara I, Villamayor J, Mohino E, Losada T and Castaño-Tierno A (2016) A review of ENSO influence on the North Atlantic. A Non-Stationary Signal. Atmosphere 7 7.

Roe GH and Steig EJ (2004) Characterization of millennial-scale climate variability. Journal of Climate 17 10 1929-1944.

Rowell D, Milford J, Folland C, Maskell K, Owen J and Ward M (1992) Modelling the influence of global sea surface temperatures on the variability and predictability of seasonal Sahel rainfall. Geophysical Research Letters 19 905-908.

Rowell DP (2001) Teleconnections between the tropical Pacific and the Sahel. Quarterly Journal of the Royal Meteorological Society 127 575 1683-1706.

Rowell DP (2003) The impact of Mediterranean SSTs on the Sahelian rainfall season. Journal of Climate 16 5 849-862.

Rowell DP (2013) Simulating SST teleconnections to Africa: What is the state of the art?. Journal of Climate 26 15 5397-5418.

Rozas V and García-González I (2012) Too wet for oaks? Inter-tree competition and recent persistent wetness predispose oaks to rainfall-induced dieback in Atlantic rainy forest. Global and Planetary Change 94–95 62-71

Rudolf B, Becker A, Schneider U, Meyer-Christoffer A and Ziese M (2011) New GPCC full data reanalysis version 5 provides high-quality gridded monthly precipitation data. Gewex News 21 2 4-5.

Sanogo S, Fink AH, Omotosho JA, Ba A, Redl R and Ermert V (2015) Spatio-temporal characteristics of the recent rainfall recovery in West Africa. International Journal of Climatology 35 15 4589-4605

Schneider N and Cornuelle BD (2005) The Forcing of the Pacific Decadal Oscillation. Journal of Climate 18 21 4355-4373

Schneider U, Becker A, Finger P, Meyer-Christoffer A, Rudolf B and Ziese M (2011a) GPCC Full Data Reanalysis Version 6.0 at 0.5□ : Monthly Land-Surface Precipitation from Rain-Gauges built on GTS-based and Historic Data. GPCC Data Rep.

Schneider U, Andreas B, Peter F, Anja M-C, Bruno R and Markus Z (2011b) GPCC full data reanalysis version 6.0 at 1.0º: Monthly land-surface precipitation from rain-gauges built on GTS-based and historic data. GPCC Data Rep.

Schneider U, Andreas B, Peter F, Anja M-C, Bruno R and Markus Z (2011c) GPCC full data reanalysis version 6.0 at 2.5º: Monthly land-surface precipitation from rain-gauges built on GTS-based and historic data.GPCC Data Rep.

Schneider U, Becker A, Finger P, Meyer-Christoffer A, Ziese M and Rudolf B (2014) GPCC's new land surface precipitation climatology based on quality-controlled in situ data and its role in quantifying the global water cycle. Theoretical and Applied Climatology 115 1 15-40.

Schurer AP, Hegerl GC, Mann ME, Tett SFB and Phipps SJ (2013) Separating forced from chaotic climate variability over the past millennium. Journal of Climate 26 18 6954-6973.

Seager R, Kushnir Y, Chang P, Naik N, Miller J and Hazeleger W (2001) Looking for the Role of the ocean in tropical Atlantic decadal climate variability. Journal of Climate 14 5 638-

655.
Semazzi FHM and Sun L (1997) The Role of orography in determining the Sahelian climate. International Journal of Climatology 17 6 581-596.
Servain J, Picaut J and Merle J (1982) Evidence of remote forcing in the equatorial Atlantic Ocean. Journal of Physical Oceanography 12 5 457-463
Servain J, Wainer I, McCreary JP and Dessier A (1999) Relationship between the equatorial and meridional modes of climatic variability in the tropical Atlantic. Geophysical Research Letters 26 4 485-488.
Shanahan TM, Overpeck JT, Anchukaitis KJ, Beck JW, Cole JE, Dettman DL, Peck JA, Scholz CA and King JW (2009) Atlantic forcing of persistent drought in West Africa. Science 324 5925 377.
Sheffield J and Wood EF (2008) Projected changes in drought occurrence under future global warming from multi-model, multi-scenario, IPCC AR4 simulations. Climate Dynamics 31 1 79-105.
Shin S-I, Sardeshmukh PD and Webb RS (2010) Optimal tropical sea surface temperature forcing of North American drought. Journal of Climate 23 14 3907-3917.
Skinner CB, Ashfaq M and Diffenbaugh NS (2011) Influence of Twenty-First-Century Atmospheric and Sea Surface Temperature Forcing on West African Climate. Journal of Climate 25 2 527-542
Smith TM and Reynolds RW (2003) Extended reconstruction of global sea surface temperatures based on COADS Data (1854–1997). Journal of Climate 16 10 1495-1510.
Smith TM and Reynolds RW (2004) Improved Extended Reconstruction of SST (1854–1997). Journal of Climate 17 12 2466-2477.
Smith TM, Reynolds RW, Peterson TC and Lawrimore J (2008) Improvements to NOAA's Historical Merged Land–Ocean Surface Temperature Analysis (1880–2006). Journal of Climate 21 10 2283-2296
Sterl A and Hazeleger W (2003) Coupled variability and air-sea interaction in the South Atlantic Ocean. Climate Dynamics 21 7-8 559-571.
Stockdale TN, Alves O, Boer G, Deque M, Ding Y, Kumar A, Kumar K, Landman W, Mason S, Nobre P, Scaife A, Tomoaki O and Yun WT (2010) Understanding and predicting seasonal-to-interannual climate variability - The producer perspective. Procedia Environmental Sciences 1 55-80.
Stommel H (1948) The westward intensification of wind-driven ocean currents. Eos, Transactions American Geophysical Union 29 2 202-206
Suárez-Moreno R, Rodríguez-Fonseca B, Barroso JA and Fink AH (2017a) Interdecadal changes in SST-driven teleconnections with Sahel rainfall. Dynamical factors and implications in predictability (submitted)
Suárez-Moreno R, Rodríguez-Fonseca B, Gaetani M and Flamant C (2017b) The North Atlantic Key role in driving the Mediterranean impact on the Sahel (submitted)
Suárez-Moreno R and Rodríguez-Fonseca B (2015) S^4CAST v2.0: sea surface temperature based statistical seasonal forecast model. Geoscientific model development 8 11 3639-3658.
Sultan B and Janicot S (2000) Abrupt shift of the ITCZ over West Africa and intra-seasonal variability. Geophysical Research Letters 27 20 3353-3356.
Sultan B and Janicot S (2003) The West African monsoon dynamics. Part II: The "preonset" and "Onset" of the summer monsoon. Journal of Climate 16 21 3407-3427.
Sultan B, Janicot S and Diedhiou A (2003) The West African Monsoon Dynamics. Part I: Documentation of Intraseasonal Variability. Journal of Climate 16 21 3389-3406
Sultan B and Gaetani M (2016) Agriculture in West Africa in the twenty-first century: Climate change and impacts scenarios, and potential for adaptation. Frontiers in Plant Science 7 1262.

Sylla MB, Diallo I and Pal JS (2013) West African monsoon in state-of-the-science regional climate models. Climate Variability—Regional and Thematic Patterns 10 55140

Taguchi B, Xie S-P, Schneider N, Nonaka M, Sasaki H and Sasai Y (2007) Decadal Variability of the Kuroshio Extension: Observations and an Eddy-Resolving Model Hindcast. Journal of Climate 20 11 2357-2377

Tang B, Hsieh WW, Monahan AH and Tangang FT (2000) Skill comparisons between neural networks and Canonical Correlation Analysis in predicting the equatorial Pacific sea surface temperatures. Journal of Climate 13 1 287-293.

Taylor KE (2001) Summarizing multiple aspects of model performance in a single diagram. Journal of Geophysical Research: Atmospheres 106 D7 7183-7192

Taylor KE, Stouffer RJ and Meehl GA (2012) An overview of CMIP5 and the experiment design. Bulletin of the American Meteorological Society 93 4 485-498.

Thorncroft C and Hodges K (2001) African Easterly Wave Variability and Its Relationship to Atlantic Tropical Cyclone Activity. Journal of Climate 14 6 1166-1179

Thorncroft CD and Blackburn M (1999) Maintenance of the African easterly jet. Quarterly Journal of the Royal Meteorological Society 125 555 763-786

Thorne PW and Vose RS (2010) Reanalyses Suitable for Characterizing Long-Term Trends. Bulletin of the American Meteorological Society 91 3 353-361

Ting M, Kushnir Y, Seager R and Li C (2009) Forced and internal twentieth-century SST trends in the North Atlantic. Journal of Climate 22 6 1469-1481.

Ting M, Kushnir Y, Seager R and Li C (2011) Robust features of Atlantic multi-decadal variability and its climate impacts. Geophysical Research Letters 38 17

Toniazzo T and Woolnough S (2014) Development of warm SST errors in the southern tropical Atlantic in CMIP5 decadal hindcasts. Climate Dynamics 43 11 2889-2913.

Trenberth KE and Caron JM (2000) The Southern Oscillation Revisited: Sea Level Pressures, Surface Temperatures, and Precipitation. Journal of Climate 13 24 4358-4365

Trenberth KE, Stepaniak DP, Hurrell JW and Fiorino M (2001) Quality of Reanalyses in the Tropics. Journal of Climate 14 7 1499-1510

Trenberth KE and Stepaniak DP (2003) Covariability of Components of Poleward Atmospheric Energy Transports on Seasonal and Interannual Timescales. Journal of Climate 16 22 3691-3705

Trenberth KE and Stepaniak DP (2003) Covariability of Components of Poleward Atmospheric Energy Transports on Seasonal and Interannual Timescales. Journal of Climate 16 22 3691-3705

Trenberth KE and Shea DJ (2006) Atlantic hurricanes and natural variability in 2005. Geophysical Research Letters 33 12.

Turner J, Bindschadler R, Convey P, di Prisco G, Fahrbach E, Gutt J, Hodgson D, Mayewski P and Summerhayes C (2009) Antarctic climate change and the environment. Report 554.

Van Oldenborgh GJ and Burgers G (2005) Searching for decadal variations in ENSO precipitation teleconnections. Geophysical Research Letters 32 15

Vannière B, Guilyardi E, Madec G, Doblas-Reyes F and Woolnough S (2013) Using seasonal hindcasts to understand the origin of the equatorial cold tongue bias in CGCMs and its impact on ENSO. Climate Dynamics 40 3-4 963-981.

Vauclair F, du Penhoat Y and Reverdin G (2004) Heat and mass budgets of the warm upper layer of the tropical Atlantic ocean in 1979–99. Journal of Physical Oceanography 34 4 903-919.

Villamayor J and Mohino E (2015) Robust Sahel drought due to the Interdecadal Pacific Oscillation in CMIP5 simulations. Geophysical Research Letters 42 1214–1222.

Vimont DJ (2005) The Contribution of the Interannual ENSO Cycle to the Spatial Pattern of Decadal ENSO-Like Variability. Journal of Climate 18 12 2080-2092

Vimont DJ (2012) Analysis of the Atlantic Meridional Mode using linear inverse modeling:

seasonality and regional influences. Journal of Climate 25 4 1194-1212.
Vislocky RL and Fritsch JM (1995) Improved model output statistics forecasts through model consensus. Bulletin of the American Meteorological Society 76 7 1157-1164.
Vizy EK, Cook KH, Crétat J and Neupane N (2013) Projections of a Wetter Sahel in the Twenty-First Century from Global and Regional Models. Journal of Climate 26 13 4664-4687
von Storch H and Zwiers F (1999) Statistical analysis in climatology. Cambridge University Press, Cambridge
Wahl S, Latif M, Park W and Keenlyside N (2011) On the tropical Atlantic SST warm bias in the Kiel Climate Model. Climate Dynamics 36 5 891-906.
Walker GT (1925) Correlation in seasonal variations of weather- A further study of word weather. Monthly Weather Review 53 6 252-254.
Wallace JM, Smith C and Bretherton CS (1992) Singular Value Decomposition of wintertime sea surface temperature and 500-mb height anomalies. Journal of Climate 5 6 561-576.
Wang G and Eltahir EAB (2000) Biosphere—atmosphere interactions over West Africa. II: Multiple climate equilibria. Quarterly Journal of the Royal Meteorological Society 126 565 1261-1280.
Wang C (2002) Atlantic climate variability and its associated atmospheric circulation cells. Journal of Climate 15 13 1516-1536.
Wang C, Dong S, Evan AT, Foltz GR and Lee S-K (2012) Multidecadal covariability of North Atlantic sea surface temperature, African dust, Sahel rainfall, and Atlantic hurricanes. Journal of Climate 25 15 5404-5415
Wang B, Liu J, Kim H-J, Webster PJ, Yim S-Y and Xiang B (2013) Northern Hemisphere summer monsoon intensified by mega-El Niño/southern oscillation and Atlantic multidecadal oscillation. Proceedings of the National Academy of Sciences 110 14 5347-5352.
Ward MN (1998) Diagnosis and short-lead time prediction of summer rainfall in tropical North Africa at interannual and multidecadal timescales. Journal of Climate 11 12 3167-3191.
Webster PJ, Magaña VO, Palmer TN, Shukla J, Tomas RA, Yanai M and Yasunari T (1998) Monsoons: Processes, predictability, and the prospects for prediction. Journal of Geophysical Research: Oceans 103 C7 14451-14510.
Webster PJ, Clark C, Cherikova G, Fasullo J, Han W, Loschnigg J and Sahami K (2002) The monsoon as a self-regulating coupled ocean—atmosphere system. International Geophysics 83 198-219.
Webster P and Fasullo J (2003) Monsoon: dynamical theory. Encyclopedia of Atmospheric Sciences 3 1370-1391.
Wheeler M, Kiladis GN and Webster PJ (2000) Large-Scale Dynamical Fields Associated with Convectively Coupled Equatorial Waves. Journal of the Atmospheric Sciences 57 5 613-640
Widmann M (2005) One-dimensional CCA and SVD, and their relationship to regression maps. Journal of Climate 18 14 2785-2792.
Wood RA, Keen AB, Mitchell JFB and Gregory JM (1999) Changing spatial structure of the thermohaline circulation in response to atmospheric CO2 forcing in a climate model. Nature 399 6736 572-575.
Xie SP and Carton JA (2004) Tropical Atlantic variability: Patterns, mechanisms, and impacts. Earth's Climate 121-142.
Xue Y and Shukla J (1993) The Influence of Land Surface Properties on Sahel Climate. Part 1: Desertification. Journal of Climate 6 12 2232-2245
Xue Y and Shukla J (1998) Model Simulation of the Influence of Global SST Anomalies on Sahel Rainfall. Monthly Weather Review 126 11 2782-2792

Xue Y, Chen M, Kumar A, Hu Z-Z and Wang W (2013) Prediction skill and bias of tropical Pacific sea surface temperatures in the NCEP Climate Forecast System Version 2. Journal of Climate 26 15 5358-5378.

Zanchettin D, Franks SW, Traverso P and Tomasino M (2008) On ENSO impacts on European wintertime rainfalls and their modulation by the NAO and the Pacific multi-decadal variability described through the PDO index. International Journal of Climatology 28 8 995-1006

Zebiak SE (1982) A Simple atmospheric model of relevance to El Niño. Journal of the Atmospheric Sciences 39 9 2017-2027.

Zebiak SE MC (1984) Tropical atmosphere-ocean interaction and the El Niño/Southern Oscillation Phenomenon. Thesis (Ph.D.) Massachusetts Institute of Technology, Dept. of Earth, Atmospheric, and Planetary Sciences

Zebiak SE (1986) Atmospheric convergence feedback in a simple model for El Niño. Monthly Weather Review 114 7 1263-1271.

Zebiak SE (1993) Air–Sea Interaction in the Equatorial Atlantic Region. Journal of Climate 6 8 1567-1586

Zhang R and Delworth TL (2006) Impact of Atlantic multidecadal oscillations on India/Sahel rainfall and Atlantic hurricanes. Geophysical Research Letters 33 17

Zhang R-H, Rothstein LM and Busalacchi AJ (1998) Origin of upper-ocean warming and El Nino change on decadal scales in the tropical Pacific Ocean. Nature 391 6670 879-883

Zhang RH and Delworth TL (2007) Impact of the Atlantic Multidecadal Oscillation on North Pacific climate variability. Geophysical Research Letters 34 23 L23708.

Zheng X and Eltahir EAB (1998) The Role of vegetation in the dynamics of West African monsoons. Journal of Climate 11 8 2078-2096.

We specially need imagination in science. It is not all mathematics, nor all logic, but it is somewhat beauty and poetry

Necesitamos especialmente de la imaginación en las ciencias. No todo es matemáticas y no todo es simple lógica, también se trata de un poco de belleza y poesía

Maria Montessori